

KUVEMPU  **UNIVERSITY**

Jnana Sahyadri Shankarghatta-577451

**“STUDIES ON RARE EARTH METAL SUBSTITUTED FERRITES
NANO PARTICLES: STRUCTURAL, MORPHOLOGICAL AND
MAGNETIC PROPERTIES”**

Thesis Submitted to the Faculty of Science, Kuvempu
University for the award of the Degree of

**DOCTOR OF PHILOSOPHY
IN
INDUSTRIAL CHEMISTRY**

Submitted By

Mr. Lakshmikantha J. M.Sc

Research Scholar

Department of Industrial Chemistry,

Sahyadri Science College,

Kuvempu University

Under the Guidance of

Dr. G. Krishnamurthy M.Sc., M.Phil., Ph.D.,

Professor

Department of Chemistry & Industrial chemistry

Sahyadri Science College, Shivamogga

2022

KUVEMPU  **UNIVERSITY**

Jnana Sahyadri Shankarghatta-577451

**“STUDIES ON RARE EARTH METAL SUBSTITUTED FERRITES
NANO PARTICLES: STRUCTURAL, MORPHOLOGICAL AND
MAGNETIC PROPERTIES”**

Thesis Submitted to the Faculty of Science, Kuvempu
University for the award of the Degree of

**DOCTOR OF PHILOSOPHY
IN
INDUSTRIAL CHEMISTRY**

Submitted By

Mr. Lakshmikantha J. M.Sc

Research Scholar

Department of Industrial Chemistry,

Sahyadri Science College,

Kuvempu University

Under the Guidance of

Dr. G. Krishnamurthy M.Sc., M.Phil., Ph.D.,

Professor

Department of Chemistry & Industrial chemistry

Sahyadri Science College, Shivamogga

2022

Dedicated To



My Beloved Parents



गुरुर्ब्रह्मा गुरुर्विष्णुः
गुरुर्देवो महेश्वरः ।
गुरुःसाक्षात् परब्रह्म
तस्मै श्रीगुरवे नमः ॥

Teachers & Friends

Declaration

I hereby declare that the research work presented in this thesis entitled “**STUDIES ON RARE EARTH METAL SUBSTITUTED FERRITES NANO PARTICLES: STRUCTURAL, MORPHOLOGICAL AND MAGNETIC PROPERTIES**” is entirely original and was carried out by me in the Department of Industrial Chemistry under the supervision of **Dr. G. Krishnamurthy**, Professor, Department of chemistry and Industrial chemistry, Sahyadri Science College, Shivamogga-577-203, Kuvempu University, Shankaraghatta -577451.

I further declare that the results presented in the thesis or any part thereof has not been submitted elsewhere for any other degree, diploma of similar title in any other Universities.

Date: 22/12/2022

Place: Shivamogga

Lakshmi Kanth J.
Lakshmikantha J.

KUVEMPU UNIVERSITY



SAHYADRI SCIENCE COLLEGE

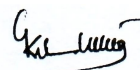


Dr. G. Krishnamurthy M.Sc., M.Phil., Ph.D.
Professor,
Department of Chemistry and Industrial Chemistry,
Sahyadri Science College, Shivamogga-577-203
e-mail: gkmnaiksahyadri@gmail.com
Mobile No: +91-9448774649

Certificate

This is to certify that the research work reported in this thesis entitled “**STUDIES ON RARE EARTH METAL SUBSTITUTED FERRITES NANO PARTICLES: STRUCTURAL, MORPHOLOGICAL AND MAGNETIC PROPERTIES**” submitted by **Mr. Lakshmikantha J** to the Faculty of Science, Kuvempu University, for the award of **Doctor of Philosophy in Industrial Chemistry** is a record of the bonafide and original research work carried out by him under my guidance and direct supervision. The work reported in this thesis has not formed the basis for the award of any degree or diploma or any other similar title.

Date: 22/12/2022
Place: Shivamogga


Dr. G. Krishnamurthy
(Guide)

Dr. G. Krishnamurthy M. Sc., M. Phil., Ph. D.
Professor,
Department of Chemistry
Sahyadri Science College
Kuvempu University

Shivamogga-577203, Karnataka

Acknowledgements

It gives me immense pleasure that I have an opportunity to place a record, the contribution of several people, who have been instrumental in crystallizing this thesis. I have benefited from several people during the course of this work and thankful to the people who lead foundations for this research. It is immense opportunity to link the people here without missing anyone.

My first and sincere thanks must go to my research guide, **Dr. G. Krishnamurthy**, Professor, Department of Chemistry, Sahyadri Science College, Shivamogga, Karnataka, for his unswerving belief in me and constant encouragement, guidance, and mentoring. Over the years, he mentored a truly remarkable group of chemistry researchers. He always gave liberty to think, express and work with, making every meeting friendly and informative. I consider myself quite fortunate to have such an understanding and caring adviser, throughout the course of my research. His friendly nature in discussions has broadened my carrier prospective and my general outlook in life. I feel myself fortunate to have such a supportive guide. I am grateful for his flexibility in supporting me to conduct my work. Finally, I present my sincere and faithful gratitude to him where words are not enough for me to express.

I would like to thank **Prof. B. P. Veerabhadrapa**, Honourable Vice Chancellor, Kuvempu University, for his support to carry out my research work.

I am thankful to **Prof. Rajeswari N.**, Principal, Prof., Sahyadri Science, arts and Commerce College, Shivamogga, for providing me lab facilities for the completion of this research work and thanks for their moral support.

It is with profound respect and devotion that I place on record my deep sense of Gratitude and indebtedness to **Prof. Bhojya Naik H. S.** Professor and Chairman, Department of P.G. Studies and Research in industrial Chemistry, Jnana Sahyadri, Kuvempu University, Shankaraghatta for valuable his constructive suggestions, unfailing patience, friendly approach, constant support and encouragement during the conduct of this research work and preparation of the thesis.

I am also quite grateful to **Dr. Paramesh Naik P., Dr. Prabhakar Chavan**, Faculty members, Dept of chemistry, Sahyadri Science College.

I'm indebted to **Dr. E. Melagiriappa**, Department of Physics, Visvesvaraya Technological University, Belagavi, for their consistent support and advice throughout my research work.

I am also thankful to **Dr. B. M. Nagabhushan**, Department of Chemistry, M. S. Ramaiah Institute of Technology, Bengaluru, Karnataka, India. For their technical and Laboratory support.

I am also thankful to **Dr. Naveen C. S.**, and **Dr. Thejas R.** Department of Physics, School of Engineering, Presidency University, Bengaluru, India. For their consistent support and advice throughout my research work

I am also thankful to my research colleges **Mrs. N. Ranjitha, Mr. Vasantha kumar naik, Dr. Malathesh Pari, Mr. Anil Kumara H. A., Mr. Tippeswamy naik. Mr. Akash G. Y.**, and other friends for their help and kind cooperation during all these years.

I am pleased to extend thanks to **Mr. Kiran Yadav C., Mr. K. G. Manjuntha., Mr. Navaneeth Gowda P.V., Mr. Nagesh S., Mr. Darshan K. S., Mrs. Ranjith Dravid, Mr. Sunil, Mr. Manjunath H. M., Mr. Maruthi, Stone Boys Football Club** and all my friends who were encouraged, and guided, during my Ph.D. work.

I would like to express my deepest love, respect, and admiration to Mother **Smt. Chayadevi P** and Family for their unconditional support, understanding and dedication throughout my life.

I also thank all the library and non-teaching staff of Sahyadri Science College, Shivamogga, and Department of P.G. Studies and Research in industrial Chemistry, Jnana Sahyadri, Kuvempu University, Shankaraghatta.

Finally, I would like to acknowledge all my friends and well-wishers who have helped me at various times but whose names I have been not able to mention here.

Mr. Lakshmikantha J.

LIST OF NOTATIONS

ϵ_0	:	Dielectric Constant Of The Material
ϵ_r	:	Dielectric Constant Of The Material
m_0	:	Mass Of The Electron At Rest
m_e	:	Mass Of The Electron
m_h	:	Mass Of The Hole
μ_0	:	Permeability In Free Space
μ_r	:	Permeability of The Material
μ_B	:	Bohr Magnetrons
μ_r	:	Relative Permeability
mi.	:	Initial Permeability
ϵ'	:	Real Part Of Complex Permittivity
ϵ''	:	Imaginary Part Of Complex Permittivity
nm	:	Nanometer
emu/g	:	Electro Magnetic Unit Per Gram
λ	:	Wavelength
ν	:	Frequency
N/mm ²	:	Netwton per Millimeter Square
M	:	Molar
ml	:	milli litre
°C	:	degree Celsius
rpm	:	Rotation per minute
hrs	:	hours
min	:	minute
Ω -cm	:	Ohm per centimetre
K	:	Kelvin
NPs	:	Nano particles
%	:	Percentage
(+)	:	Up Direction
(-)	:	Down Direction
i.e.	:	That is
kg/m ²	:	Kilo gram per meter Square
g cm ⁻³	:	Gram per Centimeter meter Cube
cm ⁻¹	:	Centimeter Inverse
cm ²	:	Centimeter Square
θ	:	Theta
g	:	Gram
V	:	Volts
μ A	:	Micro Ampere
μ M	:	Micro Meter

LIST OF ABBREVIATIONS

MRI	:	Magnetic Resonance Imaging
BCC	:	Body-Centered Cubic
DC	:	Dielectric Constant
DTA	:	Differential Thermal Analysis
E	:	Energy
EMC	:	Electromagnetic Compatibility
EMI	:	Electromagnetic Immunity
Fe ₂ O ₃	:	Ferric Oxide
FMR	:	Ferromagnetic Resonance
FTIR	:	Fourier-Transform Infrared Spectroscopy
FWHM	:	Full Width at Half Maximum
GHz	:	Giga Hertz
GMR	:	Galvano Magneto Resistance
H	:	Applied Field
H _c	:	Coercivity
JCPDS	:	Joint Committee Powder Diffraction Standards
Hz	:	Hertz
KHz	:	Kilohertz
KOe	:	Kilo Ostead
M	:	Magnetization of a Material
MFe ₁₂ O ₁₉	:	Magnetoplumbite Chemical Formula
MHz	:	Mega Hertz
Mr	:	Remanence
Ms	:	Saturation Magnetization
MWFs	:	Microwave Ferrites
RL	:	Reflection Loss
SHS	:	Self-Propagating High-Temperature Synthesis
SI	:	Signal Integrity
SrM or SrHF's	:	Pure Strontium Hexaferrite
T	:	Tesla
T _c	:	Critical Temperature
TEM	:	Transmission Electron Microscope
TG	:	Thermo Gravimetric
VSM	:	Vibrating-Sample Magnetometer
PXRD	:	X-Ray Diffraction
UV	:	Ultra violet
A-sites	:	Tetrahedral
B-sites	:	Octahedral
EDS	:	Elemental Mapping
RE	:	Rare Earth
H ₂ O	:	Water

TABLE OF CONTENTS

Page No.

- TITLE PAGE
- DEDICATION
- DECLARATION
- CERTIFICATE
- ACKNOWLEDGEMENT
- LIST OF ABBREVIATION
- TABLE OF CONTENTS
- LIST OF PUBLICATIONS

Chapter-1

Introduction.

1.1	Introduction to nanotechnology	1 – 2
1.1.1.	Historical back ground	3 – 4
1.1.2.	Nanomaterials	4 – 7
1.2.	Ferrites	7 – 8
1.2.1.	Nano ferrites	8 – 10
1.2.2.	Magnetic nanoparticles	10
1.2.3.	Classification and Types of ferrites	11 – 19
1.3.	Hexagonal ferrites	19 – 21
1.3.1.	Crystal structure of hexagonal ferrites	21 – 22
1.4.	Classification of hexaferrites	23
1.4.1	M-type hexaferrite	23 – 24
1.4.1(a)	Crystal structure of M-type hexferrite	24 – 26
1.4.2.	Y-type hexaferrite	26
1.4.3.	W-type hexaferrite	26
1.4.4.	X-type hexaferrite	26 – 27

1.4.5. U-type hexaferrite	27
1.4.6. Z-type hexaferrite	27
1.5. Strontium hexaferrite (SrFe ₁₂ O ₁₉)	27 – 28
1.5.1. Strategies for Nanoparticles Synthesis	28 – 30
1.6. Nickel ferrites	30 – 31
1.7. Rare earth substituted ferrites	31 – 32
1.7.1. Rare earth Sr nanoferrites	33
1.8. Magnetic properties of ferrites	33 – 35
1.8.1. Weiss molecular field theory of ferrimagnetism	35 – 36
1.8.2. Neel's theory of ferrimagnetism	36
1.8.3. Yaffet - Kittel Model	36 – 37
1.8.4. Hysteresis studies	38
1.9. Electrical properties of ferrites (DC electrical conductivity)	38 – 40
1.9.1. Dielectric properties	40 – 41
1.9.2. Polarization in dielectrics	41 – 43
1.9.3. Introduction to Impedance spectroscopy	43 – 44
1.10. Electro-analytical techniques	45
1.10.1. Voltammetry	45 – 48
1.10.2. Electrochemical sensor	48
1.10.3. Modification based on nanomaterials	49
1.10.4. Electro-catalytic oxidation of L-Cysteine on the SrHF's /GCE	49
1.11. Gas sensors	50 – 51
1.11.1. Nano composite gas sensors	51
1.11.2. Liquefied petroleum gas	52
1.11.3. Gas sensing importance	53
1.12. Literature survey	53 – 57
1.12.1 Aim of the work	57 – 58
1.13. References	59 – 65

Chapter-2

Experimental and Characterization techniques

2.0. Synthesis method	66
2.1. Materials and Solution combustion synthesis (SCS) method	66 – 69
2.2. Pellet preparation	70

2.3. Final sintering	71
2.4. Experimental techniques	71
2.5. X-ray diffraction studies (XRD)	72
2.5.1. Condition for X-ray diffraction	72 – 73
2.5.2. X-ray diffractometer	73 – 74
2.5.3. Experimental	74 – 75
2.6. Fourier transforms infrared spectroscopic studies (FTIR)	76
2.6.1. Introduction	76
2.6.2. Working of an FTIR spectrometer	77
2.6.3. Experimental	77 – 78
2.7. Scanning electron microscopic studies (SEM)	79
2.7.1. Introduction	79
2.7.2. Principle of scanning electron microscopic	79
2.7.3. Working of scanning electron microscopic	79 – 80
2.7.4. Experimental	80 – 81
2.8. Energy dispersive X-rays analysis (EDAX)	81
2.8.1. Introduction	81 – 82
2.9. UV- visible absorption spectroscopy	82 - 83
2.9.1. Instrumentation	83 – 85
2.9.2. Experimental	85 – 86
2.10. Dielectric properties	86
2.10.1. Experimental	87
2.10.2. Impedance spectroscopy	88
2.10.3. Experimental	88 – 89
2.11. Magnetic characterization	89
2.11.1. Vibrating sample magnetometer (VSM)	90
2.11.2. (a) Basic principle of VSM	90
(b) Working of VSM	90 – 91
2.11.3. Experimental	92
2.12. Thermogravimetric analysis & Differential scanning calorimetry(TGA-DTA)	92 – 94
2.13. Electrochemical properties analysis	94 – 96

2.13.1. Instrumentation of voltammetric sensor	96 – 97
2.13.2. Working electrode	97 – 98
2.13.3. Carbon electrode	98
2.13.4. Reference electrode	98 – 99
2.13.5. Auxiliary electrode	99
2.13.6. Chemically modified electrodes	99 - 100
2.14. Gas sensor	100
2.14.1. Fabrication of gas sensing chamber and Experimental details	100 – 102
2.14.2. Experimental	102
2.15. Reference	103 – 104

Chapter - 3

Effect of Ce³⁺ substitution on Sr²⁺; structural and magnetic properties of nanocrystalline SrFe₁₂O₁₉ hexaferrites prepared by self-propagation method using mixed fuels

3.1 Introduction	105 – 106
3.2. Experimental	106 – 107
3.3 Results and discussion	108 – 117
3.4. Conclusion	118
3.5. References	119 – 121

Chapter - 4

Dielectric properties and magnetic behavior of Gd³⁺ substituted M-type SrFe₁₂O₁₉ nanoferrites by auto combustion method using urea and citric acid mixtures as a dual fuel

4.1. Introduction	122 - 123
4.2. Experimental	123 – 125
4.3. Results and Discussion	126 – 140
4.4. Conclusion	141
4.5. References	142 – 145

Chapter - 5

Synthesis, Structure, Thermal, Magnetic, Dielectric Properties of Ce³⁺ doped M-type SrFe₁₂O₁₉ and Electrochemical Determination of L-cysteine

5.1. Introduction	146 – 149
5.2. Experimental	149 – 150
5.3. Results and Discussion	151 – 169
5.4. Conclusion	170
5.5. References	171 – 175

Chapter - 6

A study on Electrochemical, Gas sensing and Magnetic properties of Sr²⁺ doped Ni_{0.5}Cu_{0.5}MgO₃ synthesized by Auto combustion method

6.1. Introduction	176 – 177
6.2. Experimental	177 – 179
6.3. Results and Discussion	179 – 195
6.4. Conclusion	196
6.5. References	197 – 199

Chapter - 7

Electrochemical and Electrolysis of Gd³⁺ substituted to spinel (NiSrFe₂O₄) nano-ferrites; synthesis, structural, morphological and Magnetic properties.

7.1. Introduction	200 – 202
7.2. Experimental	202
7.3. Results and Discussion	203 – 220
7.4. Conclusion	221
7.5. References	222 – 225

Chapter - 8

Conclusion	226 – 230
------------	-----------

CHAPTER 1:-

INTRODUCTION



1. INTRODUCTION

1.1 Introduction to Nanotechnology

Nanotechnology has emerged as one of the most exciting fields in science and engineering in the twenty first century. Nanotechnology is the production, characterization, design and application of structures, devices and systems by controlling shape and size of matter at nanometer scale (atomic, molecular and supramolecular levels) with unique properties. One nanometer is one billionth of a meter or 10^{-9} m. However, some of these technologies have limited control over structure at the nanoscale, but these are being used to produce useful products. These are also being further developed to produce more sophisticated products with structure in controlled manners [1].

National Science and Technology Council (NSTC) of United States, states that the nanotechnology is the ability to manipulate the structure of matter at molecular level, atom by atom and super molecular level [2]. The aim is to exploit the properties by gaining control of structures and devices at atomic, molecular and supramolecular levels and to learn to efficiently manufacture and use these devices. However, nanotechnology is highly multidisciplinary in its nature, includes all aspects of science and technology includes biomedical sciences, surface science, electronics, semiconductor physics, optics, magnetism, energy production and electrochemistry [1].

Nanotechnology is most useful in aerospace, agriculture, bioengineering, national defense, the environment materials, manufacturing, medicine, military, science and technology, consumer products and transportation [3, 4]. It is truly an atomic and molecular manufacturing approach for building chemically and physically stable structures one atom or one molecule at a time. Nowadays, the active nanotechnology research areas include nanolithography, nanodevices, nanorobotics,

nanocomputers, nanopowders, and nanostructured catalysts and nanoporous materials. Moreover, nanotechnology includes molecular manufacturing, diamondoids, carbon nanotubes, fullerene products, nanolayers, molecular nanotechnology, nanomedicine, nanobiology and organic nanostructures.

Nowadays, the development of nanotechnology created many high quality products which are stronger and light, smaller and fast, more sophisticate high sensitivity and reliability at very low cost and reduced power consumptions. Nanotechnology is a platform that utilizes the unique properties of structural, electrical and magnetic properties of nanosized materials due to their change in structure of single atoms or molecules [1].

In past few years, nanotechnology areas of research include nanolithography, nanodevices, nanorobotics, nanocomputers, nanopowders, nanostructured catalysts and nanoporous materials. In addition to this, molecular manufacturing, diamondoids, carbon nanotube and fullerene products, nanolayers, molecular nanotechnology, nanomedicine, nanobiology, organic nanostructures to name a few.

The development of Nanotechnology created many high quality products can effectively made to be stronger and light, smaller and fast, more sophisticate, high sensitivity and reliability at very low cost and reduced power consumptions. Nanotechnology is a platform that utilizes the unique properties of structural, electrical and mechanical properties of nanostructured materials due to their change in structure of single atoms or molecules [1].

Nowadays, many debates arise for future implications of nanotechnology such as any advance technology regarding toxicity and environmental impact of nanomaterials. Moreover, their potential effects on the global economy and speculation about the several doomsday scenarios [2].

1.1.1 Historical back ground

The first distinguishing concept in nanotechnology was in "There's Plenty of Room at the Bottom", by the famous Noble Laureate physicist Richard P. Feynman with the landmark lecture at an American physical society meeting held at Caltech on December 29, 1959 [5]. Feynman lecture was entitled that "There's plenty of room at the bottom - An invitation to enter a new field of physics". Feynman announced that the whole Britannica encyclopaedia could be placed on the tip of a needle. Moreover, in principle there is no law preventing such an undertaking. Feynman envisioned and described that the advance and past research made in this field as the future of nanotechnology.

The word nanotechnology was first coined by Professor Norio Taniguchi in Tokyo in 1974 in order to describe the super thin processing of materials with nanometer accuracy and the creation of nanosized mechanisms [5]. The nanotechnology emergence in 1980s was due to invention and development of scanning tunneling microscopy (STM) in the early 1980s [6], subsequently other scanning probe microscopy (SPM) such as atomic force microscopy (AFM) [7], fullerenes in 1985 and carbon nanotubes a few years later have opened up new possibilities for the characterization, measurement and manipulation of nanostructures and nanomaterials.

In comparison, the typical carbon-carbon bond lengths or the spacing between these atoms in a molecule, are in the range of 0.12 nm to 0.15 nm and DNA double helix has a diameter of about 2 nm. By convention, nanotechnology is considered in the scale range of 1nm to 100 nm according to the definition used by the National Nanotechnology Initiative United States. The lower limit is determined by the size of hydrogen atoms that has the smallest atoms, which are approximately one quarter of

nm in diameter. The upper limit is more or less arbitrary, but is approximately the size of the phenomena not observed in larger structures start to become apparent and can be used for nano devices [8]. Nanotechnology created many high quality products can effectively made to be stronger and light, smaller and fast, more sophisticate, high sensitivity and reliability at very low cost, and reduced power consumptions.

Nanotechnology is the future science, which started by John Dalton who was the father of modern physics and developed the molecular and atomic structural theory. Nanotechnology developed new nano scale materials called nano particles and investigate to control the matter at atomic scale. The nanoscience has wide applications in the field of medicine, electronics and energy production which satisfying the increasing demands from society [9].

1.1.2 Nanomaterials

The word ‘nano’ refer to Greek prefix meaning dwarf or something very small and depicts one billionth of a meter or 10^{-9} m [5]. The end of the 20th century remarkable advances have been developed in the design of ‘nanomaterials’, such as materials, components and products which may have a structure of only a few tens of atoms in size. Recently, a variety of new and somewhat exotic technical terms having the prefix “nano”, nano-structured, nano-scale, nano-phase, nano-crystalline, nano-lithography, nano-electronics, etc., were entered the advanced materials industry [10, 11]. Nanomaterials act as a bridge between atomic, molecular and bulk system. Tailoring the properties of materials atom-by-atom offers the potential for improvement in device performance for applications across the entire range of human activity: from medicine to cosmetics and food, information and communication to entertainment, earth-bound transport to aerospace, future energy concepts to environment and climate change and security to cultural heritage.

Nanomaterials lead to a radically new approach to manufacturing materials and devices. From fig 1.1 nanomaterials include very clusters (zero dimension), thin surface coating (one dimension) multi-layers, nanorobotics and nanocomputers, nanorods and nanowires (two dimensions), nanoparticles or quantum dots (three dimensions), molecular manufacturing, diamondoids, carbon nanotube and fullerene products, nanomedicine and nanobiology, thin films and composite materials (semiconductor, metal, polymer, etc.) [8]. These materials can be in single, fused, aggregated or collective forms with any shapes like cannular, spherical or irregular shapes.

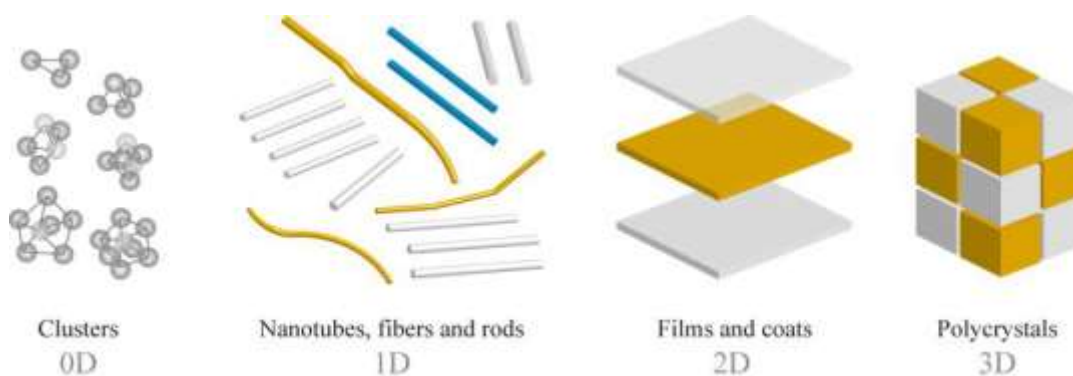


Fig 1.1: Types of nanocrystalline materials: 0D (zero-dimensional) clusters; 1D (one-dimensional) nanotubes, fibers and rods; 2D (two-dimensional) films and coats; 3D (three-dimensional) polycrystals.

The nanomaterials have drawn outstanding attention due to the fascinating size dependent mechanical, electrical, optical, thermal, chemical and magnetic properties [5]. The unique properties of nanostructured materials are due to their changed electronic structure, close to that of an isolated atom or molecule. These properties along with their great chemical and physical stability, that appears them different from their bulk counterparts [7].

Nanocrystalline materials are exceptionally strong, hard, more durable, more reactive and ductile at higher temperature. Moreover, they are wear resistant, erosion resistant, corrosion resistant materials and chemically most active. At nanoscale, electrical conductivity, fluorescence, magnetic permeability, chemical reactivity meets more exotic properties of atomic or molecular world [7, 12]. The magnetic properties of the nanoparticles depend on size, shape of domains, super paramagnetic blocking effects at particular temperature, etc.

Nanomaterials are also much more malleable than their conventional counterparts commercially available. The nanomaterials are classified into seven main categories as carbon based nanomaterial, nanocomposites, metals and alloys, biological nanomaterial, nano-polymers, nano-glasses and nano-ceramics [13]. The nanomaterials have drawn an outstanding attention due to the fascinating size dependent optical, chemical, mechanical, thermal, electrical and magnetic properties [12]. Moreover, with their great chemical and physical stability nanomaterials are different from their bulk counterparts [7].

Nanomaterials have a relatively larger surface area compared to their bulk counter parts. In addition, Quantum effects rule the behavior of nanomaterials and modify optical, electrical and magnetic properties of the materials. The nanocrystalline materials used in several scientific fields such as medicine, cosmetics, information, communication, entertainment, earth based transport, aerospace [14-17]. Moreover, they are used in biomedical sciences, surface science, optics, magnetism, energy storage and electrochemistry [14]. Materials reduced to nanoscale exhibit different electrical and magnetic properties compared to their bulk counterparts, enabling unique applications. For instance, opaque substances turn into transparent

(copper); inert materials become catalysts (platinum); stable materials turn combustible (aluminum); solids turn into liquids at room temperature and insoluble materials become soluble (gold). A material such as gold, which is chemically inert at normal scales, can serve as a potent chemical catalyst at nanoscale [8].

1.2 Ferrites

Oxide ceramics which exhibit ferrimagnetic behaviour play an important role in electronics industry and are commonly known as ferrites [16]. These materials possess a wide range of crystal structure, compositions and applications.

Ferrimagnetic ceramics exhibit spontaneous magnetization in absence of an external field, consists of self-saturated domains and show the characteristic hysteresis behavior [16 18,19]. A remarkable property of ferrites make them suitable for many applications is their high electrical resistivity which varies from 10^{-3} to 10^{11} Ω -cm. The resistivity of ferrites, depends on the composition i.e., six to twelve orders of magnitude higher than that of ferromagnetic materials such as permalloys and silicon irons. This has given ferrites a distinct advantage as magnetic materials of choice in high frequency applications, although their saturation magnetization is approximately one fifth to one eighth that of silicon irons. In most high frequency applications of ferrites is eddy currents that may be absent or negligibly small. Such intrinsic properties make them indispensable materials in communications and electronics industry, where frequencies in the range 10^3 to 10^{11} Hz have to be handled. In addition, the crystal structures of ferrite are tolerant to numerous variations in their chemical compositions, giving technologists access to wide range of properties.

The first magnetic material known to man was magnetite or natural ferrite Fe_3O_4 (FeOFe_2O_3). Hilpert [20] prepared the first synthetic ferrite and established the formula for spinel structure ($\text{Me Fe}_2\text{O}_4$), where Me is the divalent metal ion. Ferrites

came into prominence at the end of the Second World War. The early work on ferrimagnetic materials was done in Japan by Kato and Takeai [21], Kawai [22] and in Netherlands by Snoek [23].

Neel proposed the basic theory of spin–spin interactions and the two magnetic sublattices and coined the word “ferrimagnetism” [24]. Anderson and VanVleck proposed the theory of super exchange interactions [25]. Yaffet and Kittel extended the Neel’s model and introduced the concept of triangular or canted spin [26]. Guillaud and Gorter provided the direct experimental evidence for Neel’s modified theory [27, 28]. Snoek studied the homogeneity and oxygen stoichiometry effects on ferrites [23]. Verwey reported the electrical conductivity mechanism in ferrites owing to simultaneous existence of both Fe^{2+} and Fe^{3+} ions at B-sites [29]. Brabers attributed the electrical conductivity in ferrite materials is attributed to exchange of electrons between Fe^{2+} and Fe^{3+} ions on B-sites [30]. Ferrites show abnormally, high dielectric constant and resistivity. Koops studied phenomenological theory of dispersion for inhomogeneous structure which obeys Maxwell-Wagner interfacial polarization model [31-33]. It has been assumed that sintered ferrites comprising of good conducting grains surrounded by low conducting grain boundaries. Waldron has been reported infrared absorption spectra of spinel ferrites and suggested the position of ions and crystal vibrational modes [34].

1.2.1 Nanoferrites

With the new era of nanosciences, the origin of nanotechnology, the study of ferrites at nanosize is an interesting matter because of their interesting structural, electric and magnetic properties compared to their bulk materials [35, 36]. Moreover, nanoferrites exhibit the unique properties viz., higher values of chemical stability,

mechanical hardness, Curie or critical temperature, corrosion resistivity, magnetostriction, magneto-crystalline anisotropy, magneto-optical property and low loss of energy [37, 38]. The unique properties of nanomaterials are owing to their change in electronic configuration, similar to a single atom or molecule. Nowadays, nanocrystalline ferrites possess intriguing superior properties compare to their bulk counterparts [8]. Importantly, the nanoferrites have high surface to volume ratio responsible for spin canting, surface anisotropy, superparamagnetism (SP), reduced magnetisation and Curie temperature [39], and magneto-optical properties, low energy losses and low cost [40], single domain behavior, [41]. The most important properties of nanoferrites viz., crystal structure, microstructure, electric and magnetic properties. The properties depending upon synthesis method, stoichiometric composition, sintering time and sintering temperature, dopants, crystallite size and shape etc., [42-44]. The interesting and useful magnetic properties of nanoferrites depending upon the cations distribution along with Fe^{2+} and Fe^{3+} ions between tetrahedral sites (A-site) and octahedral sites (B-sites) of the crystal lattice [45].

Nowadays, the technology has progressed by leaps and bounds, especially in the field of telecommunication, mobile towers, and aircrafts. In the era of modern communication, microwave absorbing materials have attracted a lot of attention through the study of spinel ferrites. The different characteristics of nanoferrites materials, such as coercivity, magnetisation, conductivity, impedance and permittivity have contributed to its microwave absorbing property.

In recent decades, nanoferrites could not be replaced by any other magnetic materials due to relatively low cost, chemically stable and found a wide range of technological applications in microwave devices, high speed digital tapes and disk

recording, ferrofluids, magnetic refrigeration systems (MRI) [7], biosensors, recording colour imaging. Moreover, these nanoferrites are used in bioseparation as magnetic carriers in biomedicine, immobilization of proteins and enzymes, biological fluids detoxification, magnetically targeted transport of drugs anti-cancer, magnetic resonance imaging [46], sensing and cancer treatment application [47-50]. In recent years, more intensification of ferrites is in wireless technology, viz., in high speed wireless network, internet manageable cell phones, has reconnoitered the superficies of real-time intimation. Furthermore, multilayer chip inductors (MLCIs) are more important components in the miniaturization of many electronic devices like cellular phone, notebook computer, video camera [51, 52].

1.2.2 Magnetic nanoparticle

Magnetic nanoparticle emerges as one of the important areas because of its fascinating magnetic properties, synthesis flexibility and novel applications [53, 54]. Magnetic properties can be tailored by suitable dopant on the basis of site preference and matching of atomic size [55]. It is well known that because of surface spin frustration, magnetization of magnetic nano particles is lower than that of its bulk counterpart [44]. Magnetic nano particles are mainly used in Health, storage, sensor and communication sectors. Nanosized magnetic materials explore a number of unusual and more interesting magnetic properties compare to bulk smart materials. Below some of the critical sizes, magnetic nanoparticles became single-domain and shown superparamagnetic behavior [56, 57].

1.2.3 Classifications and Types of Ferrites

Ferrites are composed of iron oxides as their constituent and metal oxides. Depending upon the crystal structure, ferrites are following types and showed in the table 1.1

- i. Spinel ferrites (Soft ferrites)
- ii. Garnet
- iii. Orthoferrite
- iv. Hexagonal ferrites (Hard ferrites)

(i) Soft ferrites (Spinel ferrites)

Soft ferrites are ferrimagnetic materials with cubic crystal structure and they are characterized by chemical formula $MO \cdot Fe_2O_3$, where M is a transition metal ions like iron, nickel, manganese or zinc. Soft ferrites have high saturation magnetization (M_s), low remanence magnetization (M_r), low coercivity (H_c), high electrical resistivity (ρ), high magnetic susceptibility (χ) and high permeability (μ). Soft ferrites are not suitable for permanent magnets as they can be easily magnetized and demagnetized [58]. Soft magnetic material is one that can be both easily magnetized and demagnetized, so that it can store or transfer magnetic energy in alternating or other changing wave forms (sine, pulse, square, etc) [58]. They are widely used in high frequency applications where different losses are supplementary to the high frequency applications is more essential rather than the static magnetic characteristics [59]. Soft ferrites are used in transformer, inductors, microwave isolators, antenna rods, electromagnets, magnetic recording, storage media etc., [58].

Spinel ferrites

Spinel ferrites are magnetically soft and they are alternative to metallic magnets such as Fe and layered Fe-Si alloys, but exhibit enhanced performance due to their outstanding magnetic properties [60]. Spinel ferrites have the properties such as

high electrical resistivity and low magnetic losses. The two popular ceramic magnets; nickel-zinc ferrites and manganese-zinc ferrites are the major members of the spinel ferrite family. They have been intriguing ceramic materials due to their high electrical resistivity, high magnetic permeability and possible modification of intrinsic properties over a wide spectrum [61].

Table 1.1 Classifications and Types of Ferrites

Sl. No	Types	Molar ratio	Crystal structure	General formula	Replacements	Representations
1	Spinel	$\text{Fe}_2\text{O}_3 - 1\text{MeO}$	Cubic	$\text{A}^{\text{II}}\text{Fe}_2\text{O}_4$	$\text{A}^{\text{II}} - \text{Mn, Zn, Ni, Mg, Co}$	MeO - Transition Metal oxide
2	Garnet	$5 \text{Fe}_2\text{O}_3 - 3 \text{Me}_2\text{O}_3$	Cubic	$\text{Ln}^{\text{III}} 3\text{Fe}_5\text{O}_{12}$	$\text{Ln}^{\text{III}} - \text{Y, Sm, Eu, Gd, Tb, Dy, Ho, Er, Tm and Lu}$	Me_2O_3 is a rare earth metal oxide
3	Ortho ferrite	AFeO_3	Perovskite	$\text{Ln}^{\text{III}}\text{FeO}_3$	$\text{Ln}^{\text{III}} - \text{Y, Sm, Eu, Gd, Tb, Dy, Ho, Er, Tm and Lu}$	A is rare earth elements like Ho, Dy, Er, Y, Yb
4	Hexaferrite [Magnetoplumbite]	$6 \text{Fe}_2\text{O}_3 - 1\text{MeO}$	Hexagonal	$\text{A}^{\text{II}}\text{Fe}_{12}\text{O}_{19}$	AII- Ba, Sr, Pb	MeO -Divalent metal oxide from group IIA Ex; BaO, CaO, SrO

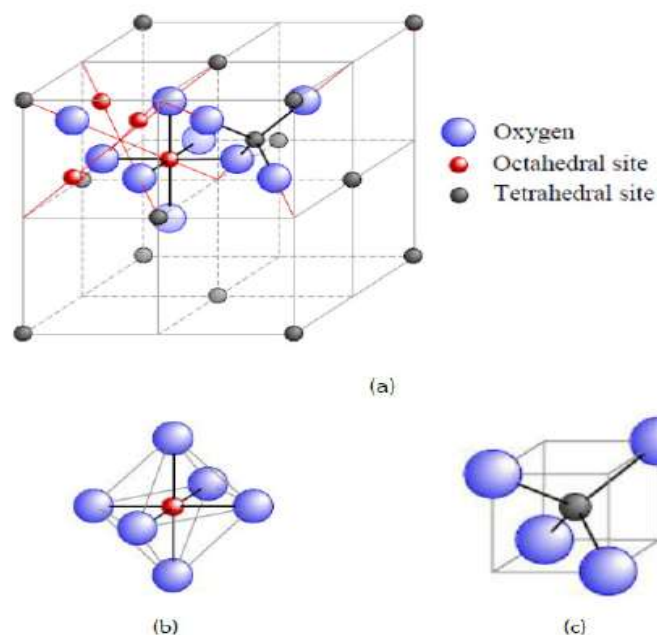
(i.a) Crystal structure of spinel ferrites

Fig.1.2. (a) Structure of spinel unit cell structure, (b) octahedral sites [B-site] and (c) tetrahedral [A-site].

The crystal structure of ferrites is an interlocking network of positively charged metal (Fe^{3+} , Me^{2+}) ions and negatively charged (O^{2-}) divalent oxygen ions [62]. The ferrites exhibit spinel structure. The ferrite crystal is ionic having cubic face centered crystal structure with space group $\text{Fd}_{3m} \text{O}_h^7$ [62]. The spinel structure takes its name from mineral spinel MgAl_2O_4 (or $\text{MgO} \cdot \text{Al}_2\text{O}_3$). The crystal structure has been determined by Bragg [40] and independently by Nishikawa [64]. Similar to mineral spinel, the general formula of spinel cubic ferrite written as $\text{Me}^{2+}\text{O} \cdot \text{Fe}^{3+}_2\text{O}_3$, where, Me^{2+} is divalent metal ion. They are Co^{2+} , Zn^{2+} , Fe^{2+} , Mg^{2+} , Ni^{2+} , Cd^{2+} and Cu^{2+} ion. The unit cell with eight formula units composed of 8 Me^{2+} ions, 16 Fe^{3+} ions and 32 O^{2-} ions. The 32 oxygen ions are arranged in a closely packed face centered cubic (FCC) structure. The oxygen ions form two kinds of interstitial sites are

commonly known as tetrahedral site or A-site and octahedral site or B-site. In this structure, A-site coordinated with four oxygen ions and B-site coordinated with six oxygen ions. In total, each unit cell of crystal structure contains of total 96 interstitial sites i.e. 64 A-sites and 32 B-sites. Among all cations occupy only 8 of the available 64 A-sites and metal ions occupy 16 of 32 B-sites respectively. The spinel structure of crystal is depicted in fig 1.2.

Types of spinel ferrites

The metal ions distributed on A-site and B-site depends on the factors (i) ionic radius of the specific ion, (ii) size of the interstices, (iii) electronic configuration (iv) temperature and (v) electrostatic energy. On this basis of cation distribution, structure of spinel ferrites is classified into three groups.

(a) Normal spinel ferrites

In a normal spinel structure, all divalent metal (Me^{2+}) ions and trivalent metal (Fe^{3+}) ions are occupy A-sites and B-sites respectively. A normal spinel is described as the cation distribution of the ferrite is $(\text{Me}_{\delta}^{2+} \text{Fe}_{1-\delta}^{3+})_{\text{A}} [\text{Me}_{1-\delta}^{2+} \text{Fe}_{1+\delta}^{3+}]_{\text{B}} \text{O}_4^{2-}$ e.g. $(\text{Zn}^{2+})_{\text{tetra}} [\text{Fe}_2^{3+}]_{\text{octa}} \text{O}_4^{2-}$ and $(\text{Cd}^{2+})_{\text{tetra}} [\text{Fe}_2^{3+}]_{\text{octa}} \text{O}_4^{2-}$.

(b) Inverse spinel ferrites

In an inverse spinel, all the divalent metal ions are occupying B-sites and all trivalent metal ions are equally occupied on A-sites and B-sites per unit cell. These ferrites are known as ferrimagnetic. The formula for an inverse spinel structure is written as $(\text{Fe}^{3+})_{\text{tetra}} [\text{Me}^{2+} \text{Fe}^{3+}]_{\text{octa}} \text{O}_4^{2-}$ where $\text{Me}^{2+} = \text{Mg}, \text{Mn}, \text{Ni}, \text{Cu}, \text{Zn}, \text{Co}, \text{Fe}$ etc.

(c) Random spinel ferrites

In these ferrites, divalent and trivalent iron ions are randomly distributed over A-sites and B-sites. The whole range of possible distribution of Me^{2+} and Fe^{3+} ions on A-sites and B-sites can represented by the general relation: $\text{Me}_{\delta}^{2+} \text{Fe}_{1-\delta}^{3+} [\text{Me}_{1-\delta}^{2+}$

$\delta\text{Fe}^{3+}_{1+\delta}]\text{O}_4^{2-}$ where δ is measure of degree of inversion and depending on method of preparation and temperature. For a completely random distribution $\delta=1/3$; for normal spinel $\delta=1$ and for an inverse spinel $\delta = 0$

(ii) Garnet ferrites

The second group of ferrites is the garnet type ferrites. Garnet is a general name applied to a group of specific silicates, minerals, having similar crystal structure. Garnets, unique magnetic ceramics have optical transparency and used in magneto-optical applications. Garnet having formula $\text{R}_3^{3+} \text{Fe}_5^{3+} \text{O}_{12}$ is body centered cubic structure with eight formula unit and three sub-lattices namely octahedral, tetrahedral and dodecahedral; R can be La^{3+} , Dy^{3+} , Gd^{3+} , Er^{3+} , Eu^{3+} , Sm^{3+} , etc. Yttrium iron garnet (YIG) is a synthetic garnet with chemical composition $\text{Y}_3\text{Fe}_5\text{O}_{12}$. Yttrium can be replaced by one of the rare earth ions like La^{3+} , Dy^{3+} , Gd^{3+} , Er^{3+} , Eu^{3+} , Sm^{3+} etc [65]. Natural garnet belongs to a wide spread class of minerals of the general chemical formula $\text{M}_3\text{Fe}_2\text{Fe}_3\text{O}_{12}$ or more informatively $(3\text{M}_2\text{O}_3)_c (2\text{Fe}_2\text{O}_3)_a (3\text{Fe}_2\text{O}_3)_d$, where M is rare earth metal ion or an yttrium ion and the super scripts c, a, d refer to lattice dodecahedral (c-site), octahedral (a-site) and tetrahedral (d-site) site. The garnet structure is one of the most complicated crystal structures and it is difficult to draw a two dimensional representation that shows clearly all ions (160) in the unit cell [65].

(ii.a) Crystal structure of Garnet ferrites

The garnets have orthorhombic crystal structure (oxygen polyhedra, surrounding the cations) but with trivalent cations (including rare earth and Fe^{3+}) occupying tetrahedral (d), octahedral (a), or dodecahedral a 12-sided distorted polyhedral (c) sites. Specifically, the interaction between tetrahedral and octahedral

sites is antiparallel, and the net magnetic moment is antiparallel to the rare earth ions on the c sites. The garnet structure is one of the most complicated crystal structures and it is difficult to draw a two dimensional representation that shows clearly all the ions (160) in the unit cell. For simplicity, only an octant of a garnet structure that shows just the cation positions is shown in fig 1.3. The garnet structure is composed of a combination of octahedral (trivalent cation surrounded by six oxygen ions), tetrahedral (trivalent cations surrounded by four oxygen ions), and 12-sided Polyhedral - dodecahedral - (trivalent cations surrounded by 8 oxygen atoms) sites, the orientations of which are shown in fig 1.4. The chemical formula for garnets is $3\text{Me}_2\text{O}_3 \cdot 5\text{Fe}_2\text{O}_3$ where Me represents the trivalent rare earth ions like non-magnetic yttrium or a magnetic rare earth such as from lanthanum through ytterbium.

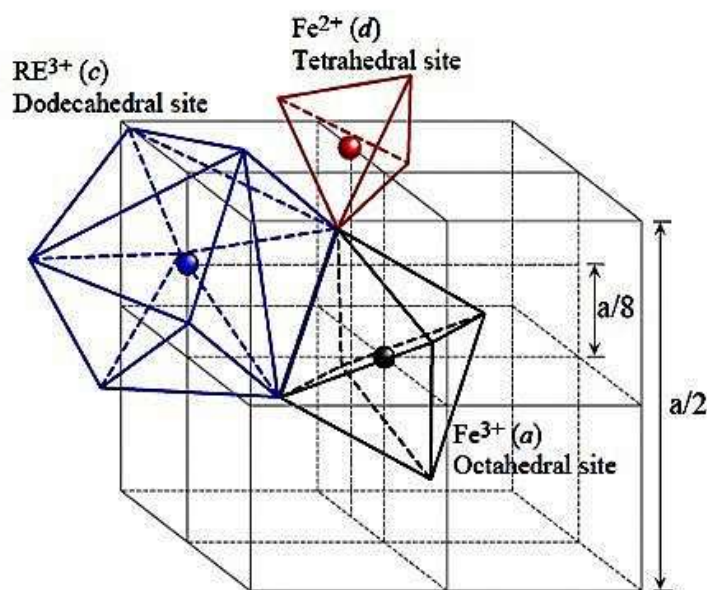


Fig 1.3: Crystal structure of Garnet ferrite [19, 20]

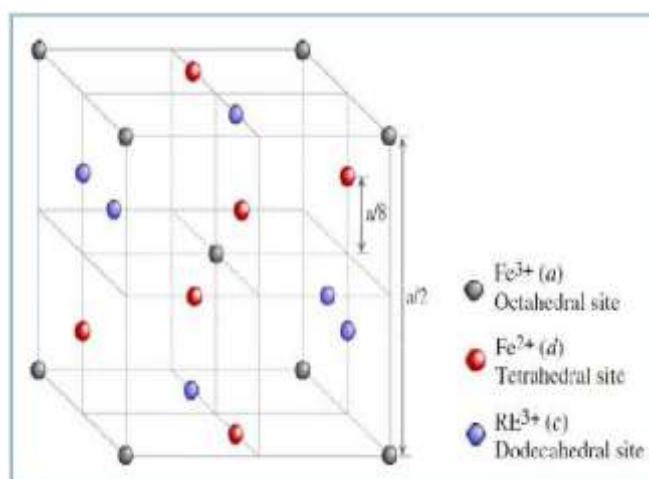


Fig 1.4. Unit cell of rare earth garnet.

The five iron (III) ions occupy two octahedral and three tetrahedral sites, with the yttrium (III) ions coordinated by eight oxygen ions in an irregular cube. The iron ions in the two coordination sites exhibit different spins, resulting in magnetic behavior. By substituting specific sites with rare earth elements, interesting magnetic properties can be obtained. Trivalent iron ions on Tetrahedral (d) and Octahedral (a) are important for magnetic property. These two sites are coupled anti-ferromagnetically [65] and yields a Ferrimagnetic crystal [65].

(iii) Ortho ferrites

Ortho ferrites possess extremely high velocities of the domain wall motion and it is used in communication techniques, in optical internet, in sensors of magnetic fields and electrical currents, mechanical quantities etc.

(iii.a) Crystal structure of ortho ferrite

Rare earth orthoferrites are classified as ferrites, although they are canted antiferromagnets. The magnetic oxides with perovskite structure, which have been an exception in the group of oxides. The perovskite structure is shown schematically in fig 1.5. Large divalent or trivalent ions (A) occupy the corners of a cube and small

trivalent or tetravalent metal ions (B) occupy the centre of the cube. The oxygen ions are situated centrally on the faces of the cube. The general chemical formula is ABO_3 , where A represents yttrium or a rare earth.

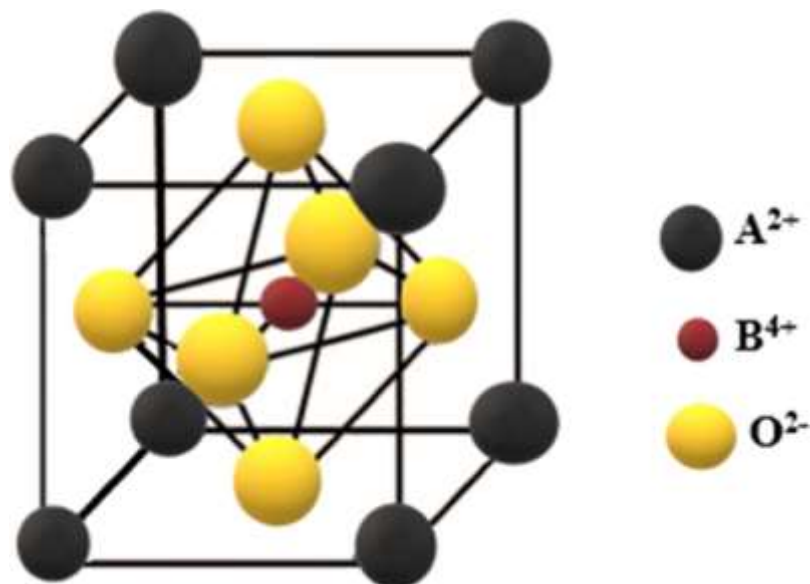


Fig. 1.5 Crystal structure of Orthoferrite

The magnetic structure inside of a sublattice is usually collinear ferromagnetic, but the different sublattices are coupled antiferromagnetically. Due to the different number of magnetic ions in different magnetic moment results into ferrimagnetism. The nature of the super exchange interaction depends not only on the type of the magnetic ion, but rather strongly on the bond length and bonding angle. This makes it possible type of the super exchange interaction

(iv) Hard ferrites

Hard ferrites are used as permanent magnets due to their low saturation magnetization (M_s), high remanence magnetization (M_r), high coercivity (H_c) and high magnetic permeability (μ). These ceramic magnets have a hexagonal crystal structure and carry out magnetic flux well in a magnetically saturated state because of

which they are capable of storing magnetic fields stronger than iron itself. A good permanent magnet produces a strong magnetic field and is rigid against the conditions which tend to demagnetize it. Uniaxial magnetic anisotropy is an essential requisite in such magnetic materials. Hard ferrites have found various applications in household products like refrigerator magnets, electrical motors, loudspeakers and also used in automotive sensors, hall effect devices, magnetic separators, MRIs etc. [66, 67]. M-type hexaferrites which include $\text{BaFe}_{12}\text{O}_{19}$ (BHF) and $\text{SrFe}_{12}\text{O}_{19}$ (SHF) are the best examples of such hard hexagonal magnetic materials.

1.3 Hexagonal ferrites

Magnetic materials are very useful in industries and have technological applications. In 1952, a new class of ferrites having permanent magnetic properties was discovered. Workers at Philips laboratory at Eindhoven in the Netherlands made the developments of hexagonal structure (hexaferrites) possible [68].

Hexagonal ferrites with general formula $\text{MeFe}_{12}\text{O}_{19}$ where Me is usually Barium (Ba^{3+}), Strontium (Sr^{3+}), Calcium (Ca^{3+}) or Lead (Pb^{3+}) have been distinguished due to their high uniaxial magnetocrystalline anisotropy which renders them perfect for permanent (hard) magnet applications [41]. However, classic magnetic materials (metals) show some limitations in the process of miniaturization which is fundamental in the advancement of the technology. This is due to their high density and high weight. Considering their excellent magnetic properties and their relatively low density, hexaferrite materials present themselves as adequate substitute of metals. Due to their magnetic properties, these hexaferrites are used in applications such as permanent magnet, magnetic record media, chip soft-magnetic components,

motor components, telecommunication, absorber material, sensors, microwave devices, military, radiation shielding, EMI devices and biomedical [69-72].

Hexagonal ferrites are one of the most common and useful materials, due to their special magnetic properties, prime applicant as permanent magnets attributed to their attractive magnetic properties like high values of magnetization, high uniaxial anisotropy and coercivity. All the more regularly, hexagonal ferrites are utilized for high-density recording and high frequency microwave devices. Hexagonal ferrites are the class of materials with electromagnetic conductivity, permittivity and permeability suitable for electromagnetic interference suppression and radar absorbing material coatings from centimetre to sub millimeter wavelengths of the electromagnetic spectrum. Moreover, Hexaferrites are being one of those materials which have a great scope as magneto dielectric material. Various parameters affect the attenuation of electromagnetic waves in the radar absorbing material. The interaction of microwaves with the material is decided by the intrinsic properties of the material such as conductivity, permittivity and permeability therefore there is need to study these properties of the hexaferrite. Furthermore, M type hexaferrites are of interest for the use as absorber in the GHz range as it exhibit FMR in this frequency range. It has been a great challenge to achieve magnetic materials with high μ and at microwave frequencies suitable for antenna applications such as magneto dielectric substrates.

The technological application of these ferrites at high frequencies needs pure material in planar form. Thick film technology is of interest because it has proved to be cost effective and highly conducive to planarization. Most of the studies on planar ferrites at high frequencies are of the ferrites in thin film form. Although the concept of thick-film structures is quite attractive, they are not very widely used till now.

Barium ferrite ($\text{BaFe}_{12}\text{O}_{19}$) and Strontium ferrite ($\text{SrFe}_{12}\text{O}_{19}$) are the examples of hexagonal ferrites and they have received much interest in recent years because of microwave device applications. Barium hexaferrite is especially of interest for use in hybrid microwave devices, monolithic microwave integrated circuits or even as a future replacement for yttrium iron garnet [73] due to its high uniaxial anisotropy and large resistivity. The next generation of magnetic microwave devices (isolators, filters, phase shifters, and circulators and related components) will be planar, self-biased, and low loss, and operate better than today's devices [74].

1.3.1 Crystal structure of Hexagonal Ferrites

Hexagonal ferrites have the general formula $\text{MeFe}_{12}\text{O}_{19}$ where Me is a divalent ion of a large ionic radius, such as Ba^{2+} , Sr^{2+} or Pb^{2+} . Some compound with trivalent Me (e.g. La^{3+} , Al^{3+} , Ga^{3+} , Cr^{3+} , Fe^{3+}) are also known. In these, one iron ions per formula unit is present as Fe^{2+} to allow for the charge compensation as showed in fig. 1.6 and table 1.2.

The unit cell is hexagonal and contains two molecules of $\text{MeFe}_{12}\text{O}_{19}$. The hexagonal ferrites have high magneto-crystalline anisotropy. They are thus ideally suited to be permanent magnetic material and having high coercivity. Their high anisotropy is attributed to the Fe^{3+} ions at the trigonal bipyramide site. The other important hexagonal ferrites have a structure related to that of magneto-plumbites. These ferrites are further sub classified into M, W, Y, Z and U compounds. The crystal structure of barium ferrite is hexagonal with unit cell made up of two unit formulae. Hexaferrite possesses magnetoplumbite structure is hexagonal. Thus, it has a major preferred axis called the 'c'-axis and a minor axis called the advantage as a permanent magnet material. Hexagonal ferrites are referred to as hard as the direction

of magnetization cannot be changed easily to another axis. The oxygen ions are close to each other in the spinel structure but there are oxygen layers which now include the Ba^{2+} , Sr^{2+} or Pb^{2+} ions which have about the same ionic radii as the oxygen ions and therefore can replace them in the lattice available all of which can be derived by combining the ferrite spinel and ferroxdure (BaO).

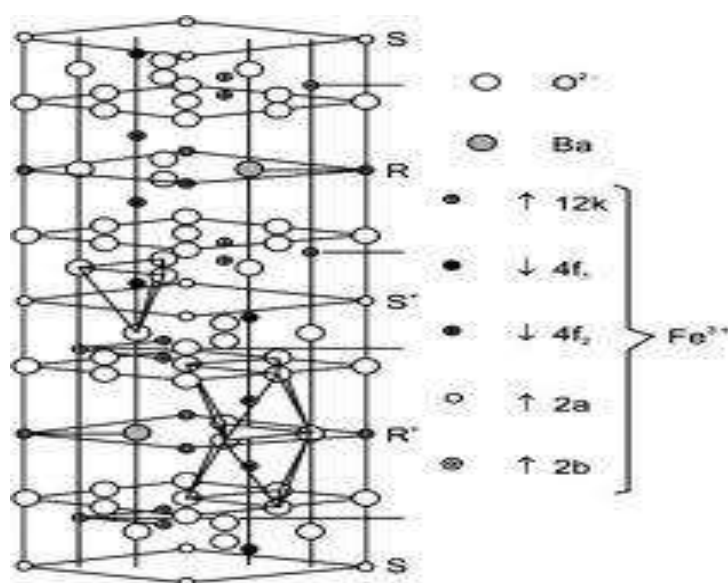


Fig.1.6. Cell structure of M-type strontium hexaferrite ($\text{MeFe}_{12}\text{O}_{19}$)

Table 1.2: Number of Fe^{3+} ions in sublattices of hexaferrites and their spin.

Site	Co-ordination	No of Fe ions	Spin	Block
12k	Octahedral	6	Up (\uparrow)	R-S
4f1	Tetrahedral	2	Down (\downarrow)	S
4f2	Octahedral	2	Down (\downarrow)	R
2a	Octahedral	1	Up (\uparrow)	S
2b	Fivefold (Trigonal Bipyramidal)	1	Up (\uparrow)	R

1.4 Classification of Hexaferrites

On the basis of the crystal structure, up to now hexaferrites are sub classified into six categories namely M, Y, W, Z, X, and U as listed in table 1.3. In our work, we have taken Me-M nomenclature to represent M type hexaferrite where Me is the element like Ba, Sr, Ca, or Pb.

Table 1.3. Different types of Hexaferrites

Sl. No.	Hexaferrite type	Chemical formula	Crystallographic build up Cell structure
1	M-type	$AFe_{12}O_{19}$	RSR*S*
2	Y-type	$A_2Me_2Fe_{12}O_{22}$	TSTST
3	W-type	$AMe_2Fe_{16}O_{27}$	RSSR*S*S*
4	X-type	$A_2Me_2Fe_{28}O_{46}$	RSTSR*S*T*S*
5	U-type	$A_4Me_2Fe_{36}O_{60}$	RSR*S*S*
6	Z-type	$A_3Me_2Fe_{24}O_{41}$	RSR*S*T*S*

1.4.1 M-type hexaferrite

Hexaferrites of M-type have a general chemical formula of $Me_{0.6}Fe_2O_3$ (with Me= Ba or Sr) has the same structure as magnetoplumbite (space group P63/mmc) with typical lattice constants of $a=5.88 \text{ \AA}$ and $c=23.2 \text{ \AA}$. Hexaferrites of M-type have a general formula $MO_6Fe_2O_3$, where M represents divalent ions such as Ba^{2+} , Sr^{2+} or Pb^{2+} has the same structure as magnetoplumbite (space group P63/mmc) with typical lattice constants of $a=5.88 \text{ \AA}$ and $c = 23.2 \text{ \AA}$ [75]. It has hexagonal structure composed of stacked spinel ionic layers with interspaced ionic layers of M^{2+} , O^{2-} , and Fe^{3+} . These types of oxide ferrites have extensive magnetocrystalline anisotropy due to their low crystal symmetry.

The magnetoplumbite unit cell contains a total of ten layers, two of which contain the Sr^{2+} four layers of four oxygen ions each followed by a layer of three

oxygen ions and one Sr^{2+} ion again followed by four layers of four oxygen as having ions each; and another layer containing three oxygen and one Sr^{2+} ion but situated diametrically opposite to the Sr^{2+} ion in the previous layer containing Sr^{2+} . The Fe^{3+} ions are located in the interstices of these ten layers. There are octahedral and tetrahedral sites plus one more type not found in the spinel structure in which the metal ion is surrounded by 5 oxygen ions forming a trigonal bi- pyramid in the same layer as the Sr^{2+} ion.

1.4.1.(a) Crystal Structure of M-type Hexaferrite

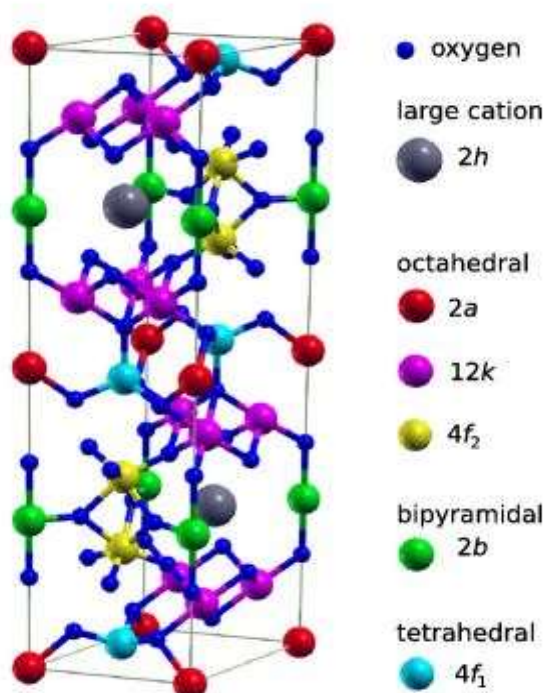


Fig. 1.7 Unit cell of M-type hexaferrite $\text{MFe}_{12}\text{O}_{19}$ and represents cell structure of M-type strontium hexaferrite ($\text{SrFe}_{12}\text{O}_{19}$).

Basic unit cell of magnetoplumbite structure includes two principle groups. Each unit/cell consists of two five-oxygen layers as showed in fig. 1.7. Every particle indicates 180° rotation uniformity around the hexagonal c-pivot. The oxygen ion layer containing M^{2+} being orthogonal to c-axis acts as a mirror plane. Hence, it may be

quoted that every unit cell comprises of ten oxygen layers, successively developed from four blocks termed as, S, R, S* and R*. Where S is spinel and R is hexagonal. The organization of atoms in S* and R* is in agreement with S and R blocks but rotated at an angle of 180° about c axis in reference to S and R. The S / S* section comprises of 2 oxygen ions layers, whereas R or R* section consist of 3 oxygen layers, with 1 site of oxygen in the center layer replaced by one M^{2+} ion [76]. In various crystallographic lattice sites, each cell has 6 interstitial Fe^{3+} ions with spins in upward and downward directions. M^{2+} , Fe^{3+} cations possess the interstitial places of the element frame. The M-type hexaferrite takes shape of hexagonal geometry with sixty-four ions for each unit dispersed in eleven completely different symmetry sites [77].

The unit cell consist of thirty-eight oxygen ions, twenty-four ions of iron and a couple of M ions where (M= Sr^{2+} , Ba^{2+} , and Pb^{2+}). The twenty-four iron ions are divided in 5 completely distinguished lattice sites i.e. 2a, 2b, 4f1, 4f2 and 12k. Amongst these 5 sites, 2a, 12k and 4f2 are octahedral, 4f1 is tetrahedral and 2b could be a symmetric bipyramid (2b) site. The sites 4e, 4f, 6h, and 12k are possessed by oxygen ions to frame a closed pack lattice structure. The divalent Me ions (Me^{2+}) occupy 2d sites. The count and spin of the twelve Fe^{3+} ions with different sites located in R and S block. They are organized as six Fe^{3+} ions are in 12k site with the spin in up position (\uparrow), a pair of particles in 4f2 and 4f1 having spin in down position (\downarrow) and one ion in 2a and 2b site again with spin in up position (\uparrow). As a result, eight Fe^{3+} are within the up direction (\uparrow) and four within the opposite direction (\downarrow), hence, four upward (\uparrow) and downward (\downarrow) cancel one another and therefore the resultant moment are obtained of four Fe^{+3} per unit cell [78-82]. As every Fe^{+3} particle has five unpaired

electrons within the 3d orbit, the conducive magnetic moment comes out to be $5\mu_B$, where μ_B means Bohr magnetons. Gray, blue red, pink, and yellow colour balls represent iron atoms in 12k, 4f2, 2a, 4f1, and 2b sites respectively. Small green solid balls represent oxygen atoms, whereas larger cyan spheres represent strontium atoms.

1.4.2 Y-type hexaferrite

The Me_2Y (Y-type) hexaferrite contains different combination of barium layers and spinel blocks. The unit cell is composed of the sequence STSTST including three formula units. In Y-type structure, tetrahedral and octahedral sites are occupied by metal ions. However, the Me_2Y has a preferred plane which is perpendicular to the c-axis in which the magnetization can move freely so Me_2Y hexaferrites cannot be used as a permanent magnet.

1.4.3 W-Type hexaferrite

The Me_2W (W-type) hexaferrite exhibits a magnetic uniaxial anisotropy along the c-axis of the hexagonal structure as in the case of the M-type hexaferrite. The unit cell of W-type composed of the sequence $\text{RSSR}^*\text{S}^*\text{S}^*$. There is a 180° rotation between R-R* and S-S* blocks around c-axis. The W structure consists of one Ba containing layer for every seventh oxygen layer of the spinel structure and is thus closely related to the M structure. Substitution of different combinations of divalent metal ions paves the way for changing the saturation magnetization and Neel temperature of the W hexaferrite.

1.4.4 X-type hexaferrite

X-type hexaferrites constructed as stack of hexagonal R-block and spinel S-block along the hexagonal c-axis with a model as $\text{RSR}^*\text{S}^*\text{S}^*$, with the (*) indicating

the rotation of corresponding block by 180° around the c-axis. The structure of X-type compound is closely related to that of M and W type. The X-type hexaferrite can be constructed by $X = 2 M + S$.

1.4.5 U-type hexaferrite

U-type hexaferrite: U-type hexaferrite having general formula $Ba_4Me_2Fe_{36}O_{60}$ with Me a bivalent transition metal ions, is very difficult to prepare in single phase condition owing to their complex crystalline structure. It can be constructed by $U = 2 M + Y$.

1.4.6 Z-type hexaferrite

Me_2Z (Z-type) being the sum of M and Y compounds, it is somewhat different in that the M portion attempts to cause a preferential direction along the c-axis while the Y portion attempts to cause planar anisotropy in the plane perpendicular to the c-axis. The slightly larger uniaxial anisotropy in M prevails, however, and all Me_2Z compounds with the exception of Co_2Z , which has planar anisotropy and are uniaxial.

1.5 Strontium hexaferrite ($SrFe_{12}O_{19}$)

The M-type strontium hexaferrite ($SrFe_{12}O_{19}$) was invented in Philip's laboratories in 1950 [78]. Hexagonal ferrites are commonly known as the M-phase ferrites (Pb, Sr, Ba) $Fe_{12}O_{19}$ with magnetoplumbite structure.

In recent years, strontium hexaferrites ($SrFe_{12}O_{19}$) is one the competitive candidates of hexaferrites and it has a wide range of application due to their excellent properties like higher coercivity, large magneto crystalline anisotropy, low conductive losses, higher saturation magnetization, high permeability, high Curie temperature, excellent chemical stability and corrosion resistance [79, 80], hexaferrites can be used as permanent magnets [81-83]. More commonly hexagonal ferrites are used in high density recordings media, permanent magnets, data storage devises and components

in electrical devices which use microwave frequencies [82]. The Strontium ferrites has high potential applications in industry like perpendicular magnetic recording media [84-87], microwave devices [88], magnetic coatings [89], electromagnetic wave absorber ferroxdures, magnetic fluids and magnetic catalysts [90-92]. On the basis of crystalline and chemical properties, hexaferrites are categorized into five categories: M-type ($\text{SrFe}_{12}\text{O}_{19}$), W-type ($\text{SrM}_2\text{Fe}_{16}\text{O}_{27}$), Y-type ($\text{SrM}_2\text{Fe}_{12}\text{O}_{22}$), X-type ($\text{Sr}_2\text{M}_2\text{Fe}_{28}\text{O}_{46}$) and Z-type ($\text{Sr}_2\text{M}_2\text{Fe}_{24}\text{O}_{41}$). Along the c-axis, two structural blocks consisting of 10 hexagonally close-packed oxygen layers: RSR^*S^* are combined to obtain the crystal structure of magnetoplumbite unit cell of the M-type hexagonal ferrite. Spinel and hexagonal structures are represented by S and R blocks. With respect to the c-axis 180o rotation of R and S blocks gives rise to R^* and S^* blocks with equivalent atomic arrangements [93, 94]

The properties of hexaferrite can be enhanced by doping the cations varying from the d-block metal ion to rare earth elements in the Fe^{3+} or Sr^{2+} sites or both and can be controlled by altering the shape and size of particles. Enhancement of respective properties and the grain growth by inhibiting agents such as rare- earth metals (La^{3+} , Nd^{3+} , Sm^{3+} and Gd^{3+}) have been reported by many researchers [95]. Secondary phases in the system are formed due to the low solubility of the rare-earth elements in hexa ferrite lattice. Super exchange interaction variations results in enhancement of magneto-crystalline anisotropy that are expected with the difference in ionic radii of rare-earth elements with respect to Fe^{3+} [71,72].

1.5.1 Crystal Structure of Sr hexaferrite

The general formula unit of M type hexaferrite is $\text{AO}\cdot 6\text{Fe}_2\text{O}_3$ or $\text{AFe}_{12}\text{O}_{19}$, where A is a divalent ion such as Ba^{2+} , Sr^{2+} , Pb^{2+} , etc., which exhibits hexagonal

crystal structure with space group P63/mmc and is constructed from 4 building blocks, namely S, S*, R, and R* [73, 74] as shown in fig.1.8. The oxygen atoms are close packed with the A and Fe ions in the interstitial sites. There are ten layers of oxygen atoms along the c-axis and the iron atoms are positioned at five crystallographically different sites. An important consideration in the preparation of garnets, spinel ferrites and hexagonal ferrites is the size of the constituent cations. The spinel accepts into its tetrahedral and octahedral interstices a great variety of small cations, mostly ions of the first transition series. The garnets, because of their larger dodecahedral interstices, accept cations which are too large to be incorporated into spinels there is however, an upper limit to the size of acceptable cations. The hexagonal crystals accept still larger cations. The chemical formula of S and R building blocks of M type hexaferrite is Fe_6O_8 and $\text{BaFe}_6\text{O}_{11}$ respectively.

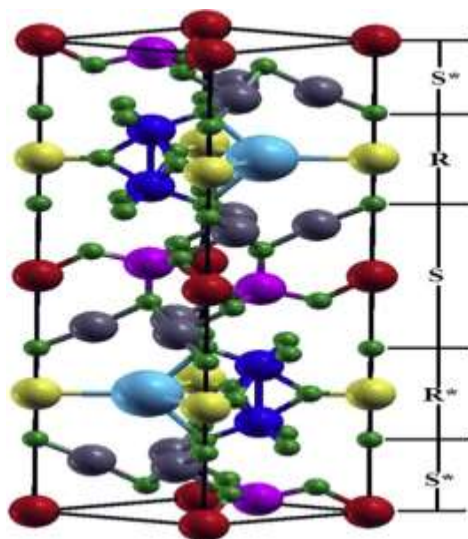


Fig. 1.8. Unit cell of M-type hexaferrite $\text{MFe}_{12}\text{O}_{19}$ and represents cell structure of M-type strontium hexaferrite ($\text{SrFe}_{12}\text{O}_{19}$).



Gray, blue red, pink, and yellow colour balls represent iron atoms in 12k, 4f2, 2a, 4f1, and 2b sites respectively. Small green solid balls represent oxygen atoms,

whereas larger cyan spheres represent strontium atoms. M-type hexaferrites have the chemical formula $MFe_{12}O_{19}$, where “A” is Ba, Sr, or Pb [96]. SrM-HFs are important materials with high chemical stability, specific saturation magnetization, uniaxial magnetocrystalline property, anisotropy, coercivity, high Curie point (temperature) and electrical resistance as well as low dielectric losses. Nanostructured SrM-HFs have received greater attention because of their technological and industrial applications that allow it to be used as a permanent magnet. The intrinsic properties of SrM-HFs ($SrFe_{12}O_{19}$) are strongly impacted by the cation exchange and synthetic methods [97]. $SrFe_{12}O_{19}$ finds a challenging and competitive application with technological evolution, the foremost unremarkably used material for ferrite permanent magnets that there is nice demand from makers of microwave gadgets, magnetic recording media, broadcast communications devices and so on. Doping $SrFe_{12}O_{19}$ with transition metal ions or rare earth ions of similar size has resulted in a significant modification of its properties [98]. The magnetic properties of doped magnetic nanoferrites based on both the parts and concentration of the doped part of element, morphology, particle size, and synthesis technique. The low amount doping of rare earth elements in $SrFe_{12}O_{19}$ leads to the significant changes in its electrical and magnetic properties.

1.6 Nickel ferrite

Nickel ferrite ($NiFe_2O_4$) have an inverse crystal structure AB_2O_4 exhibiting ferrimagnetic properties combined with relatively low electrical properties and it displays low eddy current. Nickel ferrite unit cell contains 32 oxygen atoms in a cubic close packing with eight tetrahedral sites: A-sites and sixteen octahedral sites: B-sites. Half of the ferric (Fe^{3+}) ions preferentially fill the A-sites and the others occupy the

B-sites represented by the formula $(\text{Fe}^{3+})_A[\text{Ni}^{2+}\text{Fe}^{3+}]_B\text{O}_4^{2-}$ [99]. However, it shows ferrimagnetism that originates from magnetic moment due to antiparallel spins of Fe^{3+} ions at tetrahedral site) and Ni^{2+} ions at octahedral site respectively . However, deviation in cation distribution is observed in nickel ferrite, when the particle size is in the nano range.

Nickel ferrite nanoparticles are extensively used in many applications because of its large permeability at high frequency, remarkable high electrical resistivity, moderate saturation magnetization, Curie temperature, chemical stability and cost effectiveness [100]. NiFe_2O_4 is an excellent material for electronic devices, information storage, high-density data storage, ferrofluids making, magnetic resonance imaging (MRI), drug-delivery technology, catalysis, magnetic refrigeration, etc. [101].

1.7. Rare earth substituted ferrites

Recently, rare earth doped ferrite magnetic nanoparticle materials have been studied extensively due to their novel physical and chemical properties. It is well known that rare-earth oxides are act as very good electrical insulating materials due to their very high resistivity ($>10^5 \Omega \text{ cm}$) at 300 K. Rare-earth (RE) elements have localized nature 4f electrons which are responsible for large values of magnetic moments, magnetocrystalline anisotropy and magnetostriction at lower temperatures. Rare earth ions have unpaired 4f electrons and strong spin–orbit coupling of angular momentum. Moreover, 4f shell of rare earth ions is shielded by $5\text{S}^25\text{P}^6$ and almost not affected by the potential field of the surrounding ions [102]. It is well known that the magnetic nature of ferromagnetic oxides is governed by the $\text{Fe}^{3+} - \text{Fe}^{3+}$ interaction or

spin coupling of 3d electrons. Interestingly, the $RE^{3+}-Fe^{3+}$ interactions appeared (4f–3d couplings) on substitution of a relatively very small amount of rare earth ions into ferrites. This determines the magnetocrystalline anisotropy in ferrites which affect the electrical and magnetic properties of the spinel ferrites. However, the $RE^{3+}-RE^{3+}$ interaction is very weak since their results from an indirect mechanism 4f – 5d – 5d – 4f. Magnetic therapy using rare earth substituted ferrite materials is more effective in relief from acute and chronic pain or discomfort due to various injuries or ailments [103].

Among all materials, Lanthanum family (rare earth) doped ferrites are considered to be a group of technologically important materials that are used in electronics and in optoelectronics to manufacture magnetic, electronic and microwave devices, permanent magnets, magnetic filters, transformers and magnetic switches owing to their high resistivity, negligible eddy current losses, high saturation magnetization and low coercivity. As such Lanthanum family (rare earth) doped ferrites are finding a large number of applications over a wide frequency range from a few kHz to several MHz.

Lanthanum-doped nanoferrites materials have many specifications, such as low density with broad bandwidth and flexibility. These lanthanide doped nanoferrites have magnetostriction coefficient, magnetic anisotropy, and high magnetic moment in addition to magneto-optical effects. Lanthanide-doped nanoferrites have gained immense interest by virtue of their wide applications in the fields of electronic and magnetic materials [104].

1.7.1. Rare earth Sr nanoferrites

Many researchers have studied rare earth metals that have replaced Sr or Fe from $\text{SrFe}_{12}\text{O}_{19}$ and have reported significant changes in magnetic properties like La^{3+} [105], Ce^{3+} [106], Pr^{3+} [107], Nd^{3+} [108], Sm^{3+} [109] and Gd^{3+} [110]. These magnetic materials are based on the purity and the number of particles and morphology of the fine powder. Therefore, founded fine, high synthetic homogeneity, and monodispersed particles which are the most significant method in material fabrication.

SrM-HFs with rare earth ion doping is explained the improvement in magnetic properties by a rise in a coercive field with magnetization and magnetocrystalline anisotropy [111]. Nowadays, SrM-HFs are being employed in power generation, nanocatalyst, microwave absorbers, automotive electronics, small DC motor rotors, microwave devices, and ferrite cores.

1.8. Magnetic properties of ferrites

The magnetic properties of ferrites like saturation magnetization, susceptibility and permeability are intrinsic as well as structure sensitive. Neel proposed the basic theory of spin–spin interactions and two magnetic sublattices and coined the word “ferrimagnetism” [112]. Magnetic materials exhibit different kinds of magnetic ordering depending upon the spin orientation. In ferrimagnetic materials, the magnitude of magnetic moment oriented in either way differs and so that, there is always exists a resultant uncompensated magnetic moment. Ferrites exhibit the ferrimagnetic behavior.

In ferrites, the metallic ions are occupy the tetrahedral sites: A-sites and octahedral: B-sites. Three kinds of magnetic interactions between metallic ions are possible through intermediate oxygen (O^{2-}) ions by super exchange mechanism viz., A-A, A-B and B-B interactions. The magnitude of interaction energy between

magnetic ions M^I and M^{II} depends upon the distances from metallic ions to the oxygen ion and the angle between M^I-O-M^{II} represented by the term Φ . An angle of 180° between the metallic ions gives rise to the maximum exchange energy, consequently, the energy decreases rapidly with increasing the distances of the metallic from the oxygen ion.

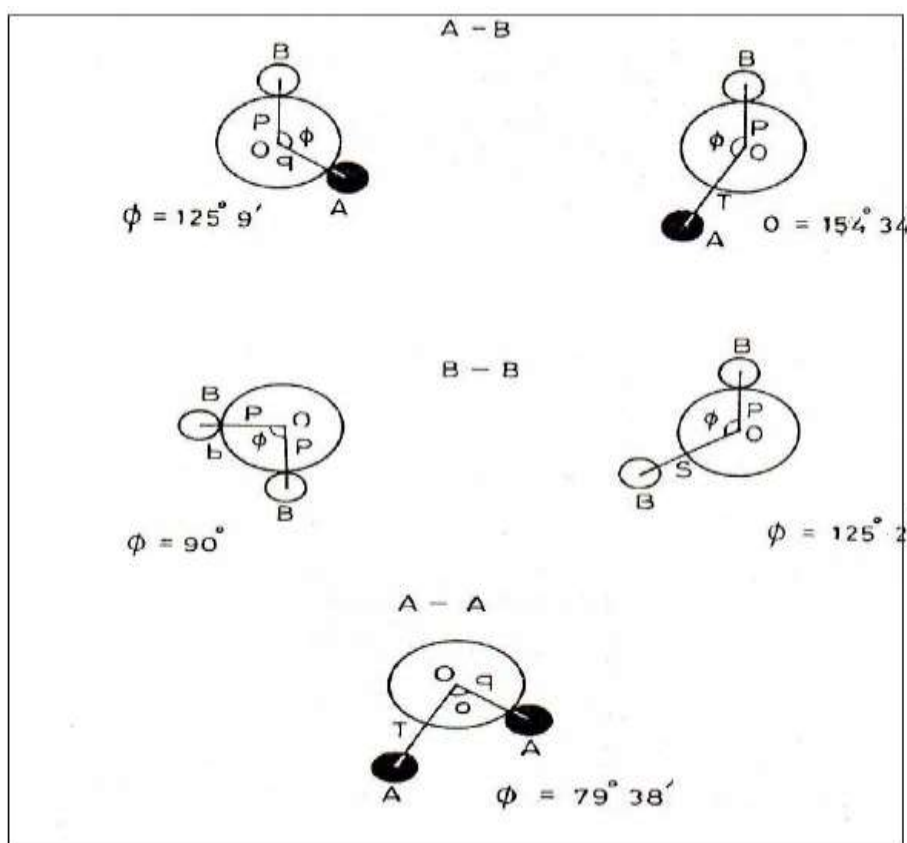


Fig 1.9 Angle between A-A, B-B & A-B cation in a spinel structure

In spinel ferrites, various possible configurations of the ion pairs with a favorable distances and angles for effective magnetic interactions investigated by Gorter [28] are given in fig 1.9. In A-A and B-B cases, the angles are too small or the distances between the metal ions and the oxygen ions are too long. Based on the inter atomic distances and angles Φ , it may be conclude that B-B interaction is weak, A-A interaction is weaker and A-B interaction is strongest. As a result the magnetic moments on A-sites are held anti parallel to those on B-sites. The value of saturation

magnetic moments of B-site (M_B) is greater than that A-site (M_A), that, resultant saturation magnetization M_S is written as $M_S = M_B - M_A$. This theory was supported by experimental studies of Neel [24], and Gorter [28].

1.8.1. Weiss molecular field theory of ferrimagnetism

In order to explain the spontaneous magnetization in a ferromagnetic material, Weiss postulated the existence of small-magnetized regions called domains [113]. The spontaneous magnetization in each domain is due to the existence of internal molecular field known as Weiss field, which tends to align the atomic dipoles in parallel direction. The magnitude of spontaneous magnetization of specimen is determined by the vector sum of the moments of individual domains. Moreover, a thin layer in which the direction of magnetization changes from one orientation to another separates the magnetic domains characteristic of domain is concerned. This transition boundary is known as domain wall or Bloch wall.

The Weiss field is found to be proportional to the intensity of magnetization and is given by,

$$H_m = \gamma M \quad (1.2)$$

Where H_m -Weiss field or molecular field, γ -molecular (Weiss field) field constant, M -Intensity of magnetization in material.

When the applied magnetic field is very small, domain wall movement achieves magnetization, which is reversible. With further increase in field magnetization increases with irreversible wall movement. Finally, at high field saturation magnetization is reached by rotation of domain magnetization. The rotations of domains have been observed by Berkhausen. In presence of external

magnetic field (H) is applied, the effective field (H_o) becomes the vector sum of internal (H_m) and external fields and is given by

$$H_o = H_m + H \quad (1.3)$$

1.8.2 Neel's theory of ferrimagnetism

In order to explain the magnetic properties of ferrites, Neel has proposed a theory by assuming two sublattices formed by the location of magnetic ions at crystallographically different sites. Neel has postulated the existence of negative interaction between the ions on A-sites and B-sites on basis of the idea of the Weiss field [113]. Besides the negative A-B, one must take into A-A and B-B interactions. These turns out to be negative as well, but are considerably weaker than the A-B interactions.

In ferrimagnetic, the sub lattice are crystallographically equivalent, making $\gamma_{AA} = \gamma_{BB}$, where γ_{AA} and γ_{BB} are respective molecular constants. Unless the sub lattices are identical, $\gamma_{AB} > 0$, favouring anti-parallel alignment of magnetic moments of A and B sites, giving rise to net magnetization of ferrimagnets. Therefore the net spontaneous magnetization in spinel ferrite can be expressed as

$$M_S = M_B - M_A \quad (1.4)$$

M_S is resultant saturation magnetization; M_A is Magnetic moment of A-site and M_B -Magnetic moment of B-site.

1.8.3 Yaffet - Kittel Model

Neel's theory holds good for pure ferrites. But it is an inadequate for the spinels, which contains ions other than iron. Yaffet and Kittel [26] have proposed a concept of triangular or canted or non-collinear type spin arrangement. They have considered the possibility of sub division of each lattice to account for the magnetic

ordering within the lattice, other than parallel arrangement of spins. They have found that when strong negative interaction exists within the B-sub lattices, the two equivalent sublattices B_1 and B_2 , being spontaneously magnetized, are not exactly antiparallel to M_A but aligned at some angle other than 180° (fig 1.10). Thus, resultant magnetization of B-sub lattice setting antiparallel to the magnetization of A-lattice.

The triangular arrangement within the lattice results in values of reduced magnetization as compared to those predicted by Neel model. If the angle between A and B subdivisions is zero, then Neel's state is obtained. The angle between A and subdivisions of B is given by the relation,

$$\cos \theta = \frac{3}{4} (J_{AB} S_A / J_{BB} S_B) \quad (1.5)$$

Where J_{AB} and J_{BB} stands for exchange integrals, S_A and S_B for spin quantum numbers of atoms.

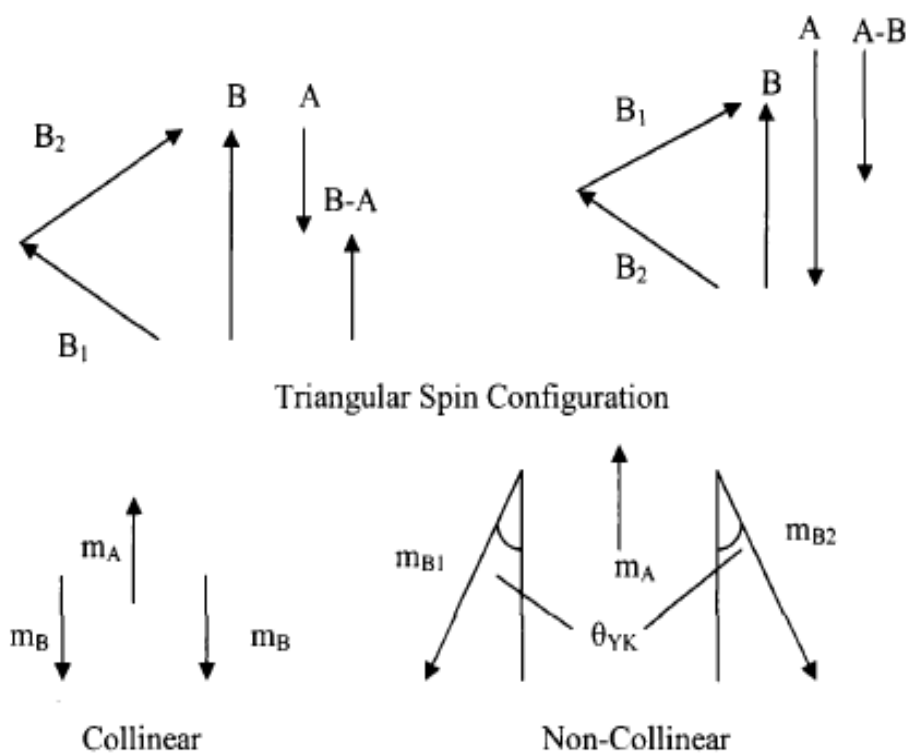


Fig 1.10: Triangular spin configuration and Configurations of the pairs in spinel ferrites

1.8.4 Hysteresis studies

The basic magnetic properties of ferrites can be characterized by hysteresis technique, AC susceptibility and permeability. Hysteresis is the phenomenon in which magnetic induction lags behind the applied magnetic field. The studies on hysteresis provide valuable information about saturation magnetization, permeability, coercivity and remanence. The hysteresis properties are mainly depending on the chemical composition, crystal structure, cation distribution and microstructure. The coercive force H_C , is the most important property in the selection of these materials for their applications. The value of H_C varies from 10^{-1} to 10^3 Oe. From fig 1.11 materials with lower H_C are called “soft ferrites” which are used in high frequency cores, microwaves devices, antennas and transformers. The ferrites with higher value of H_C are called “hard ferrites” and are used in electric motors, loud speakers, television sets etc as permanent magnets.

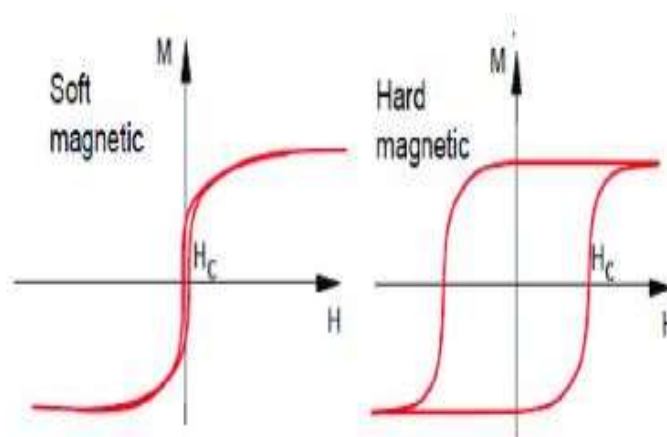


Fig 1.11 : Magnetic hysteresis loop of soft and hard ferrites

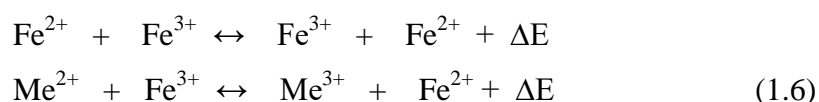
1.9 Electrical properties of ferrites (DC electrical conductivity)

Ferrites are ferrimagnetic oxides having low conductivity at room temperature in the range 10^{-10} – 10^2 ohm $^{-1}$ cm $^{-1}$, which is one of the considerations for microwave applications [114]. The mechanism of charge transport can be understood from

measurement of electrical conductivity. The phenomenon of electrical conductivity in ferrites can be takes place due electron exchange between Fe^{3+} and Fe^{2+} ions, distributed randomly over equivalent crystallographic lattice sites.

Verwey et al., [115] reported that the electrical conductivity in ferrites owing to the existence of both Fe^{2+} and Fe^{3+} ions on B-sites. Brabers has attributed the conductivity in ferrites is due to electrons exchange between Fe^{2+} and Fe^{3+} ions on B-sites. The electrical properties of ferrites are affected by the distribution of cations in sites, by magnetic and nonmagnetic substitutions, the amount of Fe^{2+} ions present, sintering conditions, grain size and grain growth effects.

The conductivity in ferrites due to simultaneous presence of ferrous (Fe^{2+}) and ferric (Fe^{3+}) ions in crystallographically equivalent sites. The high resistivity in ferrites is associated with the occupation of B-sites by divalent metal ions and trivalent iron ions. Such an arrangement requires higher activation energy for hopping of electrons. The mechanism of conductivity can be represented as



where ΔE is the activation energy. The energy required to transfer an electron from Me^{2+} to Fe^{3+} and vice versa. Me denote divalent metal ions like Cu^{2+} , Co^{2+} , Mg^{2+} , Mn^{2+} , Ni^{2+} and Cd^{2+} etc. The conductivity of ferrites can be explained in terms of electronic charge carriers like electrons and holes by the relation.

$$\sigma = e (n_e \mu_e + n_h \mu_h) \quad (1.7)$$

where n_e and n_h stands for concentrations and μ_e and μ_h for mobility of electrons (e) and holes (h) respectively. An electron moves in one direction, the holes move in opposite direction. Though the velocities of electrons and holes are the same mobility of electrons is much higher than the mobility of holes.

The temperature dependence of electrical conductivity is according to Wilson's relation $\sigma = \sigma_0 \exp [E_a/kT]$, where σ_0 is a constant, E_a is an activation energy for electrical conductivity, k is Boltzmann constant and T is absolute temperature of the sample. The plot of $\log\sigma$ v/s $1/T$ is a straight line with different slopes. The change in slopes near Curie temperature attributed to change in conductivity of the material [116].

At Curie temperature, the investigated materials are transforming from the ordered ferrimagnetic state to disordered paramagnetic state. When such a change occurs there is an abrupt change in activation energy. The activation energy in paramagnetic region is higher than the ferrimagnetic region. The electrical properties of ferrites affected by the distribution of cations on A-sites and B-sites, magnetic and non-magnetic substitutions, the amount of Fe^{3+} ion present, sintering condition and microstructure.

1.9.1 Dielectric properties

Ferrites are low conducting and very good dielectric materials owing to their technological applications in the field from microwave to radio frequencies. Moreover, during sintering of ferrite samples under slightly reducing condition, the Fe^{2+} ions formation leads to large fairly high conducting ferrite grains. These grains are separated from low conductivity layer or grain boundaries formed on cooling of ferrite material in an oxygen atmosphere [117]. Therefore, ferrite materials behave as a inhomogeneous dielectric material. This gives rise to interfacial polarization due to localized accumulation of charges under the influence of an applied electric field. As a consequence of inhomogeneous dielectric behavior, dielectric constant is as high as 10^5 are found to be in case of ferrites at low frequencies.

One important characteristic of ferrites is their high values of resistivity, low magnetic and dielectric losses which make them ideal for high frequency applications. Owing to the dielectric behavior, they are sometimes called multiferroic. Owing to the dielectric behavior, they are sometimes called multiferroic. They are commercially important because they can be used in many devices such as Phase Shifter, High frequency transformer cores, switches, resonators, computers, TVs and mobile phones.

The phenomenon of dielectrics in case of ferrites originates from its microstructure. The dielectric properties of nanoferrites are dependent upon several factors including preparation method, stoichiometric composition, sintering time and temperature, type and quantity of additives and microstructure [118]. Dielectric properties are stable at high frequency, which can be used for relevant applications. The study of frequency, temperature and composition dependent dielectric properties provides much valuable information on localized electric charge carriers. Infact, this leads to good explanation and knowledge of dielectric behavior in ferrites [119].

1.9.2 Polarization in dielectrics

Jonscher has interpreted the mechanism of polarization in ceramic materials that include the ferrites. Polarization is the process of alignment of permanent or induced atomic or molecular dipoles under the influence of an external electric field. Depending upon the type of dielectric material and the direction of application of electric field, the polarization mechanisms have been classified as (fig. 1.12)

(i) Electronic polarization (P_e)

The electric field causes deformation or translation of the originally symmetrical distribution of the electron clouds of atoms or molecules. An electronic

polarization arises due to displacement of the center of gravity of electrons relative to the center of gravity of positively charged nucleus, in presence of an external applied electric field. Thus a dipole moment is induced. The magnitude of displacement, and so also the dipole moment is proportional to the electric field strength. Electronic polarization phenomenon exists in all dielectric materials with an external applied field.

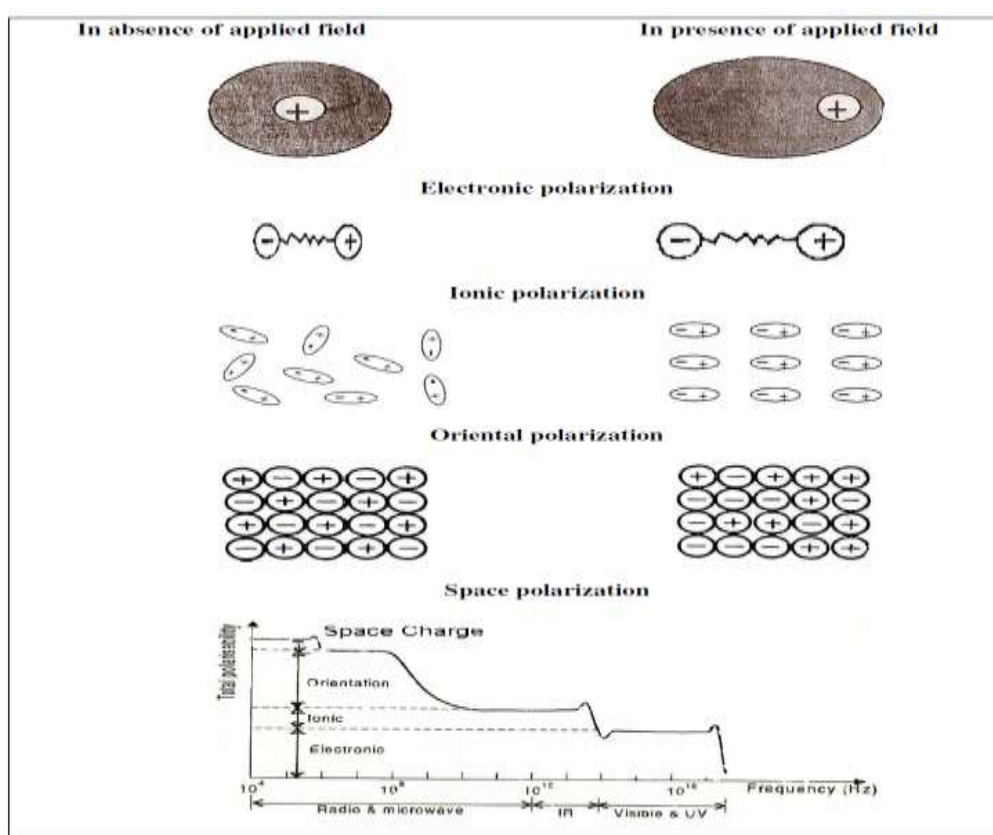


Fig 1.12: Total polarizability

(ii) Ionic or atomic polarization (P_i)

In ionic crystals each ion pair constitute an electric dipole but because of lattice symmetry and the overall charge neutrality ensure that these dipoles everywhere cancel each other. In an ionic polarization, the cations and anions get displaced from their equilibrium positions in opposite directions, within the crystal

due to effect of an external applied electric field. This is essentially the distortion of the normal lattice vibration, and sometimes referred to as vibrational polarization. Ionic polarization is sensitive below infrared frequencies.

(iii) Oriental or dipolar polarization (P_o)

Oriental polarization is the characteristic of polar dielectrics, which arises due to alignment of permanent dipole moment along the applied field direction. This polarization is limited only up to microwave frequency range.

(iv) Space charge polarization (P_s)

Space charge polarization exists in heterogeneous material containing semi-conducting impurities where the charges migrate within the impurity regions and store at interfaces are trapped at grain boundaries. There appears field distribution due to build up space charges and this shows an increase in permittivity known as interfacial polarization.

The process during which the migrational polarization sets in occurs in or decays can last for few seconds, minutes and even hours. This explains why this polarization occurs at very low frequencies. Ferrites possess high values of dielectric constant due to the interfacial polarization

$$P = P_e + P_i + P_o + P_s \quad (1.7)$$

where the symbols have their usual meaning.

1.9.3 Introduction to Impedance spectroscopy

Oliver Heaviside, in 1886, introduced the concept of impedance. Bauerle was the first to use this technique in 1969 to separate bulk from interfacial properties in polycrystalline ceramics. Impedance spectroscopy is an ideal technique to investigate the electrical response of dielectric materials as a function of frequency. The

microstructural effect is one of the important factors, which influence the impedance properties of ferrites. The complex impedance analysis technique enables to separate the resistive or real part and reactive or imaginary part of impedance of electrical material and hence provide a clearer picture regarding the material properties [120]. These properties and applications are depend upon the close control of structure, stoichiometric composition, types, amount and distribution of dopant, microstructure and defects, which functions by utilizing different frequency dependences of constituent components for their separation. The commonly used models for the impedance spectroscopy are electrically equivalent circuits consisting of resistors, capacitors, inductors and specialized distributed elements.

The complex impedance analysis provides the basic information of the dielectric properties of ferrites. The analysis allows the separation of several contributions of total impedance which arises from the bulk conductance and internal phenomenon such as grain effect, grain boundary effect and other electrode interface effect. The analysis is mainly accomplished by fitting the impedance data to an equivalent circuit, which is representative of the material under investigation. It has been among the most useful investigating techniques, since the impedance, namely grain boundaries and electrode effects.

A ferrite material is assumed to be consisting of piled up crystalline plates. In other words, on point of microstructural view, ferrite material is assumed to be its microstructure is made up of parallel conducting plates or grains separated by resistive plates or grain boundaries [121]. Impedance data of materials have resistive or real component and reactive or imaginary components.

1.10 Electro-analytical techniques

Chemical analysis is defined as application of a process which is used to identify the quality of a substance, the components of a solution or mixture and to determine the structures of chemical compounds. Chemical analysis generally consists of a chain of procedures to identify and quantify one or several components in a sample of matter. The need for improved analytical methods is increasing, especially for compounds with known or possible effects on human health on account of increasing number of environmental pollutants, drugs and their metabolites, and additives used in the food industry. Electroanalytical chemistry is a branch of chemical analysis that employs electrochemical methods to obtain information related to the amounts, properties and environment of chemical species. It is preferable to consider electroanalytical chemistry as the area of the analytical chemistry and electrochemistry in which the electrode is used as a probe, to measure something that directly or indirectly involves the electrode [122].

Electroanalytical techniques encompass a group of quantitative analytical methods that are based upon the electrical properties of a solution of the analyte when it is made a part of an electrochemical cell. These techniques are capable of producing exceptionally low detection limits and wealth of characterization information describing electrochemical addressable system [122].

1.10.1 Voltammetry

Voltammetry is an electroanalytical technique in which current-potential behaviour at an electrode surface is measured. The potential is varied in some systematic manner to cause oxidation or reduction of electroactive chemical species at the electrode. The resultant current is proportional to the concentration of electrochemical species.

Voltametric techniques are based on Faraday's Law and Fick's Law. In voltammetry, the current corresponding to the quantity of material transported by diffusion and reacting at the electrode surface is usually measured. This current is proportional to the concentration of the electroactive component present in the test solution. This current is the result of electrochemical oxidation or reduction of the electroactive compound. Additionally, if steady state convection is employed, as in flowing streams where the concentration of electroactive species is uniform, then a constant current is measured [123]. The important voltammetry techniques are:

a) Linear Sweep Voltammetry (LSV)

LSV is the simplest voltammetric technique. At the working electrode, a rapid potential scanning that varies linearly (20-100 mV/s) is applied. Capacitive current increases when velocity of scanning is increased and cannot be electronically compensated. Thus, the performance of this technique is strongly restricted. Detection limits are in mg/L levels.

b) Cyclic Voltammetry (CV)

CV has become an important and widely used electro analytical technique in many areas of chemistry. It is widely used for the study of redox processes, understanding reaction intermediates and obtaining stability of reaction products. This technique is based on varying the applied potential at a working electrode in both forward and reverse directions while monitoring the current. The important parameters in a cyclic voltammogram are peak potentials (E_{pc} , E_{pa}) and peak currents (I_{pc} , I_{pa}) of cathodic and anodic peaks respectively. If electron transfer

process is fast when compared to other processes (such as diffusion), the reaction is said to be electrochemically reversible and the peak separation is

$$\Delta E_p = E_{pa} - E_{pc} = 2.303 RT / nF \quad (1.8)$$

Thus, for a reversible redox reaction at 25 °C with n electrons, ΔE_p should be $0.0592/n$ V or about 60 mV for one electron. In reality this value is difficult to be attained because of factors such as cell resistance. Irreversibility, because of a slow electron transfer rate results in $\Delta E_p > 0.0592/n$ V, greater, say, than 70 mV for a one electron reaction. The formal reduction potential (E_0) for a reversible couple is given by

$$E_0 = (E_{pa} + E_{pc})/2 \quad (1.9)$$

For a reversible reaction, the concentration is related to peak current by the Randles-Sevick expression (at 25 °C):

$$I_p = 2.69 \times 10^5 n^{3/2} A D^{1/2} C v^{1/2} \quad (1.10)$$

where I_p is the peak current, A is the electrode area, D is the diffusion coefficient, C is the concentration and v is the scan rate.

c) **Differential Pulse Voltammetry (DPV)**

Differential pulse voltammetry (DPV) is comparable to normal pulse voltammetry in that the potential is also scanned with a series of pulses. However, it differs from NPV because each potential pulse is fixed, of small amplitude (10 to 100 mV), and is superimposed on a slowly changing base potential. Current is measured at two points for each pulse, (i) just before the application of the pulse, and the second (ii) at the end of the pulse. These sampling points are selected to allow for the decay of the non-faradaic current. The difference between current measurements at these points for each pulse is determined and plotted against the base potential.

d) Amperometric Sensor

Amperometric sensors [124] exploit the use of a potential applied between a reference and a working electrode, to cause the oxidation or reduction of an electro active species; the resultant current is measured. The instrumentation requires controlled-potential equipment and the electrochemical cell, it consists the use of a three-electrodes. While the working electrode is the electrode at which the reaction of interest occurs, the reference electrode provides a stable potential compared to the working electrode. An inert conducting material is usually used as auxiliary electrode. A supporting electrolyte is required in controlled-potential experiments to eliminate electromigration effects, decrease the resistance of the solution and maintain the ionic strength constant.

1.10.2 Electrochemical Sensor

Sensors are devices that incorporate a recognition element with a signal transducer. Such devices can be used for direct measurement of the analyte in the sample matrix. There are a variety of combinations of recognition elements and signal transducers electrochemical sensors [125], in which an electrode is used as the transduction element, represent an important subclass of chemical sensors. The field of sensors, in general, and electrochemical sensors is particular interdisciplinary and future advances are likely to occur in several disciplines. An overview of analytical method development demonstrates that electrochemical sensors represent the most rapidly growing class of chemical sensors. Electrochemical sensors are especially attractive because of their remarkable detectability, experimental simplicity and low cost. They have a leading position among the presently available sensors that have reached the commercial stage and which have found a vast range of important applications in the fields of clinical, industrial, environmental and agricultural analysis.

1.10.3 Modification Based on Nanomaterials

The electrocatalytic activity of metal nanoparticles is strongly dependent on their composition, size, surface area and surface morphology. The NPs can be immobilized as an organized mono - or multilayer on solid support with the help of short/long chain molecules having suitable functional groups like -NH₂, -SH at both ends. Arrays of NPs have been utilized for electrochemical sensors as they exhibit excellent catalytic activity towards various reactions. In these, NPs function as “electron antennae”, efficiently tunneling electrons between the electrode and electrolyte [126-127].

1.10.4 Electro-catalytic oxidation of L-Cysteine on the SrHF's /GCE

Electrochemical techniques have the intrinsic advantages of simplicity, easy of miniaturization, high sensitivity and relatively low cost. Therefore, it is very important to investigate the Electro-chemical behavior and sensitive detection of L-cysteine (Lcys). Several chemically modified electrodes have been proposed to facilitate the detection and oxidation of Lcys [128]. Lcys was most important amino acids that play an importance in biological system, low Lcys concentrations causing, growth retardation in children, gray of hair, edema, damage of liver, muscle and fat are decreases, damaged and weakness of skin. Therefore, the development of simple, rapid and inexpensive methods for the detection of Lys is necessary in physiological and clinical diagnostics. There are three intense functional groups (-COOH, -NH₂, and -SH), which can be easily used to conjugate metal atoms. The proposed sensor is useful for the quality control and routine analysis of Lcys in pharmaceutical formulations [129]. Therefore the present study show the use of synthesized SrHF's for the electrochemical detection of the Lcys.

1.11 Gas sensors

Gas sensor devices are used to detect the hazardous and toxic gases present in the environment and those expelled by the chemical automobile fuel industries and combustion which have supreme importance in technology and in routine life. There is a need to develop a simple, sensitive and stable electronic sensors suited for trace detection in a wide spectrum of applications ranging from lab-on-a-chip and *in-vivo* biosensors to environmental monitoring and warfare agent detection, as opposed to the often employed expensive, bulky and complicated instrumental methods. Inexpensive and low-power devices are fueling the exponential growth of research in this area. Researchers are trying to fabricate nanomaterials that would work as better gas sensors with fast response, long-term stability, high sensitivity, and greater selectivity with good robustness and moderate chemical stability [130]. In recent years, numerous gases and volatile organic compounds (VOCs) are being utilized in large areas of industrial production and research applications [131]. Considering a huge risk of damage to assets and human beings if a leak occurs there is an important point to be concerned to control and monitor these harmful species. There are certain gases which are toxic to human and environmental lives as they cause big explosions. Accordingly, there is a need of gas sensors with the intention of continuous and effective detection of these gases to evade predominantly the above said dangers. Ideal gas sensors should possess the following sensing properties, high sensitivity to certain gases, reversibility, fast response time and good recovery time, high selectivity, long term stability, simple principle of operation, easy to handle, simple fabrication technique, and temperature insensitive.

The sensitivity (S) of a sensor is determined by following equation 1.11

$$\text{Sensitivity } (S)\% = \left(\frac{R_g \sim R_a}{R_a} \right) * 100 \quad (1.11)$$

where, R_a is the resistance after exposure to air, R_g is the resistance after exposure to the target gas. Conveniently, S is expressed in terms of %. Selectivity refers to the characteristics that determine whether a sensor can respond selectively to a gas or a group of gases. Detection limit is the lowest concentration of the gas that can be detected by the sensor under given conditions. Response time is the time taken by the sensor to respond to a certain gas. Recovery time is the time taken by the sensor to return to its initial state after gas desorption.

1.11.1 Nano composite gas sensors

With advancing nanotechnology, it has been plausible to vary substantial properties of metal oxide nanostructures, conducting polymers, and carbon nanostructures. Regardless of the various advances, the hunt for reliable, robust gas sensors is an unending effort, and much more is expected for the upcoming future [132]. Especially with the help of nanotechnology, improvements in sensor are endlessly pursued, including sensor selectivity, response, response/recovery speed and stability, for which research is continuously performed using novel materials. Efforts are being made particularly in decreasing the operating temperature of gas sensors. Gas sensors fabricated using conducting polymers can operate at room temperature, however, the effect of humidity is amenable to ruin sensor with a sluggish response/recovery time, and poor stability. Hence, nanocomposites of the metal oxides, metal oxide-graphene oxide, metal oxide-conducting polymers, metal oxide-M Xene, graphene-MXene and ternary composites are greatly investigated for chemiresistive gas sensor applications since few decades.

1.11.2 Liquefied Petroleum Gas (LPG)

Liquefied petroleum gas (LPG) is a colourless odourless liquid which readily evaporates into a gas. The group of products includes saturated hydrocarbons propane (C_3H_8) and butane (C_4H_{10}), which can be stored/transported separately or as a mixture. LPG is odourless that can be odorized by adding an odourant as well as industrial supply to user, so as to aid the detection of any leaks. It is slightly heavier than air and hence if there is a leak it flows to lower lying areas. In a liquid form, its density is half that of water and hence it floats initially before it is vaporized. It is non-toxic but can cause asphyxiation in very high concentrations in air. LPG expands upon release and 1 liter of liquid will form approximately 250 liters of vapour. LPG is used to provide lighting through the use of pressure lanterns. While butane and propane are different chemical compounds, their properties are similar enough to be useful in mixtures. Butane and Propane are both saturated hydrocarbons, they do not react with other. Butane is less volatile and boils at 272.4 K. Propane is more volatile and boils at 231 K. These products are liquids at atmospheric pressure when cooled to temperatures lower than their boiling points. Vaporization is rapid at temperatures above the boiling points. The calorific (heat) values of both are almost equal. Both are thus mixed together to attain the vapor pressure that is required by the end user and depending on the ambient conditions. If the ambient temperature is very low, propane is preferred to achieve higher vapor pressure at the given temperature [133]. LPG can also be used as a fuel for domestic, industrial, horticultural, agricultural, heating and drying processes. LPG can be used as an automotive fuel or as a propellant for aerosols, in addition to other specialist applications.

1.11.3 Gas sensing Importance

It is necessary to detect gases like mono-nitrogen oxides, NO₂, NH₃, LPG, CO etc., especially for environmental monitoring due to their toxicity and related risk to the ecosystem. In world, gas pollution is mostly an outcome of increasing industrialization. The increasing gas pollution ensuing an ecological imbalance and global warming. Annually a huge quantity of NO₂ is expelled in to the ecosystem as a byproduct of combustion and automobiles, and hence, the NO₂ sensing has involved significant attention because of its harmful effect to plants as well as respiratory system of human beings and animals. At the same time, CO being a colorless and toxic gas generates from the burning of fossil fuel and engines with malfunctions. CO is also a widely used fault characteristic gas to estimating the insulation performance of electric power transformers as it is dissolved in transformer oil. Thus, advancement in fabrication of highly sensitive CO gas sensors is of greatest importance for environmental monitoring and industrial applications. NH₃ is a natural gas that is present all the way through the atmosphere. NH₃ shows a very important role in environment, produced by the means of natural excretion process in humans, animals, and plants and it is one of the most widely used chemicals in the world [134].

1.12 Literature Survey

Gnana Praveena Nethala et al., studied the influence of Ce³⁺ on the structural, magnetic and Mossbauer properties of Sr_{1-x}Ce_xFe₁₂O₁₉ (x = 0.0, 0.05, 0.1, 0.15, 0.2 and 0.25). They have synthesized of Sr_{1-x}Ce_xFe₁₂O₁₉ using the sol-gel technique. They were investigated the structural and magnetic properties of the grown samples using X-ray diffractometer, Scanning electron microscope, FTIR, Raman spectrometer to study the morphological properties and Vibrating sample

magnetometer [135]. They have substituted the rare-earth elements in strontium ferrite and investigated the enhancement of properties of strontium hexaferrite. They have replaced Sr with Ce to investigate the changes in the structural, spectroscopic and magnetic properties of strontium ferrite.

M-type hexagonal ferrites of composition $\text{Sr}_{1-x}\text{Nd}_x\text{Fe}_{12}\text{O}_{19}$ with $x = 0, 0.06, 0.08, 0.11,$ and 0.20 have been prepared by hydrothermal synthesis. The phase composition of the samples was investigated by X-ray diffraction and Mössbauer spectrometry. The analyses revealed the hexagonal M-type structure for all the samples phase. However, Nd containing secondary phases of the $(\text{Sr}, \text{Nd}) \text{FeO}_{3-\delta}$ type are also detected. Mössbauer spectrometry indicates that the Nd content in the M-type phase is very weak, as the hyperfine parameters of the M-type phase contribution do not vary with the Nd content. This is in agreement with the fact that both saturation magnetisation and remanence remain almost constant as the Nd content increases. The variations of the coercive field are thus attributed to microstructural changes, in relation with the presence of the Nd containing secondary phases [136].

Muhammad Naeem Ashiq et al., report the synthesis of M-type nano-strontium hexaferrites co-doped with hetrovalent cations (Dy-Ni) having composition $\text{Sr}_{(1-x)}\text{Dy}_x\text{Fe}_{12-y}\text{Ni}_y\text{O}_{19}$ ($x = 0.00-0.20, y = 0.00-0.80$). The synthesized compounds were analyzed by XRD, FE-SEM, VSM, along with electrical resistivity and dielectric property analyses. XRD peak patterns revealed the magnetoplumbite-type hexagonal crystal structure of the synthesized materials. The SEM micrographs reflected the spherical and hexagonal shaped particles with an average size 40–50 nm. The magnetic squareness ratio (M_r/M_s) of the synthesized nanoferrites particles lies in the range of 0.60–0.68 assuring their single magnetic domain nature. The rise in the

values of saturation magnetization, remanence and coercivity reflect that the fabricated compounds can be beneficial for the perpendicular magnetic recording media. Both the electrical resistivity increment and decrease in dielectric energy loss with increasing Dy-Ni substitution level authenticates that such materials can find applications in magnetic recording media and microwave device fabrication [137].

The hexagonal ferrite $\text{Sr}_{0.80}\text{La}_{0.20}\text{Fe}_x\text{Zn}_{0.15}\text{O}_{19}$ ($10.65 < x < 12.05$) magnetic powder and magnets were synthesized by the ceramics process. The phase components of the hexagonal ferrite magnetic powder were studied using X-ray diffraction (XRD). Scanning electron microscopy (SEM) was used to investigate the morphology of the sintered magnets. The effects of the iron content on magnetic properties of the magnets were studied systematically. The remanence (B_r) and maximum energy product $[(BH)_{\text{max}}]$ for the magnets at $x = 11.25$ reached the maximum value of 414.5mT and 32.24k J/m³, respectively. The intrinsic coercivity (H_{c_j}) and magnetic induction coercivity (H_{c_b}) for the magnets at $x = 11.65$ reached the maximum value of 265.8 kA/ m and 257.8kA/m, respectively [138].

The nanocrystalline strontium vanadium nanohexaferrites was undertaken using a sol-gel auto-combustion method have been synthesized. The structural and morphological properties were characterized using X-ray diffraction (XRD), Fourier transform infra-red (FT-IR) analysis, and scanning electron microscopy (SEM). The XRD analysis showed that the crystallite sizes (t) of the products vary between 55 and 60 nm, while the SEM analysis confirmed the hexagonal platelet structure of the products. The magnetic hysteresis loops indicated that the synthesized nanohexaferrites exhibit ferrimagnetic-like (FM) behavior. The deduced saturation (M_s) and the remnant (M_r) magnetizations, the coercive (H_C) and magneto-

crystalline anisotropy (H_a) fields diminished as the V^{3+} content increased. The H_a values are very high, pointing to the hard FM characteristics of the synthesized nanohexaferrites. Except for $x=0.0$, the squareness ratios, M_r/M_s , are below 0.50, suggesting the presence of multi-domain nano-sized particles for $SrFe_{12-x}V_xO_{19}$ ($0.00 \leq x \leq 0.1$) nanohexaferrites [139].

Rai et al., Influence of replacing Sr^{2+} ions by rare-earth ions (RE^{3+}) ions on the structural and magnetic properties of high coercivity (H_c) $SrFe_{10}Al_2O_{19}$ hexaferrite have been investigated using X-ray diffraction, transmission electron microscopy, differential scanning calorimeter, and SQUID. A 73% increase in intrinsic coercivity is observed for Al^{3+} doped $SrFe_{10}Al_2O_{19}$ as compared to that of pure $SrFe_{12}O_{19}$. The RE^{3+} doping brings in further 50% increase in the coercivity to $Sr_{0.9}RE_{0.1}Fe_{10}Al_2O_{19}$. Overall the Curie temperature of $Sr_{0.9}RE_{0.1}Fe_{10}Al_2O_{19}$ reduced upon RE^{3+} substitution, however, among rare-earth ions Pr^{3+} doping showed highest $T_c = 620$ K. Doping $Sr_{0.9}RE_{0.1}Fe_{10}Al_2O_{19}$ with RE^{3+} ions seems to be detrimental to the saturation magnetization but was observed to be favorable to the coercivity enhancement [140].

The rare earth gadolinium (Gd)-substituted magnetoplumbite strontium hexagonal ferrites (SrGdM) have been studied by Jiyu Hu, et al., The $Sr_{1-x}Gd_xFe_{12}O_{19}$ ($0.00 < x < 0.25$) samples are prepared by using a solid state reaction method. With these prepared SrGdM components, a series of measurements are employed to characterize the structural property, valence state behavior and magnetic performance. The experimental values of M-H at ultralow temperature and room temperature (RT) are extremely approach the calculated one through computing by the empirical law to approach saturation. An apparent improvement of magnetization (M_s) and intrinsic coercivity (H_c) can be realized by substituting gadolinium in the system which ensure the practicability of this effective way. In addition, DSC-TGA analyses of SrGdM

even reveal an excellent thermal stability since quite higher Curie temperature (T_C ¼ 736 K) for substituted sample, indicating an exceedingly wide application prospects and great interests in scientific research as well [141].

1.12.1 Aim of the present work

Hexaferrites and spinel ferrites their composites has been the subject of an extensive study because of their wide range of technical applications and their importance in understanding the theories of magnetism. They exhibit interesting microstructural, electrical and magnetic properties which depend upon various parameters like method of preparation, calcinations temperature, preparation time, amount of substitution, types and amount of surfactant etc., In recent years, chemical co-precipitation technique is used to prepare hexaferrites.

M-type hexaferrites and spinel ferrites have continuously made inroads in applications such as plastoferrites, injection-molded pieces, microwave devices, and magnetic recording media. With proper design and substitutions, passive elements including mm-wave circulators can be constructed from hexaferrites. Hexaferrite with proper design and substitution are used as passive elements at microwave frequencies. Radar absorbing paint made from ferrites is used to coat military aircrafts for stealth operation and in the expensive absorption tiles lining the rooms used for electromagnetic compatibility measurements.

Other applications of hexaferrite and spinel ferrites materials include Common Mode Chokes, EMI filters, Current Sensors, Handheld Devices, Spike Suppression and Gate Drive Transformers, shield beads, snap-on cores, flat cable beads fig 1.13, automotive industry and consumer goods. Hexaferrites having the intrinsic characteristics of Complex Permeability (μ^I & μ^{II}) and High Impedance, they are also used in

- (i) Computers and peripherals
- (ii) Communication Systems
- (iii) Automobiles
- (iv) Switch Mode Power Supplies
- (v) dc-dc converters
- (vi) Ignition coils



Fig .1.13 Hexaferrites as different beads in data cables

The aim of present work is multi fold:

- ✓ In view of the variety of applications of hexaferrites, the author has synthesis a number of novel transition metal nanoferrites and evaluated important properties which are discussed under different chapters in the present thesis.
- ✓ To synthesize M-type $\text{SrFe}_{12}\text{O}_{19}$ hexaferrite particles, using mixed fuel techniques self-propagating high temperature synthesis (SHS) and auto combustion to compare thermal, microstructural, magnetic and dielectric properties.
- ✓ To investigate effect of different rare earth metal doping on formation of Sr-hexaferrite and Ni- ferrites particles in order to find best room temperature material for magnetic properties.
- ✓ One of the major aspect of the present work is preparation of magnetically tailored, mono phase nano sized particles at relatively room temperature.
- ✓ To prepare composites of $\text{SrFe}_{12}\text{O}_{19}$ and NiFe_2O_4 using SHS route in order to improve dielectric and magnetic properties.
- ✓ Prepared composites of $\text{SrFe}_{12}\text{O}_{19}$ and NiFe_2O_4 using auto combustion method in order to investigated the electrochemical sensor and gas sensor applications.

1.13 References

- [1] I. Safarik and M. Safarikova, *Monatshefte für Chemie*, Frankfurt. 133 (2002) 737-751.
- [2] C. Buzea, I. Pacheco and K. Robbie, *Bio interphases*. 2(4) (2007) 17- 71.
- [3] G. Singh, R. Dubey and P. Srivastava, *Thermochimica Acta*. 511 (2010) 112-118.
- [4] D. S. Mathew and R. S. Juang, *Chem. Eng.*, 129 (2007) 51.
- [5] R. P. Feynman, *Micro electromechanical Systems*. 1(1) (1992) 60–66.
- [6] N. Taniguchi, *Japan Society of Precision Engineering*, (1974).
- [7] G. C. Binnig, *Phys. Rev. Lett.* 56 (1986) 930.
- [8] F. Allhoff, P. Lin and D. Moore, *New York*. 3 (2010).
- [9] P. A. Shaikh, R. C. Kambale, A. V. Rao and Y. D. Kolekar, *J. Alloys Compd.* 492 (2010) 590-596.
- [10] S. Thakur, S. C. Katyal and M. Singh, *J. Magn. Mater.* 321 (2009) 1-7.
- [11] B. P. Jacob, S. Thankachan, S. Xavier and E. M. Mohammed, *J Alloys Compd.* 541 (2012) 29–35.
- [12] M. M. Costa, G. F. M. Pire's Junior and A. S. B. Sombra, *Mater. Chem. Phys.* 123 (2010) 35–39.
- [13] K. Klabunde, *Nanoscale Materials in Chemistry*. Wiley, New York. 1 (2001).
- [14] M. Hashim, Alimuddin, Shalendra Kumar, B. H. Koob, S. E. Shirsath, E. M. Mohammed. *J. Alloys Compd.* 518 (2012) 11–18.
- [15] K. Verma, A. Kumar, D. Varshney, *J. Alloys Compds.* 526 (2012) 91–97,
- [16] C. Heck. *Crane and Russak Co.* (1974) 16-86.
- [17] B. B. Ghate and Alex Goldman, *Ferrimagnetic Ceramics*. 11 (1990) 679-730.
- [18] J. Smit and H. P. J. Wijn. *Ferrites*. John Wiley and sons, New York. (1959) 216- 241.
- [19] B. D. Cullity and C. D. Graham. *IEEE Press & Wiley*, New Jersey. (2009).
- [20] S. Hilpert, *Chem. Ges. Bd.* 42 (1909) 2248.
- [21] V. Kato and T. Takei, *Jour Instrum. Ele. Eng*, (Japan). 53 (1933) 408-412.
- [22] M. Kawai. *Soc. Chem. Ind. (Japan)*. 37 (4) (1934) 392 -394.
- [23] J. L. Snoek, *Physica*. 3 (6) (1936) 463-483.

- [24] L. Neel, *Ann. Phys.* 3 (1948) 137–198.
- [25] P. W. Anderson, *Phy. Rev.* 79 (1950) 350.
- [26] Y. Yaffet and C. Kittel, *Phys. Rev.* 87 (1952) 290.
- [27] C. J. Guillard, *J Phys. Radium.* 12 (1951) 239.
- [28] E. W. Gorter, *Nature*, 173 (1974) 123-124.
- [29] E. J. W. Verwey, F. C. Romeijn and P. W. Heilman, *Chem. Phys.* 15 (1947) 181.
- [30] V. A. M. Braber. *Appl. Phys.* (1976)7347.
- [31] C. G. Koops, *Phys. Rev.* 83 (1951) 121–124.
- [32] K. C. Maxwell, Oxford University Press, London. (1873) 328.
- [33] K. W. Wagner. *Amer. Phy.* 40 (1913) 817-855.
- [34] R. D. Waldron. *Phys. Rev.* 99 (1955) 1727.
- [35] K. Maaz, A. Mumtaz, S. K. Hasanain and M. F. Bertino, *J. Magn. Magn. Mater.* 322 (15) (2010) 2199-2202.
- [36] M. A. Ahmed, S. I El-dek, S. F. Mansour and N. Okasha, *Solid State Sciences* 13 (2011) 1180-1186.
- [37] X. Meng, H. Li, J. Chen, K. Wang, and X. Li. *Mossbauer, J. Magn. Magn. Mater.* 321 (2009) 1155–1158.
- [38] I. H. Gul, A. Maqsood, M. Naeem, and M. Naeem Ashiq, *J. Alloys Compd* 507 (2010) 201–206.
- [39] C. Breschignag, P. Houdy, M. Lahmani. (Eds.), Springer-Verlag. (2006).
- [40] V. Kumar, A. Rana, M. S. Yadav, R. P. Pant, *J. Magn. Magn. Mater.* 320 (2008) 1729.
- [41] M. Hashim, Alimuddin, S. E. Shirsath, S. Kumar, R. Kumar, A. S Roy, J. Shah and R. K. Kotnala, *J. Alloys Compd.* 549 (2013) 348-547.
- [42] H. M. Tahir Farid, I. Ahmad, I. Ali, S. M. Ramay, A. Mahmood, *J. Magn. Magn. Mater.* 434 (2017) 143–150.
- [43] M. Rahimi, P. Kameli, M. Ranjbar and H. Salamati. *J. Nanopart. Res.* 15 (2013) 1865.
- [44] K. M. Batoo and M. Shahnawaze Ansari. *Nanoscale Res. Lett.* 7 (2012) 112.
- [45] M. M. El-Okra, M. A. Salem, M. S. Salim, R. M. El-Okr, M. Ashoush, and H. M. Talaat. *J. Magn. Magn. Mater.* 323 (2011) 920–926.

- [46] B. M. Sahanashree, E. Melagiriappa, M. Veena, G. J. Shankaramurthy, A Somashekarappa, *Rad. Phys. Chem.* 139 (2017) 55–65.
- [47] S. F. Mansour and M. A. Elkestawy. *Ceram. Int.* 37 (2011) 1175-1180
- [48] M. Kaur, S. Rana and P. S. Tarsikka. *Ceram. Int* 38 (2012) 4319–4323.
- [49] X. Cao, G. Liu, Y. Wang, J. Li and Ruoyu Hong. *J. Alloys Compd.* 497(1-2) (2010) 9-12.
- [50] M. H. M Raghasudha, S. S. Meena, J. Shah, Sagar E Shirsath, Shalendra Kumar, *J. Magn. Magn. Mater.* 449 (2018) 319–327.
- [51] M. N. Akhtar, A. Rahman, A. B. Sulong and M. A. Khan, *Ceram. Int*, 43(5) (2017) 4357-4365.
- [52] S. P. Gubin (Ed.). Wiley-VCH Verlag, Weinheim (Chapter 6) 2009.
- [53] B. L. Cushing, V. L. Kolesnichenko and C. O. Connor. *J. Chem. Rev.* 104 (2004) 3893.
- [54] M. A. Willard, L. K. Kurihara, E. E. Carpenter, S. Calvin and V. G Haris, *Int. Mater. Rev.* 49 (2004) 125.
- [55] S. C. Sangeeta Thakur, A. Katyal, V. R. Reddy Gupta and M. Singh. *J. Appl. Phys.* 105 (2009) 1.
- [56] A. B. Gadkari, T. J. Shinde, and P. N. Vasambekar, *J. Alloys Compd.* 509 (2011) 966–972.
- [57] J. M. Vargas, O. Moscoso-Londono, M. Knobel, M. Singh and S. K. Sharma, *RSC Adv.* 6 (2016) 70394–70404.
- [58] C. W. Chen, North Holland Publishing Company (1997).
- [59] K. H. J. Buschow, F. R. de Boer, Kluwer Academic Publishers, New York. (2004).
- [60] G. Binnig, H. Rohrer, C. Gerber and E. Weibel. *Phys. Rev. Lett.* 49 (1982) 57.
- [61] N. Rani, Patiala, India. (2016)
- [62] A. Goldman, Van Nostrand Reinhold, New Yrk. (1990).
- [63] W. H. Bragg. *Nature Lond.* 95 (1915) 199.
- [64] S. Nishikawa. *Proc. Tokyo Math. Phy. Soc.* 8 (1915) 199-200.
- [65] A. J. Moulson, J. M. Herbert, 1st Edition, Chapman & Hall, London. (1990).
- [66] N. R. Panchal, (Thesis) Ahmedabad, India (2011).

- [67] P. Ganapathi, (Thesis), Ahmedabad, India. (2014).
- [68] M. Irfan, A. Elahi, and A. Shakoor, *Ceram. Silikaty*, 60 (2016) 34–40.
- [69] M. Irfan, M. U. Islam, I. Ali, M. A. Iqbal, N. Karamat, and H. M. Khan, *Appl. Phys.*, 14 (2014) 112–117.
- [70] B. da Costa Andrade and M. A. Macedo, *Adv. Mater. Res.*, 975 (2014) 263–267.
- [71] Z. W. Li, L. Chen, Y. Wu, and C. K. Ong, *J. Appl. Phys.*, 96 (2004) 534–539.
- [72] J. Mohammed, H. Y. Hafeez, Tchouank Tekou Carol T., C. E. Ndikilar, J. Sharma, P. K. Maji, S. K. Godara and A. K. Srivastava, *Mater. Res. Express*. 6 (2019) 056111.
- [73] H. C. Fang, C.K. Ong, *J. Applied Physics*, 86-4 (1999) 2191.
- [74] Harris, V. G. Chen, Z. Chen, Y. Yoon, S. Sakai, T. Gieler, A. Yang, A. He, Y. Ziemer, K. S. Sun, N. X. Vittoria, Carmine, *J. Appl. Phys.* 99-8 (2006) 08911.
- [75] S. H. Mahmood, M. D. Zaqsaw, O. E. Mohsen, A. Awadallah, I. Bsoul, M. A. Awawdeh, and Q. I. Mohaidat, *Solid State Phenom.* 206 (241) (2016) 93–125.
- [76] M. A. Vinnik, *Russ. J. Inorg. Chem.* 10 (9) (1965) 1164-1167.
- [77] J. Li, H.F. Zhang, G.Q. Shao, W. Cai, D. Chen, G.G. Zhao, B.L. Wu, S. X. Ouyang, , *Cond Mat. Mtrl Sci.* 1407 (2014) 605.
- [78] V. F. Belov, K. S. Ovanesyanyan, V. A. Trukhtanov, M. N. Shwko, E.V. Korneev, V. V. Korovushkin, and L. N. Korablin, *soviet physics jetp.* 32 (1971) 1484-1489.
- [79] J. J. Went, G.W. Ratheneau, E.W. Gorter, G.W. Van Dosterhout, *Philips Tech. Rev.* 13 (1951) 194.
- [80] S. R. Shinde, S. E. Lofland, C. S. Ganpule, S. M. Bhagat, S. B. Bhagat, S. B. Ogale, R. Ramesh, T. Venkatesan, *J. Appl.Phys.*74 (1999) 594-596
- [81] R. A. Pawar, S. S. Desai, Q.Y. Tamboli, Sagar E. Shirsath, S.M. Patange, J. *Magn. Mater.* 378 (2015) 59–63.
- [82] A. Zafar, A. Rahman, S. Shahzada, S. Anwar, M. Khan, A. Nisar, M. Ahmad, S. Karim, *J. Alloy. Compd.* 727 (2017) 683–690.
- [83] R. Topkaya, I. Auwal, A. Baykal, *Ceram. Int.* 42 (2016) 16296–16302.
- [84] J. Dho, E. K. Lee, J.Y. Park, N .H. Hur, *J. Magn. Mater.* 285 (2005) 164-168.

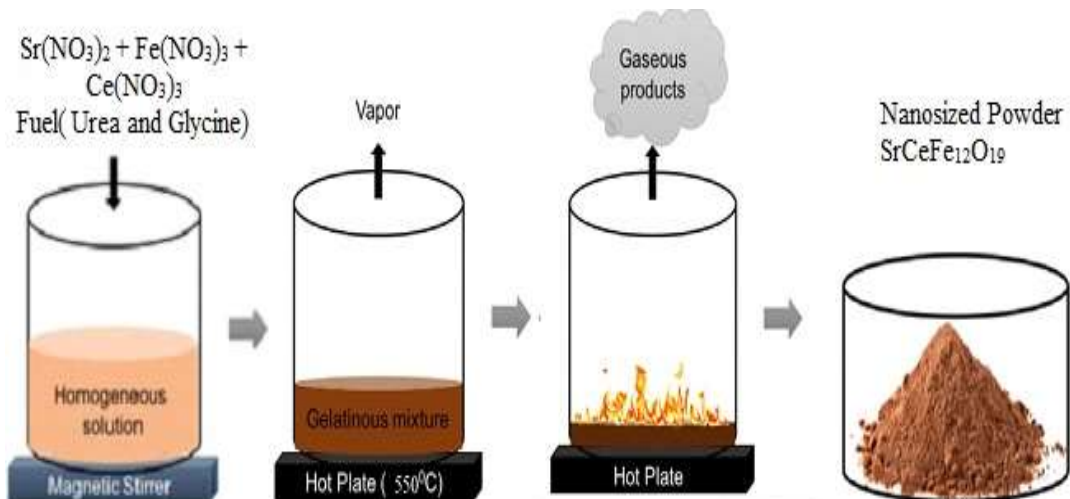
- [85] Y. W. Dou, Ferrite, Jiangsu Science and Technology, Nanjing. 417 (1996).
- [86] N. Dishovske, A. Petkov, I.V. Nedkov, IEEE Transactions on Magnetics 30 (1994) 969-971.
- [87] C. A. Van Den Brock, A. L. Stuijts, Philips Technical Review 37 (1977) 157
- [88] R. C. Pullar, Prog. Mater. Sci. 57 (2012) 1191–1334.
- [89] X. Tang, R.Y. Hong, W.G. Feng, D. Badami, J. Alloys Compd. 562 (2013) 211–218
- [90] V. G. Harris, A. Geiler, Y. J. Chen, S. D. Yoon, M. Z. Wu, A. Yang, Z.H. Chen, P. He, O. Acher, C. Vittoria, J. Magn. Magn. Mater. 321 (2009) 2035–2047.
- [91] X. Tang, Y. M. Wang, Z. Luo, L. S. Wang, R.Y. Hong, W. G. Feng, Prog. Org. Coat. 75 (2012) 124–130.
- [92] T. P. Xie, L. J. Xu, C.L. Liu, Powder Technol. 232 (2012) 87–92.
- [93] T. P. Xie, L. J. Xu, C. L. Liu, Y. Wang, Appl. Surf. Sci. 273 (2013) 684– 691.
- [94] G. M. Rai, M. A. Iqbal, K. T. Kubra, J. Alloys Compd. 495(2010) 229-233.
- [95] F. M. M. Pereira, C.A.R. Junior, M. R. P. Santos, R.S.T.M. Sohn, F.N.A. Freire, J.M. Sasaki, J. Mater. Sci. Mater. Electron. 19 (2008) 627-638.
- [96] A. Liaquat, M. Anis-ur-Rehman, Ul Haq, J. Alloys Comp. 822 (2020) 153561.
- [97] M. A. Almessiere, Y. Slimani, H. Gungüneş, H. S. El Sayed, A. Baykal, Ceram. Int. 44(9) (2018) 10470– 10477.
- [98] R. A.Pawar, S. S.Desai, Q. Y. Tamboli, S. E.Shirsath, S. M.Patange, J. Magn. Magn. Mater. 378 (2015) 59–63.)
- [99] S. Qi, Y. Yang, Y. Qin and F. Wang. J Magn. Magn. Mater. 329 (2013) 77-83.
- [100] W. Kim, S. W. Hyun, T. Kouh and C. S. Kim. Kor Phy Soc. 59 (2011) 338-3384.
- [101] K. K. Bharathi, R. S. Vemuri, M. Noor-A-Alam and C. V. Ramana. Thin Sol Films 520 (2012) 1794-1798.
- [102] M. N. Ashiq, M. J. Iqbal, M. Najam-ul-Haq, P.H. Gomez, A. M. Qureshi, J. Magn. Magn. Mater. 324 (2012) 15.
- [103]. R. C. Pullar, Prog. Mater Sci. 57 (2012) 1191–1334
- [104] B. A. Gadkari, T. J. Shinde and P. N. Vasambekar, J. Magn. Magn. Mater. 322 (2010) 3823–3827.

- [105] D. Seifert, J. Topfer, F. Langenhorst, Le Breton, H. Chiron, L. Lechevallier, J. Magn. Mater. 321 (2009) 4045.
- [106] J. Lakshmikantha, G. Krishnamurthy, B. M. Nagabhushan, C. S. Naveen and E. Melagiriappa, J Supercond Nov Magn (2022).
- [107] J. F. Wang, C. B. Ponton, I. R. Harris, J. Alloy. Compd. 403 (2005) 104–109.
- [108] B. H. Bhat, B. Want, Appl. Phys. A 122 (2016) 148.
- [109] L. Lechevallier, J. M. Le Breton, A. Morel, J. Teillet, J. Alloy. Compd. 359 (2003) 310–314.
- [110] J. Lakshmikantha, G. Krishnamurthy, B.M. Nagabhushan, E. Melagiriappa, J. of Solid State Chemistry. 315 (2022) 123465
- [111] H. F. Lu, R. Y. Hong, H. Z. Li, J. Alloys Compd. 509 (2011) 10127–10131.
- [112] C. W. Chen. Amsterdam, New York, Oxford. 209 (1977).
- [113] P. J. Wiess. Physique. 6 (1907) 661.
- [114] F. G. Brockman and K. E. Matterson, Amer. Ceram. Soc. 54 (1971) 180-183.
- [115] E. J. W. Verwey, F. C. Romeijn and P. W. Heilman. Chem. Phys. 15 (1947) 181.
- [116] V. R. K. Murthy and J. Shobanadri. Phy. Stat. Sol. 38 (1977) 647.
- [117] M. Ishaque, M. A. Khan, I. Ali, M. Athai, Hasan M. Khan, Mater. Sci. Semicond. Process. 41 (2016) 508–512.
- [118] E. Melagiriappa, H. S. Jayanna and B. K. Chougule. Mater. Chem. Phys. 112 (2008) 68–73.
- [119] E. Melagiriappa, M. Veena, A. Somashekarappa, G. J. Shankaramurthy and H. S. Jayanna, 88 (8) (2014) 795–801.
- [120] R. Sakthi, S. Saravanan and C. K. Mahadevan. J Alloys Compds. 541 (2012) 115–124.
- [121] M. A. Dar, K. M. Batoor, Vivek Verma, W. A. Siddiqui and R. K. Kotnala. J Alloy. Compd. 493 (2010) 553–560.
- [122] J. A. Plambeck, Wiley Interscience Publication, USA (1982).
- [123] D. A. Skoog, D. M. West, F. J. Holler, Fort Worth (1992).
- [124] H. H. Willard, L. L. Merrit Jr, J. A. Dean, F. A. Settle Jr, , 6th ed., D. Van Nostrand, Princeton (1981).

- [125] Y. Yang, J. Zhou, H. Zhang, P. Gai, X. Zhang, J. Chen, *Talanta*, 106 (2013) 206-211.
- [126] W. Sun, Y. Wang, Y. Lu, A. Hu, F. Shi, Z. Sun, *Sens. Actuators B*, 188 (2013) 564-570.
- [127] C. Y. Tsai, T. L. Chang, C. C. Chen, F. H. Ko, P. H. Chen, *Microelectron. Eng.* 78 (2005) 546–555.
- [128] F. de Assis dos Santos Silva, M. G. A. da Silva, P. R. Lima, M. R. Meneghetti, L. T. Kubota, M. O. Fonseca Goulart, *Biosens. Bioelec.* 50 (2013) 202–209.
- [129] S. Liua and G. Daib, *J Chi. Chemi. Soci.* 58 (2011) 617-622.
- [130] H. Nazemi, A. Joseph, J. Park, A. Emadi, *Sensors*. 19(6) (2019) 1285.
- [131] W. Zeng, Y. Liu, J. Mei, C. Tang, K. Luo, S. Li. *Sen. Actuators B: Chem.*, 301 (2019) 127010.
- [132] S. Kumar, V. Pavelyev, P. Mishra, N. Tripathi, P. Sharman.. *Mater. Sci. Semicond. Process.* 107 (2020) 104865
- [133] <http://www.hindustanpetroleum.com/En/ui/AboutLPG.aspx>
- [134] S. G. Chatterjee, S. Chatterjee, A. K. Ray, & A. K. Chakraborty,. *Sens. Actuators B: Chem.* 221 (2015) 1170-1181.
- [135] G. Pr. Nethala, R. Tadi, G. Rao Gajula , C. Kumar. *Phys B: Phy of Cond Matt.* (2018).
- [136] L. Mocuta, J. M. Le Breton, J. F. Wang, I. R. Harris *J. Alloys and Compd* 364 (2004) 48–52.
- [137] M. N. Ashiq, A. S. Asi, S. Farooq, M. Najam-ul-Haq, S. Rehman, *J. Magn. Magn. Mater.* 444 (2017) 426–431.
- [138] Y. Yang, X. Liu, D. Jin, K. Huang, Shang Gao, *J. Magn. Magn. Mater.* 355 (2014) 254–258.
- [139] M. A. Almessiere, Y. Slimani, H.S. El Sayed, A. Baykal, I. Ercan, *J. Magn. Magn. Mater.* 471 (2019) 124–132.
- [140] B. K. Rai, S. R. Mishra, V. V. Nguyen. *J. P. Liu, J. Alloys and Compd* 550 (2013) 198–203
- [141] Y. J. Yang, F. H. Wang, J. X. Shao, X. S. Liu, S. J. Feng, J. S. Yang, *J. Magn. Magn. Mater.* 401 (2016) 1039-1045

CHAPTER 2:-

EXPERIMENTAL AND CHARACTERIZATION TECHNIQUES



2.0 Synthesis methods

The synthesis methods play an important role to produce high quality ferrites materials, in terms of morphology, purity, stability, and surface area. The solution-based chemical synthetic strategies provide simple and powerful routes to nanocrystals. They are quite general, allowing the preparation of all kinds of nanomaterials, and usually hold the advantages of greater capability. Presently, various synthesis methods are being used for the preparation of ferrite materials, as each of synthesis method has its own advantages and disadvantages. The bottom-up and top-down approaches are divided into two broad categories of synthesis methods. During “bottom-up,” the ions are chemically combined together to form the particles, whereas, in “top-down” course, materials are pulverized to form tiny particles. There are several synthesis techniques considered the “bottom-up” option, which include coprecipitation, thermal decomposition, hydrothermal, solvothermal, sol-gel, solution combustion, flame spray pyrolysis, sonochemical, vapor deposition, microwave-assisted, microemulsion, polyol techniques, etc, whereas, only the mechanical milling techniques and pulsed laser ablation are under the “top-down” synthesis category.

2.1 Materials and Solution combustion synthesis (SCS) method

Nowadays, the solution combustion synthesis has emerged as propellant chemistry method for the synthesis and processing of nanomaterials especially magnetic nanoparticles. Solution combustion synthesis (SCS) is a versatile, simplest and quick process, reliability, flexibility and low cost process to produce various industrially useful materials. Importantly, SCS process involves in synthesis of a various types of nanomaterials without risk of any contamination, lower consumption of energy and

elimination of intermediary calcinations stages during the synthesis. Solution combustion synthesis is also known as self-sustained reaction in homogeneous solution of different metal nitrates used as oxidizers and urea, glycine, hydrazide, alanine as fuel, glycine, or hydrazides as fuels. During the synthesis, the method has low external energy consumption and elimination of intermediary calcinations stages [1-2]. This method involves lower costs of preparation methods. The main purpose of combustion technique synthesis used for successful synthesis of ferrites is to obtain the single-phase materials of nanocrystalline ferrite particle (<100 nm) having high surface areas with controlled microstructures and electromagnetic properties. These properties are achieved by controlling the characteristics of the powders (purity, chemical homogeneity, and morphology and particle size. The flow diagram for preparation of nanoferrites by solution combustion synthesis is shown in fig 2.1.

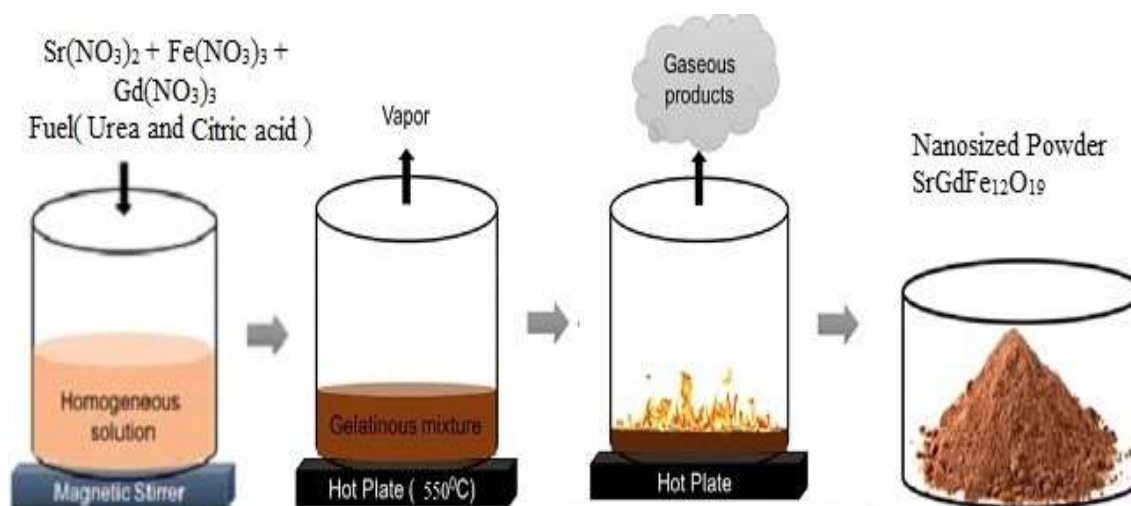


Fig 2.1. The preparation of nanoferrites by solution combustion synthesis

The chemicals used for the present research work are listed in Table 2.1.

Table 2.1: Chemicals used in the present work

Sl. No.	Name of the material/chemical	Chemical formula	Company Name	(%) Purity
1	Strontium nitrate hexahydrate	$\text{Sr}(\text{NO}_3)_2 \cdot 6\text{H}_2\text{O}$	Merck Co	$\geq 99\%$
2	Cerium nitrate hexahydrate	$\text{Ce}(\text{NO}_3)_3 \cdot 6\text{H}_2\text{O}$	Sigma Aldrich	$\geq 99\%$
3	Ferric nitrate nonahydrate	$\text{Fe}(\text{NO}_3)_3 \cdot 9\text{H}_2\text{O}$	Sigma Aldrich	99 %
4	Gadolinium nitrate hexahydrate	$\text{Gd}(\text{NO}_3)_3 \cdot 6\text{H}_2\text{O}$	Merck Co	$\geq 99\%$
5	Nickel nitrate hexahydrate	$\text{Ni}(\text{NO}_3)_2 \cdot 6\text{H}_2\text{O}$	Steam Chemicals	$\geq 99\%$
6	Copper nitrate trihydrate	$\text{Cu}(\text{NO}_3)_2 \cdot 3\text{H}_2\text{O}$	Sigma Aldrich	99 %
7	Magnesium nitrate hexahydrate	$\text{Mg}(\text{NO}_3)_2 \cdot 6\text{H}_2\text{O}$	Merck Co	$\geq 99\%$
8	Glycine	$\text{C}_2\text{H}_5\text{NO}_2$	Rankem	99 %
9	Urea	$\text{CH}_4\text{N}_2\text{O}$	Rankem	99 %
10	Citric acid	$\text{C}_6\text{H}_8\text{O}_7$	Himedia	99 %

The nano materials are prepared for the present research work were listed below:

1. $\text{Sr}_{(1-x)}\text{Ce}_x\text{Fe}_{12}\text{O}_{19}$ ($x = 0.00 < x < 0.09$) : glycine and urea
2. $\text{Sr}_{(1-x)}\text{Gd}_x\text{Fe}_{12}\text{O}_{19}$ ($x = 0.0, 0.01 < x < 0.09$: in steps of 0.02): Citric acid and urea
3. $\text{NiSrGd}_x\text{Fe}_{2-x}\text{O}_4$ ($x = 0.00, 0.01, 0.05$ and 0.09): urea
4. $\text{Sr}_{(1-x)}\text{NiCu}_x\text{MgO}_3$ ($x = 0.00, 0.01, 0.05$ and 0.1): urea

The respective metal nitrates and fuel were weighed accurately by using microbalance-having least count 0.0001gm. A clear solution is obtained by dissolving the stoichiometric ratio of metal nitrates and urea in deionized water. The aqueous solution containing precursor solutions (redox mixture) taken in a Pyrex dish was placed and heated up to 550 °C in muffle furnace. Initially, the solution begins to boil in a muffle furnace then froths, ignites and liberate large amount of heat and gases (N₂O and CO₂), vaporizes the entire solution instantly to yield fluffy voluminous nanoferrites fine powders. The entire reaction time of was less than within 10 minutes and the reaction completed less than 15 s. The gases are known as hypergolic. The slurry formed was placed in a ceramic crucible and sintered (calcined) at 1000 °C for 5 hours in air. The pre-sintered powders were again well ground. All the unreacted particles bringing close together, result in better homogenization of nanoferrites. Moreover, the process tends to decrease the diffusion distances and distribution of grain size. At this stage, pristine powders were ground in agate mortar and mixed with a binder polyvinyl pyrolidone (PVP) (C₆H₉NO)_n. The presintered powders were pressed into pellets (10 mm dia and ~2-3 mm thick) with a pressure of $5 \times 10^8 \text{ N / m}^2$ in a stainless steel pellet maker for 5 minutes. Finally, the pellets have been calcinated at 1100 °C for 20 hours in a muffle furnace and then gradually cooled to 300 K. An either sides of the pellets were well polished and coated with air-dried silver paste for good ohmic contact material for measurements of magnetic and dielectric properties.

2.2 Pellet preparation

The slurry formed was placed in a ceramic crucible and pre sintered (calcined) at 1000 °C for twenty hours in air. The pristine powders were again well ground in agate mortar. This result in better homogenization of the powders by moving particles closed together that decreases the diffusion distances and also the distribution of grain size.



Fig 2. 2. Photograph of hydraulic press

At this stage, die was cleaned by acetone and later by stearic acid. The pristine powder was mixed with PVP binder in acetone medium. Acetone was allowed to evaporate. The pristine powders were transferred into die having 10mm diameter and compressed into pellets by loading a pressure of $5-10^8 \text{ kg/m}^2$ for 5 minutes uniaxial in hydraulic press as showed in fig 2.2.

2.3 Final sintering

At the beginning of the sintering, the binder was removed (burn-off) from the pellets in the temperature range from 350-500 °C for six hours in a furnace. Finally, the pellets have been sintered at 1100 °C for 5 hours in static air atmosphere in a muffle furnace and then gradually cooled to 300 K.

2.4 Experiment Techniques

Nowadays, the characterization of synthesized nanomaterials is very important aspect because of their versatile applications in the area of materials science. In the present investigation, various experimental techniques made use for the characterization of synthesized nanoferrites and short description of the techniques with some theoretical aspects are included. The techniques used are X-ray powder diffraction (XRD) technique, Fourier transform infrared spectroscopy (FTIR), UV visible spectroscopy, Field emission scanning electron microscopy (FESEM) and Energy dispersive analysis by x-rays (EDAX). Thermo-gravimetric data analysis (TGA-DTA). The dielectric parameters and complex impedance was measured using LCR meter at room temperature. The magnetic properties have been systematically measured using Vibrating sample magnetometer (VSM) at 300 K. The electrochemical behavior of the modified electrode and it was investigated using of cyclic voltammetry (CV). The prepared sample was kept in an in-house fabricated gas-sensing chamber, and the electrical resistance of the sample was measured in air (R_a) and the presence of test gas (R_g) at room temperature.

2.5 X-rays diffraction studies

X-rays are electromagnetic radiation of wavelength about one 1 \AA or 10^{-10} m . X-ray diffraction (XRD) method is the most versatile and non-destructive characterization technique to identify the atomic and molecular structure of a crystal. This method is widely used as primary characterization technique in nanoparticles research. In the present investigation, XRD technique reveals the information about the structural parameters such as single phase nature, lattice parameter, interplanar distance, intensity phases, crystal structure, crystallite size, X-ray density, chemical composition, site radii bond lengths, grain size, defects, strain and impurity phases.

2.5.1 Condition for X-Ray Diffraction

In the figure, a parallel beam of monochromatic X-rays are allowed to incident at a glancing angle θ . These, incident X-rays gets reflected from a set of atomic parallel planes obey the condition for Bragg's law of diffraction as depicted in fig 2.3. The path difference between two x-ray beams incident on parallel crystal planes is $2d_{hkl} \sin\theta$. The inter-planar spacing between the two planes is d_{hkl} . The two reflected beams are in same phase with each other and path difference is equal to an integral multiple of wavelength of x-rays (λ) [3, 4]. The constructive interference occurs only $2d_{hkl} \sin\theta$ is equal to $n\lambda$. This condition obeys the Bragg's law

$$2d_{hkl} \sin \theta = n\lambda \quad (2.1)$$

where n - diffraction order, d_{hkl} - interplanar distance, θ is glancing angle, λ is wavelength of monochromatic x-rays :

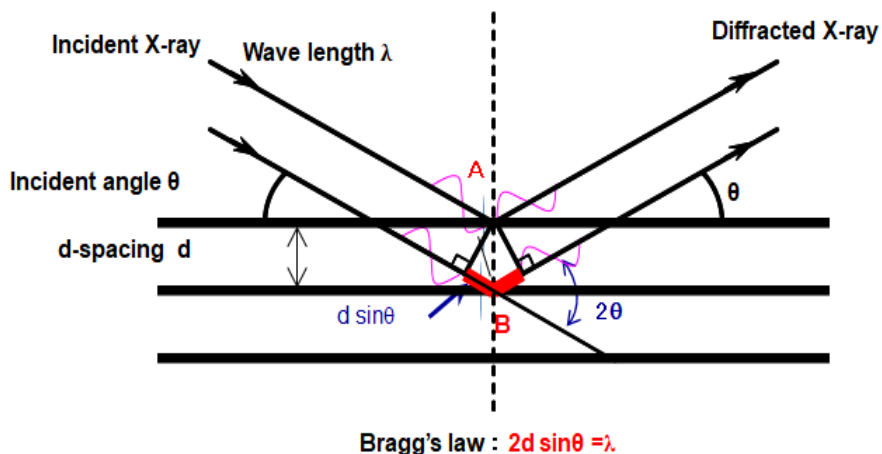


Fig 2.3. Illustration of crystal planes and Bragg's law.

2.5.2 X-ray Diffractometer

The principal and essential features of x-ray diffractometer are depicted in fig 2.4. In this method, the powdered sample is mounted on the turntable H. A monochromatic X-ray beam usually of $K\alpha$ radiation is incident on the thousands of randomly oriented crystalline in powder form. The incident x-ray beam is diffracted by crystal planes oriented to satisfy Bragg's law. The converged diffracted x-ray beam focused on the slit B and then enters the detector connected to a counter rate meter. The specially made slit B is collimates the diffracted beam in to counter. The output of the circuit is connected to fast automatic recorder, which registers counts per second versus 2θ . The diffractometer gives a record showing the variations of intensities of diffraction line with diffracting angle 2θ . The rotations of the specimen table by an angle θ cause the rotation detector carriage by an angle 2θ . However, in a modern X-ray diffractometer, proportional or scintillation counter records automatically a graph of intensity of 2θ . The main advantage of this diffractometer is that provides a quantitative measurement of intensity of diffracted beam than from the Debye-Scherrer camera.

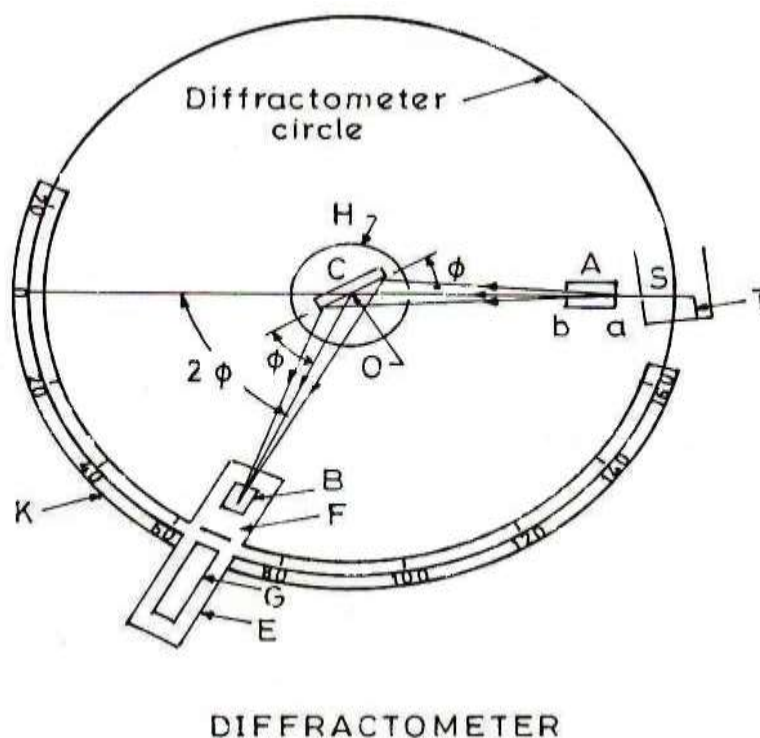


Fig 2.4. Schematic diagram of X-ray diffractometer.

2.5.3 Experimental

The X-ray diffraction patterns of pristine nanoferrites have been obtained from Mysore University, Karnataka, India using powder Bruker AXS D8 Advance powder X-ray diffractometer with $\text{CuK}\alpha$ radiation bearing wavelength 1.5406 \AA , in Bragg angle, 2θ , range from $20^\circ - 80^\circ$ at the chart speed of $20^\circ/\text{min}$.

(i) Calculation of X-ray density

The theoretical x-ray density (d_x) of each sample was calculated using the formula

$$d_x = \frac{ZM}{NV} \quad (2.2)$$

where $Z = 8$, is Number of molecules per unit cell, M is the molecular weight, N is the Avogadro's number and $V = a^3$ is the unit cell volume for cubic system in m^3 .

(ii) Calculation of crystallite size

From XRD profile, an average crystallites size of nanoferrites was determined using Debye-Scherrer equation

$$d = \frac{k\lambda}{\beta \cos\theta} \quad (2.3)$$

where, $k = 0.89$ is Scherer's constant, $\lambda = 0.15406$ nm is wavelength of the incident X-rays in nm, β is the full width at half maximum (FWHM) of diffraction peak, θ is the Bragg diffraction angle.

(iii) Calculation of interplanar distance, lattice parameter and cell volume

From Bragg's law, in cubic system, the interplanar distance 'd' was calculated with respect to the line of maximum intensity. The lattice parameter is calculated using the relation.

$$\frac{1}{d_{hkl}^2} = \frac{4}{3} \left[\frac{h^2 + hk + k^2}{a^2} + \frac{l^2}{c^2} \right] \quad (2.4)$$

where d_{hkl} is the distance between the crystal planes, a and c are the lattice parameters and $(h k l)$ are the Miller indices. The unit V_{cell} of the hexagonal system is calculated as follows:

$$V_{cell} = 0.866 a^2 c \quad (2.5)$$

where, the numerical factor is constant for the hexagonal system.

$$\rho_b = \frac{m}{\pi r^2 h} \quad (2.6)$$

where, m is the mass, r is the radius and h is the height of the pellet. Percentage porosity was calculated using the formula.

$$P = \left(1 - \frac{\rho_b}{\rho_x} \right) \quad (2.7)$$

where, ρ_x is the x-ray density and the ρ_b bulk density.

2.6 Fourier transforms infrared spectroscopic studies (FTIR)

2.6.1 Introduction

The study of infrared absorption spectrum is a non-destructive method to investigate several ordering phenomenon. Infrared spectroscopy provides the information about the ions position in a crystal lattice and as well as crystal modes of vibrations [5]. In an infrared spectroscopy, a molecule is exposed to infrared radiation thereby absorption occurs owing to matching of radiant energy with that of the specific molecular vibrational energy. The frequencies of vibrations depending upon the mass of cation, distance between the cation and oxygen ion and the bonding force [6].

Electromagnetic radiations which are lying in the wavelength region (1 μ m to 1mm) little longer than the visible light are termed as infrared radiations. In an electromagnetic spectrum infrared region lies in between visible region and microwave regions. Further, on the basis of wavenumbers the infrared region in an electromagnetic spectrum can be divided into three regions such as (i) near range from 400 cm^{-1} -10 cm^{-1} , (ii) middle range from 4000 cm^{-1} - 400 cm^{-1} and (iii) far infrared range from 14000 - 4000 cm^{-1} . An increase in the wave number correspondingly energy also increases. Waldron suggested that the high frequency absorption band ν_1 , assigned to intrinsic vibration of tetrahedral group complexes, while the low frequency absorption band ν_2 is assigned to octahedral complexes [7]. The low frequency absorption band ν_3 is attributed to octahedral metal ion–oxygen complexes. Furthermore, the low frequency absorption band ν_4 is occur due to some vibrations involved in displacement of tetrahedral ion. This band depends upon on the mass of divalent tetrahedral ion [8]. When a molecule interacts with the radiation of the proper frequency, it absorbs energy and molecule is set into

vibration. They depend upon the preparation conditions and grain size. They give rise to distinct shoulder or even splitting of the bands. The other two bands are quite sharp or weaker at low frequency bands and they are not depending upon preparation conditions.

The IR Spectra provide important information about (i) the completion of solid state reaction, (ii) distribution of cation among non-equivalent site and their valency, (iii) nature of metal oxygen bonds, (iv) calculation of force constant and (v) nature of electronic transition and calculation of activation energy (E).

2.6.2 Working of an FTIR spectrometer

The basic instrument design of FTIR is quite simple. A typical FTIR spectrometer consists of the source which is glowing black body emitted the infrared energy. A fine beam of infrared energy beam is allowed to pass through an aperture and the energy is transferred into material and finally received by detector. An interferometer receives infrared energy then spectral encoding takes place and produces resulting signal. The composition absorbs the energy beam and transmits the reflected from the sample surface. The absorption depends on particular frequencies of energy. They are uniquely characteristics of composition. Finally, the beam enters into detector for final measurement. The signal is transferred to the computer in digital form as shown in fig 2.5.

2.6.3 Experimental

Room temperature FTIR spectra of all virgin nanoferrites were recorded by employing Shimadzu IRSpirit 01994, Shimadzu, Fourier transform infrared spectrometer from the wavenumber $4000 - 300 \text{ cm}^{-1}$ from Department of Studies in Research Industrial chemistry, Sahyadri science college, Shivamoga, Karnataka, India.

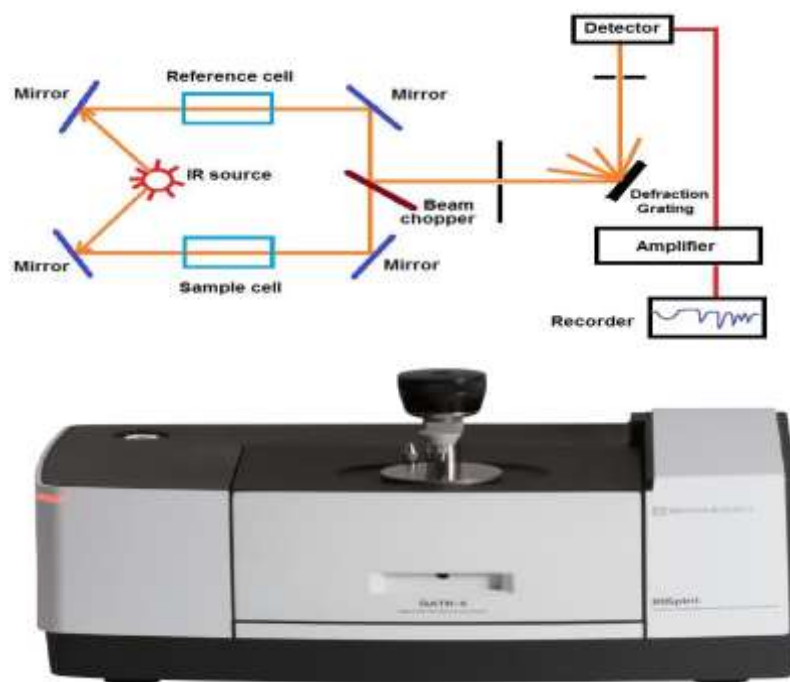


Fig 2.5. Schematic representation and Photograph of Fourier transforms infrared absorption spectrometer.

The samples (0.5 mg to 1.0 mg) were mixed with spectral grade potassium bromide (KBr) as the standard ground and then pressed to obtain circular discs of appropriate 1mm thickness. The force constants K_T and K_O for the atoms at tetrahedral sites and octahedral sites, respectively, are estimated by using following equations.

$$K_T = 4\pi^2 c^2 \nu_1^2 m \quad (2.8)$$

$$K_O = 4\pi^2 c^2 \nu_2^2 m \quad (2.9)$$

where c is velocity of light 3×10^8 m/s, ν_1 and ν_2 are vibrational frequencies at A-sites and B-sites, m is reduced mass of Fe^{3+} ions and O^{2-} ions ($\sim 2.061 \times 10^{-23}$ g).

2.7 Scanning electron microscopic studies

2.7.1 Introduction

The scanning electron microscopy (SEM) is one of the advanced and powerful techniques to explore the microstructure of ferrite materials. The scanning electron microscope possesses high resolving power, high magnification and capability to form three dimensional images. Moreover, SEM technique provides the complete information about surface topography, dielectrical conductivity, magnetic compact & composition.

2.7.2 Principle of Scanning Electron Microscope

A well-defined electron beam impinges on the specimen and leads to generation of secondary electrons, back scattered electrons, absorbed electrons, characteristic X-rays etc. These electrons can be detected by suitable detectors and give information about the microstructure and morphology of the specimens with resolutions of about a few tenths to a few nanometers.

2.7.3 Working of Scanning Electron Microscope

A very fine beam of electrons is directed on a solid surface of the specimen, resulting in the transfer of energy to the solid surface. These bombarding electrons, also referred to as primary electrons, dislodge electrons from the specimen itself. The dislodged electrons, also known as secondary electrons, are attracted and collected by a positively biased grid or detector, and then translated into a signal. To produce the SEM image, the electron beam is swept across the area being inspected, producing many such signals. These signals are then amplified, analyzed, and translated into images of the topography being inspected. Finally, the image is shown on a cathode ray tube (CRT) fig

2.6. Here an electron beam scans the object (the specimen) and because of synchronized scans of electron beam and the CRT screen (nowadays, monitor), there is one-to-one correspondence between the spot on the specimen and the spot on the screen. Unlike Optical microscopy, SEM requires the vacuum environment and specimen surface to be electrically conductive. Fig. 6, shows the general schematic diagram of SEM. An advantage of SEM is the wide variety of electron-specimen interactions that can be used to form an image to give qualitative and quantitative information. The large depth of focus, excellent contrast and the straight forward preparation of solid specimen are advantages of SEM.

2.7.4 Experimental

Scanning electron micrographs of nanoferrites in the present investigation were obtained by employing JEOL/EO/JSM-639, model scanning electron microscope from Mysore University, Karnataka, India have the following technical specifications.

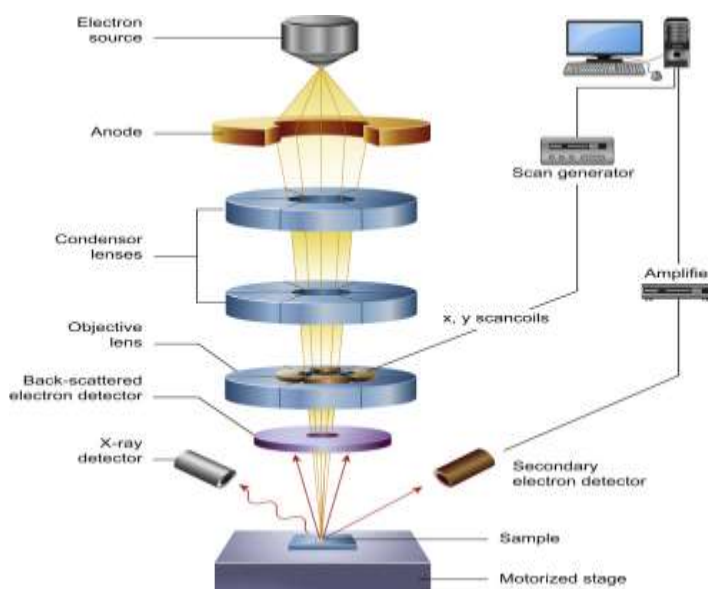


Fig 2.6. Schematic Diagram of Scanning Electron Microscope

SEM Make	:	JEOL/EO/JSM-639
Resolution	:	3 nm (Acc V 30 KV, WD 8 mm, SEI)
	:	8 nm (Acc V 3.0 KV, WD 6 mm,
Magnification	:	5 X to 300, 000 X (Both in High and Low Vacuum Modes)
Image Modes	:	SEI, BEI
Probe Current	:	1 pA to 1mA

The average grain sizes of all the samples were determined by counting a sufficiently large number of grains to ensure accuracy by using line intercept method the equation.

$$Ga = \frac{1.5L}{MN} \quad (2.10)$$

where L is total test line length (m), M is the magnification, N is the total number of intercept.

2.8 Energy Dispersive X-Rays Analysis

2.8.1 Introduction

Energy dispersive analysis by X-Rays (EDAX) or EDS analysis is an analytical technique used predominantly to determine the chemical element and the composition of the element qualitatively and quantitatively. In general, analyzer is attached with scanning electron microscope. Moreover, there are two different detectors which collect information reflected from the samples. The EDAX principle is quite simple and very similar to the SEM. An electron beam emitted by an electron gun is directed on the sample to be tested. The incident electron beam excites the electrons of the atoms inside the materials. This causes de-excitation, emission of X-rays with energies equal to binding energies of the electrons. The binding energies are specific for each element, thus each chemical components are identified. An electron beam incidents on the sample, the

sample emits different kind of information namely, backscattered electrons, reflected electrons, auger electron and x-ray. X-ray emitted from the samples are characteristics X-rays and carry qualitative and quantitative information of the samples. The detector can collect these characteristic x-rays. Finally, the energies of this characteristic x-ray to be matched with the standard lines. The weight and Atomic percentage of each element presented in the investigate nanoferrites are identified by EDAX graphs from Mysore University, Karnataka, India.

2.9 UV-Visible absorption spectroscopy

The Ultraviolet (UV)-Visible spectrophotometer is the most commonly used instrument in the scientific laboratories, it is used to analyze electronic transitions of compounds in ultraviolet and visible regions. UV-Visible spectroscopy is a type of absorption/transmission/reflectance spectroscopic technique and the spectrum ranges from 200 to 800 nm (UV region from 200 to 400 nm & visible region from 400 to 800 nm). From this spectroscopy the intensities of absorbance/ transmittance/reflectance are studied with change in wavelengths within the region. This provides an information on the percentage of absorbed radiation at individual wavelengths and in this technique, either absorption/emission is concerned. A reflectance spectrum was obtained by collecting and analyzing the surface reflected electromagnetic radiation as a function of frequency or wavelength. There are different types of reflections occurred in the reflectance spectra they are regular, speculative, and diffuse reflections. Regular and speculative reflections were associated with the smooth, shiny surface and diffuse reflection was associated with the dull surface of the samples. The optical phenomenon known as diffuse reflectance was commonly used in the UV-Visible region to obtain

molecular spectroscopic information. It was typically used to obtain the spectra of opaque powders with minimum sample preparation. In the diffused reflectance spectroscopy (DRS), electromagnetic radiations reflected from the dull/opaque surfaces were collected and analyzed, it was an alternative to conventional transmission spectroscopy.

2.9.1 Instrumentation

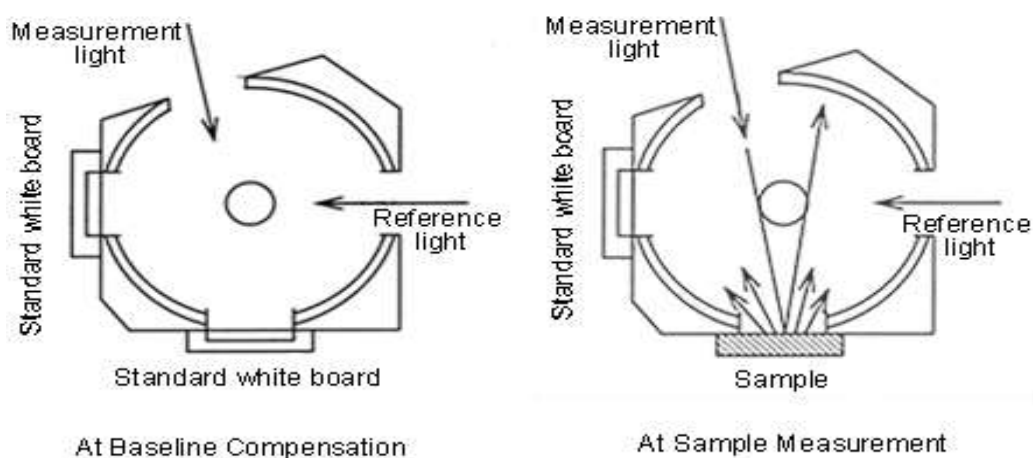


Fig 2.7. Specular reflectance measurement of UV-Vis spectrophotometer.

UV-Vis DRS was well known system which light cannot penetrate into the opaque media that can be analyzed by the reflection on the surface of the samples. Thus, dispersed radiation originating from the material was collected in an incorporation circle and recognized with relative specular reflectance measurement as shown in the fig 2.7. The reflectance data was calculated from strength ratio after comparing the light reflected from the reference sample and also from measurement sample. The reflectance of reference sample was taken to be 100%, and reflectance of certain sample with respect to the reference sample was measured. This method was often applied to examine semiconductors, optical materials, and multilayer films. The incident light reflected

symmetrically with respect to the normal line was called “specular reflection”, while incident light scattered in different directions was called “diffuse reflection”. Measurement was performed with integration of sphere by placing the sample in front of the incident light window and reflected light from the sample was concentrated using a sphere detector with barium sulphate coated inside. The obtained value becomes relative reflectance with respect to the standard reference sample which is considered to be 100 %. When light was directed at the sample at an angle of 0° , specular reflected light exits the integrating sphere, and it is not detected from that only diffuse reflected light was measured. Models of integrating spheres with different angles of incidence were available, enabling measurement of both specular and diffuse reflected light in instances [9-10].



Fig 2.8. Photograph of UV-visible Spectrophotometer.

The Shimadzu-UV-2600 was used to analyze the reflectance spectra of the non-transparent materials as shown in fig 2.8. This mid-range UV spectrophotometer can be used in various fields and quickly expanded to suit different analysis purposes. In addition, the UV-2600 achieves a significant noise reduction feature, and it can

accommodate measurements of anti-reflective films, polycrystalline silicon wafers, etc. It was a single monochromator system whose wavelengths could be easily varied from 200 to 800 nm. It was also equipped with Shimadzu's proprietary Lo-Ray-Ligh grade diffraction grating, which achieves high efficiency and low stray light levels. Barium sulfate (BaSO₄) powder was used as a standard reference sample to estimate the output scope of wavelengths. This instrument was integrated with Shimadzu LabSolutions UV-Vis software that is simple in use and ensures data integrity, which can automatically determine the spectrum's quality. The software does work faster by automatically exporting the data into text or excel files and making it easier to analyze with other applications.

2.9.2. Experimental

The prepared nanoparticles, samples were characterized by Shimadzu UV-Vis spectrophotometer in the wavelength range of 200-800 nm. From output data the optical bandgap (E_g) was calculated from optical reflection spectra utilizing Kubelka-Munk (K-M) model, & $F(R_\infty)$ was estimated from the accompanying conditions. The bandgap energy (E_g) was calculated by using below equations.

$$E_g = \frac{hc}{\pi\lambda} = \frac{1240}{\lambda} \quad (2.11)$$

$$F(R_\infty) = \frac{(1-R_\infty)^2}{2R_\infty} \quad (2.12)$$

$$\{(F(R_\infty)h\nu)^{1/n} \alpha (h\nu - E_g)\} \quad (2.13)$$

Where: h is the Planck constant (6.626×10^{-34} Js).

C is the speed of light (2.99×10^8 ms⁻¹).

λ is the wavelength that corresponds to reflectance spectra.

R_{∞} is the diffuse reflectance spectra.

α is the absorption coefficient.

ν is frequency of the incident light.

E_g is the bandgap energy.

$n = 2$ for direct bandgap.

2.10 Dielectric properties

The ferrites are usually known as very good dielectric materials. The phenomenon of dielectrics in ferrites originates from its microstructure. The dielectric parameters of ferrites are depending upon on the preparation methods, sintering temperature and time, sintering atmosphere, type and quantity of additives, stoichiometric composition and microstructure. The studies on frequency, temperature and composition dependent dielectric behavior provides the valuable information about localized electric charge carriers [11]. The dielectric parameters in ferrites are due to heterogeneous structure of dielectric material. The dielectric dispersion obeys the Maxwell-Wagner two layer heterogeneous structure of dielectric material which is in agreement with Koops phenomenological theory. The first layer consists of fairly conductive grains which are separated from a thin layer of high resistivity grain boundaries. The electrons exchange between Fe^{2+} and Fe^{3+} ions leads to local displacement of electrons along the applied filed direction determine the polarization. At very high frequencies, beyond certain frequency of applied field, electron exchange cannot follow frequency field [12].

2.10.1 Experimental

The dielectric parameters and complex impedance properties of all investigated samples were carried nanoferrites at 300 K on Impedance analyser (Model: HIOKI-3532-50, LCR-HiTESTER in the frequency range of 100 Hz to 5MHz as shown in fig 2.9. The facility was availed from Department of studies and research in Physics, Govt. Science College, Davangere University, Chitradurga, Karnataka state, India.

The pellets are polished and coated with air-dried silver paste on either side of the pellet for dielectric measurements. The connection leads are made using very short copper wires and silver past. LCR meter (Fig. 9) automatically records the capacitance (C_p) in pF, Inductance (L) in henry, Quality factor (Q), Resistance (R) in ohm, Conductance (G) in mho and dielectric loss (tanδ) of nanoferrites.

The dielectric constant of the samples was calculated using the relation

$$\epsilon' = Cd / \epsilon_0 A \quad (2.14)$$

where C_p - capacitance (pF), d- pellet thickness (cm), $\epsilon_0 = 8.854 \times 10^{-12}$ (pF/m) is absolute permittivity of free space and A - area of cross-section of the pellet (m²).

Room temperature ac electrical conductivity of each all investigated compositions estimated using obtained dielectric data.

$$\sigma_{ac} = 2\pi f \epsilon_0 \epsilon' \tan\delta \quad (2.15)$$

where $\omega = 2\pi f$, f - applied field frequency, $\epsilon_0 = 8.854 \times 10^{-12}$ (pF/m) is absolute permittivity of free space, ϵ' - dielectric constant and tanδ dielectric loss tangent.

2.10.2 Impedance spectroscopy

In 1886, Oliver Heaviside has introduced the concept of impedance. Firstly, in 1969, Bauerle has been used the impedance method to separate bulk from interfacial

properties of crystalline material. In the recent years, impedance spectroscopy has emerged as a powerful tool used to investigate the electrical response of grain and grain boundaries of ferrite material with frequency. The measurement of complex impedance with frequency of the applied field provides the valuable information about the resistive or real part and reactive or imaginary part in ferrites. The impedance properties of ferrites depend upon microstructural effect, stoichiometric composition, ceramic texture, type and amount of dopants or defects [13, 14].

2.10.3 Experimental

The frequency dependent resistive or real part and reactive or imaginary part of impedance of each compositions measure nanoferrites at 300 K on Impedance analyser [Model: HIOKI-3532-50, LCR-HiTESTER] in the frequency range from 100 Hz - 5MHz as shown in Fig 2.9. The facility was availed from Department of studies and research in Physics, Govt. Science College, Davangere University, Chitradurga, Karnataka state, India. The pellet samples are polished and coated with air-dried silver paste on either sides of pellets as contact material for impedance measurements. The capacitance (C_p), resistance (R), impedance (Z), conductance (G) and dielectric loss of all composition were recorded from LCR meter. Real part, Z' and an imaginary part Z'' of complex impedance at 300K have measured by using the relations respectively.

$$Z' = \frac{G}{G^2 + \omega^2 C_p^2} \quad (2.16)$$

$$Z'' = \frac{\omega C_p}{G^2 + \omega^2 C_p^2} \quad (2.17)$$

where G is conductance in mho, $\omega = 2\pi f$ is the angular frequency of the applied electric field in Hz, C_p is capacitance of the dielectric sample in pF.



Fig 2.9. Photograph of LCR set up for impedance measurement.

2.11 Magnetic Characterization

Nowadays, nano sized magnetic materials attracting extensive attention owing to their unique magnetic parameters viz., superparamagnetism (SP), magneto-optic, magneto-caloric effect, colossal and giant magnetic resistance etc. These properties and with more chemical and physical stability, they are different from their bulk counterparts [15]. The magnetization is due simultaneous effect of some intrinsic and extrinsic parameters namely, density and porosity. The magnetic moments are cause for magnetization. The origin of magnetic moment is due to non-compensated electron spin of individual ions and antiparallel alignments of spin in tetrahedral sites (A-sites) and octahedral sits (B-sites). The existence of magnetic order in ferrites attributed to super exchange interaction viz., A – B, A – A and B – B interactions. Importantly, A - A and B - B interactions are very weak. Moreover, A – B interaction is strongest. Thus, the magnetic moments of A-site and B-site are aligned in opposite direction. Therefore, net magnetisation is the difference of magnetic moments of A-site and B-site in the lattice represented by $\mu_B = M_B - M_A$, where M_A and M_B are magnetic moments of respectively A-site and B-site in μ_B [16].

2.11.1 Vibrating sample magnetometer

Simon Foner invented the Vibrating sample magnetometer (VSM) in 1955 at Lincoln Laboratory MIT. VSM is a powerful tool to measure magnetic parameters of the materials.

2.11.2 (a) Basic principle of VSM

A vibrating sample magnetometer (VSM) basically works on the principle of Faraday's laws of electromagnetic induction. An oscillatory motion of magnetic sample induces a magnetic field in the surrounding due to magnetisation. A sinusoidal emf is induced in a coil placed very near to the sample and the amplitude of this ac electrical signal is directly proportional to the magnetization level of a sample.

(b) Working of VSM

The experimental arrangement of a VSM depicted in fig 2.10. The operation of the VSM is fairly simple. A magnetic sample under investigation is placed in a sample holder on a long rod. The rod is driven by a mechanical vibrator. The rod is placed in between the pole pieces of electromagnets, to which detection coils have been mounted as shown in the fig 2.10. The sample holder connected to a transducer unit through a vertical sample rod. Transducer converts the electrical oscillations into mechanical vibrations. With the help of an electronic oscillator, the transducer causes vibration on the sample rod. According to Faraday's law of electromagnetic induction, an oscillatory or vibratory motion of magnetized sample produces an emf in pickup coils.

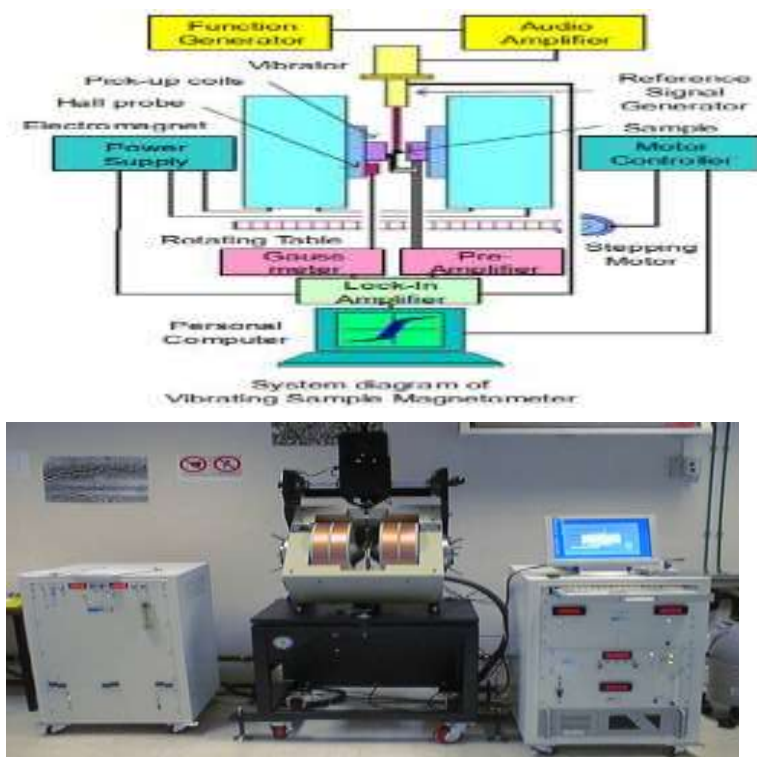


Fig 2.10. Schematic representation and Photograph VSM instrument

The strength of an induced voltage in pickup coil depends on magnetic moment of the sample, but does not on applied magnetic field strength. The material in uniform magnetic field magnetized due to alignment of magnetic domains along the field direction. The strength of magnetisation depends on magnitude of applied. The magnetic field created around the material from these magnetic dipoles [17, 18]. In a typical experimental setup, the pick-up coils detect the changes in the induced flux (an induced voltage) and induce an AC voltage. A lock-in amplifier (using piezoelectric signal as a reference signal) amplifies this AC signal and measures the induced AC voltage which is directly proportional to the magnetic moment of the sample. A plot of magnetization versus magnetic field strength is generated known as a hysteresis loop or M-H loop.

2.11.3 Experimental

The room temperature magnetic properties viz., saturation magnetization, M_s , remanent magnetization, M_r , and coercivity, H_c , of each nanoferrites have been measured using vibrating sample magnetometer IIT of Kanpur (Indian institute of technology, Kanpur), India and IIT Guwahati, Assam, India. The values of magneton number η_B and Yafet- Kittel angles i.e, $\alpha(Y-K)$ have been calculated using the relations.

$$\eta_B = \frac{M \times M_s}{5585} \quad (2.18)$$

$$S = \frac{M_r}{M_s} \quad (2.19)$$

$$K = \frac{H_c \times M_s}{0.64} \quad (2.20)$$

$$\cos \alpha(Y - K) = \left[\frac{n_B + 5(1 - x)}{(6 - x)} \right] \quad (2.21)$$

where η_B - the magnetic moment/formula unit in μ_B or number of Bohr magnetons, MW - atomic weight of sample (g), M_s - Saturation magnetisation in emu/g, 5585 - Magnetic factor and S - remanence ratio (S), M_r - remanent magnetization in emu/g, Y-K are Yafet-Kittel angle and H_c - coercivity.

2.12 Thermogravimetric analysis and Differential scanning calorimetry

Thermogravimetric analysis or thermal gravimetric analysis (TGA) and Differential scanning calorimetry (DSC) is a method of thermal analysis in which changes in physical and chemical properties of materials are measured as a function of increasing temperature (with constant heating rate) or as a function of time (with constant temperature and/or constant mass loss). TGA and DSC can provide information about

physical phenomena such as second-order phase transitions, including vaporization, sublimation, absorption, adsorption and desorption. Likewise, it can provide information about chemical phenomena including chemisorptions, desolvation (especially dehydration), decomposition, chemical reaction kinetics, specific heat capacity, thermal stability (oxidation onset) and solid-gas reactions (e.g., oxidation or reduction). TGA is commonly used to determine selected characteristics of materials that exhibit either mass loss or gain due to decomposition, oxidation or loss of volatiles (such as moisture). Common applications of TGA and DSC are (1) material characterization through analysis of characteristic decomposition patterns, (2) studies of degradation mechanisms and reaction kinetics, (3) determination of organic content in a sample and (4) determination of inorganic (e.g. ash) content in a sample, which may be useful for corroborating predicted material structures or simply used as a chemical analysis [19].



Fig 2.11 Schematic representation and photograph of the TGA measurement

The schematic representation of the TGA is shown in the fig 2.11. The sample is heated under nitrogen or synthetic air with constant heat rate while the difference of the

mass during this process is measured. A mass loss indicates that a degradation of the measured substance takes place. The reaction with oxygen from the synthetic air for example could lead to an increase of mass.

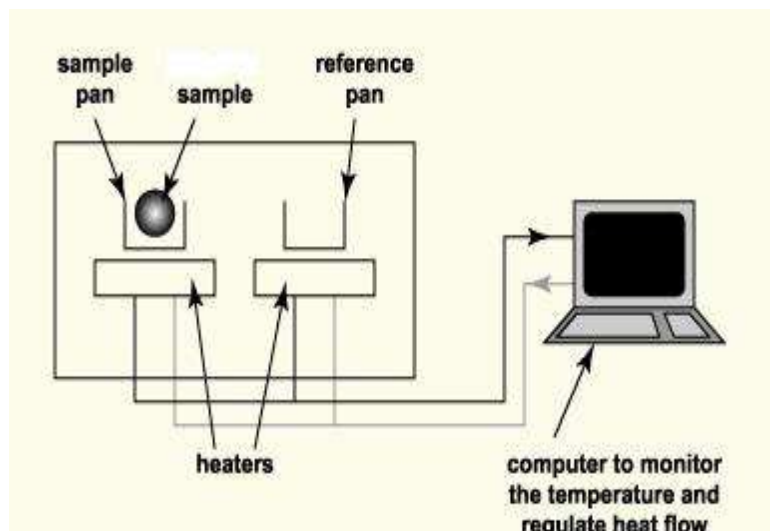


Fig 2.12. Schematic view of DSC

DSC is a thermo analytical technique in which the difference in the amount of heat required to increase the temperature of a sample and reference is measured as a function of temperature. fig 2.12 represents the schematic view of DSC. Both the sample and reference are maintained at nearly the same temperature throughout the experiment. Generally, the temperature program for a DSC analysis is designed such that the sample holder temperature increases linearly as a function of time. The reference sample should have a well-defined heat capacity over the range of temperatures to be scanned [20].

2.13 Electrochemical properties analysis

Cyclic voltammetry or CV is a type of potentiodynamic electrochemical measurement. In a cyclic voltammetry experiment the working electrode potential is ramped linearly versus time like linear sweep voltammetry. Cyclic voltammetry takes the

experiment a step further than linear sweep voltammetry which ends when it reaches a set potential. When cyclic voltammetry reaches a set potential, the working electrode's potential ramp is inverted. This inversion can happen multiple times during a single experiment. The current at the working electrode is plotted versus the applied voltage to give the cyclic voltammogram trace. Cyclic voltammetry is generally used to study the electrochemical properties of an analyte in solution [21]. In cyclic voltammetry, the electrode potential ramps linearly versus time. This ramping is known as the experiment's scan rate (V/s). The potential is applied between the reference electrode and the working electrode and the current is measured between the working electrode and the counter electrode. As the waveform shows, the forward scan produces a current peak for any analytes that can be reduced (or oxidized depending on the initial scan direction) through the range of the potential scanned. The current will increase as the potential reaches the reduction potential of the analyte, but then falls off as the concentration of the analyte is depleted close to the electrode surface. If the redox couple is reversible when the applied potential is reversed, it will reach the potential that will reoxidize the product formed in the first reduction reaction and produce a current of reverse polarity from the forward scan. This oxidation peak will usually have a similar shape to the reduction peak. As a result, information about the redox potential and electrochemical reaction rates of the compounds is obtained. For instance if the electronic transfer at the surface is fast and the current is limited by the diffusion of species to the electrode surface, then the current peak will be proportional to the square root of the scan rate. This relationship is described by the Cottrell equation. The CV experiment then samples only a small portion of the solution, the material within the diffusion layer. Fundamentally, the CV measurements

are helpful to know the electron transfer kinetics and chemical reactions of oxidation and reduction potential [22]. The measurement set-up for a typical electrochemical 3-electrode measurement is shown the fig 2.13.

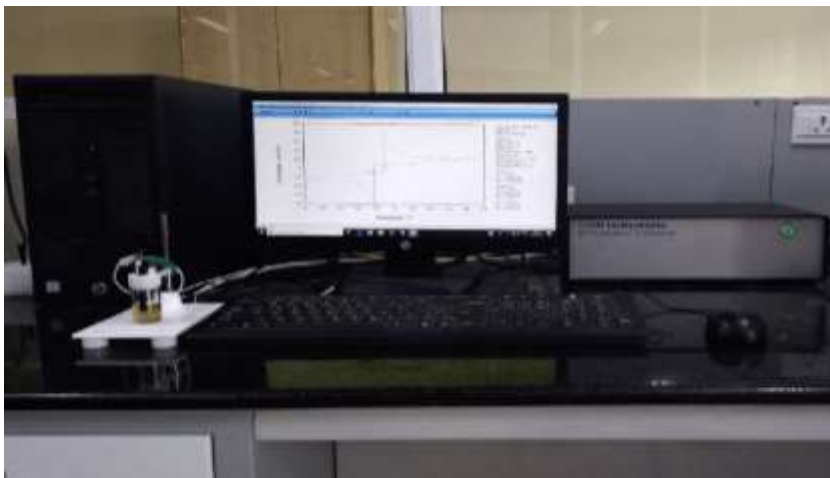


Fig 2.13. Photograph of electrochemical cell measurement

Electrochemical Impedance Spectroscopy (EIS) is frequently less interested in the bulk sample material but especially in the properties of the polarization layer at a metal to electrolyte or ion conductor interface and the related chemical reactions. This is just the opposite to dielectric, conductivity or impedance material spectroscopy where these effects are known as electrode polarization.

2.13.1 Instrumentation of Voltammetric Sensor

The instrumentation for voltammetric sensors is more complex than that for potentiometric sensors. To control the applied potential and register current at working electrode, a potentiostat is necessary-most voltammetric techniques are based on potential control. The development of voltammetric techniques dates back to the pioneering work of Jaroslav Heyrovsky in 1922 which was acknowledged by a Nobel Prize in 1959. The

voltammetric cell incorporates the sample solution and a pair of electrodes of unequal size, as well as reference electrode. Three electrodes are usually necessary in order to avoid the passage of current through the reference electrode, which otherwise would alter its potential via changes in the activities of the various species. The electrical circuit, through which the current passes, is between the working (indicator) electrode and an auxiliary electrode. The reference electrode serves in a three-electrode system to control potential of working electrode and hence the reactions which can occur there. The working electrode is an ideally polarizable electrode, i.e. the electrode shows a large change in potential when an infinitesimally small current passes through. Reference electrode is a non-polarizable electrode i.e. an electrode of fixed potential. The auxiliary or counter-electrode is a current conducting electrode. The voltammetric measurements are usually performed in a quiescent solution in the presence of a large excess of inert salt, called supporting electrolyte. A typical electrochemical cell consists of the sample dissolved in a solvent, an ionic electrolyte, and three electrodes. Cells come in a variety of sizes, shapes, and materials. The type used depends on the amount and type of sample, the technique, and the analytical data to be obtained. The material of the cell is selected to minimize reaction with the sample. In most cases the reference electrode should be as close as possible to the working electrode in some cases, to avoid contamination, it may be necessary to place the reference electrode in a separate compartment.

2.13.2 Working Electrode

The working electrode is an electrode in an electrochemical system in which the reaction of interest is occurring. Depending on whether the reaction on the electrode is a reduction or an oxidation, the working electrode can be referred to as either cathodic or

anodic. Common working electrodes consist of inert metals such as gold, silver or platinum and inert carbon such as glassy carbon or pyrolytic carbon and mercury drop and film electrodes.

2.13.3 Carbon Electrode

As an inert electrode material, carbon is useful for both oxidation and reduction in both aqueous and nonaqueous solutions. Several different forms of carbon have been used to make satisfactory electrodes including spectroscopic-grade graphite (usually impregnated with ceresin or paraffin wax), pyrolytic graphite (a high density highly oriented form of graphite), carbon paste (spectroscopic-grade graphite mulled in sufficient Nujol to form a stiff paste), graphite dispersed in epoxy resin or silicone rubber and vitreous or glassy carbon. Vitreous or Glassy Carbon: The use of glassy carbon as an electrode material was suggested in 1962. Glassy carbon is an electrically conductive and gas impermeable material, highly resistant to chemical attack and obtainable in pure state. Some of its cited advantages relative to platinum are low cost, pretreatment by polishing with metallographic paper, larger over potential for production of hydrogen and dissolved oxygen and increased reversibility for several redox couples and reactions that involve subsequent proton transfer. Glassy carbon has a unique advantage in determination of trace bio-molecules by voltammetry techniques.

2.13.4 Reference Electrode

The reference electrode should provide a reversible half-reaction with Nernstian behaviour, be constant over time, and be easy to assemble and maintain. The most commonly used reference electrodes for aqueous solutions are the calomel electrode, with

potential determined by the reaction $\text{Hg}_2\text{Cl}_2(\text{s}) + 2\text{e}^- = 2\text{Hg}(\text{l}) + 2\text{Cl}^-$ and the silver/silver chloride electrode (Ag/AgCl), with potential determined by the reaction $\text{AgCl}(\text{s}) + \text{e}^- = \text{Ag}(\text{s}) + \text{Cl}^-$. These electrodes are commercially available in a variety of sizes and shapes.

2.13.5 Auxiliary Electrode

In voltammetric studies the current flows between the working electrode and auxiliary electrode. If a two electrode system consisting of only reference and working electrodes is used, then current flow through the reference electrode will cause a change in its potential. So a three electrode system, incorporating a third electrode called the auxiliary electrode is used. The main condition for an electrode to act as auxiliary electrode is that it should not dissolve in the medium of the electrochemical cell and that the reaction product at the auxiliary electrode should not react at the working electrode. The electrode area of the auxiliary electrode must also be larger than that of working electrode to ensure that the area of the electrode does not control the limiting current. Platinum electrodes in the form of coils or thin foils are the most widely used auxiliary electrodes in aqueous, non-aqueous and molten salt media. Carbon electrodes are also used in molten salt media.

2.13.6 Chemically Modified Electrodes (CMEs)

A chemically modified electrode (CME) is an electrical conductor that has its surface modified for different electrochemical functions. The area of surface modified electrodes is of particular interest because of its application in sensors. Such modifications in the electrode surface lead to greater control on the reactivity at the interface. The distinguishing feature of a CME is that a thin film of a selected material is coated on the surface of electrode to endow the electrode with the chemical,

electrochemical, optical, electrical and other desirable properties of the film. Chemically modified electrodes represent a modern approach to electrode systems. These electrodes rely on the placement of a reagent onto the surface, to impart the behaviour of that reagent to the modified surface. One of the important methods is the incorporation of a modifier to the electrode surface is covering the electrode surface with suitable polymer film.

2.14. Gas sensor

Sensing devices are the transducers that convert one form of energy into another form suitable for further processing by concern of the change in the material resistivity. There are wide variety of gas sensors have been developed over the years for different purposes viz., industries, agricultural purposes, medical diagnosis, household safety, etc. A variety of materials have been used for sensors (metal oxides, polymers, CNTs, graphene, etc) which are chemically and physically stable at room/higher temperatures [23]. Even though the development of highly sensitive materials is progressing at an exceptional rate. Several factors depends on gas sensing behavior of a materials, in accordance with the various parameters viz., surface defects, particle size, surface morphology, film thickness, aspect ratio, speed of chemical reaction on the surface, rate of diffusion of gas molecules to the surface etc., [24].

2.14.1 Fabrication of Gas Sensing Chamber and Experimental Details

Fig 2.14 depicts the schematic diagram of the gas sensing chamber and fig 2.15 shows the in-house fabricated gas sensing chamber used for sensing studies of the prepared samples. The in-house fabricated gas sensing chamber was made up of double walled chamber, inner sensing chamber is made up of higher-grade stainless steel, heater

is placed in the basement of the inner chamber and the two-probe sample holder setup was united to the base of the chamber, in the top high grade toughened glass was placed to view the setup clearly. The outer chamber was made up of powder coated steel and in between inner and outer chamber it was insulated by using glass wool to prevent the heat dissipation. The upper lid of the chamber can be opened to place the sample and double walled rubber gasket used to avoid the moisture/atmospheric air enter into the chamber. The total volume of the inner sensing chamber is ~4350 ml, the thermocouple placed near the sample holder to record the working temperature of the sensor. Gas inlet and outlet port is used for injection and ejection of gas/VOC's, desired amount gas/VOC's are injected into the chamber with the help syringe through the inlet port. The resistance values are measured before and after passing the test gas/VOC's were measured by using a multimeter.

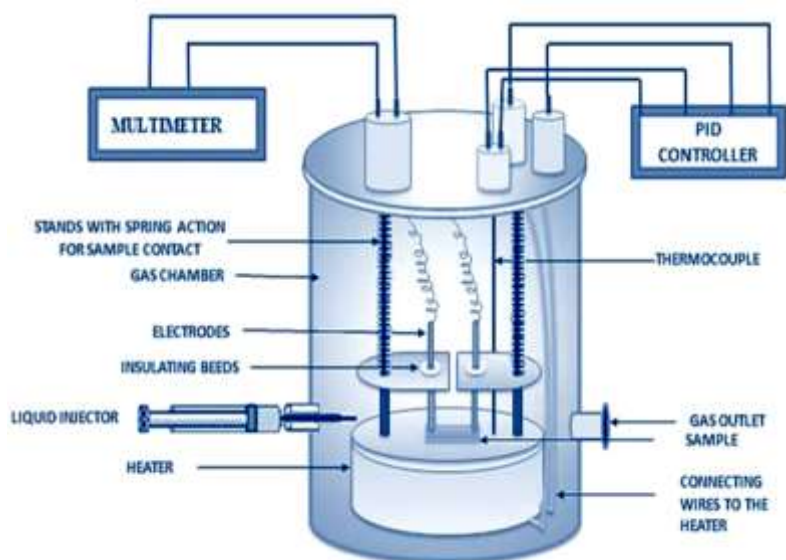


Fig 2.14 Schematic view of the gas sensing chamber

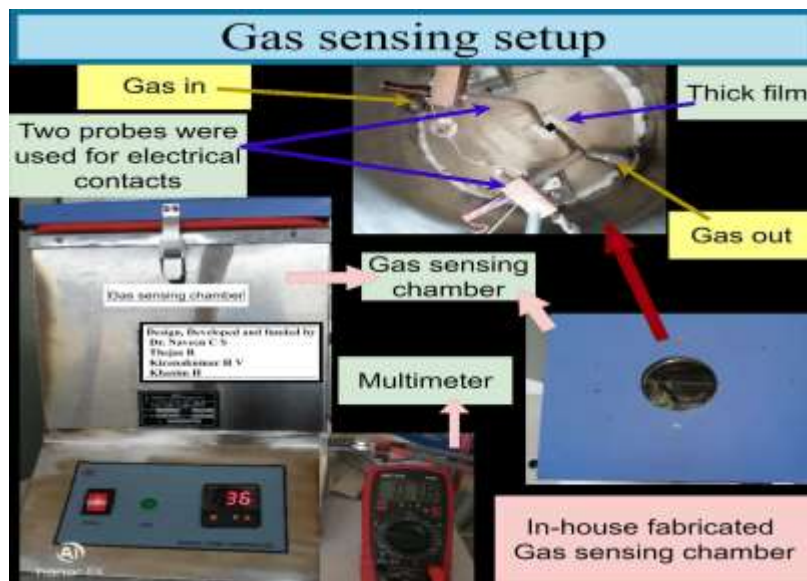


Fig 2.15. Photograph of experimental arrangement of gas/VOC sensing studies

2.14.2. Experimental

To evaluate the gas sensing response of synthesized powder nanocomposites were deposited as a thick film on an alumina substrate, the conductive silver paste was painted at the two opposite sides of the films to get the ohmic contacts. These sensor materials were examined for various gases/volatile organic compounds viz., butane, acetone, and ethanol, by making use of an in-house fabricated gas sensing chamber. The gas molecules were diffused onto the surface of the sensor materials, resulting in change in resistance/conductance with respect to the type and concentrations of the gases. The change in resistance of the sample in the presence and absence of butane gas can be used as the sensing performance in terms of sensitivity, the sensitivity of the sensor can be calculated by using following equation.

$$\text{Sensitivity } (S)\% = \left(\frac{R_g \sim R_a}{R_a} \right) * 100 \quad (2.22)$$

where, R_a is the resistance of a sensing material in air,

R_g is the resistance of a sensing material in the presence of test gas,

2.15 Reference

- [1] S. P. Gubin (Ed.). Magnetic Nanoparticles, Wiley-VCH Verlag, Weinheim (Chapter 6) (2009).
- [2] B. L. Cushing, V. L. Kolesnichenko and C O Connor. J. Chem. Rev. 104 (2004) 3893.
- [3] S. A. Mazen, S. F. Mansour and H. M .Zaki. Cryst. Res. Technol. 38 (2003) 471-478.
- [4] H. Wang, J H. Liu, W. F. Li, J. Wang, L. Wang, L. J. Song, S. J. Yuan and F. S. Li. J. Alloys Compd. 461 (2008) 373-377.
- [5] M. Ishil, M. Nakahita, and Yamanka, J. Solid State Commun. 11 (1972) 209.
- [6] T. Prabhakaran and J. Hemalatha. J. Alloys Compd. 509 (2011) 7071–7077.
- [7] S. M. Patange, S. E. Shirsath, K. S. Lohar, S. G. Algude, S. R. Kamble, N. K. D. R. Mane and K. M. Jadhav. J. Magn. Magn. Mater. 325 (2013) 107–111.
- [8] R. D. Waldron. Infrared spectra of ferrites. Phys. Rev. 99 (1955) 1727.
- [9] G. Kortüm, Reflectance Spectroscopy, 1st ed., Springer Berlin, Heidelberg. (1969). <https://doi.org/10.1007/978-3-642-88071-1>.
- [10] Relative Diffuse Reflectance Measurement, (n.d.). <https://www.shimadzu.com/an/products/molecular-spectroscopy/uv-vis/uvvis-nir-spectroscopy-consumables/relative-diffuse-reflectancemeasurement/index.html>.
- [11] W. D Kingery, H. L. Bower and U. R. Uhlman. Introduction to ceramics, Second edn, Wiley, New York, (1976).
- [12] J. R. Macdonald and B. Evgenij. Impedance Spectroscopy: Theory, Experiment and Applications, Second ed., John Wiley & Sons, Inc., Hoboken, New Jersey. (2005).
- [13] A. C. F. M. Costa, V. J. Silva, D. R. Cornejo, M. R. Morelli, R. H. G. A Kiminami and L Gama. J Magn. Magn. Mater. 320 (2008) 370-372.
- [14] M. M. Costa, G. F. M. Pires Junior and A. S. B. Sombra. Mater. Chem. Phys. 123 (2010) 35–39.

- [15] S. Tebble and D. J. Craik. *Magnetic Materials*. Wiley Inter Science, London, New York, Sydney, Toronto, 264 (1969).
- [16] K. Maaz, S. Karim, A. Mumtaz, S. K. Hasanain, J. Liu and J. L. Duan. *J. Magn. Magn. Mater.* 321 (2009) 1838–1842.
- [17] M. N. Ashiq, R. B. Qureshi, M. A. Malana, and M. F. Ehsan, *J. Alloys Compd.* 651 (2015) 266-272.
- [18] A. Pradeep, P. Priyadharsini and G. Chandrasekaran. *J. Alloys Compd.* 509 (2011) 3917–3923.
- [19] A. W. Coats and J. P. Redfern. *Analyst* 88 (1963) 906.
- [20] E. Pungor and G. Horvai. *A practical guide to instrumental analysis*. CRC press, (1994).
- [21] A. J. Bard and L. R. Faulkner. *Electrochemical methods: fundamentals and applications*, 2nd. Hoboken: Wiley and Sons (2001).
- [22] M. E Orazem, and B. Tribollet. *Electrochemical impedance spectroscopy*. John Wiley & Sons, 48 (2011).
- [23] N. Parvatikar, S. Jain, S. Khasim, M. Revansiddappa, S.V. Bhoraskar, M.V.N.A. Prasad, *Sens. Actuators B Chem.* 114 (2006) 599-603.
- [24] S. Kotresh, Y.T. Ravikiran, S.C. Vijayakumari, S. Thomas, *Compos. Interfaces.* 24 (2017) 549-561.

CHAPTER 3:-

EFFECT OF Ce^{3+} SUBSTITUTION
ON Sr^{2+} ; STRUCTURAL AND
MAGNETIC PROPERTIES OF
NANOCRYSTALLINE $\text{SrFe}_{12}\text{O}_{19}$
HEXAFERRITES PREPARED BY
SELF-PROPAGATION METHOD
USING MIXED FUELS

**Published in Journal of Superconductivity and Novel
Magnetism. Springer Publication impact factor – 1.675**

3.1 Introduction

Ferrites are unit metal oxides mixed with iron oxides because the main part with the final formula AB_2O_4 . Nano crystalline ferrites play a very vital role in the manufacture of magnetic materials on account of novel physical properties, high-frequency devices, magnetic recording media, catalysis, transformer cores, radiation and absorption devices, medical diagnostics, ferrous fluids and biomedical fields [1-3]. M-type hexaferrites have the chemical formula $AFe_{12}O_{19}$, where, 'A' is Ba, Sr or Pb [3]. SrM-HF's are important materials with high chemical stability, specific saturation magnetization, uniaxial magneto-crystalline property, anisotropy, coercivity, high Curie point (temperature) and electrical resistance as well as low dielectric losses [4-6]. Nanostructured SrM-HF's have received greater attention because of their technological and industrial applications that allow it to be used as a permanent magnet [7]. The intrinsic properties of SrM-HF's ($SrFe_{12}O_{19}$) are strongly impacted by the cation exchange and synthetic methods [8]. $SrFe_{12}O_{19}$ finds a challenging and competitive application with technological evolution, the foremost unremarkably used material for ferrite permanent magnets [9] that there's nice demand from makers of microwave gadgets, magnetic recording media, broadcast communications devices and so on [10]. Doping $SrFe_{12}O_{19}$ with transition metal ions or rare earth ions of similar size has resulted in a significant modification of its properties [11, 12]. The magnetic properties of doped magnetic nanoferrites based on both the parts and concentration of the doped part of element, morphology, particle size and synthesis technique [13, 14]. The low amount doping of rare earth elements in $SrFe_{12}O_{19}$ leads to the significant changes in its electrical and magnetic properties [8, 11]. Many researchers have studied rare earth metals that have replaced Sr or Fe from $SrFe_{12}O_{19}$ and have reported significant changes in magnetic properties [15] like,

La³⁺ [16], Ce³⁺ [17], Pr³⁺ [18], Nd³⁺ [19], Sm³⁺ [20], Gd³⁺ These magnetic material are based on the purity[21] and the number of particles and morphology of the fine powder [22]. Therefore, founded fine, high synthetic homogeneity and monodispersed particles which are the most significant method in material fabrication [22]. SrM-HF's with rare earth ion doping is explained the improvement in magnetic properties by a rise in a coercive field with magnetization and magnetocrystalline anisotropy [23]. Nowadays, SrM-HF's are being employed in power generation, nanocatalysts, microwave absorbers, automotive electronics, small DC motor rotors, microwave devices, and ferrite cores. Several material synthesis methods were used to synthesize SrM-HF's, including the hydrothermal method [24], sono chemical method [25], reverse micelle technique [26], micro-emulsion [27], combustion routes [28] co-precipitation [29] and sol-gel [30]. The self-propagating high temperature technique includes simple, lower price, higher crystallinity and purity, a fine synthetic homogeneity, short time interval and particle size distribution [31].

From the literature survey, no reports have emerged regarding the synthesis of SrFe₁₂O₁₉ by self-propagating method by using mixed fuels. Therefore, the research evidence concerning that effect of Ce³⁺ ion doping on Sr²⁺ ion on the structural and magnetic properties of nanocrystalline hexaferrites, Sr_(1-x)Ce_xFe₁₂O₁₉ (x = 0.00 < x < 0.09) prepared by self-propagating technique using mixed fuels.

3.2 Experimental Method

The self-propagation with using mixed fuels synthesis technique was successfully used to synthesize Sr_(1-x)Ce_xFe₁₂O₁₉ nanoferrites (where, x = 0.00 < x < 0.09) using analytical reagent grade (Sr(NO₃)₂) [Merck], (Fe(NO₃)₃.9H₂O), (Ce(NO₃)₃.6H₂O) [Sigma Aldrich], glycine [C₂H₅NO₂] and urea [CH₄N₂O]. The stoichiometric ratios of the reactants to the fuels are dissolved in de-ionized H₂O. The

resulting solution containing the reaction mixture was placed in a cylindrical petri dish and heated over a quenching furnace maintained at 500 ± 10 °C. The reaction mixture underwent dehydration and ignited at one spot with the, releasing large amounts of gas (N_2O and CO_2). The self-propagation (combustion) propagates throughout the reaction mixture without the need for additional external heating, as the heat of the reaction is sufficient for the decomposition of the redox mixture. The self-propagation (combustion) type is smoldering in nature and the actual ignition responses time 16-18s. These gases are known to be hypergolic. At this stage, the virgin powders were ground in an agate mortar and mixed with a binder. The powders were ground into a fine powder and further calcined at 1000 °C for 3 hours. The powders was compressed into pellets with a diameter of 10 mm and a thickness of ~2-3 mm in by loading a pressure of $5-10^8$ kg/m² for 5 minutes. In addition, the pellets were sintered for 20 hours at a temperature of 1100 °C in an furnace and then cooled gradually until they reached room temperature. The purity series of samples obtained by the result of the self-propagating process with mixed fuel which involved a fast exothermic reaction between glycine, urea and metal nitrates. The Powder X-ray diffraction of the nanoferrites were examined by an X-ray diffractometer (Make: Bruker, Model: D8 Advance, Germany) with $CuK\alpha$ radiation of the wavelength 1.5406 Å, in Bragg angle, 2θ , range from 20° - 80° at the chart speed of 2°C min at 300K. Micrographs of sintered pellets and composition analysis of all the samples examined using (FESEM, JEOL/EO JSM—639, EDS Make: Carl Zeiss, Model: EVOLSI5, Germany). M_s , M_r and the H_c of all nanoferrites were determined at 300K using a vibrating sample magneto meter (Make: Crest, Model: 20130523-01).

3.3 Results and Discussion

3.3.1 Powder X-ray diffraction

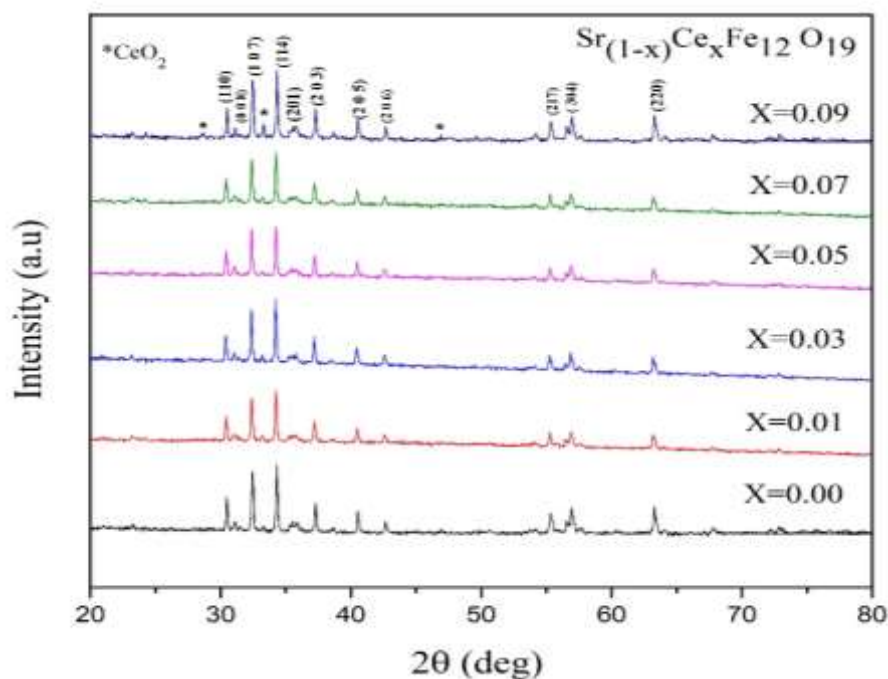


Fig 3. 1 XRD patterns of $\text{Sr}_{(1-x)}\text{Ce}_x\text{Fe}_{12}\text{O}_{19}$ ($x = 0.0, 0.01, 0.3, 0.5, 0.07, 0.09$) nanoferrites

The patterns of PXRD for the $\text{Sr}_{(1-x)}\text{Ce}_x\text{Fe}_{12}\text{O}_{19}$ ($x = 0.00 < x < 0.09$) nanoferrites were showed in fig 3.1. The patterns of PXRD, shows that peaks with (hkl) a values of [planes] (110), (008), (107), (114), (201), (203), (205), (206), (217), (304) and (220) are counted with the JCPDS card number: 84 - 1531 for the hexagonal phase $\text{SrFe}_{12}\text{O}_{19}$ type. In addition, it is observed that the sample $x = 0.09$ sample showed around 5% of phase of secondary cerium oxide (JCPDS: 80-2377) [32]. The lattice parameter is calculated using the relation.

$$\frac{1}{d_{hkl}^2} = \frac{4}{3} \left[\frac{h^2 + hk + k^2}{a^2} + \frac{l^2}{c^2} \right] \quad (3.1)$$

where d_{hkl} is the crystal planes are comparing the distance, a and c are the lattice parameters and $(h k l)$ are the Miller indices. From XRD studies showed that the lattice parameter increased slightly (from 0.58796-0.58847 nm) with increasing the

Ce³⁺ ion concentration because of the substitution of larger ionic radius Sr²⁺ ions (0.112 nm) with smaller ionic radius Ce³⁺ ions (0.1034 nm) [32].

The unit V_{cell} of the hexagonal system is determined as follows:

$$V_{cell} = 0.866 a^2 c \quad (3.2)$$

where, the numerical values is sustained for the hexagonal system.

From XRD profile, an average size of nanoferrite crystallites was determined using Debye-Scherrer equation (d) is determined by the Scherrer's formula (33):

$$d = \frac{k\lambda}{\beta \cos\theta} \quad (3.3)$$

where, $k = 0.89$ is constant of Scherrer's value for the hexagonal system, $\lambda=0.15406$ nm wavelength of the incident X-rays, β is the FWHM of diffraction peak, θ is the Bragg diffraction angle. The average value of crystallite size was obtained at 42-46 nm and values are tabulated in table 3.1.

Hypothetical X-ray thickness (dx) of each sample was determined using the formula

$$d_x = \frac{ZM}{NV} \quad (3.4)$$

where $Z = 2$, Number of particles per unit cell, M is atomic weight, N is Avogadro's number and V is unit cell volume.

The cell volume of the SrFe₁₂O₁₉ patterns were set in the various boundaries a , c and V are tabulated in table 3.1. The values of X-ray thickness are of the order of 4.73-5.11 g cm⁻³. The decrease in the X-ray thickness increase was because of the larger molecular weight (140.116 amu) and ion volume (0.1034 nm) of the Ce³⁺ ion compared to the smaller molecular weight (87.62 amu) and largest ion radius (0.112 nm) of strontium ions.

Table 3.1: Crystallite size (D), lattice constant (a & c), cell volume (V) and X-ray density (qx-ray) of $\text{Sr}_{(1-x)}\text{Ce}_x\text{Fe}_{12}\text{O}_{19}$ ($x = 0.00, 0.01, 0.03, 0.05, 0.07$ and 0.09) nanoferrites.

Composition	Crystallite size (D) /nm	Lattice constant (a)/Å	Lattice constant (c)/Å	(c)/(a) Å	Cell volume (V)/Å ³	X-ray density (qx-ray)/g cm ⁻³
$\text{SrFe}_{12}\text{O}_{19}$	45.54	5.8847	23.0552	3.918	691.4	5.10
$\text{Sr}_{0.09}\text{Ce}_{0.01}\text{Fe}_{12}\text{O}_{19}$	43.54	5.8796	23.0493	3.920	690.0	4.73
$\text{Sr}_{0.07}\text{Ce}_{0.03}\text{Fe}_{12}\text{O}_{19}$	42.25	5.8809	23.0475	3.919	690.3	4.74
$\text{Sr}_{0.05}\text{Ce}_{0.05}\text{Fe}_{12}\text{O}_{19}$	43.84	5.8823	23.0493	3.918	690.7	4.74
$\text{Sr}_{0.03}\text{Ce}_{0.07}\text{Fe}_{12}\text{O}_{19}$	43.53	5.8835	23.0518	3.918	691.0	4.74
$\text{Sr}_{0.01}\text{Ce}_{0.09}\text{Fe}_{12}\text{O}_{19}$	42.86	5.8828	23.0534	3.919	690.9	4.75

3.3.2 Morphological studies

The FE-SEM micrographs of the synthesized composition of $\text{Sr}_{(1-x)}\text{Ce}_x\text{Fe}_{12}\text{O}_{19}$ ($x = 0.00 < x < 0.09$) are shown in fig 3.2 (a-c). From the fig 3.2(a), it was observed that the grains grew in magnetically stacked compact aggregations for the $\text{SrFe}_{12}\text{O}_{19}$ nanoferrites. These hexaferrite particles clipped for interaction because of its magnetic nature and the association of primary particles. Moreover, the samples are highly porous in nature. The particle size is in the scope of 42 - 46 nm. These values correspond to the values calculated from the PXRD. fig 3.2(b-c) reveals a SrM-HF's derivative. Furthermore, the fine powders having the strong tendency to form of aggregates into large mass [34]. Report indicate that the self-propagating technique with mixed fuel reaction involves crystallization compared with crystals from a solution of nanoparticles to the HF's, because of the long period of time and high temperature to complete the synthesis technique. For the consummation of self-propagating technique by using sovereign mixed fuel with variable particle size distribution. [35-36].

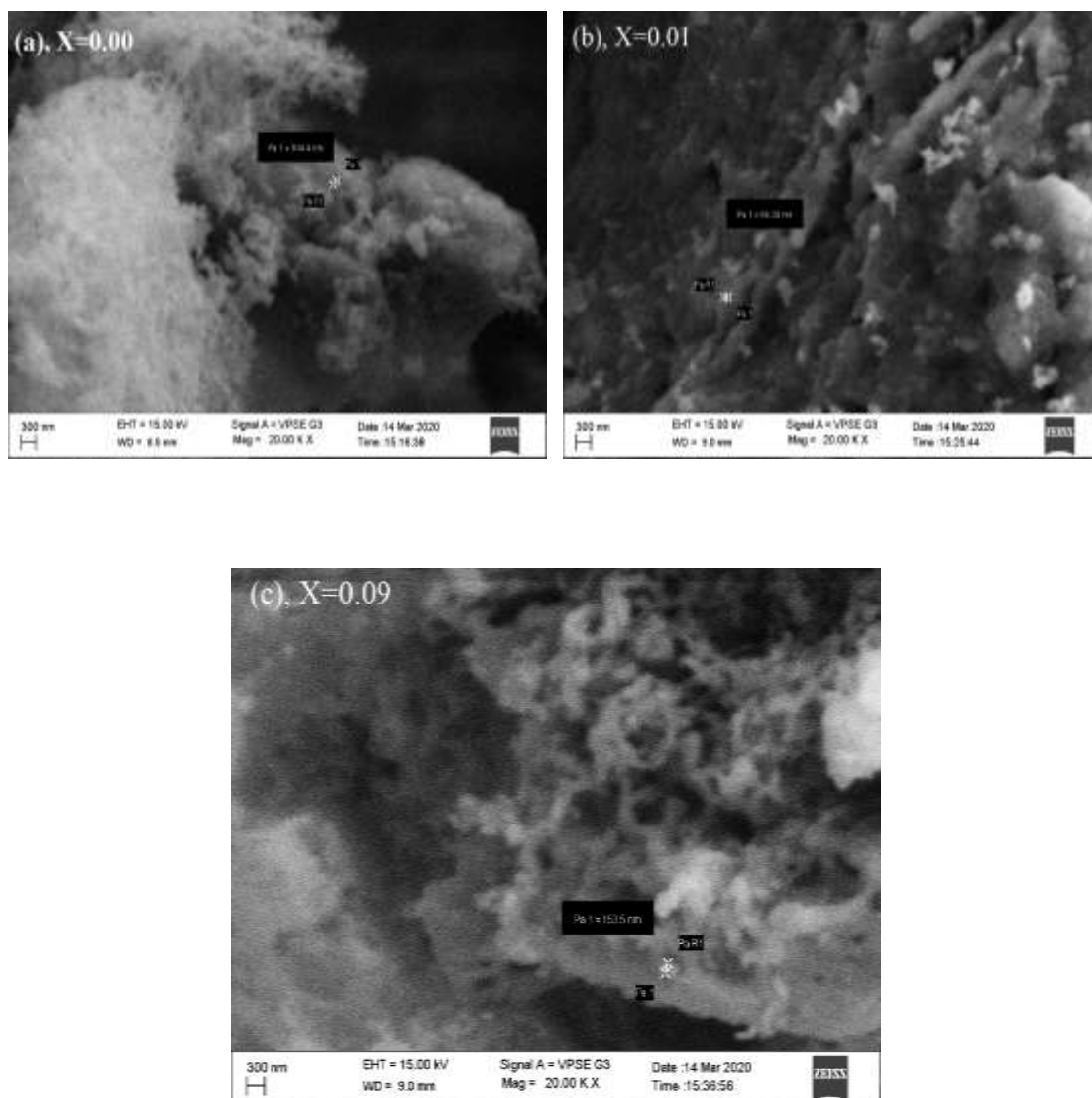


Fig 3.2 FESEM Micrographs of $\text{Sr}_{(1-x)}\text{Ce}_x\text{Fe}_{12}\text{O}_{19}$ ($x = 0.0$ (a), 0.01 (b) and 0.09 (c)) nanoferrites.

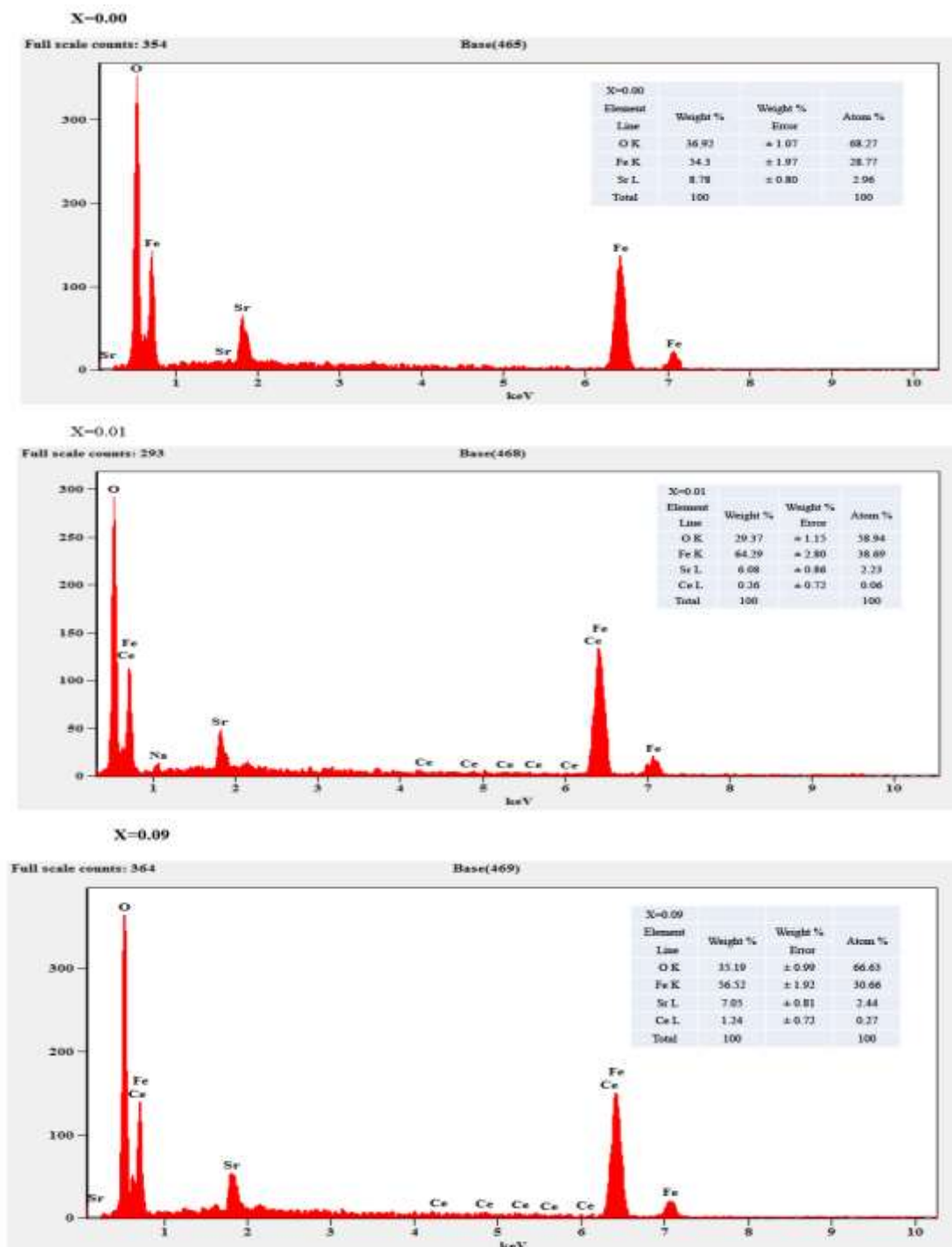


Fig 3.3 EDAX Spectrum of $Sr_{(1-x)}Ce_xFe_{12}O_{19}$ ($x = 0.0$ (a), 0.01 (b) and 0.09 (c)) nanoferrites

The chemical proportions of the samples, $Sr_{(1-x)}Ce_xFe_{12}O_{19}$ ($x = 0.00 < x < 0.09$) are recorded using Energy dispersive X-ray analysis (EDAX) and are shown in fig 3.3. The spectra indicate the presence of Sr, Fe, Ce and O atoms and their elemental composition with high crystallinity. The greater crystallinity of SrM-HF's

is due to self-propagating technique in mixed fuel reaction with prolonged time span and high temperature produces rapid crystal growth leading to nucleation of nanoparticles.

3.3.3 Magnetic measurements

The variations of the saturation magnetization (M_s), coercive field (H_c), remanence magnetization (M_r), and squareness ratio (M_r/M_s) of the nanohexaferrites $Sr_{(1-x)}Ce_xFe_{12}O_{19}$ ($x = 0.00 < x < 0.09$) with at room temperature is shown fig 3.4. The magnetic parameters were calculated using the following relationship.

$$\eta_B = \frac{M \times M_s}{5585} \quad (3.5)$$

$$S = \frac{M_r}{M_s} \quad (3.6)$$

$$K = \frac{H_c \times M_s}{0.64} \quad (3.7)$$

where n_B is the magnetic moment / formula unit in μ_B , M_s - saturation magnetization (emu/g), M_r - remanence magnetization, M - molecular weight in g, 5585 - magnetic factor, k - magnetic anisotropic constant and H_c - coercivity. The Yafet and Kittel angles are given by the relation.

$$\cos \alpha(Y - K) = \left[\frac{n_B + 5(1 - x)}{(6 - x)} \right] \quad (3.8)$$

fig 3.4, MH- loops have shown that the prepared SrM-HF's exhibit behaviour of a ferrimagnetic and hard magnetic nature. In addition, saturation magnetization (M_s) and remanence magnetization (M_r), coercive (H_c) and magnetocrystalline anisotropy (K) decreased as the concentration of Ce^{3+} ion increases. The very high value of H_c indicates the hard ferrimagnetic properties of the nanohexaferrites. Furthermore, it appears that the values of M_r/M_s , are almost constant for all nanohexaferrites. The values of M_s , M_r , H_c , (M_r/M_s), n_B , K and $\alpha(Y-K)$ angles are tabulated in listed table 3.2.

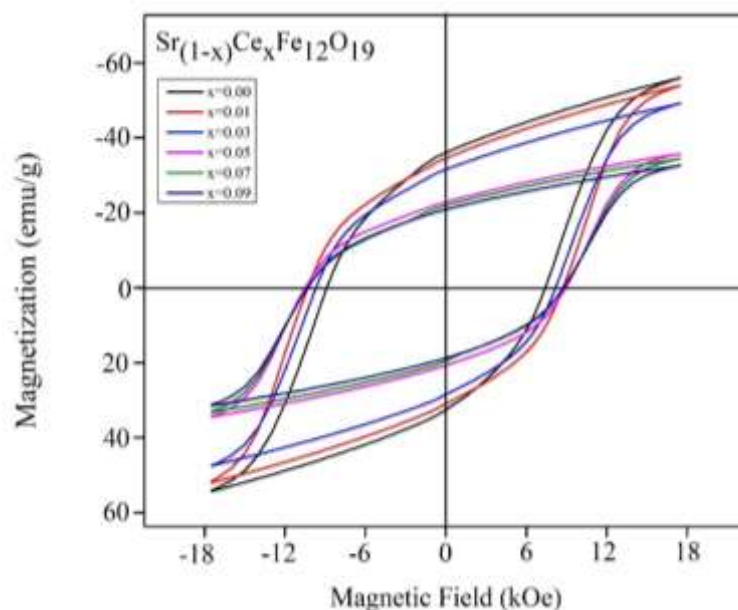


Fig 3.4 Hysteresis curves of $\text{Sr}_{(1-x)}\text{Ce}_x\text{Fe}_{12}\text{O}_{19}$ ($x = 0.0, 0.01, 0.3, 0.5, 0.07, 0.09$) nanoferrites

The Fe^{3+} ions that occupy the five different sub-lattices from a unit cell of SrM-HF's, Fe^{3+} in the 12k, 2a and 2b sites exhibit spins-upward direction, but those in the 4f₁ and 4f₂ sites exhibit spins-downward direction. The unit cell of the net magnetic moment is comparing between the spin- upward direction and spin-downward direction with magnetic moments. According to Neel, the calculated magneton number is given by $M_S = M_B - M_A$ here, M_B is the magnetic moment of the cation at position B (octahedral) and M_A is the magnetic moment of the cation at position A (tetrahedral). To calculate M_B and M_A the possible cation distribution of the current system, M decreases with the replacement of B-site. The substitute for the Fe^{3+} ion preferably occupies the B-site. The magnetic moment of Ce^{3+} ions is greater than that of the Fe^{3+} ions. As the amount of $\text{Fe}^{3+}\text{-O-Fe}^{3+}$ super-exchange interactions decreased at sites-B, the magnetization of sublattice-B decreased. However, if substitution ions replace Fe^{3+} ions at the sites of downward spin site, the net magnetic moment increases [12, 37-38]. The magnetic moment of the strontium ion decreased

with the increasing of the Ce^{3+} ions, this action for this increase in value is due to the increasing of the super exchange interaction between the different sites, leading to an increase in the values (13.77 – 8.33 μB). This indicates the increasing of the super-exchange interactions [39]. Magnetization values of the $\text{SrFe}_{12}\text{O}_{19}$ samples are decreased from for M_s 72.18 emu/g - 43.81 emu/g with increase of the Ce^{3+} ion content [17, 40]. M_r in the range of 44.7 4- 27.06 emu/g at room temperature. H_c is in the scope of 9786 - 8146 Oe at room temperature. This reduction is associated with the equivalent reduction of Fe^{3+} ions to charge-compensating Fe^{2+} ions replacing Ce^{3+} ions replace of Sr^{2+} ions. Moreover, the magnetic moment of Fe^{2+} ions (4 μB) is lower than that of the Fe^{3+} ions (5 μB) [12, 41].

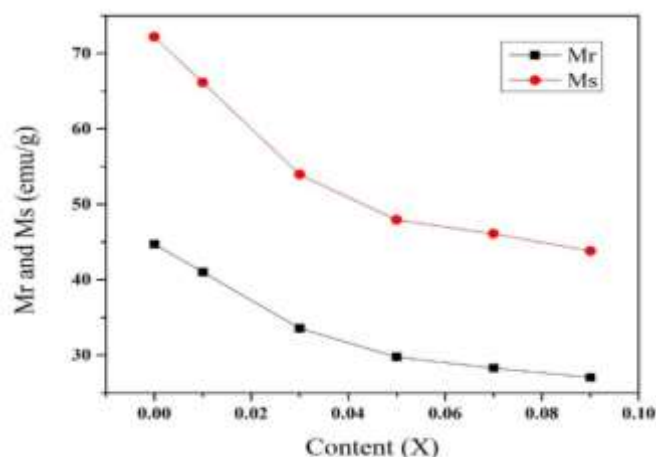


Fig 3.5 Variation of M_s and M_r of $\text{Sr}_{(1-x)}\text{Ce}_x\text{Fe}_{12}\text{O}_{19}$ ($x=0.00, 0.01, 0.03, 0.05, 0.07$ and 0.09) as a function of Ce^{3+} contents

Fig 3.5. Show this variation of M_s and M_r with respect to the concentrations of the Sr^{2+} ion site of cerium ion substitution. In addition, Ce^{3+} substituted ions occupy the spins-up sites. The contrast of these ionic radii can cause strains that cause variations in electronic states and disorder in hexaferrite systems [12, 42]. Another possible substitute for the reduction of M_s and M_r is the spin tilt. If we increase the Ce^{3+} ion to strontium ion, the electron spin deviates from collinear by a specific angle

called spin tilt [43]. The squareness ratio values are observed in the scope of 0.61–0.62 emu/g, shows that all the synthesized nanohexaferrites investigate the nature of a single magnetic domain [44-45].

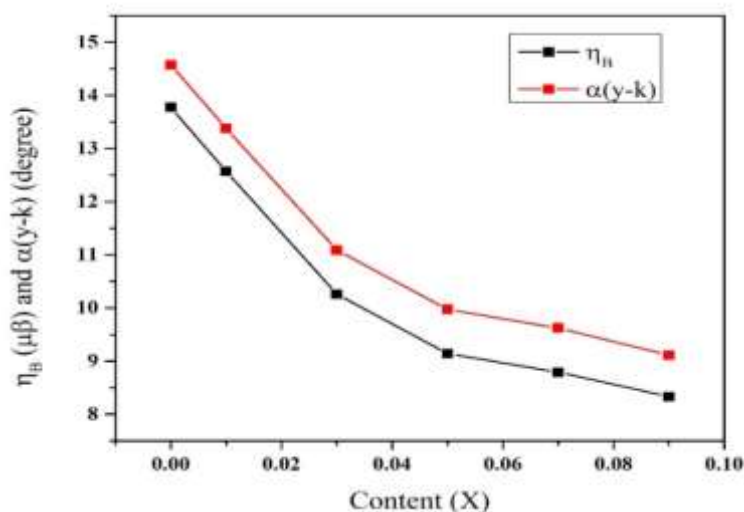


Fig 3.6 Variation of η_B and $\alpha(Y-K)$ of $Sr_{(1-x)}Ce_xFe_{12}O_{19}$ ($x=0.00, 0.01, 0.03, 0.05, 0.07$ and 0.09) as a function of Gd^{3+} contents

Fig 3.6. This indicates that the variation of η_B with $\alpha(Y-K)$ respect to the concentrations of the cerium ion substitution Sr^{2+} ion site. M_r remanence for permanent magnetic field applications is a strong function of thickness, concentration and orientation. Furthermore, variants of could explain the variations of the magnitudes of M_s for their relationship between η_B and M_s [46]. Furthermore, this suggests that the observed non-interacting and anisotropic particles are of the cubic anisotropy type. The anisotropy of decreasing $SrFe_{12}O_{19}$ with the increase of Ce^{3+} ions is due to the reduced particle size values are found to be 1.11-0.65 (erg/Oe). Therefore, the surface spin causes an increase in the coercivity ratio and the surface layer because the anisotropy increases with increasing Ce^{3+} ions due to the mixed fuel. In this investigation, the coercive value decreases as the Ce^{3+} ion content increases. The coercive force obtained by reversing the direction of movement of the wall and that of rotation of the province to change the opposite direction of the

applied magnetic field [40]. In generally, effective clamping of the domain walls leads to coercivity, consequently a larger grain size H_c decreases. Smaller particle size materials were used to achieve high core loss. The H_c is mainly determined by the magnetocrystalline anisotropy and by typical particle size the variations of H_c and particle size are inversely proportional.

α (Y-K) Yafet-Kittel angle, the degree of spin canting effect is explained using Yafet- Kittle angle α (Y-K) [47]. The calculated values of α (Y-K) decrease from 15 – 9 degrees with increasing in Ce^{3+} ion concentration due to the approximation of the molecular field using a non-collinear three sub-lattice model and an increasing tendency for triangular spin arrangement exchange interaction [48].

Table 3.2: Magnetic properties i.e. coercivity (H_c), saturation magnetization (M_s), remanence (M_r), squareness ratio (M_r/M_s), anisotropy (K), Magnetic moment ($\eta\beta$) and α (y-k) of $Sr_{(1-x)}Ce_xFe_{12}O_{19}$ ($x = 0.00, 0.01, 0.03, 0.05, 0.07$ and 0.09) nanoferrites.

Composition	M_s (emu/g)	H_c (Oe)	M_r (emu/g)	S (emu/g)	$\eta\beta$ (μB)	K (erg/Oe)	Cos α (y-k) (degree)
$SrFe_{12}O_{19}$	72.18	9786	44.74	0.62	13.77	1.11	14.57
$Sr_{0.09}Ce_{0.01}Fe_{12}O_{19}$	66.14	9735	40.99	0.62	12.57	1.01	13.38
$Sr_{0.07}Ce_{0.03}Fe_{12}O_{19}$	53.95	9519	33.56	0.62	10.26	0.69	11.09
$Sr_{0.05}Ce_{0.05}Fe_{12}O_{19}$	47.93	9642	29.75	0.62	9.14	0.72	9.97
$Sr_{0.03}Ce_{0.07}Fe_{12}O_{19}$	46.08	9527	28.29	0.61	8.79	0.69	9.62
$Sr_{0.01}Ce_{0.09}Fe_{12}O_{19}$	43.81	8146	27.06	0.62	8.33	0.65	9.11

3.4 Conclusions

$\text{Sr}_{(1-x)}\text{Ce}_x\text{Fe}_{12}\text{O}_{19}$ nanocrystalline ($x = 0.00 < x < 0.09$) hexaferrite was synthesized by self-propagation method using mixed fuels. X-ray diffraction studies confirmed the unique hexagonal magneto-plumbite phase for the all prepared SrM-HF's. The FESEM studies confirmed that the morphological structure was agglomerated with size of the nanoparticles. The magnetic parameter decreased with increasing concentration of the Cerium ion. The synthesized hexaferrite exhibit a hard magnetic nature. The different route of exchange between the iron sub-lattices are discussed based on the improvement of the hyperfine fields. Such nanomaterials generally used in magnetic high density recording material, memory storage devices and permanent magnets of high frequency applications etc.

3.5 References

- [1] K. K. Mallick, Philip Shepherd, R.J. Green, *J. Eur. Ceram. Soc.* 27 (2007) 2045–2052.
- [2] A. Goldman, *Modern Ferrite Technology II*, Springer Science Inc., USA. 63 (2006).
- [3] A. Liaquat, M. Anis-ur-Rehman, A. ul Haq, *J. Alloys Comp.* 822 (2020) 153561.
- [4] M.A. Almessiere, Y. Slimani, H. Güngüneş, H.S. El Sayed, A. Baykal, *Ceram. Int.* 44(9) (2018) 10470-10477.
- [5] R.A. Pawar, S.S. Desai, Q.Y. Tamboli, S. E. Shirsath, S.M. Patange, *J. Magn. Magn. Mater.* 378 (2015) 59–63.
- [6] A. Zafar, A. Rahman, S. Shahzada, S. Anwar, M. Khan, A. Nisar, M. Ahmad, S. Karim, *J. Alloy. Compd.* 727 (2017) 683–690.
- [7] K. Kamishima, T. Mashiko, K. Kakizaki, M. Sakai, K. Watanabe, H. Abe, *AIP Adv.* 5. (2015).
- [8] J. Töpfer, D. Seifert, J.-M. Le Breton, F. Langenhorst, V. Chland, K. Kourčild, H. Štěpánková, *J. Solid State Chem.* 226 (2015)133–141.
- [9] R. C. Pullar, *Prog. Mater Sci.* 57 (2012) 1191–1334.
- [10] T. J. Pérez-Juache, A.L. Guerrero, J.G. Cabal-Velarde, M. Mirabal-García, S. A. Palomares-Sánchez, J.A. Matutes-Aquino, *Phys. B.* 503 (2016) 183–188.
- [11] M. N. Ashiq, A. S. Asi, S. Farooq, M. Najam-ul-Haq and S. Rehman, *J. Magn. Magn. Mater.* 444 (2017) 426–431 .
- [12] M.A. Almessiere, Y. Slimani, H.S. El Sayed, A. Baykal, I. Ercan, *J. Magn. Magn. Mater.* 471 (2019)124–132.
- [13] A. G. Abraham, A. Manikandan, E. Manikandan, S. Vadivel, S.K. Jaganathan, A. Baykal, P. Sri Renganathan, *J. Magn. Magn. Mater.* 452 (2018) 380-388.
- [14] E. Hema, A. Manikandan, M. Gayathri, M. Durka, S.A. Arul, B. R. Venkatraman, *J. Nanosci and Nanotec.* 16 (2016) 5929-5943.

-
- [15] Y. Li, Y. Huang, S. Qi, L. Niu, F. Niu, Y. Zhang, Y. Wu, *Adv. Mat. Res.* 239-242 (2011) 481-485.
- [16] D. Seifert, J. Töpfer, F. Langenhorst, J.-M. Le Breton, H. Chiron, L. Lechevallier, *J. Magn. Magn. Mater.* 321 (2009) 4045.
- [17] Z. Mosleh, P. Kameli, A. Poorbaferani, M. Ranjbar, H. Salamati, *J. Magn. Magn. Mater.* 397(2016)101.
- [18] J. F. Wang, C. B. Ponton, I.R. Harris, *J. Alloy. Compd.* 403 (2005) 104–109.
- [19] B.H. Bhat, B. Want, *Appl. Phys. A* 122 (2016) 148.
- [20] L. Lechevallier, J.M. Le Breton, A. Morel, J. Teillet, *J. Alloy. Compd.* 359 (2003) 310–314.
- [21] G. Litsardakis, I. Manolakis, C. Serletis, K.G. Efthimiadis, *J. Magn. Magn. Mater.* 316 (2007) 170–173.
- [22] H. F. Lu, R.Y. Hong, H.Z. Li, *J. Alloys and Compd.* 509 (2011)10127–10131.
- [23] D. Seifert, J. Töpfer, M. Stadelbauer, R. Grössinger, J.-M.L. Breton, *Am. Ceram. Soc.* 94 (2011) 2109.
- [24] M. Sivakumar, A. Gedanken, W. Zhong, Y.W. Du, D. Bhattacharya, Y. Yeshurun, I. Felner, *J. Magn. Magn. Mater.* 268 (2004) 95–104.
- [25] J. Fang, J.Wang, L.-M. Gan, S.-C. Ng, J. Ding, X. Liu, *J. Am. Ceram. Soc.* 83 (2000) 1049–1055.
- [26] D. H. Chen, Y.Y. Chen, *J. Colloid Interface Sci.* 236 (2001) 41–46.
- [27] D.S. Mathew, R.S. Juang, *Chem. Eng. J.* 129 (2007) 51–65.
- [28] Z.X. Yue, J. Zhou, L.T. Li, H.G. Zhang, Z.L. Gui, *J. Magn. Magn. Mater.* 208 (2000) 55–60.
- [29] J.F. Crider, *Eng. Sci. Proc.* 3(7-12) (1982) 519.
- [30] P. Shepherd, K.K. Mallick, R.J. Green, *J. Magn. Magn. Mater.* 311 (2007) 683-692.
- [31] A. Ghasemi, A. Morisako, X. Liu, *J. Magn. Magn. Mater.* 320 (18) (2008) 2300– 2304.

- [32] M. J. Iqbal, M .N. Ashiq, I. H. Gul, J. Magn. Magn. Mater. 322 (2010) 1720–1726.
- [33] H. Klug, L. Alexander, Wiley, New York, 79(6) (1962) 553.
- [34] Kurian, M. Thankachan, S. Nair, D.S. et al. J Adv Ceram. 4 (2015) 199–205.
- [35] N. Venugopal , G. Krishnamurthy , H. S. Bhojyanaik , M. Madhukar Naik & N. Sunilkumar, Inorganic Nano-Metal Chem. (2020).
- [36] Y. Slimani, H. Güngüneş, M. Nawaz, A. Manikandan, H.S. El Sayed, M.A. Almessiere, H. Sözeri, Ceram Int. 44 (2018) 14242-14250.
- [37] Y. Slimani, A. Baykal, Md. Amir, N. Tashkandi, H. Güngüneş, S. Guner, H.S. El Sayed, Ceram Int. 44 (2018) 15995-16004.
- [38] S. Katlakunta, S.S. Meena, S. Srinath, M. Bououdina, R. Sandhya, K. Praveena, Mater. Res. Bull. 63 (2015) 58-66.
- [39] R. Topkaya, I. Auwal, A. Baykal, Ceram. Int. 42 (2016) 16296–16302.
- [40] K.S. Jithendra Kumara, G. Krishnamurthy, N.S. Kumar, N. Naik, T.M. Praveen, J. Magn. Magn. Mater. 451 (2017) 808-821.
- [41] M. A. Almessiere, Y. Slimani, H. S. El Sayed, A. Baykal, Ceram Int. 44 (2018) 12511-12519.
- [42] M.A. Almessiere, Y. Slimani and A. Baykal, Ceram Int, 44 (2018) 9000-9008.
- [43] D. S. Winataputra, T.L. Ujyanti, W.A. Adi, Mater. Sci. Eng. 202 (2017) 012090.
- [44] A. R. Kagdi, P. Neha. Solanki, E. Francisco. Carvalho, S. S. Meena, P. Bhatt, R. C. Pullar, Rajshree B. Jotania, J. Alloy. Compd. 741 (2018), 377–391.
- [45] M.A. Almessiere, Y. Slimani, A. Baykal, J. Alloy. Compd. 767, 966-975 (2018).
- [46] Y. Yaffet, C. Kittel, Phys. Rev. 87 (1952) 290.
- [47] M. Atif, M. Nadeem, R. Grossinger, R. S. Turtelli, J. Alloys Compd. 509 (2011) 5720–5724.
- [48] B. Ashok, Gadkari, T. J. Shinde, P. N. Vasambekar, J. Magn. Magn. Mater. 322 (2010) 3823–3827.

CHAPTER 4:-

DIELECTRIC PROPERTIES AND
MAGNETIC BEHAVIOR OF Gd^{3+}
SUBSTITUTED M-TYPE
 $SrFe_{12}O_{19}$ NANOFERRITES BY
AUTO COMBUSTION METHOD
USING UREA AND CITRIC ACID
MIXTURES AS A DUAL FUEL

**Published in Journal Solid State of Chemistry, Elsevier
Publication impact factor – 3.656**

4.1 Introduction

M-type strontium hexaferrites (M-SrHF's) have attracted more demand in the field of science and technology owing to their high Curie temperature (720 K), high saturation magnetization or high hysteresis loss, large magneto-crystalline, anisotropy, high intrinsic coercivity and good thermal or chemical stability [1-2]. In recent years, strontium hexaferrites ($\text{SrFe}_{12}\text{O}_{19}$) is the suitable are materials of optical, electrical and magnetic properties [3]. $\text{SrFe}_{12}\text{O}_{19}$ has heat thermal resistance, resistance of corrosion and significant for many applications [4]. Strontium hexaferrites are used as microwave gadgets [5, 6], radiation and absorption devices [7], and magnetic recording media [8] due to their low cost and chemically stable materials. $\text{SrFe}_{12}\text{O}_{19}$ are used in broadcast communications devices [9], high-frequency devices, magnetic coatings [10], absorbing ferric oxides, electric power generation, automotive electronics and magnetic catalysts [11]. The application are mainly depends on the composition, the magnitude and orientation of the magnetic moment. Furthermore, the substitution of small amount of rare-earth elements (Sm^{3+} , Gd^{3+} , Er^{3+} , Ce^{3+} , Eu^{3+} , Nd^{3+} , Dy^{3+} etc.) into $\text{SrFe}_{12}\text{O}_{19}$ nanoferrites significantly improves the electrical and magnetic properties of M-SrHF's [12]. The modifications are more bound up with the size, shape, orientation, and domain configuration of the nano structured [13-17].

In case of ferrites, the dielectric phenomenon can be explained on the basis of microstructural factors. The dielectric properties are stable at high frequencies and depend on synthesis process, sintering time and temperature, chemical composition of additives and grain structure. The study of dielectric properties provides the valuable information for potential applications [18]. In the present investigation, Fe^{3+} magnetic ions are distributed in five sub-lattices with a hexagonal structure (space group

P63/mmc) [19]. 12(k), 2(a) and 2(b) sites exhibit spins (+) direction, but those in the 4(f₁) and 4(f₂) sites exhibit spins (-) direction. The net magnetic moment is comparing between the spin (+) direction and spin (-) direction with magnetic moments [20].

Several synthetic methods viz., solution combustion method [21], hydrothermal, co-precipitation and ceramic method have been used for synthesis of M-SrHF's [22-23]. Among these methods, auto combustion method is a very promising method for synthesizing the desired phase. It is very simple, easy manufacture, low cost, high purity of crystallinity, chemical uniformity, short processing time and fine particles size distribution [24]. In this work, we studied the effect of, synthesis of Gd³⁺ ions substituted SrFe₁₂O₁₉ by auto combustion method using dual fuels (urea and citric acid) and structural, morphological, dielectric and magnetic properties of nanoferrites M-type Sr_(1-x)Gd_xFe₁₂O₁₉ ($x = 0.00, 0.01 < x < 0.09$; in steps of 0.02).

4.2 Experimental method

Nanocrystalline Sr_(1-x)Gd_xFe₁₂O₁₉ ($x=0.00, 0.01 < x < 0.09$) ferrites have been synthesized by the auto combustion method using dual fuel. The analytical reagent grade Strontium nitrate hexahydrate: [Sr (NO₃)₂.6H₂O], (Merck Co, ≥ 99% purity), Ferric nitrate nonahydrate: [Fe(NO₃)₃.9H₂O], (Merck Cof, ≥ 99 % purity) and Gadolinium nitrate hexahydrate: [Gd(NO₃)₃.6H₂O] (Merck Co, 99% purity) are used as oxidizers and urea and citric acid are used as fuel [reducing agent]. The required chemicals are dissolved in de-ionized water in the stoichiometric ratio. The chemical analysis method involves an exothermic, self-propagating, gas-producing redox reaction between the respective metal nitrate and a suitable organic fuel to produce the desired products. The petri dish carrying the solution of redox mixture is placed in a muffle furnace and gradually heated up to 500 ± 20 °C in an air atmosphere.

Initially, the solution begins to boil and undergoes combustion with the development of releasing large amounts of gas (N_2O and CO_2). Initially, the solution starts to burn and releases a lot of heat. The whole reaction completed within three minutes with smoldering process.

The powders are calcinated at $1000\text{ }^\circ\text{C}$ for 3 hours. The sintered powders are ground in an agate mortar and mixed with a binder polyvinyl pyrolidone (PVP) (C_6H_9NO)_n. The powders are compressed into pellets using die with a dia 10 mm and a thickness of about $\sim 2\text{-}3$ mm by loading a pressure of $5\text{-}10^8\text{ kg/m}^2$ for 5 minutes. The pellets are sintered in a furnace at temperature of $1100\text{ }^\circ\text{C}$ for 3 hours and then gradually cooled to room temperature. In general, self-propagation high temperature was favorable for significant crystallite sizes.

The standard X-ray diffraction patterns (XRD) were obtained 2θ angle in the range $20^\circ\text{--}80^\circ$ with scanning rate 2° per min on a Philips diffractometer (Make: Bruker, Model:d8 Advance, Germany) using CuK radiations ($\lambda = 1.5406\text{ \AA}$) is employed at 300 K to study the crystal orientation of all the ferrite nanoparticles. The room temperature Fourier infrared spectroscopy (FTIR) of all the samples was recorded on a Perkin Elmer spectrometer (Model: Spectrum 2, USA) in the wavenumber range $4000\text{ cm}^{-1}\text{--}300\text{ cm}^{-1}$. The morphology of samples was examined by field emission scanning electron microscopy analysis using (FESEM, JEOL/EO/JSM-639]. The energy dispersive X-ray spectrum were recorded using (EDS) Carl Zeiss, Model: EVOLS15, Germany). The dielectric properties of the samples have been measured at room 300 K using LCR Hi- tester (Model: HIOKI, JAPAN) in the frequency range 50Hz-5MHz. LCR meter automatically records the capacitance (Cp) in pF, Inductance (L) in henry, Quality factor (Q), Resistance (R) in ohm, Conductance (G) in mho and dielectric loss ($\tan\delta$) of nanoferrites. The values of

dielectric constant, ac conductivity of all the samples have been calculated using relations [25] the dielectric constant

$$\epsilon' = Cd / \epsilon_0 A \quad (4.1)$$

The ac electrical conductivity evaluated from the dielectric data

$$\sigma_{ac} = 2\pi f \epsilon_0 \epsilon' \tan\delta \quad (4.2)$$

where ϵ' is dielectric constant, C is the capacitance of the dielectric sample holder loaded with sample (pF), d is the thickness of the pellet (cm), A is area of active electrode surface of the sample holder (cm^2) and ϵ_0 is the free space permittivity (8.854×10^{-14} pF/cm), f is the frequency of the applied electric field (Hz), ϵ'' is the dielectric constant and $\tan\delta$ is dielectric loss tangent. Vibrating sample magnetometer (VSM) (Make: CREST, Model: 20130523-01) was employed to characterize the magnetic properties. The values of, Magneton number (η_B) and Yafet- Kittel angle α (Y-K), were calculated using the relations [26]

$$\eta_B = (M_w \times M_s) / 5585 \quad (4.3)$$

where η_B is the magnetic moment (number of Bohr magnetons), M_w is molecular weight of the composition (x) in g, M_s is the saturation magnetization in emu/g, 5585 is the magnetic factor and H_c is the coercivity.

4.3 Results and Discussion

4.3.1 Structural studies

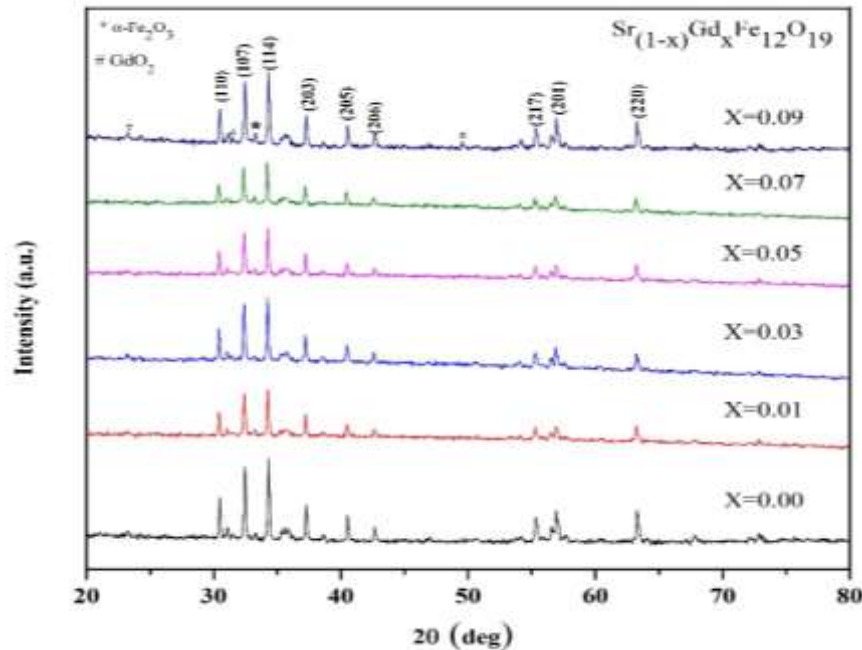


Fig 4.1 PXRD patterns of $\text{Sr}_{(1-x)}\text{Gd}_x\text{Fe}_{12}\text{O}_{19}$ ($x = 0.00, 0.01 < x < 0.09$) nanoferrites

The PXRD patterns of $\text{Sr}_{(1-x)}\text{Gd}_x\text{Fe}_{12}\text{O}_{19}$ ($x = 0.00, 0.01 < x < 0.09$; in steps of 0.02) nanoferrites are depicted in fig 4.1. From the figure, peaks of the XRD pattern of all samples matched with the JCPD card No. 00-051-1879 and space group $P63/mmc$ [27]. These are indexed as (110), (107), (114), (108), (203), (205), (206), (217), (201), (220) and (317) for M-SrHF's with hexagonal phase. The planes confirm the formation of nanoparticle. However, it is observed that samples with $x = 0.09$ exhibits about 5% of secondary phase of $\alpha\text{-Fe}_2\text{O}_3$ [28]. The values of lattice parameter are listed in table 4.1. The lattice parameters a and c are calculated from the value of d_{hkl} corresponds to (008) peak and (107) peak according to the following equation.

$$\frac{1}{d_{hkl}^2} = \frac{4}{3} \left[\frac{h^2 + hk + k^2}{a^2} + \frac{l^2}{c^2} \right] \quad (4.4)$$

where, d_{hkl} is the distance between the crystals, a and c are lattice parameters, and $(h k l)$ are Miller indices. V_{cell} is the unit of the hexagonal system and is determined as follows: formation of M-type single phase,

$$V_{cell} = 0.866 a^2 c \quad (4.5)$$

where, the numerical values is sustained for the hexagonal system. From, the XRD peaks, an average crystallite sizes of the nanoferrites are determined using Debye-Scherrer equation (d) and is calculated by:

$$d = \frac{k\lambda}{\beta \cos\theta} \quad (4.6)$$

where, $k = 0.89$ is Scherer's constant, $\lambda = 0.15406$ nm is wavelength of the incident X-rays in nm, β is the full width at half maximum (FWHM) of diffraction peak, θ is the Bragg diffraction angle [28]. The average value of crystallite size is found in the range 41 nm to 45 nm and values are tabulated in table 4.1. The theoretical X-ray density (d_x) of each sample is calculated using the formula

$$d_x = \frac{ZM}{NV} \quad (4.7)$$

where $Z = 2$ is number of molecules per unit cell, M is the molecular weight, N is the Avogadro's number and V - volume of the unit cell.

From the table 4.1, it is observed that, the lattice parameters (a and c) increases slightly from 0.58781 to 0.58849 Å as the concentration Gd^{3+} ion increases. It may be due to shrinkage of unit cell and replacement of larger Sr^{2+} ions (1.13 Å) by smaller Gd^{3+} ions (0.93Å) without changing the crystal structure [29]. Further, the X-ray density is increasing from 4.74 to 5.10 gcm^{-3} . The decrease in the X-ray density due to larger molecular weight (157.25 amu) and smaller ionic radius of the Gd^{3+} ions (0.93Å) and smaller molecular weight (87.62 amu) and larger ionic radius of strontium ions (1.13Å) and between Fe^{3+} (0.67Å) and Fe^{2+} (0.80 Å).

Table 4.1: Crystallite size (D), lattice constant (a & c), cell volume (V) and X-ray density (qx-ray) of $\text{Sr}_{(1-x)}\text{Gd}_x\text{Fe}_{12}\text{O}_{19}$ ($x=0.00, 0.01 < x < 0.09$) nanoferrites.

Composition	Crystallite size (D) /nm	Lattice constant (a)/Å	Lattice constant (c)/Å	(c)/(a) Å	Cell volume (V)/Å ³	X-ray density (qx-ray)/g cm ⁻³
$\text{SrFe}_{12}\text{O}_{19}$	45.36	5.8849	23.0562	3.918	691.5	5.10
$\text{Sr}_{0.09}\text{Gd}_{0.01}\text{Fe}_{12}\text{O}_{19}$	43.74	5.8781	23.0476	3.921	689.6	4.74
$\text{Sr}_{0.07}\text{Gd}_{0.03}\text{Fe}_{12}\text{O}_{19}$	41.33	5.8810	23.0423	3.918	690.2	4.74
$\text{Sr}_{0.05}\text{Gd}_{0.05}\text{Fe}_{12}\text{O}_{19}$	43.75	5.8837	23.0501	3.918	691.0	4.74
$\text{Sr}_{0.03}\text{Gd}_{0.07}\text{Fe}_{12}\text{O}_{19}$	43.53	5.8839	23.0524	3.918	691.1	4.75
$\text{Sr}_{0.01}\text{Gd}_{0.09}\text{Fe}_{12}\text{O}_{19}$	42.86	5.8828	23.0513	3.918	690.8	4.76

4.3.2 Spectral analysis

FTIR spectrum of provides the information on molecular bonding and chemical structure of materials to confirm single phase ferrites. Fig 4.2 shows the room temperature FT-IR spectra of $\text{Sr}_{(1-x)}\text{Gd}_x\text{Fe}_{12}\text{O}_{19}$ ($x = 0.00, 0.01 < x < 0.09$: in steps of 0.02) nanohexaferrites measured in the wave number range of 4000 to 300 cm^{-1} . From the fig 4.2, it is observed that the spectra of each samples show two strong absorption bands which is to designated structural integrity of the magnetoplumbite. The absorption band is the characteristic of lattice vibrations of octahedral and tetrahedral sites.

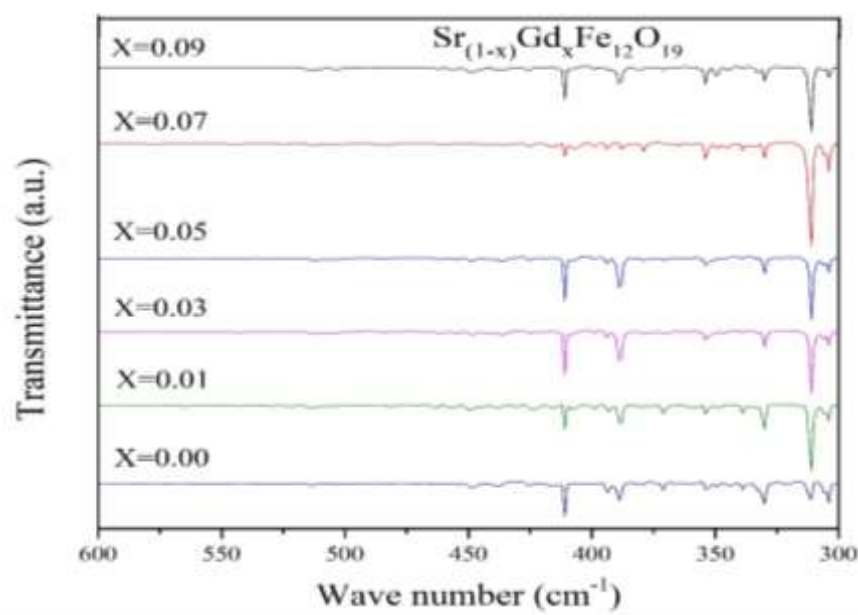


Fig 4.2 FT-IR spectra of $\text{Sr}_{(1-x)}\text{Gd}_x\text{Fe}_{12}\text{O}_{19}$ ($x = 0.00, 0.01 < x < 0.09$) nanoferrites

The M-SrHF's are shown two intense vibrational bands, which are associated with vibrational bands in the wavenumber range $309 - 311 \text{ cm}^{-1}$ correspond to tetrahedral sites and the range $403 - 411 \text{ cm}^{-1}$ correspond to octahedral sites (fig 4.2) [30, 31]. The position of peak slightly changed in Gd^{3+} ion substituted samples. Therefore, the gadolinium replaces the Sr^{2+} ions without changing the crystal structure of the composition. Furthermore, the absence of bands in the wavenumber range $3200-3500 \text{ cm}^{-1}$ indicating that the non-existence of an OH group in the reaction method. A force constant is a secondary potential energy identified by the radius of the site. The force constants for tetrahedral and octahedral sites are given by the relations.

$$K_T = 4\pi^2 c^2 \nu_1^2 m \quad (4.8)$$

$$K_O = 4\pi^2 c^2 \nu_2^2 m \quad (4.9)$$

where c - speed of light $2.99 \times 10^8 \text{ m/s}$, ν_1 and ν_2 are the vibrational frequencies cm^{-1} at A- and B-sites cm^{-1} respectively, m - decreased mass of Fe^{3+} and O^{2-} ions.

From table 4.2, it is observed that the value of force constant from 7.01 – 7.10 newton/m for tetrahedral sites (K_T) is lower than that for octahedral site (K_O) from 12.25 – 12.31 newton/m. Furthermore, the values K_T and K_O are found to be increased with increase in Gd^{3+} ion substitution. However, the K_T values are less than the K_O values in the samples substituted with Gd^{3+} ions.

Table 4.2: Position of IR absorption bands and force constant of $Sr_{(1-x)}Gd_xFe_{12}O_{19}$ ($x = 0.00, 0.01 < x < 0.09$) nanoferrites.

Composition	Position of ν_1 (cm^{-1})	Force constant Tetrahedral (K_T) newton/m	Position of ν_2 (cm^{-1})	Force constant Octahedral (K_O) newton/m
$SrFe_{12}O_{19}$	310	7.10	411	12.25
$Sr_{0.09}Gd_{0.01}Fe_{12}O_{19}$	311	7.05	410	12.31
$Sr_{0.07}Gd_{0.03}Fe_{12}O_{19}$	309	7.05	411	12.31
$Sr_{0.05}Gd_{0.05}Fe_{12}O_{19}$	309	7.01	411	12.25
$Sr_{0.03}Gd_{0.07}Fe_{12}O_{19}$	310	7.05	409	12.25
$Sr_{0.01}Gd_{0.09}Fe_{12}O_{19}$	311	7.05	409	12.25

4.3.3 Morphological studies

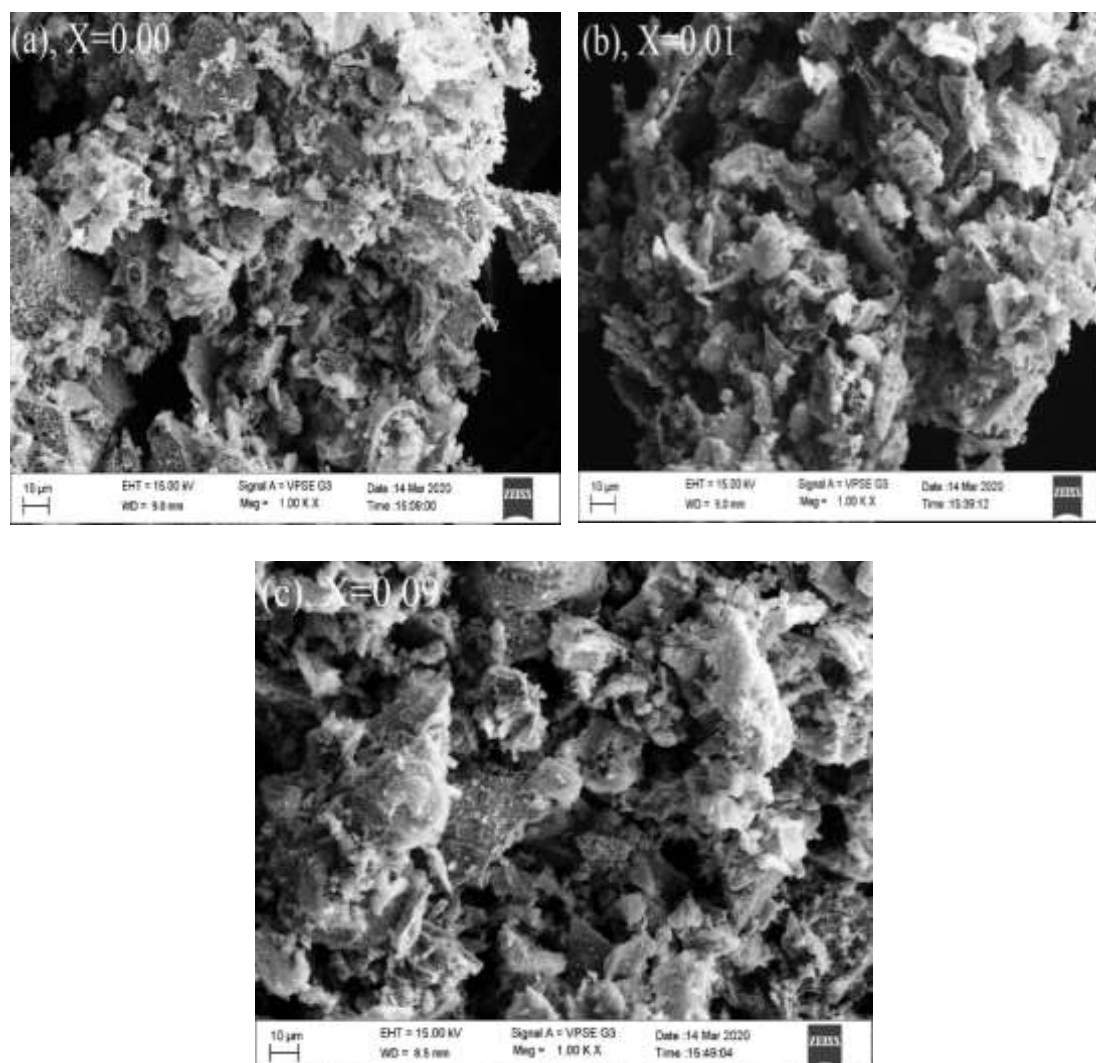


Fig 4.3 FESEM Micrographs of $\text{Sr}_{(1-x)}\text{Gd}_x\text{Fe}_{12}\text{O}_{19}$ ($x = 0.00, 0.01 < x < 0.09$) nanoferrites

The FE-SEM images of the synthesized compositions of $\text{Sr}_{(1-x)}\text{Gd}_x\text{Fe}_{12}\text{O}_{19}$ are shown in fig 4.3 (a, b and c). From the figures, it is observed that the particles tend to grow aggregates and are in a porous nature. The micrographs shown the hexaferrite particles clipped for the interaction due to their magnetic properties and the association of primary particles. The line intercept procedure is used to estimate an average grain size using the relation: $G_{av} = 1.5 L / MN$ where L-total length of test line in m, M – magnification, N - total number of grains intercept. The particles sizes are

calculated and they are found to be in the range of 41 - 45 nm. Further, the fine powders have strong tendency to form of aggregates into large mass [32]. It has been reported that the auto combustion technique using citric acid and urea mixtures as a dual fuel reaction involves crystallization compared with crystals from a solution of nanoparticles to the M-HF's. This is due to short period of time and high temperature to complete the reaction. For the consummation of auto combustion method with sovereign mixture of dual fuel with variable particle size distribution [33, 34]. EDS analysis clearly indicates presence of Sr, Gd, Fe and oxygen elements in the material and confirms the purity of the prepared nanoparticle.

4.3.4 Dielectric studies

4.3.4.1 Dielectric constant

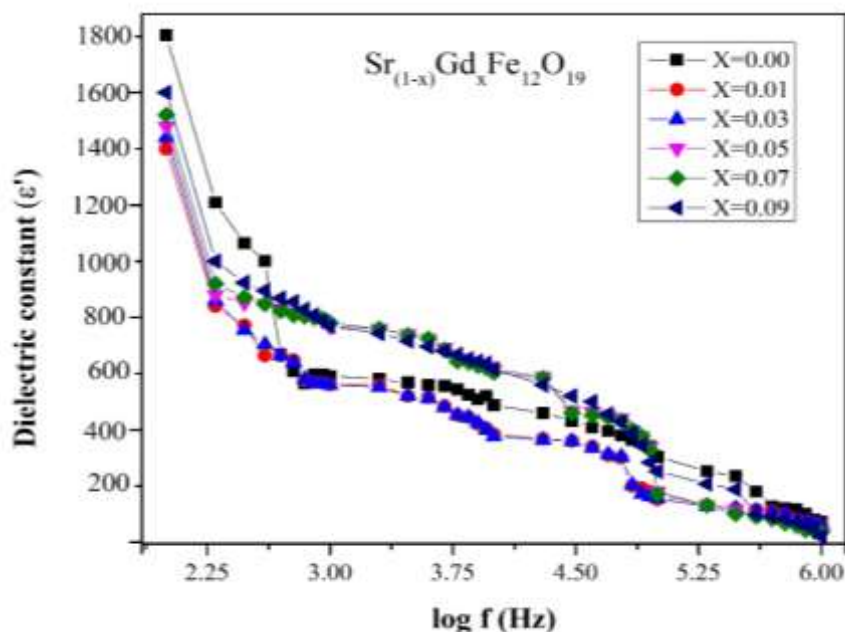


Fig 4.4 Dielectric constant of $\text{Sr}_{(1-x)}\text{Gd}_x\text{Fe}_{12}\text{O}_{19}$ ($x = 0.00, 0.01 < x < 0.09$) nanoferrites.

The dielectric constant symbolizes the ability to store dielectric energy. Fig 4.4, reveal the frequency dependent dielectric constant for all the samples measured at 300 K. From the figures, the dielectric constant shows the dispersion with increasing

in frequencies. This dispersion is sharp at lower frequencies and almost level off at higher frequencies. This dielectric behavior obeys Maxwell-Wagner [31, 32] type interfacial polarization in accordance with Koop's theory [35, 36]. This is normal dielectric behavior of ferrites. Iwauchi was established a strong correlation between polarization mechanism and conduction mechanism [37]. Iwauchi has theoretically shown that conduction mechanisms in ferrites is similar to polarization due to electrons exchange between Fe^{2+} ions to Fe^{3+} ions at octahedral sites [37]. The Fe^{3+} ions also contribute toward dielectric properties.

The higher values of dielectric constant at lower frequencies is due to the predominance of species such as Fe^{2+} ions, grain boundary defects, oxygen vacancies and interfacial dislocation clusters. The lower values of dielectric constant are due to homogeneity, better symmetry, uniform grain and smaller particles [38]. Moreover, the polarization decreases with increasing frequency and reaches a constant value. At higher frequencies, beyond a certain frequency, the electron exchange between $\text{Fe}^{3+} \leftrightarrow \text{Fe}^{2+}$ cannot keep up with the alternating field and polarization lags behind the applied field [39]. It was reported that Gd^{3+} ions prefers to occupy octahedral sites in place of the Fe^{3+} ions and thereby reduces the Fe^{3+} ions or increase the number of Fe^{2+} ions [40, 41]. It clears that dielectric constant is increase with increasing Gd^{3+} ions substitution.

4.3.4.2 Dielectric loss tangent

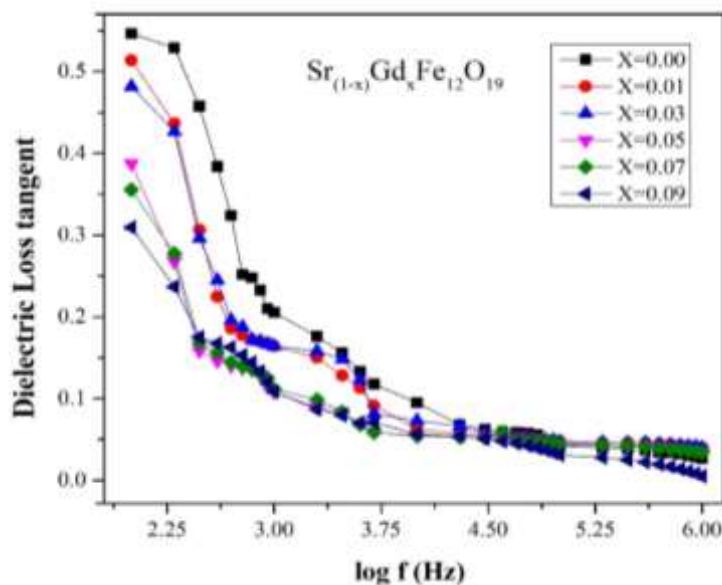


Fig 4.5 Dielectric loss tangent of $\text{Sr}_{(1-x)}\text{Gd}_x\text{Fe}_{12}\text{O}_{19}$ ($x = 0.00, 0.01 < x < 0.09$) nanoferrites

The dielectric loss tangent ($\tan\delta$) represents the loss of electrical energy in the dielectric material at various frequencies which is a significant part of the total loss in the core of the ferrite. Therefore, the low dielectric loss device application is desirable for the low core loss achieved an investigated sample [42]. Fig 4.5 shows the variation of room temperature loss tangent ($\tan\delta$) with the frequency of the field for all the compositions. It is observed that the dielectric loss decreases with increasing frequency due to Maxwell-Wagner polarization. The higher values of $\tan\delta$ at lower frequencies correspond to lower conductivity of the grain boundaries, which requires more energy to exchange electrons between $\text{Fe}^{2+} \leftrightarrow \text{Fe}^{3+}$ ions, resulting in higher losses. At higher frequencies, electron transfer between $\text{Fe}^{2+} \leftrightarrow \text{Fe}^{3+}$ ions requires a small amount of energy, resulting in lower energy loss [43]. The value of $\tan\delta$ depends on the sample stoichiometry, ferrous ion content, structural homogeneity, composition and sintering time. It is also observed that $\tan\delta$ values of all Gd doped samples are low as compared to the undoped sample.

4.3.4.3 AC Conductivity studies

AC measurements are an important tool for studying the dynamic properties of the semiconductor and dielectric materials. Fig 4.6 shows the variation of room temperature $\ln\sigma_{ac}$ versus $\log f$. It is evident that the electrical conductivity of AC increases as the frequency of the applied electric field increases. Therefore, AC conductivity is proportional to the angular frequency and linearity is confirmed [44]. Moreover, an electron exchange between $\text{Sr}^{2+} + \text{Fe}^{3+} \leftrightarrow \text{Fe}^{2+} + \text{Sr}^{3+}$ ions at adjacent tetrahedral sites is involved in the conductivity of ferrite. The frequency dependence of AC electrical conductivity can be explained on the basis of Maxwell-Wagner two-layer model of ferrite. In this model, the first layer consists of large, highly conductive ferrite particles (Fe^{2+} ions) separated by thin, low-conductivity grain boundaries [45].

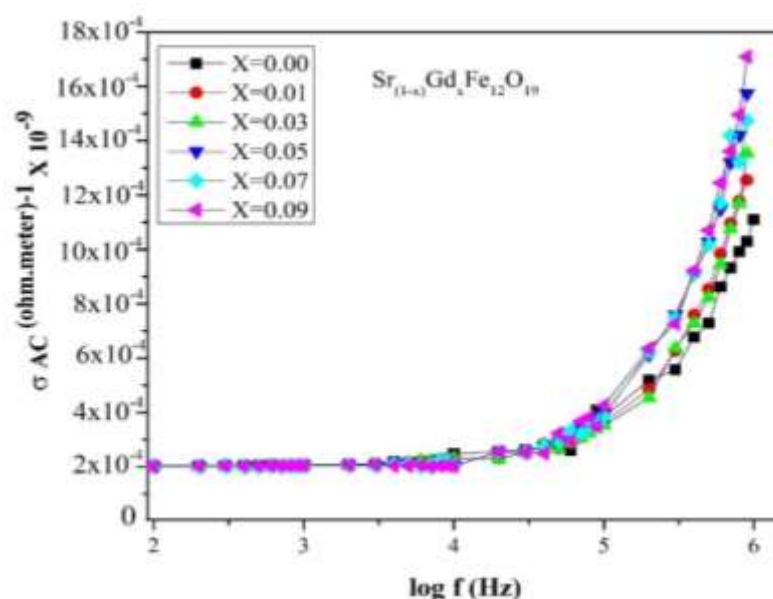


Fig 4.6 AC Conductivity studies of $\text{Sr}_{(1-x)}\text{Gd}_x\text{Fe}_{12}\text{O}_{19}$ ($x = 0.00, 0.01 < x < 0.09$) nanoferrites

At lower frequencies, the grain boundaries are become more active, therefore the electron hopping frequency between Fe^{2+} and Fe^{3+} ions is lower. At higher frequencies, the conductive grains became more active, which promotes electron hopping between Fe^{2+} and Fe^{3+} ions, increasing the hopping frequency. Therefore, the

AC electrical conductivity increases with increase in frequency [46]. Furthermore, at very high frequencies, the graph is nearly linear, confirming the conductivity due to the small polaron hopping in the ferrite. For ferrite, it is clear that the dielectric constant is directly proportional to the square root of the conductivity [46]. AC electrical conductivity of all Gd^{3+} doped samples is high as compared to undoped sample.

4.3.5 Magnetic measurements

The room temperature M-H curves for $Sr_{(1-x)}Gd_xFe_{12}O_{19}$ ($x = 0.00: 0.01 < x < 0.09$: in step of 0.02) hexaferrites with maximum applied magnetic field within ± 70 kOe. The magnetic parameters are calculated using the following relations [46].

$$S = \frac{M_r}{M_s} \quad (4.10)$$

$$K = \frac{H_c \times M_s}{0.64} \quad (4.11)$$

Where μ_B is the magnetic moment/unit in μ_B , M_s is saturation magnetization (emu/g), M_r is remanent magnetization, $k = 0.64$ is constant magnetic anisotropic and H_c is the coercivity. The Yafet and Kittel angles are given by the relation

$$\cos \alpha(Y - K) = \left[\frac{n_B + 5(1-x)}{(6-x)} \right] \quad (4.12)$$

From the fig 4.7. It is also observed that all the samples are magnetically hard. The information about saturation magnetization (M_s), remanence magnetization (M_r), Coercivity (H_c), squareness ratio (S), Magneton number (n_B), anisotropy constant (K) and Yafet-Kittel angle $\alpha(Y-K)$ fields was deduced from respective M-H curves of the sample and table 4.3.

In M-type hexaferrites, the iron ions occur on five different sites: the octahedral sites, crystallographically known as 2a, 12k and 4f₂, and the tetrahedral sites 4f₁ and 2b. The magnetically ordered state in $SrFe_{12}O_{19}$, is 12k, 2a and 2b sites

which have their spins aligned parallel to each other [(+) spin direction] and to the crystallographic c-axis, while opposite direction in the $4f_2$ and $4f_1$ sites (down ward spin directions). Replacement of divalent Sr by trivalent Gd is associated with a valence change of one Fe^{3+} per formula unit to Fe^{2+} [47].

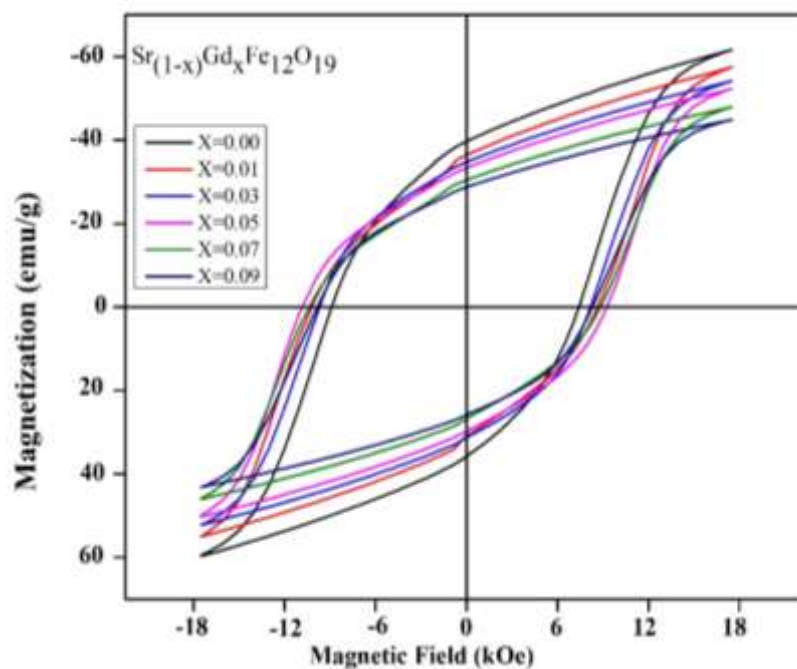


Fig 4.7 Hysteresis curves of $Sr_{(1-x)}Gd_xFe_{12}O_{19}$ ($x = 0.00, 0.01 < x < 0.09$) nanoferrites

The magnetic properties of hexaferrites depend upon synthesis conditions and the type of doped ions and their occupancy at the five different sites of Fe^{3+} crystallographic sites, viz., trigonal bipyramidal (2b), octahedral (12k, 2a and $4f_2$) and tetrahedral ($4f_1$) [48, 49]. Eight Fe^{3+} ions out of 12 are with spin up at lattice and four with spin down results net effect of four Fe^{3+} ions (having spin up state). These ions contribute towards the magnetization of material.

The magnetization value of all the samples decrease from M_s 66.25 emu/g to 39.16 emu/g with the increase in Gd^{3+} ion concentration [50]. The substituted Gd^{3+} ions for the Fe^{3+} ion prefers to occupy B-sites. The magnetic moment of Gd^{3+} ion is

larger than that of the Fe^{3+} ion. As the number of super-exchange interactions $\text{Fe}^{3+}\text{-O-Fe}^{3+}$ at B-sites decreased, the magnetization of the B-sublattice decreased. Moreover, substitution of Gd^{3+} ions in place of Fe^{3+} ions [(-) spin] the net magnetic moment increases [51, 52]. While, the magnetic moment decreases by the substitution of smaller Gd^{3+} ions for larger sized Sr^{2+} ions due to increase in super exchange interaction between different sites, which leads to decrease the values from 12.59 to $7.44 \mu\text{B}$ due to increase of the super-exchange interactions [53].

Further, the room temperature values of M_r are in the range from 40.91 - 24.25 emu/g. The coercivity (H_c), values is in the range of 9587 - 8146 Oe at 300 K. This reduction is attributed to the reduction of Fe^{3+} ions equivalent to charge-compensating Fe^{2+} and Sr^{2+} ions by replacing the Gd^{3+} ions. Moreover, the magnetic moment of Fe^{2+} ($4 \mu\text{B}$) ions is lower than that of the Fe^{3+} ($5 \mu\text{B}$) ions [54, 55].

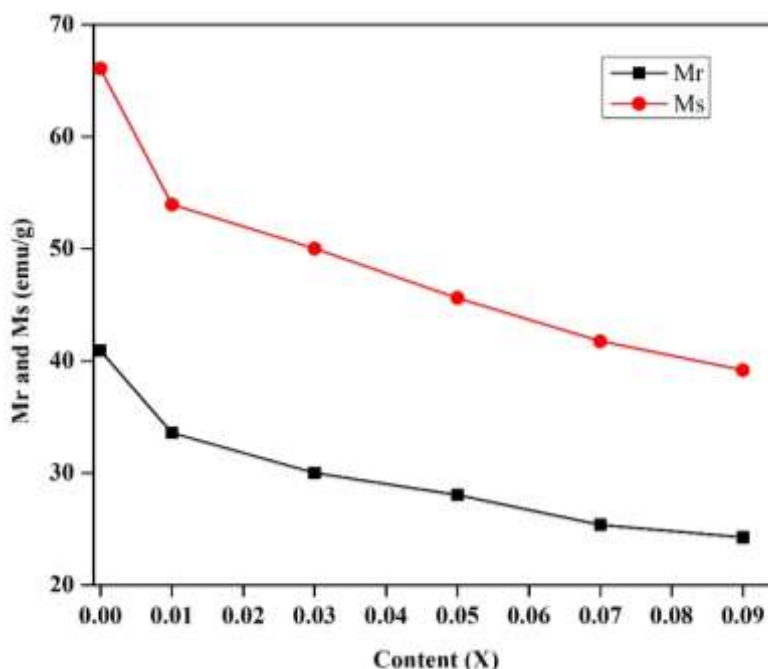


Fig 4.8 Variation of M_s and M_r of $\text{Sr}_{(1-x)}\text{Gd}_x\text{Fe}_{12}\text{O}_{19}$ ($x = 0.00, 0.01 < x < 0.09$) as a function of Gd^{3+} contents

Fig 4.8 shows the variation of room temperature M_s and M_r values with composition of Gd^{3+} ion concentration. Furthermore, the substituted Gd^{3+} occupied the spin-up sites. The ionic radii cause strain that instigate disorder of the M-SrHF's and variations of electronic state [55]. In other words the reduction of M_s and M_r is due to spin-canting. On substitution of Gd^{3+} ions, the spins of the electrons deviate from the collinear by a specific angle called spin-canting [27]. The squareness ratio was also calculated from the magnetic data. It is found that the values of the squareness ratio is in the range 0.61–0.62 emu/g, suggesting that all the synthesized M-SrHF's explore the single magnetic domain structure [56]. The decrease in the squareness ratio may be due to increase in nonmagnetic impurity phase [57].

The coercivity values are the measure of the strength of magnetic field required to demagnetize a ferromagnetic material. The coercive force obtained by reversing the direction of the applied magnetic field by reversing the direction of movement of the wall and the direction of rotation of the region [58]. In the present investigation, the coercivity value decreases with increase in Gd^{3+} ion concentration. The changes in coercivity values is attributed to the decrease in magneto crystalline anisotropy of the magnetic phase, change in morphology and particle size [59]. Furthermore, this indicates that the observed non-strongly interacting and anisotropic particles are a type of cubic anisotropy. The anisotropy of the strontium hexaferrites decreases with increasing Gd^{3+} ion due to decreasing in particle size value from 0.93 erg/Oe to 0.55 erg/Oe. Therefore, the surface spin causes an increase in the coercivity ratio and the surface layer. Fig 4.9 shows the change of η_β and $\alpha(Y-K)$ for the concentration of the Sr^{2+} ion substitution site of the Gd^{3+} ion. The Yafet-Kittel angle (Y-K angles), the degree of spin canting effect is explained using Yafet- Kittle angle $\alpha(Y-K)$ [60].

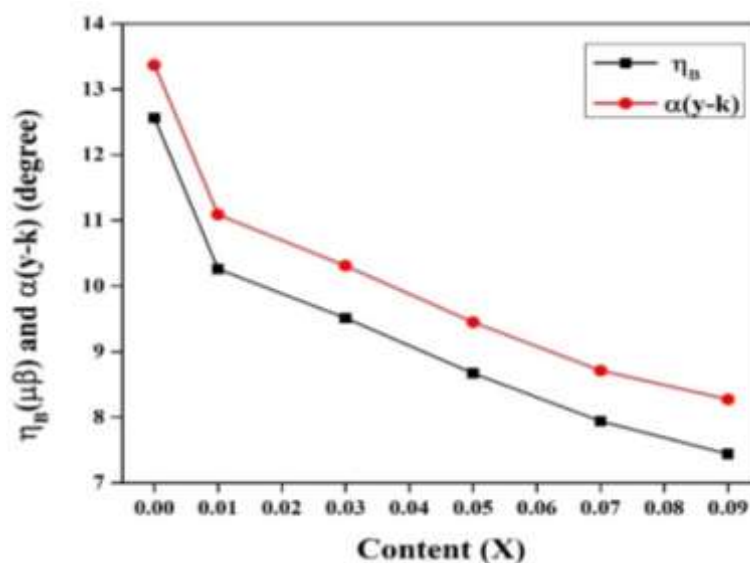


Fig 4.9 Variation of η_{β} and $\alpha(Y-K)$ of $Sr_{(1-x)}Gd_xFe_{12}O_{19}$ ($x=0.00, 0.01 < x < 0.09$) as a function of Gd^{3+} contents

The calculated $\alpha(Y-K)$ value decreases at 13-8 degrees as the concentration of Gd^{3+} ions increased due to the approximation of the molecular field using the non-collinear three-sublattice model and the increasing trend of exchange interactions triangular spin arrangement [61].

Table 4.3: Magnetic properties i.e. coercivity (H_c), saturation magnetization (M_s), remanence (M_r), squareness ratio (M_r/M_s), η_{β} , K and $\alpha(Y-K)$ of $Sr_{(1-x)}Gd_xFe_{12}O_{19}$ ($x=0.00, 0.01 < x < 0.09$) nanoferrites.

Composition	M_s (emu/g)	H_c (Oe)	M_r (emu/g)	S (emu/g)	η_{β} ($\mu\beta$)	K (erg/Oe)	$\text{Cos } \alpha(y-k)$ (degree)
$SrFe_{12}O_{19}$	66.25	8972	40.91	0.62	12.59	0.93	13.42
$Sr_{0.09}Gd_{0.01}Fe_{12}O_{19}$	53.95	8146	33.56	0.62	10.26	0.69	11.09
$Sr_{0.07}Gd_{0.03}Fe_{12}O_{19}$	49.93	9419	29.98	0.60	9.49	0.73	10.30
$Sr_{0.05}Gd_{0.05}Fe_{12}O_{19}$	45.42	9513	28.03	0.61	8.63	0.68	9.43
$Sr_{0.03}Gd_{0.07}Fe_{12}O_{19}$	41.65	9587	25.37	0.61	7.92	0.62	8.70
$Sr_{0.01}Gd_{0.09}Fe_{12}O_{19}$	39.16	9064	24.25	0.62	7.44	0.55	8.21

4.4 Conclusion

M-SrHF's Powders $\text{Sr}_{(1-x)}\text{Gd}_x\text{Fe}_{12}\text{O}_{19}$ ($x = 0.00, 0.01 < x < 0.09$; in steps of 0.02) was prepared by auto combustion method using urea and citric acid mixtures as a dual fuel. The X-ray diffraction analysis confirms the M type-phase hexagonal structure. Crystallite size of the synthesized sample is 41 - 45 nm, it was observed that samples $x = 0.09$ exhibits about 5% of secondary phase of $\alpha\text{-Fe}_2\text{O}_3, \text{GdO}_2$ as a minor impurity phase. The FT-IR spectrum showed two absorption band that are characteristic of nanoferrites and with force constant the K_T values were less than the K_O values in the samples substituted with Gd^{3+} ions. FE-SEM Micrographs images were confirmed that the morphological structure is aggregated to the size of nanoparticles. The dielectric parameters decrease while AC conductivity increases with frequency. At a particular frequency, the dielectric constant, dielectric loss attain maximum, then begins to decrease with increase in composition. M-H curves were measured at room temperature, its reveals that hard magnetic material, magnetic parameters decrease as gadolinium ion concentration increases. The various exchange routes between iron sub-lattices due to increased hyperfine fields are discussed. The data obtained with Gd^{3+} doping on $\text{SrFe}_{12}\text{O}_{19}$ are with super exchange interaction, single domine particle structure and noncollinear three sub-lattice model and indicating an exceedingly wide application. The synthesized nanoparticles shows extraordinary properties, $\text{SrFe}_{12}\text{O}_{19}$ can be used for electro-magnetic devices, opto-electronic devices, high frequency permanent magnets, storage devices, galvanometers, motors and recording media.

4.5 Reference

- [1] M.A. Almessiere, Y. Slimani, H.S. El Sayed, A. Baykal, *Ceram. Int.* 44 (2018) 12511–12519.
- [2] R.C. Pullar, Hexagonal ferrites, *Prog. Mater Sci.* 57 (2012) 1191–1334.
- [3] V. Banihashemi, Ghazi, M.E. & Izadifard, *Mater Sci: Mater Electron.* 30 (2019)
- [4] X. Tang, R.Y. Hong, W.G. Feng, D. Badami, *J. Alloys Compd.* 562 (2013) 211–218.
- [5] Z. Ullah, S. Atiq, S. Naseem, *J. Alloys Compd.* 555 (2013) 263-267.
- [6] T.M.H. Dang, V.D. Trinh, D.H. Bui, M.H. Phan, D.C. Huynh, *Adv. Nat. Sci.: Nanosci. Nanotechnol.* 3 (2012) 025015.
- [7] A.U. Rashid, P. Southern, J.A. Darr, S. Awan, S. Manzoor, *J. Magn. Magn. Mater.*, 344 (2013) 134.
- [8] M. J. Iqbal, M.N. Ashiq, P.H. Gomez, *J. Alloys Compd.* 478 (2009) 736.
- [9] T. J. Pérez-Juache, A.L. Guerrero, J.G. Cabal-Velarde, M. Mirabal-García, S.A. Palomares-Sánchez, J.A. Matutes-Aquino, *Phys. B.* 503 (2016) 183-188.
- [10] T. P. Xie, L.J. Xu, C.L. Liu, *Powder Technol.* 232 (2012) 872.
- [11] M.N. Ashiq, M.J. Iqbal, M. Najam-ul-Haq, P.H. Gomez, A.M. Qureshi, *J. Magn. Magn. Mater.* 324 (2012) 15.
- [12] S. Katlakunta, S.S. Meena, S. Srinath, M. Bououdina, R. Sandhya, K. Praveena, *Mater. Res. Bull.* 63 (2015) 58.
- [13] J. Luo, Y. Xu, H. Mao, *J. Magn. Magn. Mater.* 381(2015) 365–371.
- [14] C. Sun, K. N. Sun, P.F. Chui, *J. Magn. Magn. Mater.* 324 (2012) 802–805.
- [15] S. Amiri, H. Shokrollahi, *J. Magn. Magn. Mater.* 345 (2013) 18–23.
- [16] J.H. Luo, *Mater. Lett.* 80 (2012) 162–164.
- [17] N. Niazia, O. Farooq, Fatima-tuz-Zahracand, M. Anis-ur-Rehmand, *Eng. Mater.*, 778 (2018) 195-199.

- [18] S. A. Saafan, S.T. Assar, S.F. Mansour, *J. Alloy. Compd.* 542 (2011) 192–198.
- [19] X. B. Chen, N.T.M. Hien, K. Han, J.C. Sur, N.H. Sung, B.K. Cho, I.S. Yang, *J. Appl. Phys.* 114 (2013) 13912.
- [20] G. M. Suarez, L. P. R. Vazquez, J. C. C. Huacuz, A. F. Fuentes, J. I. E. García, *Phys. B.* 339 (2003) 110-118.
- [21] J. J. Kingsley and K. C. Patil, *Mater. Lett.* 6 (1988) 427-32.
- [22] J. F. Wang, C. B. Ponton, and I. R. Harris, *J. Alloys Compd.* 369 (1–2), (2004) 170–177.
- [23] H. F. Lu, R. Y. Hong and H. Z. Li, *J. Magn. Magn. Mater.* 509 (41), (2011) 10127–10131.
- [24] A. Ghasemi, A. Morisako and X. Liu, *J Magn. Magn .Mater.* 320 (18), (2008) 2300– 2304.
- [25] M. Veena, A. Somashekarappa, G. J. Shankaramurthy, H. S. Jayanna, H. M. Somashekarappa, *J. Magn. Magn. Mater.* 419 (2016) 375–385.
- [26] B. Ashok. Gadkari, Tukaram, J. Shinde, Pramod N. Vasambekar, *J. Magn. Magn. Mater.* 322 (2010) 3823–3827.
- [27] A. Liaquat, M. Anis-ur-Rehman, A. ul Haq, *J. Alloys Compd.* 822 (2020) 153561.
- [28] H. Klug, L. Alexander, Wiley, New York, (1962). 491
- [29] G. Litsardakis, I. Manolakis, C. Serletis, K.G. Efthimiadis, *J. Magn. Magn .Mater.* 316 (2007) 170–173.
- [30] D. H. Chen, Y.Y. Chen, *J. Colloid Interface Sci.* 236 (2001) 41–46.
- [31] G. R. Gordani, A. Ghasemi, A. Saidi, *Ceram. Int.* 40 (2014) 4945–4952.
- [32] M. N. Ashiq, A. S. Asi, S. Farooq, Najam-ul-Haq, S. Rehman, *J. Magn. Magn .Mater* 444 (2017) 426–431.
- [33] P. Kaur, S.K. Chawla, S.S. Meena, S.M. Yusuf, S.B. Narang, *Ceram Int.* 42 (2016) 14475–89.

- [34] K. S. Jithendra kumara, G. Krishnamurthy, B. E. Kumara swamy, N. D. Shashi kumar, Satish naik, B. S. Krishna and Nagaraj naik, *Appl. Organometal. Chem.* 31 (2016) 3549.
- [35] C. G. Koops, *Phys. Rev.* 83 (1953) 121-124.
- [36] S. Mazumdar, F. Alam, U.Tanni, K. Kali, B. Das, and M. Khan, *Mater Sci App.* 10 (2019) 733-745.
- [37] K. Iwauchi, *Jpn. J. Appl. Phys.* 10 (1971) 152.
- [38] E. Melagiriappa, H. S. Jayanna, B. K. Chougule, *Mater. Chem. Phys.* 112 (2008) 68–73.
- [39] B. Unal, M. Almessiere, Y. Slimani, A. Baykal, A. V. Trukhanov and I. Ercan, *Nanomaterials*, 9 (2019) 1168.
- [40] J. Singh, C. Singh, D. Kaur, S.B. Narang, R. Joshi, S. Mishra, R. Jotania, M. Ghimire, C. C. Chauhan, *Mater. Des.* 110 (2016) 749-761.
- [41] N. Niazi, O. Farooq, F. tuz-Zahra, M. Anis-ur-Rehman, *Key Eng. Mater.* 778 (2017) 195-199.29.
- [42] P. Kumar, A. Gaur, and R. K. Kotnala, *Ceram. Int.* 43 (2017) 1180-1185
- [43] M. N. Ashiq, R. B. Qureshi, M. A. Malana, and M. F. Ehsan, *Fabrication, J. Alloys Compd.* 651 (2015) 266-272.
- [44] G. Asghar, M. Anis-ur-Rehman, *J. Alloys Comp.* 526 (2012) 85–90.
- [45] M.U. Muhammad Irfan, Asmat Elahi, U. Khan, Tahira Khan, K. Javed, S. S. Ali, Abdul Shakoor, *J Mater Sci: Mater Electron*, 27 (2015) 3637-3644.
- [46] B. K. C. R. S. Devan, *J Appl Phys.* 101 (2007) 141.
- [47] X. Liu, W. Zhong, S. Yang, Z. Yu, B. Gu, Y. Du, *J. Magn. Magn. Mater.* 238 (2002) 207–214.
- [48] S. Singhal, T. Namgyal, J. Singh, K. Chandra, S. Bansal, *Ceram. Int.* 37 (6), (2011) 1833-1837.
- [49] X. Luo, J. Wang, M. Dooner, J. Clarke, *Appl. Energy.* 137 (2015) 511-536.

- [50] M. Almessiere, Y. Slimani, S. Güner, M. Nawaz, A. Baykal, F. Aldakheel, S. Akhtar, I. Ercan, İ. Belenli, B. Özçelik, *Ceram. Int.* 45 (2019) 8222-8232.
- [51] M.A. Almessiere, Y. Slimani, A. Baykal, *Ceram. Int.* 44 (2018) 9000.
- [52] J. Hu, C. Liu, X. Kan, X. Liu, S.Feng, Q. Lv, Y. Yang, W. Wang, M. Shezad, K. Rehman, *J. Alloys Compd.* 820 (2020) 153-180.
- [53] S.M.E. Sayed, T.M. Meaz, M.A. Amer, H.A.E. Shersaby, *Phys. B.* 426 (2013) 137–143.
- [54] K.S. Jithendra Kumara, G. Krishnamurthy, N.S. Kumar, N. Naik, T.M. Praveen, *J. Magn. Magn. Mater.* 451 (2017) 808-821.
- [55] A. R. Kagdi, N. P. Solanki, F. E. Carvalho, S. S. Meena, P. Bhatt, R. C. Pullar, R. B. Jotania, *J. Alloys Compd.* 741 (2018) 377-391.
- [56] C. C. Chauhan, A. R. Kagdi, Rajshree B. Jotania, A. Upadhyay, C. S. Sandhu, S. E. Shirsath, S. S. Meena, *Ceram. Int.* 44 (2018) 17812-17823.
- [57] C. Sudakar, G. N. Subbanna, T.R.N. Kutty, *J. Magn. Magn. Mater.* 263 (2003) 253-268.
- [58] S.M. Mirkazemi, S. Alamolhoda, Z. Ghiami, *J. Supercond. Nov. Magn.* 28 (2015) 1551-1558.
- [59] E.C. Stoner, E.P. Wohlfarth, *Philos. Trans. R. Soc. A Math. Phys. Eng. Sci.* 240 (826) (1948) 599-642,
- [60] Y. Yaffet, C. Kittel, *Phys. Rev.* 87 (1952) 290.
- [61] M. Atif, M. Nadeem, R. Grossinger, R. Sato Turtelli, *J. Alloys Compd.* 509 (2011)

CHAPTER 5:-

SYNTHESIS, STRUCTURE,
THERMAL, MAGNETIC,
DIELECTRIC PROPERTIES OF
Ce³⁺ DOPED M-TYPE SrFe₁₂O₁₉
AND ELECTROCHEMICAL
DETERMINATION OF
L-CYSTEINE

**Published in Journal Inorganic Chemistry
Communications, Elsevier Publication impact factor –
3.428**

5.1 Introduction

Hexaferrites has been shown to be supreme for the best permanent magnetic materials owing to their suitable properties for physical and chemical behaviors in optical, electrical and magnetic in nature [1, 2]. Strontium Hexaferrites (SrHF's) have unique properties including more values of magnetic anisotropy, electrical resistance, Curie high temperature and low dielectric loss. Moreover, they possessed excellent chemical stability and corrosion resistance [3]. SrHF's nanomaterials are much lower electro-conductive than ferro-metallic magnets, assuring suppression of eddy currents and reduced energy loss in higher frequency [4-5]. They have been in a scouting of hexagonal ferrites based on the growing demand for low cost, narrative magnetic compounds with specific adjustable properties for a variety of industrial and technological applications [6], such as micro-electrochemical systems, electricity generation, nanocatalysts [7, 8]. The area of research is more attracted to the researchers from last few decades due to their promising magnetic nanomaterials with appropriate physicochemical properties, functionalized surface and improved biocompatibility have been broadly examined for different restorative, indicative, and remedial applications, for example, magnetic nanofluids (Ferrofluids), specific drug delivery, fluid hyperthermia, as a contrast enhancer in magnetic resonance or reverberation imaging (MRI), cell detachment, tissue fixing, biosensors, and magnetic fluid hyperthermia therapies (MFHT) of cancerous cells in human body. Nano-scaled materials with these attributes are primarily implementable in both the 'in-vitro' and 'in-vivo' bio-applications such as biological imaging (as contrast enhancer). Magnetic nanoparticles are alluring catalyst since they can be isolated from the response medium by applying an outside magnetic attractive field. Magnetic partition is a charming option in contrast to filtration or centrifugation as it keeps the loss of catalyst and upgrades

reusability, rendering the catalyst cost-adequacy and is promising for modern applications [9-12].

Apart from the conventional dopant, rare earth (RE) metal ion dopant such as Dy^{3+} , Sm^{3+} , Eu^{3+} , Ce^{3+} , Nd^{3+} , Gd^{3+} etc., with nominal concentration give rise to radical changes in SrHF's for improving the optical, magnetic and dielectric properties [13-17]. These properties are determined by the anti-ferromagnetic super-exchange interaction between $\text{Fe}^{3+} \leftrightarrow \text{Fe}^{3+}$ ions and the amount of dopant in the SrHF's lattice will induce Re^{3+} - Fe^{3+} interaction with cationic doping, which greatly affects the intrinsic properties of hexaferrite [18-20]. Ce^{3+} is the most prominent inner transition metal used as a dopant in the production of magnetic materials, photocatalyst, dielectric, thermal, electro-chemical and luminescent materials, etc. [21]. In the present investigation, Fe^{3+} magnetic ions are distributed in five sublattices with a hexagonal structure (space group P63/mmc) [22]. 12(k), 2(a) and 2(b) sites exhibit spins (+) direction, but those in the 4(f_1) and 4(f_2) sites exhibit spins (-) direction. The net magnetic moment is comparing between the spin (+) direction and spin (-) direction with magnetic moments [23].

In the case of ferrite, the appearance of the dielectric is due to microstructural factors. The dielectric properties are persistent at high frequencies and depend on variety of factors such as preparation technique, sintering time and temperature, chemical composition types, additive amount, structure of grains and so on. The dielectric properties studies can provide valuable information about potential applications [24]. Impedance spectroscopy is an impressive method for studying the electrical response of grain and grain boundaries in ferrite materials as a function of frequency. Primary information for the dielectric properties of a material can be obtained from complex impedance analysis, which allows to separating various

contributions to total impedance resulting from grain, grain boundaries and other electrode interface effects [25].

Electrochemical techniques have the intrinsic advantages of simplicity, easy of miniaturization, high sensitivity and relatively low cost. Therefore, it is very important to investigate the Electro-chemical behavior and sensitive detection of L-cysteine (Lcys). Several chemically modified electrodes have been proposed to facilitate the detection and oxidation of Lcys [26]. Lcys was most important amino acids that play an importance in biological system, low Lcys concentrations causing, growth retardation in children, gray of hair, edema, damage of liver, muscle and fat are decreases, damaged and weakness of skin. Therefore, the development of simple, rapid and inexpensive methods for the detection of Lys is necessary in physiological and clinical diagnostics. There are three intense functional groups (-COOH, -NH₂, and -SH), which can be easily used to conjugate metal atoms. The proposed sensor is useful for the quality control and routine analysis of Lcys in pharmaceutical formulations [27-28]. Therefore the present study shows the uses of synthesized SrHF's for the electrochemical detection of the Lcys.

Many synthesis methods have been adopted to produce SrHF's such as sol-gel, hydrothermal, solution combustion, micro-emulsion, green synthesis [29] and co-precipitation methods [30-35]. Among these, auto-combustion method with a dual fuel (urea and glycine) is simple and economically feasible reducing agent to obtain nano sized SrFe₁₂O₁₉ ferrite. In addition, the process is simple, the reaction time is short, inexpensive and produce a fine and homogeneous crystalline powder. In view of the above key points, we aimed to prepare Ce³⁺ doped SrFe₁₂O₁₉ nano ferrites (SrHF's) with stoichiometrically amount of chemical composition i.e., Sr_(1-x)Ce_xFe₁₂O₁₉ (with $x = 0.00, 0.01, 0.05$ and 0.09) by auto-combustion method

with dual fuels. The improvement in the structural, thermal, dielectric, magnetic and electro-chemical parameters via influential rare earth metal ion (Ce^{3+}) doping SrHF's was studied by the standard characterization tools.

5.2. Experimental Method

5.2.1. Synthesis and characterization

The samples of $\text{Sr}_{(1-x)}\text{Ce}_x\text{Fe}_{12}\text{O}_{19}$ ($x = 0.00, 0.01, 0.05$ and 0.09) nanoparticles were prepared via auto-combustion method with dual fuel. The small amount of Ce^{3+} ion substituted stoichiometrically to SrHF's of analar grade, the starting chemicals used are: $\text{Sr}(\text{NO}_3)_2$ (Merck), $\text{Fe}(\text{NO}_3)_3 \cdot 9\text{H}_2\text{O}$ (Sigma Aldrich), $\text{Ce}(\text{NO}_3)_3 \cdot 6\text{H}_2\text{O}$ (Sigma Aldrich), glycine ($\text{C}_2\text{H}_5\text{NO}_2$) and urea ($\text{CH}_4\text{N}_2\text{O}$). The petri dish carrying the solution of redox mixture and then placed into heat furnace attained at 600 ± 10 °C. The solution begins to boil in a furnace and heat reduction and ignition at one point, followed by decomposition and generate an amount of gas (N_2O and CO_2). When a solution reaches its self-ignition point, it begins to burn, releasing a large amount of heat and instantly evaporating all the solution, solidifying and burning, forming a fluffy with loose powder. The type of combustion was smoldering, and the actual ignition reaction time was 15-18 seconds. This leads to better product homogeneity by bringing the unreacted particles closer together, which tends to reduce the diffusion distance as well as the particle size distribution. The pristine powder were ground and mixed with a binder polyvinyl pyrolidone (PVP) ($\text{C}_6\text{H}_9\text{NO}$)_n binder and calcinated at for 4 hours at 1000 °C. By applying load of $5 \cdot 10^8$ kg/m² for 5 minutes and powder compressed into pellets. The dimensions of the pellet are 10 mm in diameter and 2-3 mm thickness and sintered at 1100 °C for 3 hours. The furnace is gradually cooled to ambient temperature. The set of all the purity of samples were obtained as a result of

auto-combustion with a mixed fuel, including a rapid exothermic reaction involving metal nitrates, glycine and urea.

The PXRD patterns of $\text{Sr}_{(1-x)}\text{Ce}_x\text{Fe}_{12}\text{O}_{19}$ nanoferrites were captured on a Bruker XRD with $\text{CuK}\alpha$ radiation having wavelength 1.5406 Å (Model: D8 Advance, Germany). In the Bragg angle range of $20^\circ - 80^\circ$ at a scan rate of 2° min at 300 K. Room temperature FTIR spectra of all nanoferrites were recorded by employing Thermo-Nicolet 6700 FTIR (Make: Perkin Elmer, Model: Spectrum Two, USA) in the wavenumber range $4000 - 300 \text{ cm}^{-1}$. The samples (0.5 to 1.0 mg) were mixed with spectral grade potassium bromide (KBr) as the standard ground and then pressed to obtain circular discs of appropriate 1mm thickness. The morphology of sintered pellets was obtained using FESEM (Model: JEOL/EO JSM-639, Germany). The capacitance of the sintered pellets was measured to calculate the room temperature dielectric and impedance parameters using impedance analyzer (Make: HIOKI Model: 3532-50 LCR HiTESTER) in the frequency range of 100 Hz - 5 MHz's. At room temperature, cyclic voltammetry (CV) measurements were performed with a (Model: CHI620E) and the most recent windows based acquisition software. For the electrochemical study, three electrode systems were used GCE as a working electrode (area 0.05 cm^2), saturated Ag/AgCl (saturated KCl) as a reference electrode, and Platinum wire as a counter electrode. Vibrating sample magnetometer (VSM) (Make: CREST, Model: 20130523-01) was employed to characterize the magnetic properties. We have employed TGA (make: NETZSCH, model: STA 2000) for the analysis of thermal behaviors of the prepared samples.

5.3 Results and Discussion

5.3.1 Powder X-ray diffraction studies

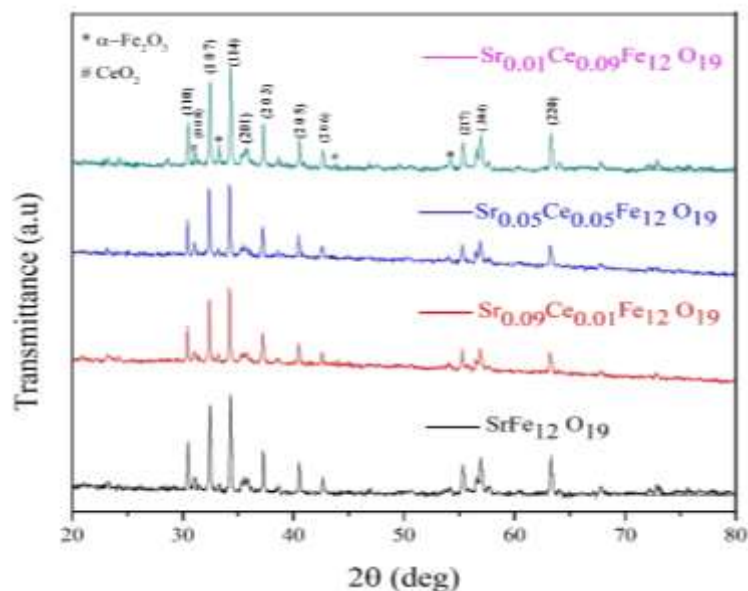


Fig. 5.1 PXRD patterns of $\text{Sr}_{(1-x)}\text{Ce}_x\text{Fe}_{12}\text{O}_{19}$ ($x = 0.00, 0.01, 0.05$ and 0.09) nanoferrites

PXRD analysis were investigated the crystallographic parameters of the $\text{Sr}_{(1-x)}\text{Ce}_x\text{Fe}_{12}\text{O}_{19}$ ($x = 0.00, 0.01, 0.05$ and 0.09) of synthesized by auto-combustion method with dual fuel. The crystallization of all samples were showed magnetoplumbite type hexagonal structure, peaks can be perfectly indexed to the standard M-hexagonal phase (ICSD-00-051-1879) and assuring the purity of the synthesized compounds as showed in fig. 5.1. The two most noticeable peaks are 107 and 114 at 2θ of 32.36 and 34.20. Furthermore, the $x = 0.09$ sample revealed about 5% secondary phase of CeO_2 , with a small percentage of $\alpha\text{-Fe}_2\text{O}_3$ impurity (JCPDS, number 84-1531) [30]. The lattice constant (a and c), cell volume (V_{cell}), and density of x-ray and crystalline size (D) were calculated and tabulated in table 5.1. The lattice parameters a and c are calculated from the value of d_{hkl} corresponds to (008) peak and (107) peak according to the following equation [36].

$$\frac{1}{d_{hkl}^2} = \frac{4}{3} \left[\frac{h^2 + hk + k^2}{a^2} + \frac{l^2}{c^2} \right] \quad (5.1)$$

where, d_{hkl} is the distance between the crystals, a and c are lattice parameters and $(h k l)$ are Miller indices. V_{cell} is the unit of the hexagonal system and is determined as follows: formation of M-type single phase,

$$V_{cell} = 0.866 a^2 c \quad (5.2)$$

where, the numerical values is sustained for the hexagonal system. From, the XRD peaks, an average crystallite sizes of the nanoferrites are determined using Debye-Scherrer equation (d) and is calculated by:

$$d = \frac{k\lambda}{\beta \cos\theta} \quad (5.3)$$

where, $k = 0.89$ is Scherer's constant, $\lambda = 0.15406$ nm is wavelength of the incident X-rays in nm, β is the full width at half maximum (FWHM) of diffraction peak, θ is the Bragg diffraction angle [36]. The average value of crystallite size is found in the range 42 - 46 nm and values are tabulated in table 5.1. The theoretical X-ray density (d_x) of each sample is calculated using the formula

$$d_x = \frac{ZM}{NV} \quad (5.4)$$

where $Z = 2$ is number of molecules per unit cell, M is the molecular weight, N is the Avogadro's number and V - volume of the unit cell.

According to the XRD results, the Sr^{2+} ion with a larger ionic radius (0.112 nm) was substituted with a Ce^{3+} ion with a smaller ionic radius (0.1034 nm), the lattice constant increases moderately from 0.58847 - 0.58798 nm, because their shrinkage of unit cell. The values of "a" and "c" decreases with increase in Ce^{3+} ion substitution, since V_{cell} depends on "a" and "c", a similar trend was observed in the variation. This can be explained by the interaction of microstructural defects and

substituted cations [37, 38]. It reveals that the ratio of c/a of all the prepared samples is less than 3.98. Therefore, it reveals the material is hexaferrite structure [39, 40]. The density of x-ray range between 4.73 and 5.10 g cm⁻³.

Table 5.1: Crystallite size (D), lattice constant (a & c), cell volume (V) and X-ray density (q_{x-ray}) of Sr_(1-x)Ce_xFe₁₂O₁₉ ($x = 0, 0.01, 0.05$ and 0.09) nanoferrites.

Composition	Crystallite size (D) /nm	Lattice constant (a)/Å	Lattice constant (c)/Å	(c)/(a) Å	Cell volume (V)/Å ³	X-ray density (dx) /g cm ⁻³
SrFe ₁₂ O ₁₉	45.54	5.8847	23.0552	3.918	691.4	5.10
Sr _{0.09} Ce _{0.01} Fe ₁₂ O ₁₉	43.84	5.8835	23.0534	3.920	690.9	4.73
Sr _{0.05} Ce _{0.05} Fe ₁₂ O ₁₉	43.57	5.8823	23.0502	3.919	690.6	4.74
Sr _{0.01} Ce _{0.09} Fe ₁₂ O ₁₉	42.86	5.8798	23.0493	3.919	690.1	4.75

5.3.2 FTIR studies

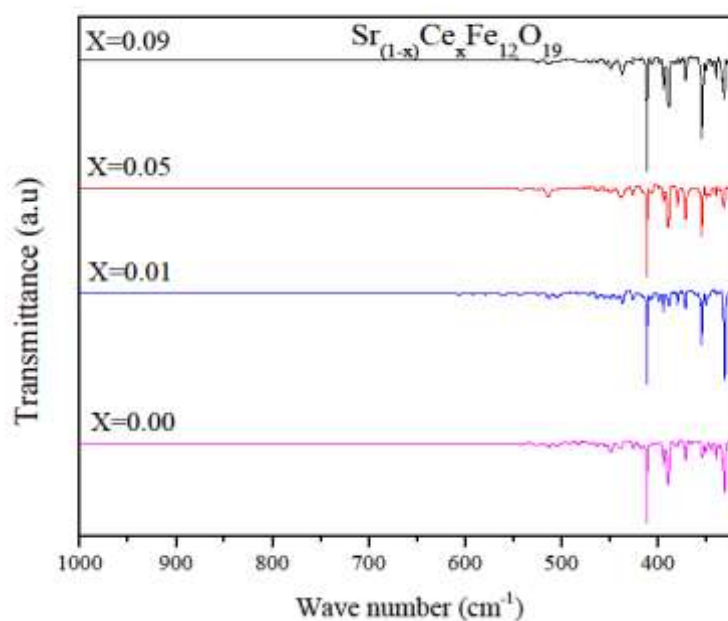


Fig. 5.2 FT-IR spectra of Sr_(1-x)Ce_xFe₁₂O₁₉ ($x = 0.00, 0.01, 0.05$ and 0.09) nanoferrites

FTIR spectroscopy is a characterization tool with this help the presence of functional groups which are the residue of the precursors utilized during the synthesis are determined. In fig. 5.2, it is observed that two strong characteristic absorption bands in the range $300 - 1000 \text{ cm}^{-1}$, which are assigned to the intrinsic vibrations of tetrahedral and octahedral positions in the M-hexagonal lattice. The absorption band in the region $408 - 410 \text{ cm}^{-1}$ and $310 - 312 \text{ cm}^{-1}$ corresponds to intrinsic vibrations of tetrahedral and octahedral positions respectively [41]. These observations confirmed the formation of an M-type SrHF's structure. The no absorption band appeared in the region $3200 - 3500 \text{ cm}^{-1}$ indicates the absence of an OH group/moisture in the synthesised samples and confirming the completion of the reaction [42].

5.3.3 Morphological studies

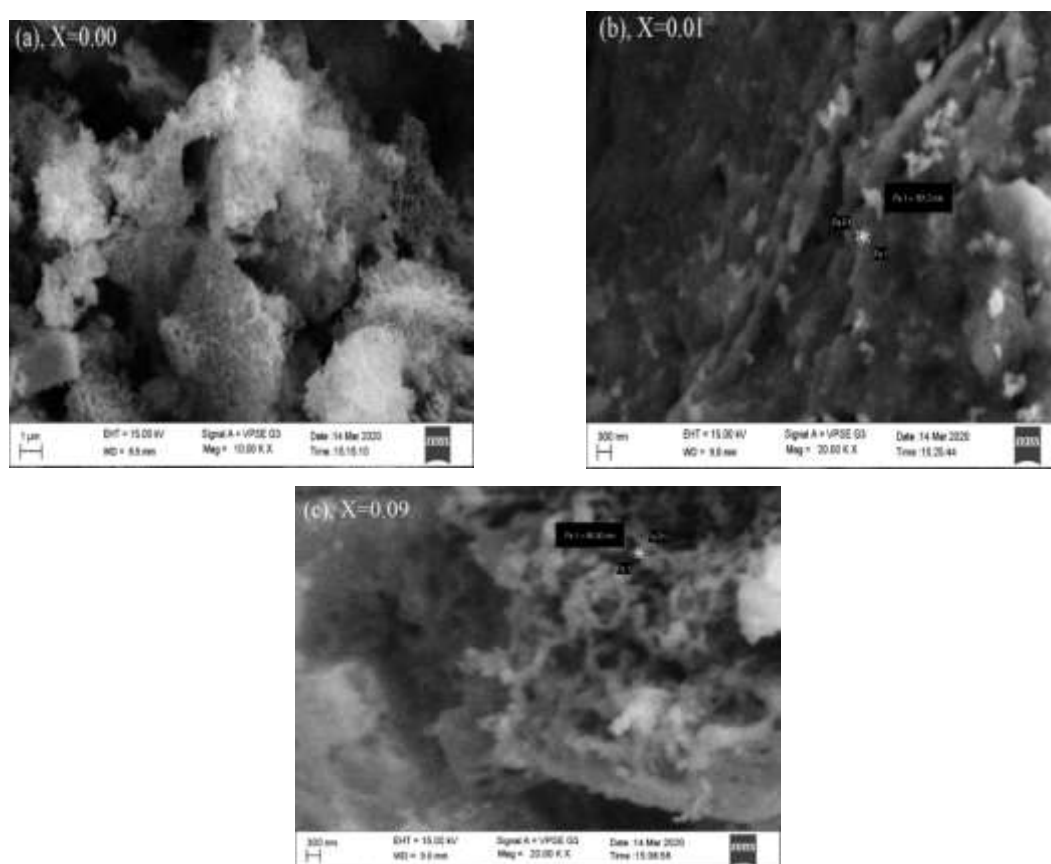


Fig. 5.3 SEM Micrographs of $\text{Sr}_{(1-x)}\text{Ce}_x\text{Fe}_{12}\text{O}_{19}$ ($x = 0.00$ (a), 0.01 (b) and 0.09 (c)) nanoferrites

The SEM micrographs in fig. 5.3 (a, b and c) confirmed the complete morphology of nanostructured ferrite formation. It is clearly evident that the particles have hexagonal aggregations produced from large groups of particles, leading to agglomeration and overlap between these particles [43]. Moreover, the average particle size of the sample can be estimated as 70-95 nm. It is observed that particle size tends to increase with increasing dopant content [44]. The chemical proportions of the samples, $\text{Sr}_{(1-x)}\text{Ce}_x\text{Fe}_{12}\text{O}_{19}$ ($x = 0.00, 0.01, 0.05$ and 0.09) are recorded using Energy dispersive X-ray analysis (EDAX) and are shown in fig 5.3. The spectra indicate the presence of Sr, Fe, Ce and O atoms and their elemental composition with high crystallinity. The greater crystallinity of SrM-HF's is due to auto-combustion method in dual fuel reaction with prolonged time span and high temperature produces rapid crystal growth leading to nucleation of nanoparticles.

5.3.4. Thermal studies

The investigations of TGA for the development process of as prepared pure nano-hexaferrites $\text{Sr}_{(1-x)}\text{Ce}_x\text{Fe}_{12}\text{O}_{19}$ ($x = 0.00, 0.01, 0.05$ and 0.09) sample was studied from 25 °C to 1000 °C as appeared in fig 5. 4 (a, b, c and d). Thermogravimetric data analysis of the $\text{SrFe}_{12}\text{O}_{19}$ sample produced via auto-combustion method with dual fuel technique was performed under an nitrogen atmosphere with heating rate 10 °C/min [36]. TGA results revealed that the elimination of H_2O , breakdown of metal hydroxide and development of hexagonal ferrite can be completely performed below 650 °C.

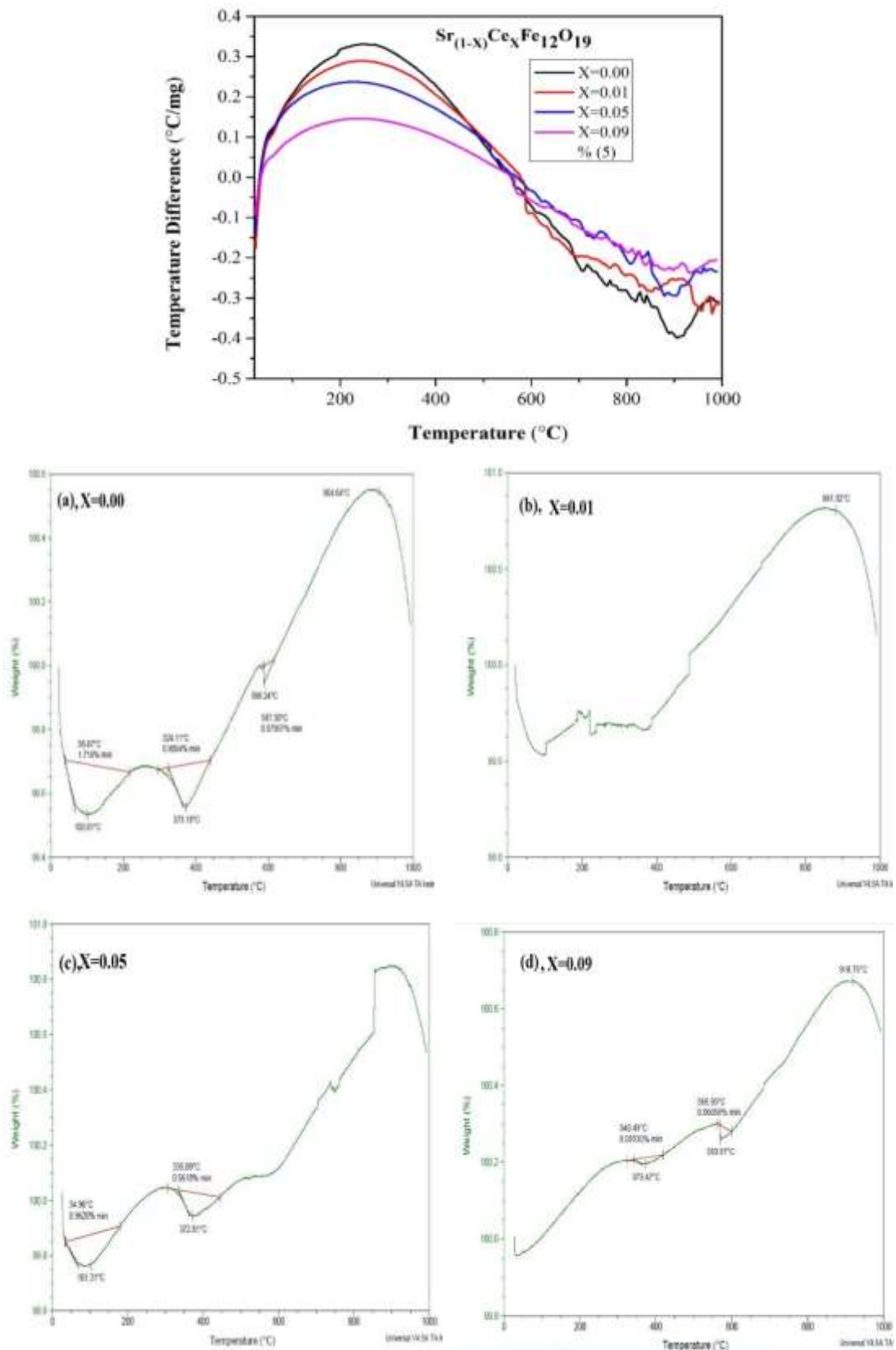


Fig 5.4 (a, b, c and d) TG-DTA curves of Sr_(1-x)Ce_xFe₁₂O₁₉ (x = 0.00, 0.01, 0.05 and 0.09) nanoferrites

In TGA plot, the preliminary weight loss of ~ 2% displays the elimination of moisture at 105 °C. The second weight loss of ~ 1% indicates the decomposition of nitrates at 340 °C with corresponding exothermic peak at 380 °C observed in DTA curve. The third weight loss of ~ 1% indicates the establishment of ferrite nanoparticles at 570 °C. The total weight loss in SrFe₁₂O₁₉ nanoparticles was completely performed below 600 °C. Above 600 °C no noteworthy weight loss and heat loss observed, indicating the phase formation of ferrite crystals [45]. Therefore, all the produced solids were calcinated at ~ 1000 °C for 4 hours in high-temperature muffle furnace and exploited for intended investigations.

5.3.5. DIELECTRIC STUDIES

5.3.5.1 Dielectric constant

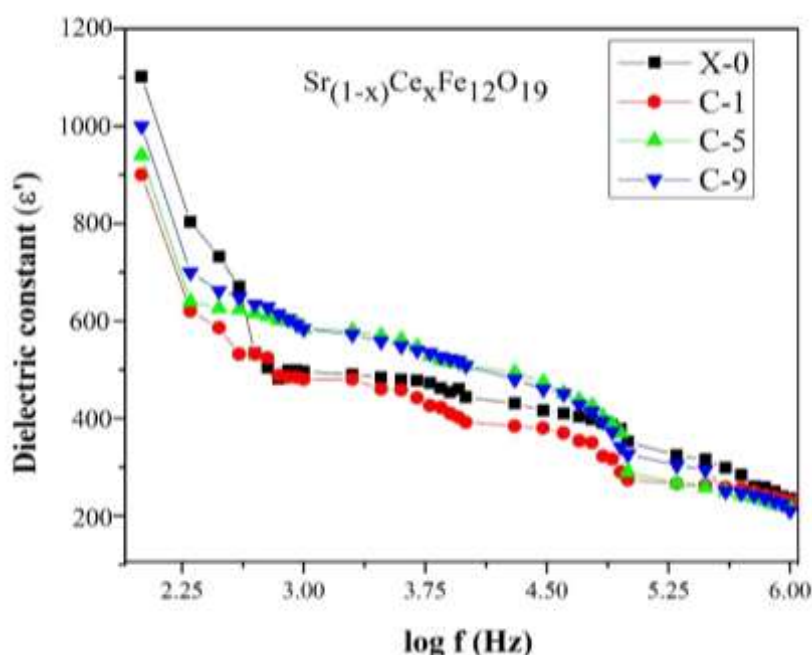


Fig 5.5 Dielectric constant of Sr_(1-x)Ce_xFe₁₂O₁₉ ($x = 0.00, 0.01, 0.05$ and 0.09) nanoferrites

The dielectric constant symbolizes the storage capability of dielectric energy. The variation in the ambient temperature dielectric constant (ϵ') with frequency of the

applied field is showed in fig 5.5. From the fig 5.5, at lower frequencies, it is observed that the dielectric constant decreases sharply with increasing frequency and remains almost constant at higher frequencies. According to the Koop's phenomenological theory the variation discloses the dispersion [46], Maxwell-Wagner caused by space charge polarization [41, 47]. In ferrites, the local displacement of electrons in the direction of the applied electric field is attributed to exchange of electrons ($\text{Fe}^{2+} \leftrightarrow \text{Fe}^{3+}$ ions) at B-sites, which leads to interfacial polarization in the lower frequency range. According to Rabinkin and Novikova, the conduction and polarization mechanisms in ferrites are strongly correlated [48]. In addition, Fe^{2+} ions formed during in the sintering of ferrite under moderately reducing conditions result in highly conducting grains, and it is feasible for low conducting layers (grain borders) to occur during the cooling of ferrite in an O_2 environment [49]. Due to which interfacial polarization occur as a result of this, a limited concentration of Fe^{2+} ions under the applied field. The values of dielectric constant, ac conductivity of all the samples have been calculated using relations [50].

The dielectric constant

$$\epsilon' = Cd / \epsilon_0 A \quad (5.5)$$

The ac electrical conductivity evaluated from the dielectric data

$$\sigma_{ac} = 2\pi f \epsilon_0 \epsilon' \tan\delta \quad (5.6)$$

where ϵ' is dielectric constant, C is the capacitance of the dielectric sample holder loaded with sample (pF), d is the thickness of the pellet (cm), A is area of active electrode surface of the sample holder (cm^2) and ϵ_0 is the free space permittivity (8.854×10^{-14} pF/cm), f is the frequency of the applied electric field (Hz), ϵ' is the dielectric constant and $\tan\delta$ is dielectric loss tangent. The dielectric constant in Ce^{3+} ion substituted in the place of Sr^{3+} ions, the dielectric constant at lower

frequencies is contributing to the strong influence of species such as Fe^{2+} ions, interfacial dislocation clusters, oxygen vacancies and grain boundary defects [41]. The low dielectric constant values observed were due to homogeneity, improved symmetry, uniformity and small grain size [51]. Furthermore, polarization decreases with increasing frequency and reaches a constant value above a certain frequency owing to electron exchange ($\text{Fe}^{3+} \leftrightarrow \text{Fe}^{2+}$) cannot take place and lag behind the direction of applied field at higher frequencies [52].

5.3.5.2 Dielectric loss

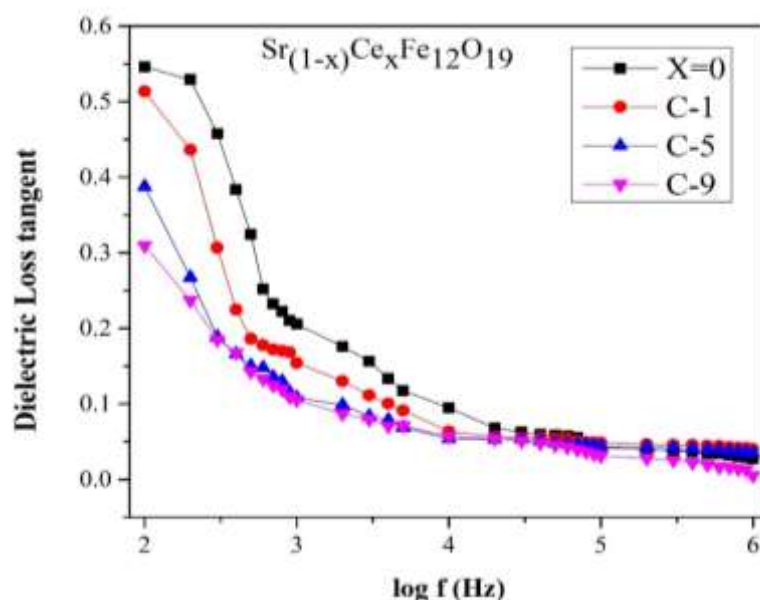


Fig 5.6 Dielectric Loss Tangent of $\text{Sr}_{(1-x)}\text{Ce}_x\text{Fe}_{12}\text{O}_{19}$ ($x = 0.00, 0.01, 0.05$ and 0.09) nanoferrites

The dielectric loss tangent ($\tan \delta$) represents the electrical energy loss within the dielectric material at various frequencies, which accounts for a significant portion of the total loss in the core of the ferrite. The value of dielectric losses of the studied samples is very low. Therefore, investigated samples are desirable for low core loss devices [53]. For all compositions, fig 5.6 depicts the variation of the room temperature dielectric loss ($\tan \delta$) tangent with frequency of the field. It has been found that the Maxwell-Wagner polarization induces the dielectric loss to decrease as

frequency increases, as a result Ce^{3+} ion substituted to Sr^{3+} ion concentration. The low conductivity of the grain boundaries caused by the high value of $\tan\delta$ at lower frequencies results in a greater loss because of Fe^{2+} and Fe^{3+} ion electron exchange requires more energy. A small amount of energy is essential for the electron hopping between Fe^{2+} and Fe^{3+} ions in the higher frequency range, leading to reduced energy loss [54]. The values of $\tan\delta$ depend on the composition of the substances, stoichiometry, structural uniformity, sintering duration and content of ferrous ion [55].

5.3.5.3 AC Conductivity studies

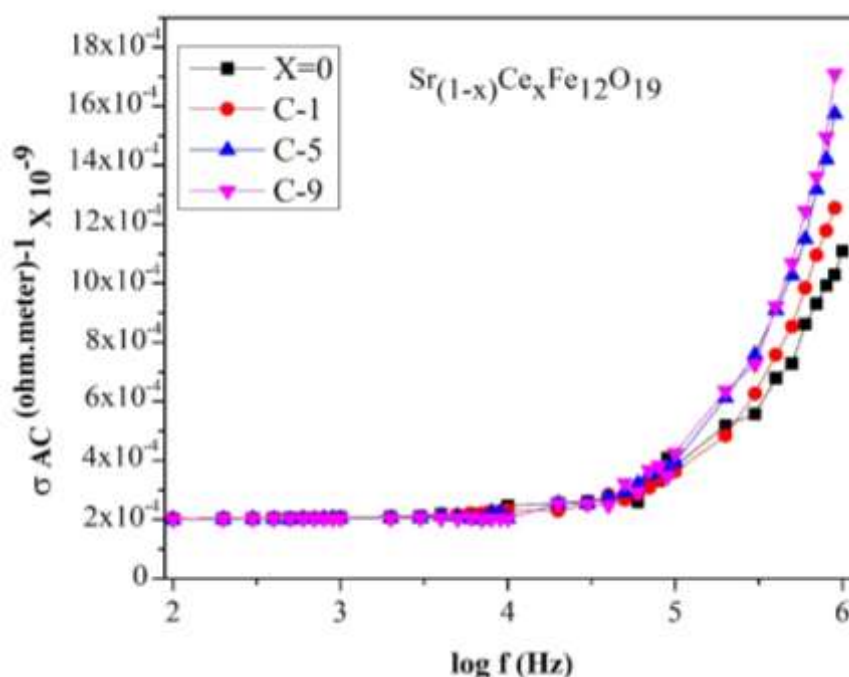


Fig 5.7 AC Conductivity studies $\text{Sr}_{(1-x)}\text{Ce}_x\text{Fe}_{12}\text{O}_{19}$ ($x = 0.00, 0.01, 0.05$ and 0.09) nanoferrites

AC measurements were useful tool for investigating the dynamic characteristics of semiconductor and dielectric materials. The variation of room temperature $\ln\sigma_{ac}$ with $\log f$ as showed in the fig 5.7. It is observed that the AC electrical conductivity increases gradually with increase in frequency of the applied electric field. It reveals that AC conductivity is directly proportional to angular

frequency [56]. The conduction mechanism in ferrites is due to electron exchange between $\text{Sr}^{2+} + \text{Fe}^{3+} \leftrightarrow \text{Fe}^{2+} + \text{Sr}^{3+}$ ions at adjacent tetrahedral sites. The phenomenon can be explained using the two-layer Maxwell-Wagner model in ferrites. The first layer is of relatively well conducting grains (Fe^{2+} ions) which are separated by thin and low-conducting grain boundaries [57]. At lower frequencies, the grain boundaries are more active and reduces the electron hopping frequency between Fe^{2+} and Fe^{3+} ions. At higher frequencies, the conductive grains become more active, facilitating electron hopping between Fe^{2+} and Fe^{3+} ions, thereby increasing the hopping frequency. Therefore, AC electrical conductivity increases with increase in frequency [57]. The plot is nearly linear at very high frequencies, confirming conduction by the small polaron hopping of ferrite. The dielectric constant is precisely proportional to the square root of conductivity for ferrites [58].

The Verwey and de-Boer mechanism reveals that conduction in $\text{SrFe}_{12}\text{O}_{19}$ ferrites is due to electron exchange between ions of the same element of multiple valence states. In case of Ce^{3+} ions substitution for Sr^{2+} ions, the number of Fe^{3+} ions on B-sites enhanced, leads to electron exchange at the B-sites, an increase the dielectric constant. However, increasing the substitution of Ce^{3+} ions decreases the concentration of Fe^{3+} ions, lowering the intensity of dielectric relaxation [59]. Thus the number of Fe^{2+} ions at B-site influences both conduction and dielectric polarization. Therefore, in samples with lower Ce^{3+} content, the conduction mechanism is primarily due to the electron exchange between Sr^{3+} and Sr^{2+} ions. In case of higher Ce^{3+} ion composition, the conduction mechanism is due to electron exchange from Fe^{2+} to Fe^{3+} ions at B-sites. The magnitude of the electron exchange interaction between Fe^{2+} to Fe^{3+} is proportional to the concentration of $\text{Fe}^{2+}/\text{Fe}^{3+}$ ions [60].

5.3.5.4 Impedance spectroscopy

Impedance spectroscopy is an important method for studying the electrical properties of ferrites on the basis of separation of the grain impedance from other impedance sources such as electrode impedance and grain boundaries. The impedance depends on the microstructure of the nano ferrites. The frequency dependence of impedance provides the source about the resistance (real part) and reactive (imaginary part) parameters of investigated complex electrical nano material [61].

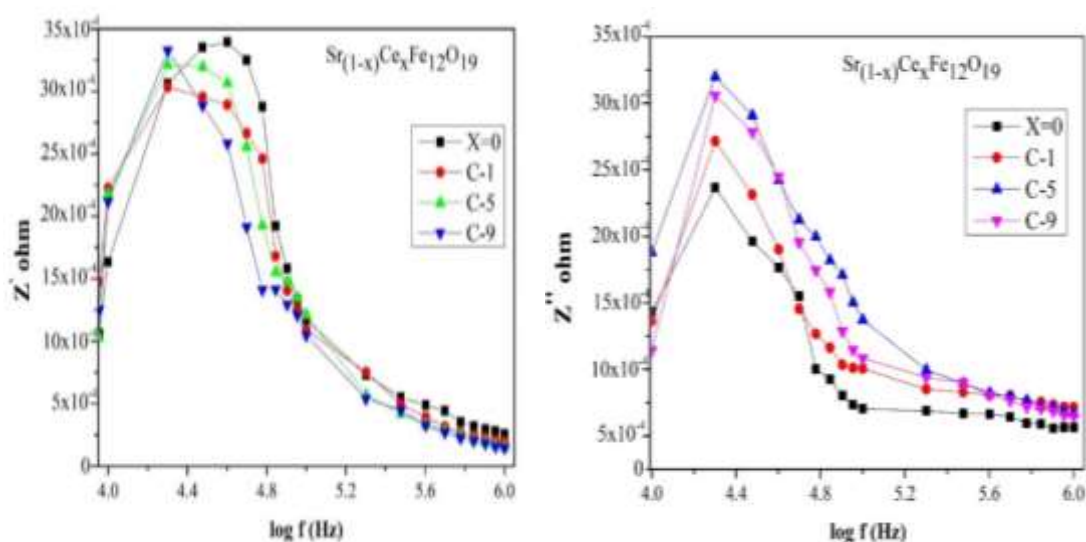


Fig 5.8 and 5.9 Real part and Imaginary part impedance of $\text{Sr}_{(1-x)}\text{Ce}_x\text{Fe}_{12}\text{O}_{19}$ ($x = 0.00, 0.01, 0.05$ and 0.09) nanoferrites

Fig 5.8 and 5.9 shows the variation in impedance of real (Z') and imaginary (Z'') at room temperature with frequency from 100 kHz to 10 MHz. Based on an examination of impedance spectra. On incorporation of Ce^{3+} ions for Sr^{2+} ions, the values of Z' and Z'' decrease continuously with increase in the frequency. Moreover, the peaks are appeared and attain constant value at higher frequencies. The decrease in the real part of impedance Z' with frequency causes increase in the AC conductivity at higher frequencies due to the influence of space charge polarization in the

materials. The peaks at lower frequencies in the imaginary part of complex impedance (Z'') attributed to space-charge relaxation, depends on charge carriers in oxygen vacancies [62]. The peaks at lower intensity in Ce^{3+} ion substituted nanoferrites are observed that is similar to the variation of real and imaginary impedance with Sr^{2+} ion content in dielectric measurements. It is shown that the position of peak intensity shifting towards higher frequencies.

5.3.6 Magnetic measurements

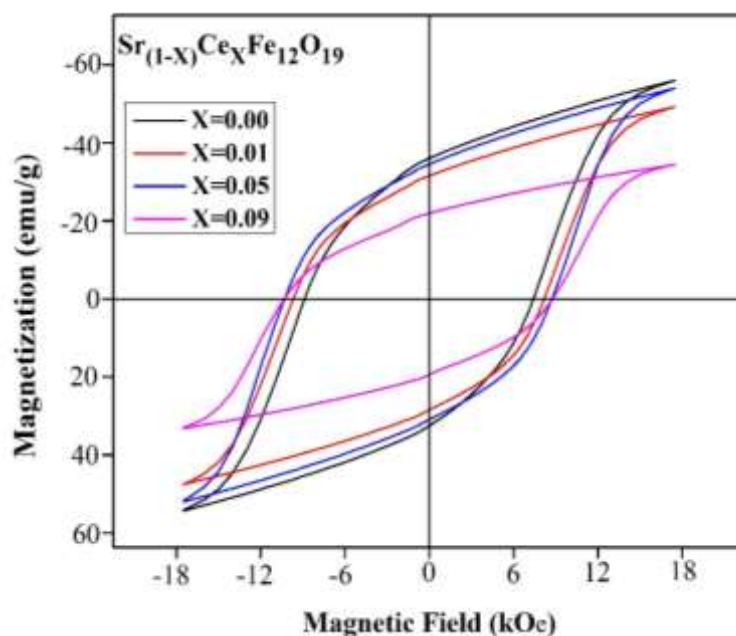


Fig 5.10 Hysteresis curves of $\text{Sr}_{(1-x)}\text{Ce}_x\text{Fe}_{12}\text{O}_{19}$ ($x = 0.00, 0.01, 0.05$ and 0.09) nanoferrites

The M-H curves of $\text{SrFe}_{12}\text{O}_{19}$ particles investigated using vibrating sample magnetometer at room temperature under an applied field of 70 kOe is shown in fig 5.10. The nano-hexaferrites samples exhibit hysteresis nature which confirms the presence of ferromagnetic ordering in all the samples. The variations of the saturation magnetization (M_s), coercive field (H_c), remanence magnetization (M_r), and squareness ratio (M_r/M_s) of the nano-hexaferrites $\text{Sr}_{(1-x)}\text{Ce}_x\text{Fe}_{12}\text{O}_{19}$ ($x = 0.00, 0.01,$

0.05 and 0.09). The magnetic parameters were calculated using the following relationship and listed in table 5.2.

$$\eta_{\beta} = \frac{M \times M_S}{5585} \quad (5.7)$$

$$S = \frac{M_r}{M_s} \quad (5.8)$$

$$K = \frac{H_C \times M_S}{0.64} \quad (5.9)$$

Where n_B is the magnetic moment / formula unit in μ_B , M_s - saturation magnetization (emu/g), M_r - remanence magnetization, M - molecular weight in g, 5585 - magnetic factor, k - magnetic anisotropic constant and H_c - coercivity. The Fe^{3+} ions that occupy the five different sub-lattices from a unit cell of $SrM-HF$'s, Fe^{3+} in the 12k, 2a and 2b sites exhibit spins-upward direction, but those in the $4f_1$ and $4f_2$ sites exhibit spins-downward direction. The unit cell of the net magnetic moment is comparing between the spin- upward direction and spin- downward direction with magnetic moments. According to Neel, the calculated magneton number is given by $M_S = M_B - M_A$ where, M_B is the magnetic moment of the cation at position B (octahedral) and M_A is the magnetic moment of the cation at position A (tetrahedral). To calculate M_B and M_A the possible cation distribution of the current system, M decreases with the replacement of B-site [63-65]. The substitute for the Fe^{3+} ion preferably occupies the B-site. The magnetic moment of Ce^{3+} ions is greater than that of the Fe^{3+} ions. As the amount of Fe^{3+} -O- Fe^{3+} super-exchange interactions decreased at sites-B, the magnetization of sublattice-B decreased. However, if substitution ions replace Fe^{3+} ions at the sites of downward spin site, the net magnetic moment increases [66]. The magnetic moment of the strontium ion decreased with the increasing of the Ce^{3+} ions, this action for this increase in value is due to the increasing of the super exchange interaction between the different sites, leading to an increase in the values (13.68 – 8.26 μ_B). This indicates the increasing of the super-

exchange interactions. Magnetization values of the $\text{SrFe}_{12}\text{O}_{19}$ samples are decreased from for M_s 72.26 emu/g - 43.62 emu/g with increase of the Ce^{3+} ion content [67]. M_r in the range of 43.98- 26.12 emu/g at room temperature. H_c is in the scope of 9753 - 8275 Oe at room temperature. This reduction is associated with the equivalent reduction of Fe^{3+} ions to charge-compensating Fe^{2+} ions replacing Ce^{3+} ions replace of Sr^{2+} ions. Moreover, the magnetic moment of Fe^{2+} ions (4 μB) is lower than that of the Fe^{3+} ions (5 μB) [66, 68].

The variation of M_s and M_r with respect to the concentrations of the Sr^{2+} ion site of cerium ion substitution. In addition, Ce^{3+} substituted ions occupy the spins-up sites. The contrast of these ionic radii can cause strains that cause variations in electronic states and disorder in hexaferrite systems [66, 69]. Another possible substitute for the reduction of M_s and M_r is the spin tilt. If we increase the Ce^{3+} ion to strontium ion, the electron spin deviates from collinear by a specific angle called spin tilt [70]. The squareness ratio values are observed in the scope of 0.61–0.62 emu/g, shows that all the synthesized nanohexaferrites investigate the nature of a single magnetic domain.

In addition, variants of could explain the variations of the magnitudes of M_s for their relationship between η_B and M_s . Moreover, this suggests that the observed non-interacting and anisotropic particles are of the cubic anisotropy type. The anisotropy of decreasing $\text{SrFe}_{12}\text{O}_{19}$ with the increase of Ce^{3+} ions is due to the reduced particle size values are found to be 1.12 - 0.68 (erg/Oe). Therefore, the surface spin causes an increase in the coercivity ratio and the surface layer because the anisotropy increases with increasing Ce^{3+} ions due to the duel fuel. In this investigation, the coercive value decreases as the Ce^{3+} ion content increases. The coercive force obtained by reversing the direction of movement of the wall and that of rotation of the province to change the opposite direction of the applied magnetic field [71, 72]. In

generally, effective clamping of the domain walls leads to coercivity, consequently a larger grain size H_c decreases. Smaller particle size materials were used to achieve high core loss. The H_c is mainly determined by the magnetocrystalline anisotropy and by typical particle size the variations of H_c and particle size are inversely proportional.

Table 5.2: Magnetic properties i.e. coercivity (H_c), saturation magnetization (M_s), remanence (M_r), squareness ratio (M_r/M_s), anisotropy (K), and Magnetic moment ($\eta\beta$) of $\text{Sr}_{(1-x)}\text{Ce}_x\text{Fe}_{12}\text{O}_{19}$ ($x = 0.00, 0.01, 0.05$ and 0.09) nanoferrites.

Composition	M_s (emu/g)	H_c (Oe)	M_r (emu/g)	S (emu/g)	$\eta\beta$ (μB)	K (erg/Oe)
$\text{SrFe}_{12}\text{O}_{19}$	72.26	9753	43.98	0.62	13.68	1.12
$\text{Sr}_{0.09}\text{Ce}_{0.01}\text{Fe}_{12}\text{O}_{19}$	66.44	9682	39.59	0.61	12.43	1.03
$\text{Sr}_{0.05}\text{Ce}_{0.05}\text{Fe}_{12}\text{O}_{19}$	47.73	9351	29.63	0.62	9.27	0.75
$\text{Sr}_{0.01}\text{Ce}_{0.09}\text{Fe}_{12}\text{O}_{19}$	43.62	8275	26.12	0.62	8.26	0.68

5.3.7 ELECTROCHEMICAL CHARACTERIZATION

5.3.7.1. Charge transfer behavior of SrHF's electrode

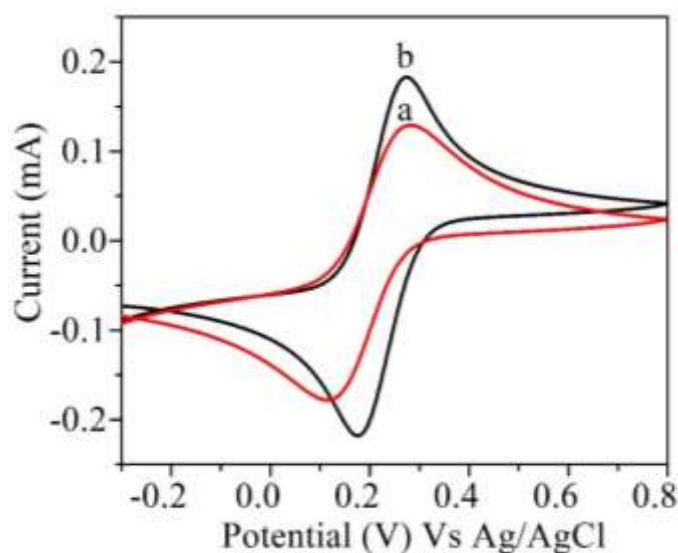


Fig 5.11 CVs of 0.5 M KCl solution containing 5 mM $\text{K}_3[\text{Fe}(\text{CN})_6]$ / $\text{K}_4[\text{Fe}(\text{CN})_6]$ at the GCE (a) and SrHF's -GCE (b) Scan rate: 50 mV s^{-1} .

Fig 5.11. The charge transfer behaviour of the SrHF's electrode was investigated using $K_4[Fe(CN)_6]$ as a redox probe. The bare glassy carbon electrode (GCE) exhibits the expected ferri/ferrocyanide cyclic voltammetric response, whereas the SrHF's electrode exhibits a faster and more proficient electron transfer rate than the bare glassy carbon electrode and comparison of different sensors for L-Cysteine determination as shown in Table 5.3. This is due to the higher surface area of SrHF's composite GCE, which decreases the ΔE separation between oxidation and reduction peak potentials as peak currents increase and it also behaves as a good transfer of electrons between phosphate buffer solution and GCE [73].

Table 5.3: Comparison of different sensors for L-Cysteine determination.

Sensor	Linear range (μmolL^{-1})	LOD (μmolL^{-1})	Sensitivity ($\mu\text{A}\mu\text{M}^{-1}\text{cm}^{-2}$)
OMC/GCE	18-2500	0.002	23.6
Co(II)-salophen-GCE	10-2	1	-
CoPc-SPE	2.6-200	4	0.78
SPE/PEDOT	0.05–200	0.03	0.0527
CoTBrImPc	0.01-0.1	0.03	0.0029
SrHF's/GCE	0.5-1.2	0.166	6.638

5.3.7.2. Electro-catalytic oxidation of L-Cysteine on the SrHF's /GCE

A cyclic voltammogram curve fig 5.12 was optimized SrHF's electrode towards different concentration of L-cysteine (Lcys) was obtained using CVs at the buffer solution pH (7.0), over the potential range 0.5 V to 0.7 V. The increasing anodic current of L-cysteine at the surface SrHF's electrode was linearly related to the concentration of L-cysteine. The calibration graph was linear in the range of 0.5-12 μM with a coefficient of correlation was 0.9899, the limit of detection was

0.166 M as showed in (Figs. 10 a and b), and the sensitivity value is $6.638 \mu\text{A}/\mu\text{M}$, indicating that the SrHF's sensor can be easily applied for the L-cysteine identification.

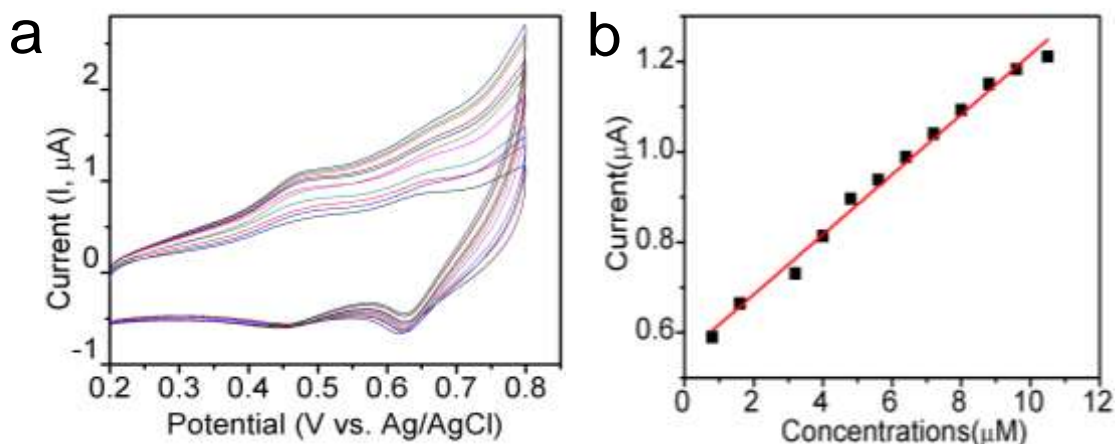


Fig 5.12 (a) Cyclic voltammogram of L-cysteine at SrHF's /GCE concentration ranging from (0.5–12 μM). (b) Inset: Calibration plot of current Vs concentration.

We investigated the stability of the SrHF's electrode compared with the Lcys catalytic anode in the cyclic voltametric characterization by restoring the addition of Lcys in the solution. The standard addition method was used to determine the amount of Lcys added. table 5.3 showed that the information about the data obtained that have been used several times in the analysis of Lcys.

5.3.7.3. Effect of scan rate

The cyclic voltammogram profile (fig 5.13.a) of 12 μM L-cysteine in PBS solution was measured at various scan rates using SrHF's electrode ($10\text{-}100 \text{ mVs}^{-1}$). It was discovered that increasing the scan rate increased the oxidation peak current. The plot of oxidation peak current vs square root of scan rate signifies that L-cysteine oxidation on SrHF's / GCE is a diffusion controlled process [74], with a linear regression line of $I = .066v - 0.513$ and a coefficient of correlation of 0.9878 has been showed in (fig 5.13 b & c) [75].

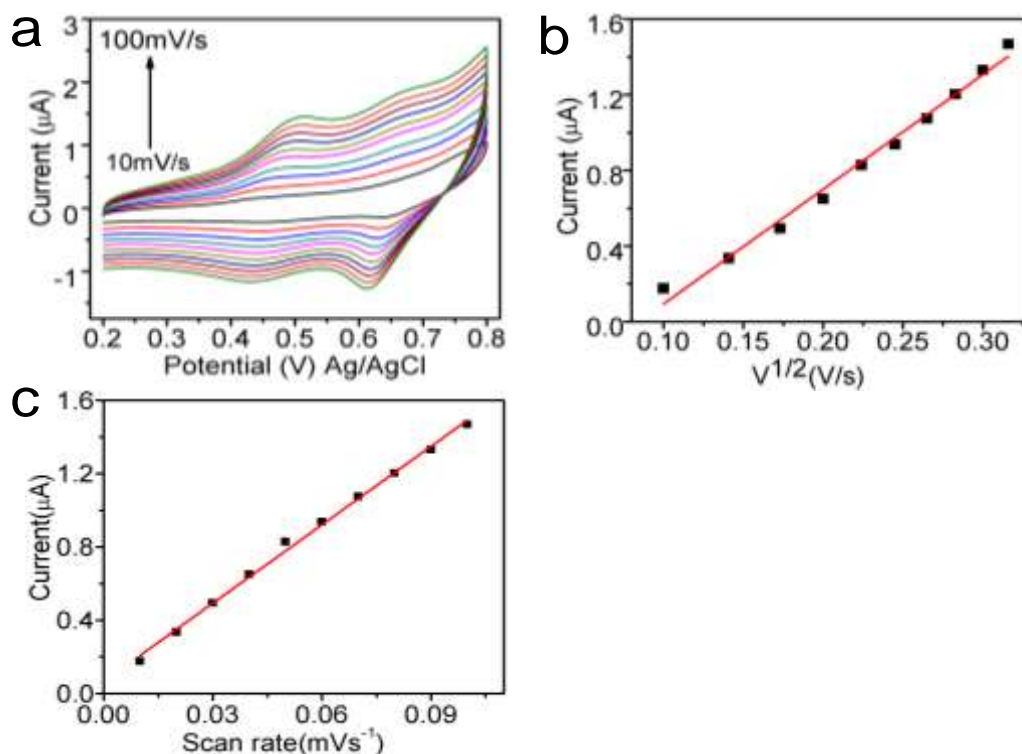


Fig 5.13. (a) Cyclic voltammogram of L-cysteine at SrHF's /GCE scanning rate ranging from (10 mV⁻¹ to 100 mVs⁻¹). (b) The plot of current (I) vs. $v^{1/2}/mV^{1/2}s^{-1/2}$. (c) Inset: Calibration graph of peak current vs scan rate

5.3.7.4. Electrode stability and reproducibility

The stability of the sensor was tested by immersing it in phosphate buffer solution for 72 hours, then evaluating its response to L-cysteine. It is oxidized at the same potential and the current response was observed in comparison to that achieved using freshly prepared sensors, indicating that the electrode had a stable response. This electrode has been shown to be stable even after two weeks of storage in dry conditions. In addition, the reproducibility of this electrode's response was determined by three subsequent voltammetry analyzes of L-cysteine. The percentage of RSD in these experiments was 2.75 (n=3, L-cysteine concentration = 10 μM), suggesting that the fabricated sensors are reproducible (2.1%).

5.4 Conclusions

A series of nanoferrites, $\text{Sr}_{(1-x)}\text{Ce}_x\text{Fe}_{12}\text{O}_{19}$ ($x = 0.00, 0.01, 0.05$ and 0.09) were successfully synthesized by auto-combustion method with dual fuel (urea and glycine). PXRD, FT-IR, FE-SEM and EDAX confirmed the formation of crystalline nanoparticles with a single-phase magnetoplumbite hexagonal structure. The average crystallite size was found in the range of 42 - 46 nm. The dielectric parameters decreases while AC conductivity increases with frequency. At a particular frequency, the dielectric constant, dielectric loss real part and imaginary part of impedance increases, attain maximum, then begins to decrease with increase in composition. M-H curves were measured at room temperature, it confirmed that these are hard magnetic particles and the values of magnetic parameters decreases as the cerium ion concentration increases. The data showed that the Ce^{3+} doping on $\text{SrFe}_{12}\text{O}_{19}$ induces super exchange interaction, noncollinear three sub-lattice model and single domine particle structure. The electro-catalysis of the $\text{SrHF}'\text{s}/\text{GCE}$ was investigated via cyclic voltammetric technique by using drop-coat method. The results indicated that $\text{SrHF}'\text{s}/\text{GCE}$ is efficient towards the detection of L-cysteine at different concentration.

5.5 Reference

- [1] K. K. Mallick, P. Shepherd, R. J. Green, *J. Eur Ceram Soc.* 27 (2007) 2045–2052.
- [2] H. Pfeiffer, R. W. Chantrell, P. Gornert, W. Schuppel, E. Sinn and M. Rosler, *J. Magn Magn Mater.* 125 (1993) 373– 376.
- [3] P. Kuru, P. R. Matli, B. Mohammad, S. Reddigari, S. Katlakunta, *J. Magn Magn Mater.* 382 (2015) 172–178.
- [4] K. Kamishima, T. Mashiko, K. Kakizaki, M. Sakai, K. Watanabe, H. Abe, *AIP. Adv.* 5 (2015) 107132.
- [5] S. P. Dalawai, T.J. Shinde, A. B. Gadkari, *J. Elec. Mater.* 46 (2017) 1427–1438.
- [6] K.S. Jithendra Kumara, G. Krishnamurthy, N. S. Kumar, N. Naik, T. M. Praveen, *J. Magn Magn Mater.* 451 (2017) 808-821.
- [7] M. A. Malana¹, R. B. Qureshi¹, M. N. Ashiq, M. F. Ehsan, *Ceram. Int.* 42 (2016) 2686–2692.
- [8] K. S. Jithendra kumara, G. Krishnamurthy, B. E. Kumara swamy, N. D. Shashi kumar, S. Naik, B. S. Krishna and N. Naik, *App Organ Chem.* 31 (2016).
- [9] P. B. Kharat, A.V. Humbe, J. S. Kounsalye. *J Supercond Nov Magn* 32 (2019) 1307-1317.
- [10] P. B. Kharat, B. Sandeep. Somvanshi, P. Pankaj. Khirade, and K. M. Jadhav. *ACS omega.* (2020)
- [11] B. Sandeep. Somvanshi, P. B. Kharat, M. V. Khedkar, K. M. Jadhav, *Ceram. Int.* (2019)
- [12] R. M. Borade, B. Sandeep. Somvanshi, B. Swati, P. Rajendra, K. M. Jadhav, *Mater Research Express.* (2020).
- [13] M. A. Almessiere, Y. Slimani, H. Gungunes, A. Manikandan, A. Baykal, *Results. Phys.* 13 (2019) 102166.

- [14] K. M. Rehmana, M. Riaz, X. Liu, M. W. Khan, Y. Yang, K. M. Batood. *J Magn Mater.* 474 (2019) 83–9.
- [15] M. A. Almessiere, Y. Slimani, A. Baykal. *Ceram Int.* 44 (2018) 9000–8
- [16] N. Rezlescu, C. Doroftei, E. Rezlescu, P. D. Popa, *J Alloy Compd.* 451 (2008) 492–6.
- [17] I. A. Auwal, A. Baykal, S. Guner, M. Sertkol, H. Sozeri, *J Magn Mater.* 409 (2016) 92–8.
- [18] C. Murugesan and G. Chandrasekaran, *RSC Adv.* (2015).
- [19] R. C. Kambale, K. M. Song, Y. S. Koo and N. Hur, *J. Appl. Phys.* 110 (2011) 053910.
- [20] A. A. Kadam, S. S. Shinde, S. P. Yadav, P. S. Patil and K. Y. Rajpure, *J. Magn. Mater.* 329 (2013) 59.
- [21] J. Lakshmikantha, G. Krishnamurthy, B. M. Nagabhushan, C. S. Naveen and E. Melagiriappa, *J Supercond Nov Magn* (2022).
- [22] X. B. Chen, N.T.M. Hien, K. Han, J.C. Sur, N.H. Sung, B.K. Cho, I.S. Yang, *J. Appl. Phys.* 114 (2013) 13912.
- [23] G. M. Suarez, L. P. R. Vazquez, J. C. C. Huacuz, A. F. Fuentes, J. I. E. García, *Phys. B.* 339 (2003) 110-118.
- [24] S. A. Saafan, S. T. Assar, S. F. Mansour, *J. Alloy. Compd.* 542 (2011) 192–198.
- [25] M. Abhishek, E. Melagiriappa, V. Jagadeehsa Angadi, B. N. Anandaram, M. Veena, Mohammed Irfan, K. Swaroop Acharya, *J Mater Sci: Mater Ele.* (2020).
- [26] S. Liua and G. Daib, *J Chi. Chemi. Soci.* 58 (2011) 617-622.
- [27] F. de Assis dos Santos Silva, M. G. A. da Silva, P. R. Lima, M. R. Meneghetti, L. T. Kubota, M. O. Fonseca Goulart, *Biosens. Bioelec.* 50 (2013) 202–209.
- [28] S. Shahrokhian, *Anal. Chem.* 73 (2001) 5972–5978.
- [29] G. Wang, F. Zhou, X. Li, J. Li, Y. Ma, J. Mu, Z. Zhang, H. Che, X. Zhang, *Ceram Int.* (2018).

- [30] A. R. Chavan, P. P. Khirade, B. Sandeep, Somvanshi, V. Sachin, K. M. Mukhamale, Jadhav, J. Nano struc Chem. (2020).
- [31] M. A. Almessiere, Y. Slimani, M. Sertkol, M. Nawaz, A. Baykal, I. Ercan, Results Phys. 13 (2019) 102244.
- [32] P. Shepherd, K. K. Mallick, R. J. Green, J. Magn. Magn. Mater. 311 (2007) 683-692.
- [33] J. Lakshmikantha, G. Krishnamurthy, B. M. Nagabhushan, E. Melagiriappa, J. Solid State Chem. 315 (2022) 123465.
- [34] D.S. Mathew, R.S. Juang, Chem. Eng. J. 129 (2007) 51–65.
- [35] Du Y, Liu Y, Lian L, Du J, J Magn Magn Mater. 469 (2019) 189–95.
- [36] A. Sharma, A. Rani, A. Singh, O. P. Modi. K. Gaurav, Gupta, Appl Nanosci. (2013).
- [37] B. Sandeep, Somvanshi, V. Mangesh, Khedkar, B. Prashant, K. M. Jadhav, Ceram. Int. 46 (2019) 8640-8650.
- [38] M. J. Iqbal, M .N. Ashiq, I. H. Gul, J. Magn. Magn. Mater. 322 (2010) 1720–1726.
- [39] S. Kumar, T. Kaur, S. Kumar, and A. K. Srivastava, J. Supercond. Nov. Magn. 28 (2015)
- [40] P. Kuruva, P. R. Matli, B. Mohammad, S. Reddigari and S. Katlakunta, J. Magn. Magn. Mater. 382 (2015) 172–178.
- [41] K. M. Ur Rehman, X. Liu, M. Li, S. Jiang, Y. Wu, C. Zhang, C. Liu, X. Meng, and H. Li, J. Magn. Magn. Mater. 426 (2017) 183–187.
- [42] M. A. Almessiere, Y. Slimani, H. S. El Sayed, A. Baykal, I. Ercan, J. Magn. Magn. Mater. 471 (2019) 124–132.
- [43] G. R. Gordani, A. Ghasemi, A. Saidi, Ceram. Int. 40 (2014) 4945 – 4952.
- Kurian, M. Thankachan, S. Nair, J Adv. Ceram. 4 (2015) 199–205.

- [44] Y. Slimani, H. Gungunes, M. Nawaz, A. Manikandan, H. S. El Sayed, M. A. Almessiere, H. Sözeri, S. E. Shirsath, I. Ercan, A. Baykal, *Ceram Int.* 44 (2018) 14242-14250.
- [45] Sandeep B. Somvanshia, Swapnil A. Jadhava, Mangesh V. Khedkara, Prashant B. Kharata, S.D. Morec, K. M. Jadhava, *Ceram. Int* 2020.
- [46] C. G. Koops, *Phys. Rev.* 83 (1953) 121-124.
- [47] K. Iwauchi, *Jpn. J. Appl. Phys.* 10 (1971) 152.
- [48] E. Melagiriappa, H. S. Jayanna, B. K. Chougule, *Mater. Chem. Phys.* 112 (2008) 68–73.
- [49] M. Ishaque, M. A. Khan, I. Ali, M. Athai, H. M. Khan, M. A. Iqbal, M. U. Islam, M. F. Warsi, *Mate Sci Semicond Pro.* 41 (2016) 508–512.
- [50] P. Mathur, A. Thakur, M. Singh, *Phys. Scr.* 77 (2008) 1-5.
- [51] B. Unal, M. Almessiere, Y. Slimani, A. Baykal, A. V. Trukhanov and I. Ercan, *Nanomaterials*, 9 (2019) 1168.
- [52] P. Kumar, A. Gaur and R. K. Kotnala, *Ceram. Int.* 43 (2017) 1180-1185.
- [53] M. N. Ashiq, R. B. Qureshi, M. A. Malana, and M. F. Ehsan, *J. Alloys Compd.* 651 (2015) 266-272.
- [54] S. M. El-sayed, T. M. Meaz, M. A. Amer, and H. A. El Shersaby, *Phys. B Phys. Condens. Matter.* 426 (2013) 137–143.
- [55] G. Asghar, M. Anis-ur-Rehman, *J. Alloys Comp.* 526 (2012) 85–90.
- [56] M. U. Muhammad Irfan, A. Elahi, U. Khan, T. Khan, K. Javed, S. S. Ali, A. Shakoor, *J Mater Sci: Mater Electron*, 27 (2015) 3637-3644.
- [57] B. K. C. R. S. Devan, *J. Appl. Phys.* 101 (2007) 141.
- [58] N. Okasha, *J. Alloy. Compd.* 490, (2010) 307–310
- [59] Ming-Ru, Syuea, Fu-Jin, Wei, Chan-Shin, Chou, Chao-Ming, *Thin Solid Films*, 519 (2011) 8303–8306.
- [60] B. P. Jacob, S. Thankachan, S. Xavier, E. M. Mohammed, *J. Alloys Compd.* 541 (2012) 29–35.

- [61] M. Hashim, S. E. Shirsath, Alimuddin, S. Kumar, R. Kumar, A. S. Roy, J. Alloys Compd. 549 (2013) 348–357.
- [62] M. A. Dar, K. Mujasam, Batoo, Vivek, Verma, W. A. Siddiqui, R. K. Kotnala, J. Alloy. Compd. 493 (2010) 553–560.
- [63] A.V. Humbe, J. S. Kounsalyea, B. Sandeep, Somvanshi, Arun Kumar, K. M. Jadhava, Mater Adv. 1 (2020) 880-890.
- [64] A. Bhosale, S. B. Somvanshi, V. D. Murumkar, K. M. Jadhav, Ceram Int. (2020).
- [65] V. A. Bharati, S. B. Somvanshi, A. V. Humbe, V. D. Murumkar, V. V. Sondur, K. M. Jadhav, J. Alloys Compd, 821 (2020) 153501.
- [66] M.A. Almessiere, Y. Slimani, H.S. El Sayed, A. Baykal, I. Ercan, J. Magn. Mater. 471(2019) 124–132.
- [67] Z. Mosleh, P. Kameli, A. Poorbaferani, M. Ranjbar, H. Salamati, J. Magn. Mater. 397 (2016) 101.
- [68] Y. Slimani, A. Baykal, Md. Amir, N. Tashkandi, H. Güngüneş, S. Guner, H.S. El Sayed, F. Aldakheel, T.A. Saleh, A. Manikandan, Ceram Int. 44 (2018) 15995-16004.
- [69] S. Katlakunta, S.S. Meena, S. Srinath, M. Bououdina, R. Sandhya, K. Praveena, Mater. Res. Bull. 63 (2015) 58-66.
- [70] R. Topkaya, I. Auwal, A. Baykal, Ceram. Int. 42 (2016) 16296–16302.
- [71] M. A. Almessiere, Y. Slimani, H. S. El Sayed, A. Baykal, Ceram Int. 44 (2018) 12511-12519.
- [72] M.A. Almessiere, Y. Slimani and A. Baykal, Ceram Int, 44 (2018) 9000-9008.
- [73] P. Malathesh, K. R. V. Reddy, Fasiulla, K. B. Chandrakala, Sensors and Actuators A 316 (2020) 112377.
- [74] P. Malathesh and K. R. V. Reddy, Anal. Bioanal. Elec. chem, 10 (2019) 1383-1397.
- [75] E. Laviron, J. Elec. anal. Chem. Inter Elec. chem. 101 (1979) 19–28.

CHAPTER 6:-

A STUDY ON
ELECTROCHEMICAL, GAS
SENSING AND MAGNETIC
PROPERTIES OF Sr²⁺ DOPED
Ni_{0.5}Cu_{0.5}MgO₃ SYNTHESIZED BY
AUTO COMBUSTION METHOD

6.1 Introduction

The nanoparticle oxides have a high surface area, so they use good carriers, absorbents and catalysts [1]. Recently, the cancer cell is one of the most difficult diseases that the world has faced in recent years due to the increase in the number of cases up to 25 million annually in last recent years. There are many common methods of treating cancer, such as radiotherapy, surgery, and chemotherapy [2]. Among the potential supports, MgO has been widely reported as being effective because of its high thermal stability, low cost, and unique ability to form a solid solution with NiO.[3 - 4] MgO has the same crystal structure as NiO, and Mg^{2+} has almost the same ionic radius as Ni^{2+} (~3 pm difference), allowing them to form an ideal MgO-NiO solid solution.[5-6] Upon reduction, the strong interaction between the Ni atoms and MgO support favors the formation of small, highly dispersed Ni particles, enhancing the catalytic activity [7]. In recent years, researchers have focused more on the synthesis of MgO nanoparticles due to its novel applications in advanced technologies [8]. Metal oxides are extremely important technological materials to be used in electronic and photonic devices [9]. The magnesium oxide (MgO) is a very suitable candidate for insulation applications due to its low heat capacity and high melting point [10]. Recently, it has been reported that MgO has a good bactericidal performance in aqueous environments due to the formation of super-oxide [11]. Alkaline oxides are important materials for investigating the magnetism that arises due to *p*-orbitals [12]. The materials that are chiefly being considered for this investigation are MgO [13, and CaO [14]. In the wake of theoretical studies on these materials carried out by various groups, a number of experimental reports are available, especially for MgO, giving support to the ferromagnetism of these materials

[15]. Based on simulation results for these oxides, this kind of magnetism is believed to originate from defects, which has led to debate among researchers. In this context, a number of authors have studied the magnetic behavior of magnesium oxides experimentally [16-17]. Gas sensors operating at room temperature are more important because of their low power operation and also the life time of sensors is enhanced. The efficiency of gas sensors depends on low density and large surface area to increase gas exposure, thus gas sensing devices that use ferrite nanoparticles are exhibited enhanced performance. Various kinds of fabrication techniques are employed to synthesize MgO nanoparticles such as chemical vapour deposition(CVD) [18], plasma enhanced chemical vapour deposition (PECVD) [19], pulsed laser deposition(PLD) [20], laser ablation [21], molecular beam epitaxy (MBE) sputtering method [22], hydrothermal method [23], solgel method [24], co-precipitation method [25] and solution combustion method [26]. Among these methods, auto combustion method is a very promising method for synthesizing the desired phase. It is very simple, easy manufacture, low cost, high purity of crystallinity, chemical uniformity, short processing time and fine particles size distribution. The present investigation was aimed on the systematic analysis on the structural, morphological, optical, magnetic properties, electro-chemical and gas sensor of the $\text{Ni}_{(0.5)}\text{Cu}_{(0.5-x)}\text{Sr}_x\text{MgO}_3$ ($x = 0.00, 0.01, 0.05$ and 0.1) nanoparticles prepared by auto combustion method.

6.2. Experimental Method

6.2.1. Synthesis method and Characterization

The samples of $\text{Ni}_{(0.5)}\text{Cu}_{(0.5-x)}\text{Sr}_x\text{MgO}_3$ ($x = 0.00, 0.01, 0.05$ and 0.1) nanoparticles (NP's) were prepared via auto combustion method. The small quantity of Sr^{2+} ion substituted stoichiometrically of analar grade, the starting chemicals used

are: $\text{Ni}(\text{NO}_3)_2 \cdot 6\text{H}_2\text{O}$ (Merck), $\text{Sr}(\text{NO}_3)_2$ (Merck), $\text{Mg}(\text{NO}_3)_2 \cdot 6\text{H}_2\text{O}$ (Sigma Aldrich), $\text{Cu}(\text{NO}_3)_2 \cdot 3\text{H}_2\text{O}$ (Sigma Aldrich), urea ($\text{CH}_4\text{N}_2\text{O}$). The petri dish carrying the solution of redox mixture and then placed into heat furnace attained at 550 ± 10 °C. The solution begins to boil in a furnace and heat reduction and ignition at one point, followed by decomposition and generate an amount of gas (N_2O and CO_2). When a solution reaches its self-ignition point, it begins to burn, releasing a large amount of heat and instantly evaporating all the solution, solidifying and burning, forming a fluffy with loose powder. This leads to better product homogeneity by bringing the unreacted particles closer together, which tends to reduce the diffusion distance as well as the particle size distribution.

The powders are calcinated at 1000 °C for 3 hours. The sintered powders are ground in an agate mortar and mixed with a binder polyvinyl pyrolidone (PVP) ($\text{C}_6\text{H}_9\text{NO}$)_n. The powders are compressed into pellets using die with a dia 10 mm and a thickness of about ~2-3 mm by loading a pressure of $5 \cdot 10^8$ kg/m² for 5 minutes. The pellets are sintered in a furnace at temperature of 1100 °C for 3 hours and then gradually cooled to room temperature. In general, self-propagation high temperature was favorable for significant crystallite sizes.

The standard X-ray diffraction patterns (XRD) were obtained 2θ angle in the range $20^\circ - 80^\circ$ with scanning rate 2° per min on a Philips diffractometer (Make: Bruker, Model:d8 Advance, Germany) using CuK radiations ($\lambda = 1.5406$ Å) is employed at 300 K to study the crystal orientation of all the ferrite nanoparticles. The room temperature Fourier infrared spectroscopy (FTIR) of all the samples was recorded on a Perkin Elmer spectrometer (Model: Spectrum 2, USA) in the wavenumber range $4000 \text{ cm}^{-1} - 300 \text{ cm}^{-1}$. The morphology of samples was examined

by field emission scanning electron microscopy analysis using (FESEM, JEOL/EO/JSM-639]. The energy dispersive X-ray spectrum were recorded using (EDS) Carl Zeiss, Model: EVOLS15, Germany). The UV–Visible spectroscopy is a useful tool to investigate the absorption, transmission or reflection band of a semiconducting material. We have conducted the(Shimadzu-UV-2600) UV–Vis spectra measurement of all synthesized samples in absorption mode over the range of $200 \text{ nm} \leq \lambda \leq 800 \text{ nm}$. Vibrating sample magnetometer (VSM) (Make: CREST, Model: 20130523-01) was employed to characterize the magnetic properties.

6.3 Results and Disussion

6.3.1 Study of Powder X-ray diffraction

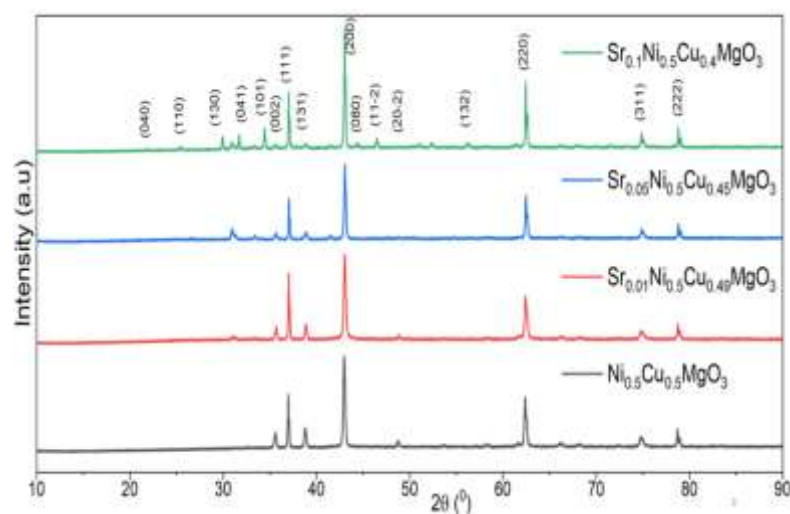


Fig 6.1 PXR patterns of $\text{Ni}_{(0.5)}\text{Cu}_{(0.5-x)}\text{Sr}_x\text{MgO}_3$ ($x = 0.00, 0.01, 0.05$ and 0.1) NiMgO NP's

The structural examination of the NiMgO NP's was investigated by the X-ray beam diffraction. The PXR patterns of $\text{Ni}_{(0.5)}\text{Cu}_{(0.5-x)}\text{Sr}_x\text{MgO}_3$ ($x = 0.00, 0.01, 0.05$ and 0.1) nanoparticles as shown in the fig 6.1, peaks of the XRD pattern of all samples matched with the JCPDS card No. 78-0643 [27] and these are indexed as (040), (110), (130), (041), (101), (002), (111), (131), (200), (080), (11-2), (20-2),

(132), (220), (311) and (222) planes indicating the cubic phase structure of NiMgO. The XRD data was used to evaluate different structural parameters by using the following relations and their values are given in table 6.1. [28].

$$a = d\sqrt{h^2 + k^2 + l^2} \text{ \AA} \quad (6.1)$$

where, utilizing the estimations of Bragg's angle (2θ) and interplanar spacing (d), the estimations of lattice parameter. V_{cell} is the unit of the cubic spinel ferrites and is determined as follows:

$$V_{\text{cell}} = a^3 \text{ \AA}^3 \quad (6.2)$$

where, the numerical values is sustained for the spinel system. From, the XRD peaks, an average crystallite sizes of the nanoferrites are determined using Debye-Scherrer equation (d) and is calculated by:

$$d = \frac{k\lambda}{\beta \cos\theta} \quad (6.3)$$

where, $k = 0.89$ is Scherer's constant, $\lambda = 0.15406$ nm is wavelength of the incident X-rays in nm, β is the full width at half maximum (FWHM) of diffraction peak, θ is the Bragg diffraction angle. The average value of crystallite size is found in the range ~ 25 nm, increases with Sr^{2+} content and values are tabulated in table 6.1. The measured x-density is calculated by using relation as follows,

$$\rho_x = \frac{8M}{Na^3} \quad (6.4)$$

where, M is the molecular weight of the sample, N the Avogadro's number and a^3 the volume of the cubic unit cell. The bulk density is calculated by using relation as mentioned below:

$$\rho_b = \frac{m}{\pi r^2 h} \quad (6.5)$$

where, m is the mass, r is the radius and h is the height of the pellet. Percentage porosity was calculated using the formula.

$$P = \left(1 - \frac{\rho_b}{\rho_x}\right) \quad (6.6)$$

where, ρ_x is the x-ray density and the ρ_b bulk density.

The lattice constant (a) increases slightly for all the compositions. The variation can be explained on the basis of ionic radii of the substituted ions. The replacement of the smaller Cu^{2+} ions (0.73 Å) with larger Sr^{2+} ions (0.113 Å) causes dilation of the host spinel lattice which results in the slightly increase of lattice constant 4.21 to 4.28 Å without changing the crystal structure. The influence of Sr^{2+} concentration on X-ray density (ρ_x) and bulk density (ρ_b) are tabulated in table 6.1. X-ray density exhibits an increasing trend with Sr^{2+} contents as it mainly depends upon the molecular weight of the samples. It decreases from 8.21 to 11.89 g/cm³. The bulk density also decreases with Sr^{2+} contents from 7.11 to 9.36 g/cm³ which can be attributed to the difference in atomic weight of Sr^{2+} (87.62 amu) and iron (63.546 amu) as described in CRC book. Therefore, a decrease in the percentage porosity can be expected with Sr^{2+} contents are showed in table 6.1 [29-30].

Table 6.1: Crystallite size (D), lattice constant (a), cell volume (V), X-ray density (qx-ray), bulk density and percentage porosity of $\text{Ni}_{(0.5)}\text{Cu}_{(0.5-x)}\text{Sr}_x\text{MgO}_3$ (x = 0.00, 0.01, 0.05 and 0.1) NiMgO NP's.

Composition	Crystallite size (D) /nm	Lattice constant (a)/Å	Cell volume (V)/Å ³	X-ray density(q x-ray)/g cm ³	Bulk Density g/cm ³	Percentage Porosity (%)
$\text{Ni}_{0.5}\text{Cu}_{0.5}\text{MgO}_3$	25.6	4.23	75.7	11.89	9.36	21.28
$\text{Ni}_{0.5}\text{Sr}_{0.01}\text{Cu}_{0.49}\text{MgO}_3$	25.3	4.21	74.6	9.15	7.40	19.13
$\text{Ni}_{0.5}\text{Sr}_{0.05}\text{Cu}_{0.45}\text{MgO}_3$	25.7	4.26	77.3	8.67	7.26	16.26
$\text{Ni}_{0.5}\text{Sr}_{0.1}\text{Cu}_{0.4}\text{MgO}_3$	25.4	4.28	78.4	8.21	7.11	13.40

6.3.2 FT-IR analysis

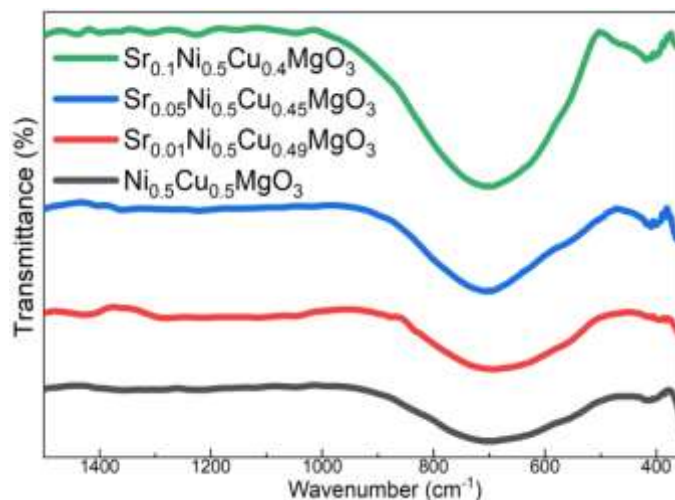


Fig 6.2 FT-IR spectra of $\text{Ni}_{(0.5)}\text{Cu}_{(0.5-x)}\text{Sr}_x\text{MgO}_3$ ($x = 0.00, 0.01, 0.05$ and 0.1) NiMgO NP's

The formation of functional groups was confirmed by Fourier transform infrared (FT-IR) spectroscopy. The FT-IR spectra of the prepared series of $\text{Ni}_{(0.5)}\text{Cu}_{(0.5-x)}\text{Sr}_x\text{MgO}_3$ ($x = 0.00, 0.01, 0.05$ and 0.1) nanoparticles are depicted in fig 6.2. Two metal–oxygen (M–O) vibration modes were revealed by FT-IR spectra within the range of 1500 to 350 cm^{-1} confirming the successful formation of spinel ferrites. The first band (ν_1) with the maximum frequency was observed in the range 415 cm^{-1} and the second band (ν_2) with minimum frequency in the range 710 cm^{-1} , which indicates metal–oxygen stretching at tetrahedral (A) site and octahedral (B) site, respectively [31]. Therefore, the Sr^{2+} replaces the Fe^{2+} ions without changing the crystal structure of the composition. Furthermore, the absence of bands in the wavenumber range $3200 - 3500\text{ cm}^{-1}$ indicating that the non-existence of an OH group in the reaction method [32]. A force constant is a secondary potential energy identified by the radius of the site. The force constants for tetrahedral and octahedral sites are given by the relations.

$$K_T = 4\pi^2 c^2 \nu_1^2 m \quad (6.7)$$

$$K_O = 4\pi^2 c^2 \nu_2^2 m \quad (6.8)$$

where c - speed of light 2.99×10^8 m/s, ν_1 and ν_2 are the vibrational frequencies cm^{-1} at A- and B-sites cm^{-1} respectively, m - decreased mass of Fe^{3+} and O^{2-} ions.

From table 6.2, it is observed that the value of force constant from 1.22 – 1.26 newton/m for tetrahedral sites (K_T) is lower than that for octahedral site (K_O) from 3.59 – 3.67 newton/m. Furthermore, the values K_T and K_O are found to be increased with increase in Sr^{2+} ion substitution. However, the K_T values are less than the K_O values in the samples substituted with Sr^{2+} ions [33].

Table 6.2: Position of IR absorption bands and force constant of $\text{Ni}_{0.5}\text{Sr}_{0.5}\text{Gd}_x\text{Fe}_{2-x}\text{O}_4$ ($x=0.00, 0.01 < x < 0.09$) nanoferrites.

Composition	Position of $\nu_1(\text{cm}^{-1})$	Force constant Tetrahedral (K_T) newton/m	Position of $\nu_2(\text{cm}^{-1})$	Force constant Octahedra l (K_O) newton/m
$\text{Ni}_{0.5}\text{Cu}_{0.5}\text{MgO}_3$	415	1.26	702	3.59
$\text{Ni}_{0.5}\text{Sr}_{0.01}\text{Cu}_{0.49}\text{MgO}_3$	410	1.22	704	3.61
$\text{Ni}_{0.5}\text{Sr}_{0.05}\text{Cu}_{0.45}\text{MgO}_3$	410	1.23	704	3.61
$\text{Ni}_{0.5}\text{Sr}_{0.1}\text{Cu}_{0.4}\text{MgO}_3$	413	1.24	710	3.67

6.3.3 FE-SEM analysis

The microstructure of pure $\text{Ni}_{(0.5)}\text{Cu}_{(0.5-x)}\text{Sr}_x\text{MgO}_3$ ($x = 0.00, 0.01$ and 0.1) NiMgO NP's as showed in fig 6.3. It is clear from the micro-graphs that both pure and Sr^{2+} substituted nanoparticles have almost irregular morphology and grain boundaries are not prominent. The agglomeration of the particles is more visible in the nanoparticles, it is due to the accumulation of some Sr^{2+} ions at grain boundaries instead of replacing Cu^{+2} ions at octahedral sites of spinel lattice.

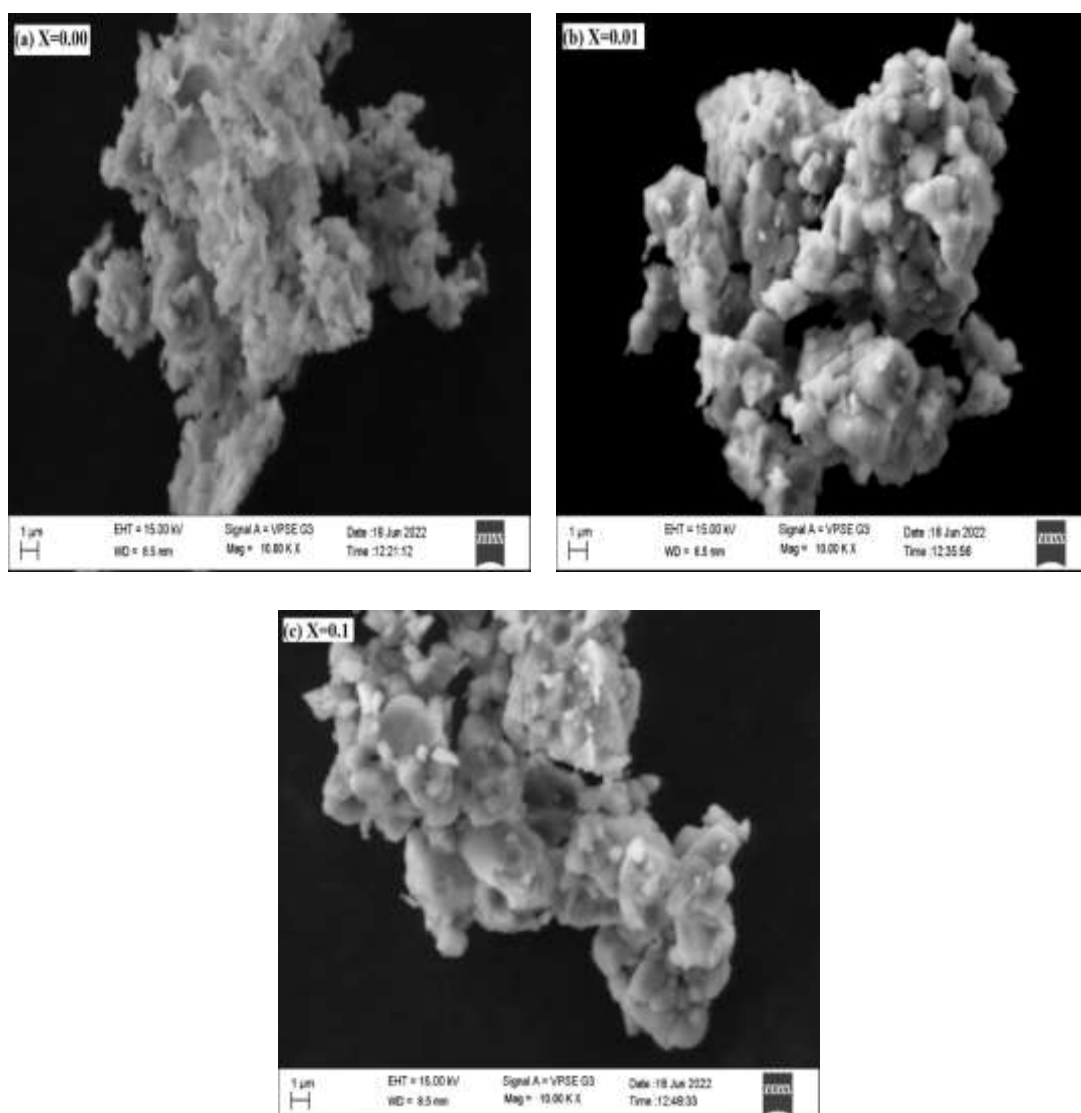


Fig 6.3 FESEM Micrographs of $\text{Ni}_{(0.5)}\text{Cu}_{(0.5-x)}\text{Sr}_x\text{MgO}_3$ ($x = 0.00$ (a), 0.01 (b) and 0.1 (c)) NiMgO NP's

In the result of this aggregation, particle size reduction was observed which is in agreement with the crystallite size obtained from XRD results [58]. The line intercept procedure is used to estimate an average grain size using the relation: $G_{av} = 1.5 L / MN$ where L-total length of test line in m, M – magnification, N - total number of grains intercept. The particles sizes are calculated and they are found to be in the range of 52 - 76 nm. As particle sizes are in the nano scale range (1–100 nm) so, FE-SEM analysis confirmed the formation of nanoparticles [34].

6.3.4 EDAX analysis

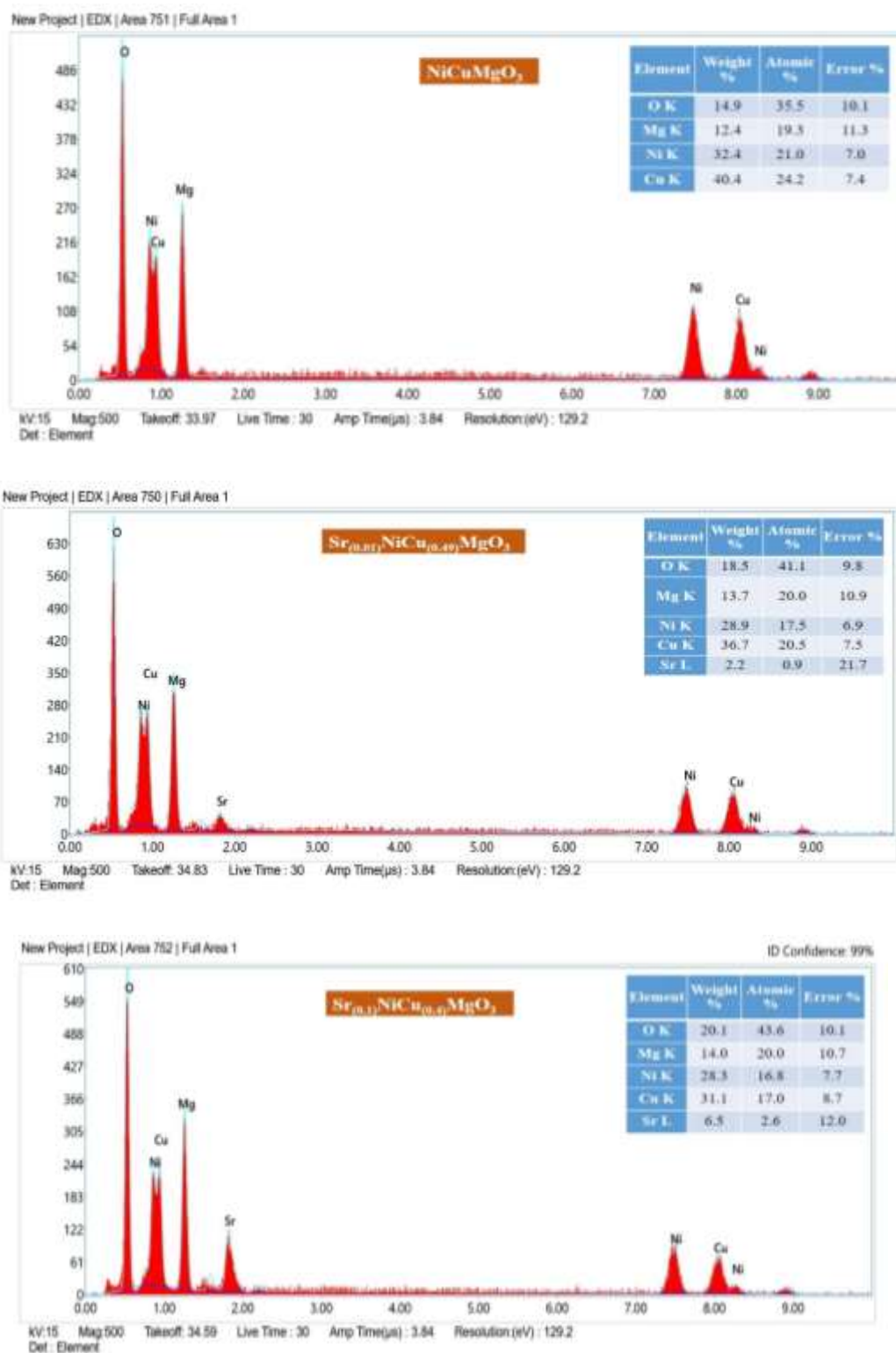


Fig 6.4 EDAX of $\text{Ni}_{0.5}\text{Cu}_{0.5-x}\text{Sr}_x\text{MgO}_3$ (x = 0.00(a), 0.01(b) and 0.1(c)) NiMgO NP's

The elemental analysis of the $\text{Ni}_{(0.5)}\text{Cu}_{(0.5-x)}\text{Sr}_x\text{MgO}_3$ ($x = 0.00, 0.01$ and 0.1) are showed fig 6.4. The elemental composition analysis of all the composites are presence of elements, Ni, Sr, Cu, Mg and O as shown in fig 6.4. There was no other elements are observed in all the samples of spectra which confirms the high crystallinity of all the samples.

6.3.5 OPTICAL properties

The UV–Visible spectroscopy is a useful tool to investigate the absorption, transmission or reflection band of a semiconducting material. Optical reflection spectra utilizing Kubelka-Munk (K-M) model, & $F(R)$ was estimated from the accompanying conditions. The absorption spectrum of pure $\text{Ni}_{(0.5)}\text{Cu}_{(0.5-x)}\text{Sr}_x\text{MgO}_3$ ($x = 0.00, 0.01, 0.05$ and 0.1) showed in fig 6.5, two characteristic absorption peaks attributed to the conducting emeraldine salt, one is around 276 nm and other is at 415 nm. The first absorption band assigned at ~ 300 nm is due to the $\pi\text{-}\pi^*$ electronic transitions and other is assigned at 415 nm due to the polaron band also represents the presence of lone pair electrons of nitrogen [28, 35].

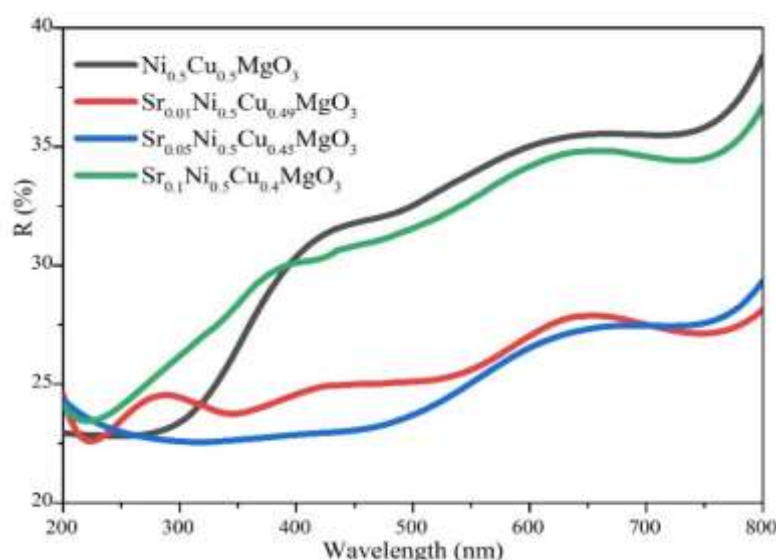


Fig 6.5 The reflectance Spectra of $\text{Ni}_{(0.5)}\text{Cu}_{(0.5-x)}\text{Sr}_x\text{MgO}_3$ ($x = 0.00, 0.01, 0.05$ and 0.1) NiMgO NP's

The absorption increases with increasing Sr^{2+} concentration of NiCuMgO nanocomposites. In accordance with Beers law, the absorption is proportional to the number of absorbing molecules. These results suggest that there are interactions with $\text{Ni}_{(0.5)} \text{Cu}_{(0.5-x)} \text{Sr}_x \text{MgO}_3$ nanoparticles. The optical band gap of all Gd^{3+} doped nanoparticles were analyzed using the following equations.

$$E_g = \frac{hc}{\pi\lambda} = \frac{1240}{\lambda} \quad (6.9)$$

$$F(R_\infty) = \frac{(1 - R_\infty)^2}{2R_\infty} \quad (6.10)$$

$$\{(F(R_\infty)h\nu\}^{1/n} \propto (h\nu - E_g) \quad (6.11)$$

Where: h is the Planck constant (6.626×10^{-34} Js).

c is the speed of light (2.99×10^8 ms^{-1}).

λ is the wavelength that corresponds to reflectance spectra.

R_∞ is the diffuse reflectance spectra.

α is the absorption coefficient.

ν is frequency of the incident light.

E_g is the bandgap energy.

$n = 2$ for direct bandgap.

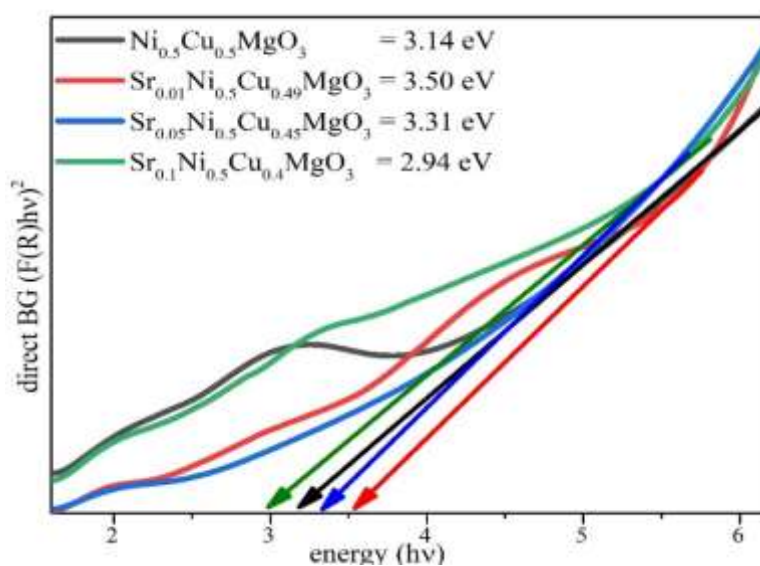


Fig 6.6 Bandgap energy of $\text{Ni}_{(0.5)} \text{Cu}_{(0.5-x)} \text{Sr}_x \text{MgO}_3$ ($x = 0.00, 0.01, 0.05$ and 0.1) NiMgO NP's

The direct energy band gap (E_g) values were obtained by extrapolating the linear part of the $(\alpha h\nu)^2$ curve versus $(h\nu)$ as shown in fig 6.6. The energy band gap (E_g) values are tabulated in table 6.3. It is clear that there is a decrease in the band gap 2.94 to 3.50 eV of the Sr^{2+} doped NiCuMgO samples when compared to pure NiCuMgO. The shift in band gap of the $\text{Ni}_{(0.5)}\text{Cu}_{(0.5-x)}\text{Sr}_x\text{MgO}_3$ nanoparticles with decreasing crystallite size is the result of quantum confinement effects arising from the small size regime [36].

Table 6.3: UV-Vis absorption band gap values of of $\text{Ni}_{(0.5)}\text{Cu}_{(0.5-x)}\text{Sr}_x\text{MgO}_3$ ($x = 0.00, 0.01, 0.05$ and 0.1) NiMgO NP's

Sl. No	Composition	Band gap (eV)
1	$\text{Ni}_{0.5}\text{Cu}_{0.5}\text{MgO}_3$	3.14
2	$\text{Ni}_{0.5}\text{Sr}_{0.01}\text{Cu}_{0.49}\text{MgO}_3$	3.50
3	$\text{Ni}_{0.5}\text{Sr}_{0.05}\text{Cu}_{0.45}\text{MgO}_3$	3.31
4	$\text{Ni}_{0.5}\text{Sr}_{0.1}\text{Cu}_{0.4}\text{MgO}_3$	2.94

6.3.6 Magnetic Measurements

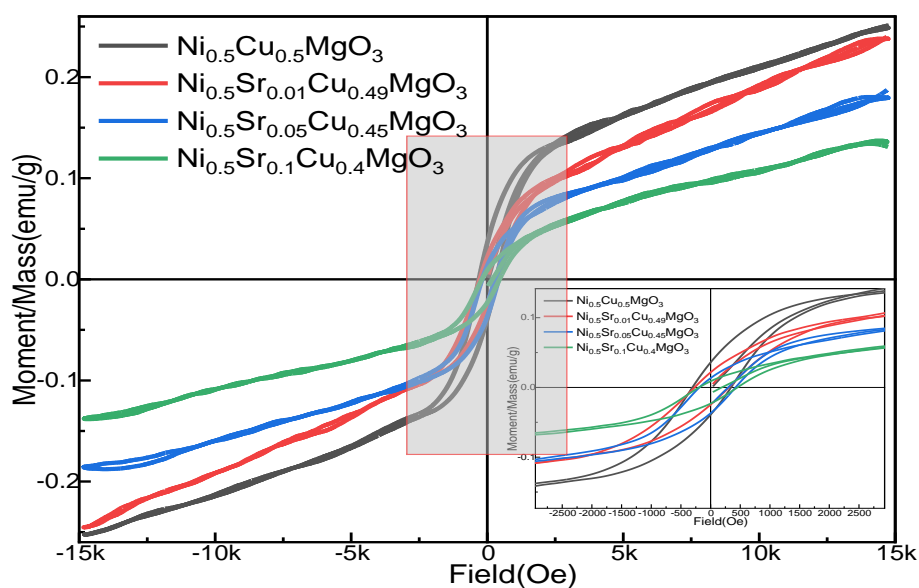


Fig 6.7 Hysteresis curves of $\text{Ni}_{(0.5)}\text{Cu}_{(0.5-x)}\text{Sr}_x\text{MgO}_3$ ($x = 0.00, 0.01, 0.05$ and 0.1) NiMgO NP's

The magnetic hysteresis loops of $\text{Ni}_{(0.5)}\text{Cu}_{(0.5-x)}\text{Sr}_x\text{MgO}_3$ measured at room temperature are shown in fig 6.7. It can be observed from M–H loops that soft magnetic behaviour exists for the pure and Sr^{2+} doped NiMgO NP's with a decrease in magnetization with increase in the concentration of Sr^{2+} ions ($x = 0.00, 0.01, 0.05$ and 0.1). The information about saturation magnetization (M_s), remanence magnetization (M_r), Coercivity (H_c), squareness ratio (S) and Magneton number (η_B) fields was deduced from respective M-H curves of the sample and Table 6.4. The magnetic parameters are calculated using the following relations [37-38].

$$S = \frac{M_r}{M_s} \quad (6.12)$$

where, M_s is saturation magnetization (emu/g), M_r is remanent magnetization. The values of, Magneton number (η_B) are given by the relation

$$\eta_B = \frac{M \times M_s}{5585} \quad (6.13)$$

where η_B is the magnetic moment (number of Bohr magnetons), M_w is molecular weight of the composition (x) in g, M_s is saturation magnetization (emu/g), 5585 is the magnetic factor.

The magnetic properties of the NiMgO NP's with an inverse spinel structure can be explained in terms of the cations distribution and magnetization originates from Sr^{2+} and Cu^{2+} ions have A-A exchange at tetrahedral sites, while Ni^{2+} , Cu^{2+} , and Mg^{2+} ions have B-B interactions at octahedral sites. Both the tetrahedral and octahedral ions have A-B super exchange interaction. [38]. Hysteresis loops in fig 6.7 are typical for soft magnetic materials and the “S” shape of the curves together with the negligible coercivity ($H_c = \leq 0.60$ Qe) indicate the presence of small magnetic particles exhibiting super paramagnetic behaviors [39-40]. The observed magnetic behaviour of the present samples can also be explained on the basis of Neel's model [41]. According to Neel, the Neel's magnetic moment (calculated magneton number)

is given by $M_S = M_B - M_A$, where M_B is a magnetic moment of B sublattice and M_A is magnetic moment of A sublattice. It is known that, the spinel crystal structure consists of two interstitial sites namely tetrahedral (A) and octahedral [B] site. Among these interstitial sites, the inter sublattice A-B superexchange interaction and intra sublattice A-A and B-B superexchange interaction exists. A-B interaction is much stronger than the A-A interaction and B-B interaction. The substitution of Sr^{2+} ions at the B site will affect the interaction between Ni–O–Sr ions, and affect the sublattice exchange energy between Ni–O–Cu [42-43].

The magnetic moment of the Cu^{2+} ion decreased with the increasing of the Sr^{2+} ions, this action for this increase in value is due to the increasing of the super exchange interaction between the different sites, leading to an increase in the values (0.05 – 0.03 $\mu\beta$). This indicates the increasing of the super-exchange interactions [40]. Magnetization values of the $Ni_{(0.5)} Cu_{(0.5-x)} Sr_x MgO_3$ samples are decreases from for M_s 0.136 emu/g – 0.268 emu/g with increase of the Sr^{2+} ion content. M_r in the range of 0.018 – 0.035 emu/g at room temperature. H_c is in the scope of 195.77 – 306.42 Oe at room temperature. This reduction is associated with the equivalent reduction of Cu^{2+} ions to replacing of Sr^{2+} ions[39]. The squareness ratio values are observed in the scope of 0.13 – 0.12 emu/g indicates that the particles are in the single magnetic domain, and those < 0.5 indicate particles with a multi-domain structure, shows that all the synthesized nickel nano-ferrites investigate the nature of a single magnetic domain [43].

Table 6.4: Magnetic properties i.e. coercivity (Hc), saturation magnetization (Ms), remanence (Mr), squareness ratio (Mr/Ms), and $\eta\beta$ Ni_(0.5) Cu_(0.5-x) Sr_xMgO₃ (x = 0.00, 0.01, 0.05 and 0.1) NiMgO NP's

Composition	M _s (emu/g)	H _c (Oe)	Mr (emu/g)	S (emu/g)	$\eta\beta$ ($\mu\beta$)
Ni _{0.5} Cu _{0.5} MgO ₃	0.268	306.42	0.035	0.13	0.05
Ni _{0.5} Sr _{0.01} Cu _{0.49} MgO ₃	0.237	270.49	0.031	0.13	0.05
Ni _{0.5} Sr _{0.05} Cu _{0.45} MgO ₃	0.199	187.95	0.023	0.12	0.04
Ni _{0.5} Sr _{0.1} Cu _{0.4} MgO ₃	0.136	195.77	0.018	0.14	0.03

6.3.7 Gas sensing Measurements

Gas sensing measurement were carried out by making use of an in-house fabricated gas sensing chamber. The prepared samples were pressed into pellets of the thickness of 0.7 – 1 mm and diameter of 13 mm, the two dots of silver paste were placed on the surface of the samples to get the ohmic contacts. The prepared pellet sample was kept inside the gas-sensing chamber and the electrical resistance of the sample was measured in air (R_a) and the presence of test gas (R_g) at room temperature. The butane gas sensing studies were characterized for all the prepared Ni_(0.5) Cu_(0.5-x) Sr_xMgO₃ samples at 150 °C temperature are shown in Fig 6.8. There are many parameters effects the gas sensing behavior of the sample such as aspect ratio, particle size, defects on surfaces, surface morphology, thickness of the pellet, chemical reaction rate etc., thus changes the material resistance as the gas molecules diffuses on the surface.

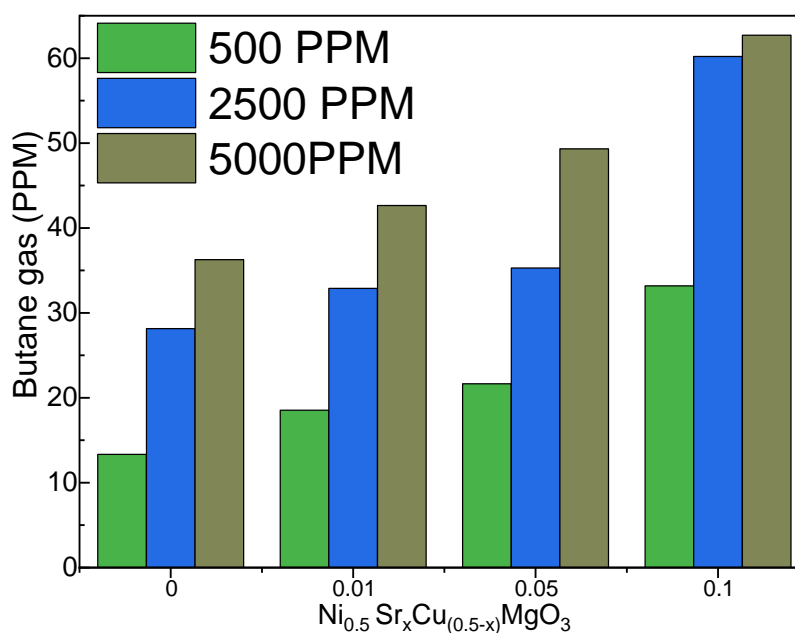


Fig 6.8 Variation of sensitivities of Ni_(0.5) Cu_(0.5-x) Sr_xMgO₃ ($x = 0.00, 0.01, 0.05$ and 0.09) nanocomposite thick films for 500, 2500, 5000 PPM of butane gas vapors at room temperature

The change in resistance of the sample in the presence and absence of butane gas can be used as the sensing performance in terms of sensitivity, the sensitivity of the sensor can be calculated by using following equation and listed in table 6.5.

$$Sensitivity (S)\% = \left(\frac{R_g - R_a}{R_a} \right) * 100 \quad (6.14)$$

Where, R_a is the resistance of a sensing material in air,

R_g is the resistance of a sensing material in the presence of test gas,

In this work, effect of different mol% Sr²⁺ incorporated to the B site of the Ni_(0.5)Cu_(0.5)MgO₃ is investigated. The various concentrations of butane gas sensing performances of the all the prepared samples were studied at a constant temperature. The sensitivity of pure Ni_(0.5)Cu_(0.5)MgO₃ nanoparticles for the 500, 2500 and 5000 PPM of butane gas was 13.33%, 28.15%, 36.27% and its response time is 22s, 19s, 11s and recovered in 245, 188, 133s. The incorporation of Sr²⁺ to Ni_(0.5)Cu_(0.5)MgO₃ nanoparticles, sensitivity of the samples increases with the concentration the Sr²⁺

because of the increase in the defect centers occurred in the Fe^{3+} . The sensitivities of $\text{Ni}_{0.5}\text{Sr}_{0.01}\text{Cu}_{0.49}\text{MgO}_3$ nanoparticles for the 500, 2500 and 5000 PPM of butane gas was 18.54%, 32.89%, 42.65% and its response time is 21s, 18s, 10s and recovered in 258s, 193s, 135s. Sensitivities of $\text{Ni}_{0.5}\text{Sr}_{0.05}\text{Cu}_{0.45}\text{MgO}_3$ nanoparticles for the 500, 2500 and 5000 PPM of butane gas was 21.65%, 35.28%, 49.33% and its response time is 24s, 16s, 9s and recovered in 198s, 103s, 96s. Sensitivities of $\text{Ni}_{0.5}\text{Sr}_{0.1}\text{Cu}_{0.4}\text{MgO}_3$ nanoparticles for the 500, 2500 and 5000 PPM of butane gas was 33.19%, 60.20%, 62.70% and its response time is 25s, 12s, 9s and recovered in 165s, 65s, 64s.

Table 6.5: Butane gas - sensitivity, response time and recovery time of $\text{Ni}_{(0.5)}\text{Cu}_{(0.5-x)}\text{Sr}_x\text{MgO}_3$ ($x = 0.00, 0.01, 0.05$ and 0.1) NiMgO NP's.

Composition	Butane (PPM)	Sensitivity (%)	Response time (s)	Recovery time (s)
$\text{Ni}_{0.5}\text{Cu}_{0.5}\text{MgO}_3$	500 2500 5000	13.33 28.15 36.27	22 19 11	245 188 133
$\text{Ni}_{0.5}\text{Sr}_{0.01}\text{Cu}_{0.49}\text{MgO}_3$	500 2500 5000	18.54 32.89 42.65	21 18 10	258 193 135
$\text{Ni}_{0.5}\text{Sr}_{0.05}\text{Cu}_{0.45}\text{MgO}_3$	500 2500 5000	21.65 35.28 49.33	24 16 9	198 103 96
$\text{Ni}_{0.5}\text{Sr}_{0.1}\text{Cu}_{0.4}\text{MgO}_3$	500 2500 5000	33.19 60.20 62.70	25 12 9	165 65 64

6.3.8 ELECTROCHEMICAL CHARACTERIZATION

6.3.8.1. Charge transfer behavior of NiMgO electrode

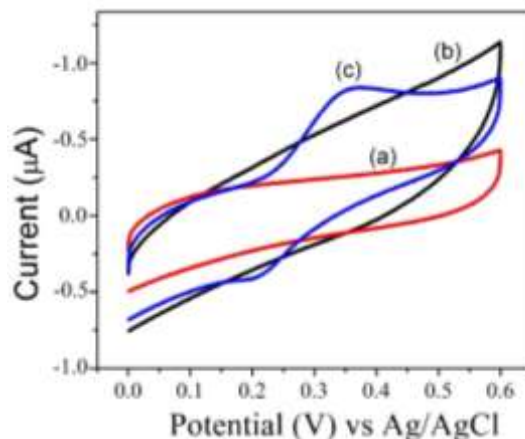


Fig 6.9 CVs of pH-4.0 at the (a) Bare electrode (b) NiMgO -GCE (c) 10 μ M dopamine with NiMgO -GCE

The charge transfer behaviour of the NiMgO electrode was investigated using pH 4.0 as a supporting electrolyte. The bare glassy carbon electrode (GCE) exhibits the expected cyclic voltammetric response shown in the fig 6.9. The NiMgO/GCE exhibits a faster and more proficient electron transfer rate than the bare glassy carbon electrode, this is due to the higher surface area at the NiMgO/GCE. However, at the comparison of different sensors for dopamine shows a prominent electro catalytic activity [73].

6.3.8.2 Effect of scan rate

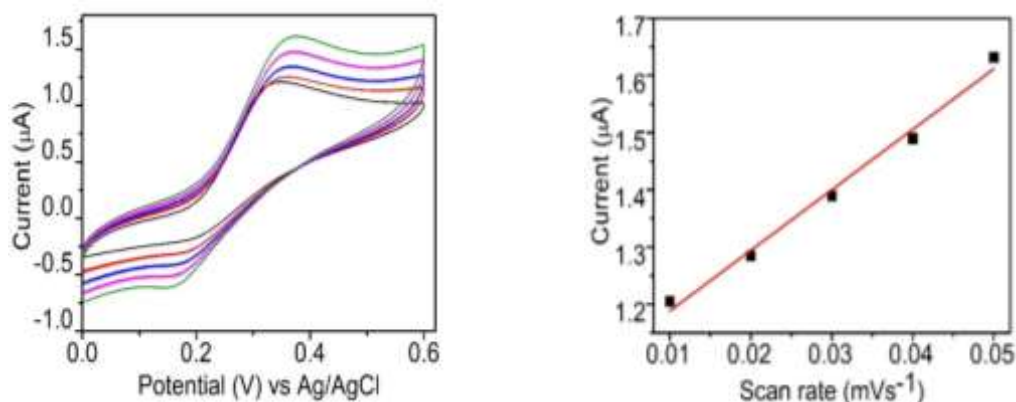


Fig 6.10. Cyclic voltammogram of dopamine at NiMgO /GCE scanning rate ranging from (10 mV^{-1} to 100 mVs^{-1}) and Inset: Calibration graph of peak current vs scan rate.

The cyclic voltammogram profile (fig 6.10) of 10 μM dopamine in PBS solution was measured at various scan rates using NiMgO /GCE electrode (10-100 mVs^{-1}). It was discovered that increasing the scan rate increased the oxidation peak current. The plot of oxidation peak current vs scan rate signifies that dopamine oxidation on NiMgO /GCE is a adsorption controlled process [74], with a linear regression line of $I = .066v-0.513$ and a coefficient of correlation of 0.9868 has been showed in (fig 6.10) [75].

6.4 Conclusion

A series of rare earth Sr^{2+} doped $\text{Ni}_{(0.5)}\text{Cu}_{(0.5-x)}\text{Sr}_x\text{MgO}_3$ nanoparticles were prepared by auto combustion method. The room temperature XRD patterns verified the existence of cubic phase structure. Crystallite size of the synthesized sample is ~ 25 nm. The FT-IR spectrum showed two absorption band that are characteristic of nanoferrites and with force constant the K_T values were less than the K_O values in the samples substituted with Sr^{2+} ions. FE-SEM Micrographs images were confirmed that the morphological structure is aggregated to the size of nanoparticles. The EDX spectrum confirms the doping concentration and freedom from impurity elements. The Tauc plots revealed an indirect allowed band gap in the range of 2.94 to 3.50 eV. The VSM analysis of coercivity showed a peak with particle size at a value smaller than the previously reported value of single-domain limit for $\text{NiSrGdFe}_2\text{O}_4$ that has been attributed to the enhanced role of the surface anisotropy as compared to the bulk for small sizes, which is the result of reduction in super exchange interaction. The maximum gas sensitivity is observed $\text{Ni}_{(0.5)}\text{Cu}_{(0.5-x)}\text{Sr}_x\text{MgO}_3$ 5000 ppm of butane gas at room temperature. This sample's response and recovery time are 11s and 133s, respectively. We can conclude that tailoring of structural, optical, gas sensor and magnetic properties can be achieved by substitution of proper amount of rare earth ions in cubic spinel phase. The electro-catalysis of the NiMgO/GCE was investigated via cyclic voltammetric technique. The results indicated that NiMgO/GCE is efficient towards the detection of dopamine at different concentration.

6.5 References

- [1] Shajudheen, V.M., M. Sivakumar, and S.S. Kumar, *Mater Today: Proc.* 3(6) (2016) 2450-2456.
- [2] Vinardell, M.P. and M. Mitjans, *Nanomaterials*, 5(2) (2015) 1004-1021.
- [3] Z. Alipour, M. Rezaei, F. Meshkani, *J. Ind. Eng. Chem.*, 20 (5) (2014) 2858-2863.
- [4] M. Khajenoori, M Rezaei, F. Meshkani, *J. Ind. Eng. Chem.* 21 (2015) 717-722.
- [5] Choudhary, V. R. Mamman, A. S. *Appl. Energy.* 66 (2) (2000) 161-175.
- [6] J. Min, Y Lee, H. Park, C. Zhang. *J. Ind. Eng. Chem.* 26 (2015) 375-383.
- [7] M. Millet, A. V. Tarasov, F. Girgsdies, G. Algara-Siller, R. Schlögl. *E Frei, ACS Catal.* 9 (9) (2019) 8534-8546.
- [8] M. A. Karimi, S. H. Roozbahani, R. Asadiniya, A. Hatefi- Mehrjardi, *Int. Nano Lett.* 1(1) (2011) 43-51.
- [9] M. C. Wu, J. S. Corneille, C. A. Estrada, J. W. He and D. W. Goodman, *Chem. Phys. Lett.* 182 (1991) 472-478.
- [10] S. K. Shukla, G. K. Parashar, A. P Mishra, P. Misra, B. C. Yadav, R. K. Shukla, L. M. Bali and G. C. Dubey, *Nano-like, Sensors Actuat B Chem.* 98 (2004) 5-11.
- [11] J. Sawai, H. Kojima, H. Igarashi, A. Hashimoto, S. Shoji, M. Sawaki. *J. Phys. Condens. Matter* 22 (2010) 074211.
- [12] J. P. Singh and K. H. Chae, *Condensed Matter* 2 (2017) 36.
- [13] J. Osorio-Guill'en, S. Lany, S. V. Barabash and A. Zunger, *Phys. Rev. Lett.* 96 (2006) 107203.
- [14] N. Pathak, S. K. Gupta, C. L. Prajapat, S. K. Sharma, P. S. Ghosh, B. Kanrar, P. K. Pujari and R. M. Kadam, *Phys. Chem. Chem. Phys.* 19(2017) 11975.
- [15] M. Cao, Y. Ma, X. Wang, C. Ma, W. Zhou, X. Wang, W. Tan and J. Du, *AIP Advances* 7 (2017) 056413.

- [16] Ch. N. Rao, Umesh T. Nakate, R. J. Choudhary and S. N. Kale, *Appl. Phys. Lett.* 103 (2013) 151107.
- [17] Ryu, B. K. Singh and K. S. Bartwal, *Adv. Cond. Matter Phys.* (2008) 1-6.
- [18] Matthew R, Maschmann, Placidus B, Amama, Amit Goyal, Zafar Iqbal, Roy Gat, Timothy S, Fisher. 44 (2006) 10-18.
- [19] Rizwan Wahab, S. G. Absari, M. A. Dar, Y. S. Kim, H. S. Shin. *Mater sci. forum* 558-559 (2007) 983-986.
- [20] X. Tran. H. Phuoc, Bret. Howard, V. Donald. Martello, YeeSoong and K. Minking. *Chyu. Opt. Laser. Eng.* 46 (2008) 829-834.
- [21] Y. Ding, Zhang, H. Wu, B. Hai, L. Wang and Y. Qian, *Nanoscale Chem. Mater.* 13 (2001) 435-439.
- [22] J. A. Wang, O. Novaro, X. Bokhimi, T. Lopez, R. Gomez, J. Navarrete, M. E. Llanos and E. Lopez-Salinas, *Mater. Lett.* 35 (1998) 317-323.
- [23] S. Utamapanya, K. J. Klabunde, J. R. Schlup, *Chem. Mater.* 3 (1991) 175-180.
- [24] C. Henrist, J. P. Mathieu, C. Vogels, A. Rulmont and R. Cloots, *J. Cryst. Growth.* 249 (2003) 321-325.
- [25] J. P. Singh, W. C. Lim, S. O. Won, J. Song and K. H. Chae. *J Kor Phy Soc.* 72 (2018) 890-899
- [26] Meybodi, S.M., et al., *Ultra sonochem.* 19(4) (2012) 841-845.
- [27] R. Bhargava, S. Khan¹, N. Ahmad and M. M. Nizam Ansari, *IOP Conf. Series: Mat Sci Eng.* 577 (2019) 012050.
- [28] S. Azzaza, M. El-Hilo, S. Narayanan, J.J. Vijaya, N. Mamouni, A. Benyoussef, A. El Kenz, M. Bououdina, *Mater. Chem. Phys.* 143 (2014) 1500.
- [29] S. Suwanboon, P. Amornpitoksuk, A. Sukolrat, *Ceram. Int.* 37 (2011) 1359
- [30] Lingaraju, K., et al., *Arab J Chem.* 13(3) (2020) 4712-4719.
- [31] Anand, G.T., et al., *Surf Inter.* 18 (2020) 100460.
- [32] Budiredla, N., et al., *Inter Sch Res Not.* (2012).

- [33] K. Kaviyarasu and Prem Anand Devarajan, *Adv. Appl Sci. Res*, 2(6) (2011) 131- 138.
- [34] Lin K-F, Cheng H-M, Hsu H-C, Lin L-J and Hsieh W-F. *Chem. Phys. Lett.* 409 (2005) 208–11.
- [35] Ahmad, M., et al., *J. Alloys Compd.* 577 (2013) 717-727.
- [36] J. Lakshmikantha, G. Krishnamurthy, B.M. Nagabhushan, E. Melagiriappa, *J. of Solid State Chemistry.* 315 (2022) 123465.
- [37] J. Lakshmikantha, G. Krishnamurthy, R. Hanumantha Nayak, Malathesh Pari, N. Ranjitha, Nagaraj Naik. *J Ing chem com.* (2022) 110175.
- [38] M. Kapilashrami, J. Xu, K.V. Rao, L. Belova, *Process. Appl. Ceram.* 4 (2010) 225.
- [39] Bokhimi, A. Morales, T. Lopez, R. Gomez, *J. Solid State Chem.* 115 (1995) 411.
- [40] S. Alone, S.E. Shirsath, R. Kadam, K. Jadhav, *J. Alloys Compd*, 509 (2011) 5055-5060.
- [41] G. Fischer, M. Deane, A. Ernst, P. Bruno, M. L€uders, Z.Szotek, W. Temmerman, and W. Hergert, *Phys. Rev. B.* 80(1) (2009) 014408.
- [42] M. Li, D. Long, R.Ahuja, and Yunbin He *Phys. Status Solidi B.* (2017) 1700085.
- [43] M. A. Almessiere, Y. Slimani, H.S. El Sayed, A. Baykal, I. Ercan, *J. Magn. Mater.* 471 (2019) 124–132.

CHAPTER 7:-

ELECTROCHEMICAL AND
ELECTROLYSIS OF Gd^{3+}
SUBSTITUTED TO SPINEL
($NiSrFe_2O_4$) NANO-FERRITES;
SYNTHESIS, STRUCTURAL,
MORPHOLOGICAL AND
MAGNETIC PROPERTIES

7.1 Introduction

Nickel ferrite (NiFe_2O_4) is one of the most important materials in the inverse spinel family exhibiting ferrimagnetic properties combined with relatively low electrical properties and it displays low eddy current loss in alternating current applications [1]. These materials are preferred over other magnetic materials i.e. alloys because of their excellent chemical stability, good mechanical hardness, high electrical resistivity and reasonable cost. Nickel ferrite unit cell contains 32 oxygen atoms in a cubic close packing with eight tetrahedral (A) and sixteen octahedral (B) sites. Half of the ferric ions preferentially fill the A-sites and the others occupy the B-sites. Thus the compound can be represented by the formula $(\text{Fe}^{3+})_A [\text{Ni}^{2+} \text{Fe}^{3+}]_B \text{O}_4^{2-}$ [2,3]. However, it shows ferrimagnetism that originates from magnetic moment of antiparallel spins between Fe^{3+} ions at tetrahedral sites and Ni^{2+} ions at octahedral sites [4]. The area of research is more attracted to the researchers from last few decades due to their promising magnetic nanomaterials with appropriate physicochemical properties, functionalized surface and improved biocompatibility have been broadly examined for different restorative, indicative, and remedial applications, for example, magnetic nanofluids (Ferrofluids), specific drug delivery, fluid hyperthermia, as a contrast enhancer in magnetic resonance or reverberation imaging (MRI), cell detachment, tissue fixing, biosensors, and magnetic fluid hyperthermia therapies (MFHT) of cancerous cells in human body. Magnetic nanoparticles are alluring catalyst since they can be isolated from the response medium by applying an outside magnetic attractive field. Magnetic partition is a charming option in contrast to filtration or centrifugation as it keeps the loss of catalyst and upgrades reusability, rendering the catalyst cost-adequacy and is promising for modern applications [5-10].

In order to improve the electrical and magnetic properties of spinel ferrites rare earth ions like Gd^{3+} , La^{3+} , Ce^{3+} , Sm^{3+} and Dy^{3+} have been doped by some of the researchers. It was reported that rare earth ion substitution lead to the structural distortion and improvement in the electrical and magnetic properties. Rare earth ions are known to have unpaired 4f electrons and strong spin orbit coupling of angular momentum. The magnetic anisotropy is a key parameter that controls the magnetic transition temperature between super paramagnetic and ferromagnetic phases in nanoparticles [11-14]. From the literature, they were found to be suitable as gas sensing materials. They were explored to detect various gases, some of the ferrites, for example, Fe_2O_4 , $CoFe_2O_4$, $CuFe_2O_4$, $NiFe_2O_4$, $ZnFe_2O_4$, etc., have been studied extensively for different gas-sensing applications. It is very important to detect and identify the hazardous gas molecules which are combined in the atmosphere, if humans are continuously exposure to high concentrations of toxic gases leads to neurological sequelae, unconsciousness and sometimes death [15, 16]. Gas sensors operating at room temperature are more important because of their low power operation and also the life time of sensors is enhanced. The efficiency of gas sensors depends on low density and large surface area to increase gas exposure, thus gas sensing devices that use ferrite nanoparticles are exhibited enhanced performance.

The preparation and characterization of $NiFe_2O_4$ in nanoscale would allow investigating the fundamental aspects of anomalous properties different from those of bulk properties. There are plenty of methods available to synthesize $NiFe_2O_4$ nanostructures including, sonochemical, sol-gel route, hydrothermal, co-precipitation, micro emulsion technique, self-propagation and combustion methods [17-23]. Among these methods, auto combustion method is a very promising method for

synthesizing the desired phase. It is very simple method which have many advantages like easy manufacture, low cost, high purity of crystallinity, chemical uniformity, short processing time and finer particles size distribution. The present investigation was aimed on the systematic analysis of the structure, morphological, optical, magnetic properties, electro-chemical and gas sensor ability of the $\text{Ni}_{0.5}\text{Sr}_{0.5}\text{Gd}_x\text{Fe}_{2-x}\text{O}_4$ ($x = 0.00, 0.01, 0.05$ and 0.09) nickel ferrite nanoparticles prepared by auto combustion method.

7.2. Experimental Method

7.2.1. Synthesis method

The samples of $\text{Ni}_{0.5}\text{Sr}_{0.5}\text{Gd}_x\text{Fe}_{2-x}\text{O}_4$ ($x = 0.00, 0.01, 0.05$ and 0.09) nanoparticles were prepared via auto combustion method. The small quantity of Gd^{3+} ion substituted stoichiometrically of analar grade. The starting chemicals used are: $\text{Ni}(\text{NO}_3)_2 \cdot 6\text{H}_2\text{O}$ (Merck), $\text{Sr}(\text{NO}_3)_2$ (Merck), $\text{Fe}(\text{NO}_3)_3 \cdot 9\text{H}_2\text{O}$ (Sigma Aldrich), $\text{Gd}(\text{NO}_3)_3 \cdot 6\text{H}_2\text{O}$ (Sigma Aldrich), urea ($\text{CH}_4\text{N}_2\text{O}$). The petri dish carrying the solution of redox mixture placed into a heat furnace attained at 550 ± 10 °C. The solution begins to boil in a furnace and heat reduction and ignition at one point, followed by decomposition and generate an amount of gas (N_2O and CO_2). When a solution reaches its self-ignition point, it begins to burn, releasing a large amount of heat and instantly evaporating all the solution, solidifying and burning, forming a fluffy with loose powder. This leads to better product homogeneity by bringing the unreacted particles closer together, which tends to reduce the diffusion distance as well as the particle size distribution. All the prepared $\text{Ni}_{0.5}\text{Sr}_{0.5}\text{Gd}_x\text{Fe}_{2-x}\text{O}_4$ samples of nanomaterial's were undergoes characterized and their optical, magnetic properties, electrochemical and gas sensor application has been studied

7.3 Results and Disussion

7.3.1 Powder X-ray diffraction studies

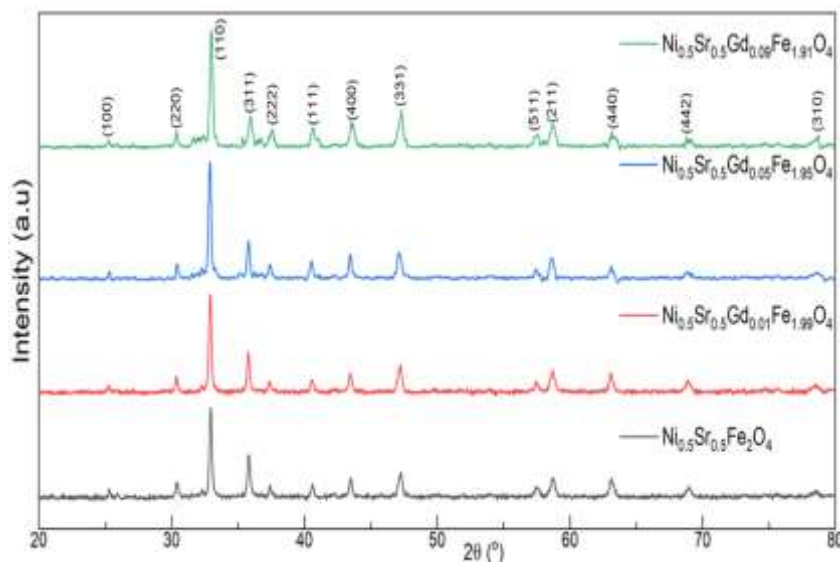


Fig 7.1 PXRD patterns of $\text{Ni}_{0.5}\text{Sr}_{0.5}\text{Gd}_x\text{Fe}_{2-x}\text{O}_4$ ($x = 0.00, 0.01, 0.05$ and 0.09) nanoferrites

The structural examination of the nickel ferrite nanoparticles was investigated by the x-ray beam diffraction. The PXRD patterns of $\text{Ni}_{0.5}\text{Sr}_{0.5}\text{Gd}_x\text{Fe}_{2-x}\text{O}_4$ ($x = 0.00, 0.01, 0.05$ and 0.09) nanoferrites were captured on a Bruker XRD with $\text{CuK}\alpha$ radiation having wavelength 1.5406 \AA (Model: D8 Advance, Germany). In the Bragg angle range of $20^\circ - 80^\circ$ at a scan rate of 2° min at 300 K . From the fig 7.1, peaks of the XRD pattern of all samples matched with the JCPDS card No. 86-2267 [24] and these are indexed as (100), (220), (110), (311), (222), (111), (400), (331), (511), (211), (440), (442), (310) planes indicating the cubic spinel structure of nickel ferrite. The XRD data was used to evaluate different structural parameters by using the following relations and their values are given in table 7.1. [25, 26]

$$a = d\sqrt{h^2 + k^2 + l^2} \text{ \AA} \quad (7.1)$$

where, utilizing the estimations of Bragg's angle (2θ) and interplanar spacing (d), the estimations of lattice parameter. V_{cell} is the unit of the cubic spinel ferrites and is determined as follows:

$$V_{cell} = a^3 \text{ \AA}^3 \quad (7.2)$$

where, the numerical values is sustained for the spinel system. From, the XRD peaks, an average crystallite sizes of the nanoferrites are determined using Debye-Scherrer equation (d) and is calculated by:

$$d = \frac{k\lambda}{\beta \cos\theta} \quad (7.3)$$

where, $k = 0.89$ is Scherer's constant, $\lambda = 0.15406$ nm is wavelength of the incident X-rays in nm, β is the full width at half maximum (FWHM) of diffraction peak, θ is the Bragg diffraction angle. The average value of crystallite size is found in the range 27 nm to 30 nm, increases with Gd^{3+} content and values are tabulated in table 6.1. The measured x-density is calculated by using relation as follows,

$$\rho_x = \frac{8M}{Na^3} \quad (7.4)$$

where, M is the molecular weight of the sample, N the Avogadro's number and a^3 the volume of the cubic unit cell. The bulk density is calculated by using relation as mentioned below:

$$\rho_b = \frac{m}{\pi r^2 h} \quad (7.5)$$

where, m is the mass, r is the radius and h is the height of the pellet. Percentage porosity was calculated using the formula.

$$P = \left(1 - \frac{\rho_b}{\rho_x}\right) \quad (7.6)$$

where, ρ_x is the x-ray density and the ρ_b bulk density.

The lattice constant (a) increases slightly for all the compositions. The variation can be explained on the basis of ionic radii of the substituted ions. The replacement of the

smaller Fe³⁺ ions (0.64 Å) with larger Gd³⁺ ions (0.93 Å) causes dilation of the host spinel lattice which results in the increase of lattice constant 8.34 to 8.59 Å without changing the crystal structure. The influence of gadolinium concentration on X-ray density (ρ_x) and bulk density (ρ_b) are tabulated in Table 7.1. X-ray density exhibits an increasing trend with gadolinium contents as it mainly depends upon the molecular weight of the samples. It increases from 5.93 to 8.44 g/cm³. The bulk density also increases with gadolinium contents from 4.67 to 6.85 g/cm³ which can be attributed to the difference in atomic weight of gadolinium (157.25 amu) and iron (55.845 amu) as described in CRC book [27]. The formation of secondary phase (GdFeO₃) fills inter granular voids and exhibits good densification. Therefore, a decrease in the percentage porosity can be expected with gadolinium contents are showed in Table 7.1 [28].

Table 7.1: Crystallite size (D), lattice constant (a), cell volume (V), X-ray density (q_{x-ray}), bulk density and percentage porosity of Ni_{0.5}Sr_{0.5}Gd_xFe_{2-x}O₄ (x =0.00, 0.01 < x < 0.09) nanoferrites.

Composition	Crystallite size (D) /nm	Lattice constant (a)/Å	Cell volume (V)/Å ³	X-ray density(q _{x-ray})/g cm ³	Bulk Density g/cm ³	Percentage Porosity (%)
Ni _{0.5} Sr _{0.5} Fe ₂ O ₄	28.31	8.34	580.1	5.93	4.67	29.35
Ni _{0.5} Sr _{0.5} Gd _{0.01} Fe _{1.99} O ₄	27.97	8.45	603.4	8.19	6.78	19.19
Ni _{0.5} Sr _{0.5} Gd _{0.05} Fe _{1.95} O ₄	29.49	8.52	618.5	8.44	6.82	16.22
Ni _{0.5} Sr _{0.5} Gd _{0.09} Fe _{1.91} O ₄	30.48	8.59	633.8	7.91	6.85	13.40

7.3.2 FT-IR analysis

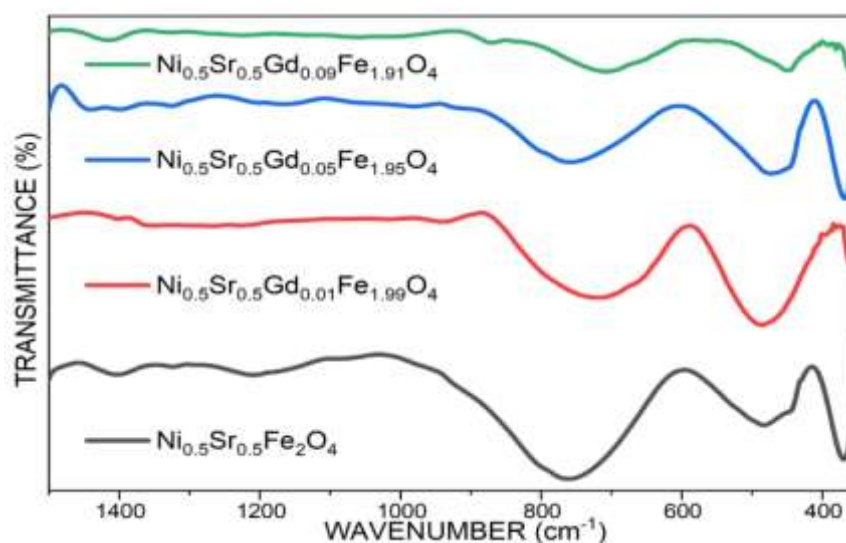


Fig 7.2 FT-IR spectra of Ni_{0.5}Sr_{0.5}Gd_xFe_{2-x}O₄ ($x = 0.00, 0.01, 0.05$ and 0.09) nanoferrites

The formation of functional groups was confirmed by Fourier transform infrared (FT-IR) spectroscopy. At room temperature FTIR spectra of all nickel ferrites were recorded by employing Thermo-Nicolet 6700 FTIR (Make: Perkin Elmer, Model: Spectrum Two, USA) in the wavenumber range 4000 - 300 cm⁻¹. The samples (0.5 to 1.0 mg) were mixed with spectral grade potassium bromide (KBr) as the standard ground and then pressed to obtain circular discs of appropriate 1mm thickness. The FT-IR spectra of the prepared series of Ni_{0.5}Sr_{0.5}Gd_xFe_{2-x}O₄ ($x = 0.00, 0.01, 0.05$ and 0.09) nanoparticles are depicted in fig 6.2. Two metal–oxygen (M–O) vibration modes were revealed by FT-IR spectra within the range of 1500 to 350 cm⁻¹ confirming the successful formation of spinel ferrites. The first band (ν_1) with the maximum frequency was observed in the range 370 cm⁻¹ and the second band (ν_2) with minimum frequency in the range 490 cm⁻¹, which indicates metal–oxygen stretching at tetrahedral (A) site and octahedral (B) site, respectively [29]. The peaks with wavenumber of ~ 800 cm⁻¹ are due to the vibration of the Fe – OH bond. The

position of peak slightly changed in Gd^{3+} ion substituted samples. Therefore, gadolinium ions replaces Fe^{2+} ions without changing the crystal structure of the composition. Furthermore, the absence of bands in the wavenumber range 3200 - 3500 cm^{-1} indicating that the non-existence of an OH group in the reaction method [30]. A force constant is a secondary potential energy identified by the radius of the site. The force constants for tetrahedral and octahedral sites are given by the relations.

$$K_T = 4\pi^2 c^2 \nu_1^2 m \quad (7.7)$$

$$K_O = 4\pi^2 c^2 \nu_2^2 m \quad (7.8)$$

where c - speed of light 2.99×10^8 m/s, ν_1 and ν_2 are the vibrational frequencies cm^{-1} at A- and B-sites cm^{-1} respectively, m - decreased mass of Fe^{3+} and O^{2-} ions.

From table 7.2, it is observed that the value of force constant from 0.99 – 1.09 newton/m for tetrahedral sites (K_T) is lower than that for octahedral site (K_O) from 1.73 – 1.77 newton/m. Furthermore, the values K_T and K_O are found to be increased with increase in Gd^{3+} ion substitution. However, the K_T values are less than the K_O values in the samples substituted with Gd^{3+} ions [31].

Table 7.2: Position of IR absorption bands and force constant of of $Ni_{0.5}Sr_{0.5}Gd_xFe_{2-x}O_4$ ($x=0.00, 0.01 < x < 0.09$) nanoferrites.

Composition	Position of $\nu_1 (cm^{-1})$	Force constant Tetrahedral (K_T) newton/m	Position of $\nu_2 (cm^{-1})$	Force constant Octahedral (K_O) newton/m
$Ni_{0.5}Sr_{0.5}Fe_2O_4$	370	0.998	488	1.73
$Ni_{0.5}Sr_{0.5}Gd_{0.01}Fe_{1.99}O_4$	369	0.993	490	1.75
$Ni_{0.5}Sr_{0.5}Gd_{0.05}Fe_{1.95}O_4$	371	1.03	491	1.75
$Ni_{0.5}Sr_{0.5}Gd_{0.09}Fe_{1.91}O_4$	372	1.09	493	1.77

7.3.3 FE-SEM analysis

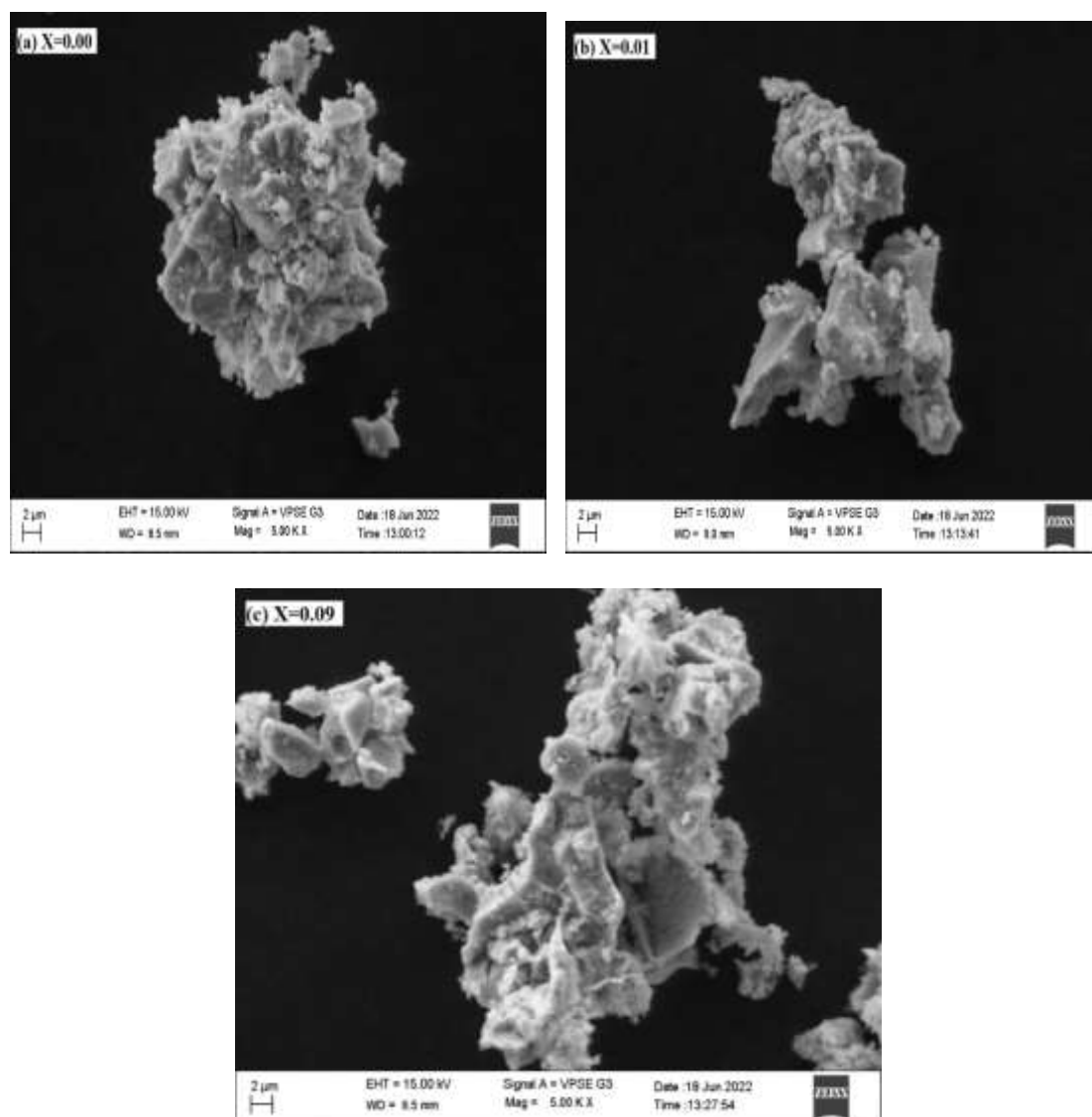
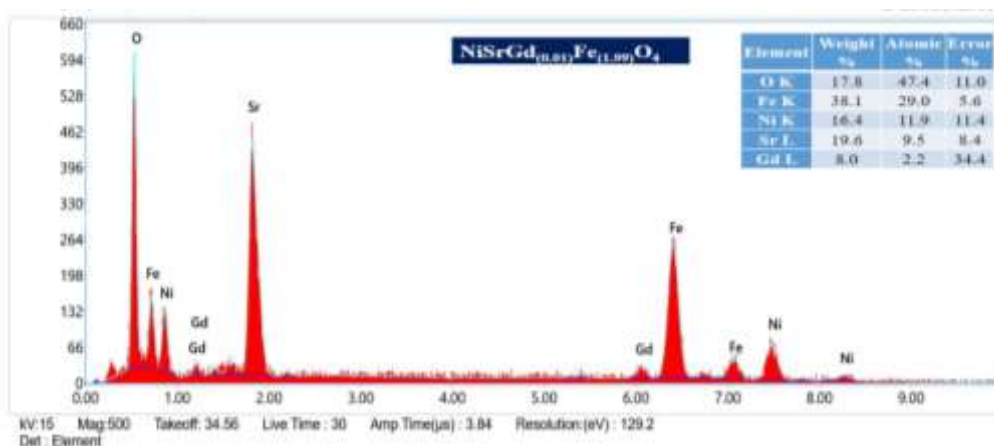
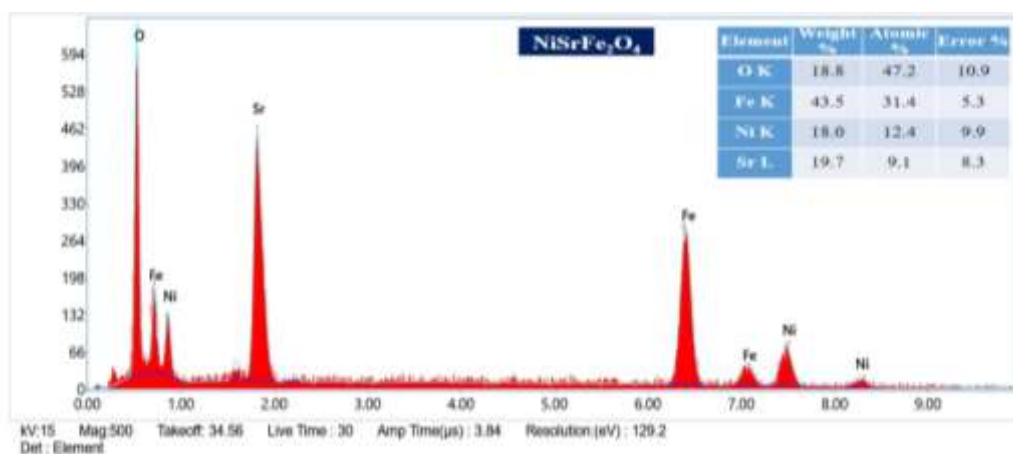


Fig 7.3 FESEM Micrographs of $\text{Ni}_{0.5}\text{Sr}_{0.5}\text{Gd}_x\text{Fe}_{2-x}\text{O}_4$ ($x = 0.00$ (a), 0.01 (b) and 0.09 (c)) nanoferrites

The microstructure of pure nano ferrites of $\text{Ni}_{0.5}\text{Sr}_{0.5}\text{Gd}_x\text{Fe}_{2-x}\text{O}_4$ ($x = 0.00$, 0.01 , 0.05 and 0.09) were examined by FESEM (Model: JEOL/EO JSM-639, Germany) as showed in fig 7.3. It is clear from the micro-graphs that both pure and Gd^{3+} substituted nanoparticles have almost irregular morphology and grain boundaries are not prominent. The agglomeration of the particles is more visible in the nanoparticles, it is due to the accumulation of some Gd^{3+} ions at grain boundaries

instead of replacing Fe^{+3} ions at octahedral sites of spinel lattice. In the result of this aggregation, particle size reduction was observed which is in agreement with the crystallite size obtained from XRD results [58]. The line intercept procedure is used to estimate an average grain size using the relation: $G_{av} = 1.5 L/ MN$ where L-total length of test line in m, M – magnification, N - total number of grains intercept. The particles sizes are calculated and they are found to be in the range of 35 - 60 nm. As particle sizes are in the nano scale range (1–100 nm) so, FE-SEM analysis confirmed the formation of nanoparticles [32].

7.3.4 EDAX analysis



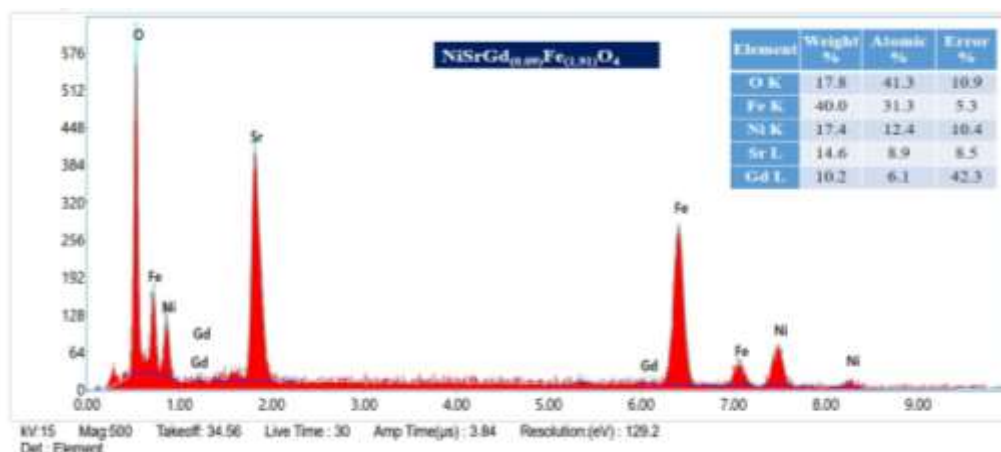


Fig 7.4 EDAX of $\text{Ni}_{0.5}\text{Sr}_{0.5}\text{Gd}_x\text{Fe}_{2-x}\text{O}_4$ ($x=0.00, 0.01$ and 0.09) nanoferrites

The chemical proportions of the samples are recorded using Energy dispersive X-ray analysis spectra EDS (Carl Zeiss, Model: EVOLS15, Germany). The elemental analysis of the $\text{NiSrGd}_x\text{Fe}_{2-x}\text{O}_4$ ($x = 0.00, 0.01, 0.05$ and 0.09) of all the composites are presence of elements, Ni, Sr, Gd, Fe and O as shown in fig 7.4. There was no other elements are observed in all the samples of spectra which confirms the high crystallinity of all the samples.

7.3.5 OPTICAL properties

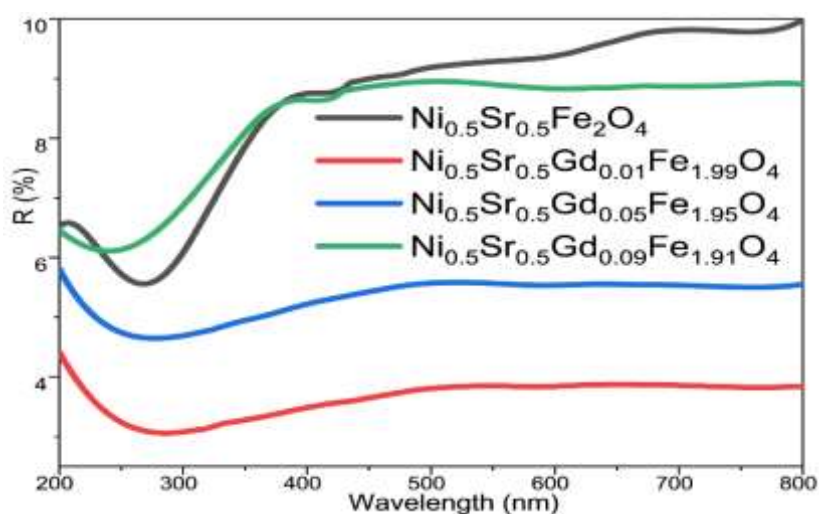


Fig 7.5 The reflectance Spectra of $\text{Ni}_{0.5}\text{Sr}_{0.5}\text{Gd}_x\text{Fe}_{2-x}\text{O}_4$ ($x = 0.00, 0.01, 0.05$ and 0.09) nanoferrites

The UV–Visible spectroscopy is a useful tool to investigate the absorption, transmission or reflection band of a semiconducting material. We have conducted the (Shimadzu-UV-2600) UV–Vis spectra measurement of all synthesized samples in absorption mode over the range of $200 \text{ nm} \leq \lambda \leq 800 \text{ nm}$. Optical reflection spectra utilizing Kubelka-Munk (K-M) model, & $F(R)$ was estimated from the accompanying conditions. The optical band gap of all Gd^{3+} doped nanoparticles were analyzed using the following equations.

$$E_g = \frac{hc}{\pi\lambda} = \frac{1240}{\lambda} \quad (7.9)$$

$$F(R_\infty) = \frac{(1-R_\infty)^2}{2R_\infty} \quad (7.10)$$

$$\{(F(R_\infty)h\nu\}^{1/n} \propto (h\nu - E_g) \quad (7.11)$$

Where: h is the Planck constant ($6.626 \times 10^{-34} \text{ Js}$).

c is the speed of light ($2.99 \times 10^8 \text{ ms}^{-1}$).

λ is the wavelength that corresponds to reflectance spectra.

R_∞ is the diffuse reflectance spectra.

α is the absorption coefficient.

ν is frequency of the incident light.

E_g is the bandgap energy.

$n = 2$ for direct bandgap.

The absorption spectrum of pure $\text{NiSrGd}_x\text{Fe}_{2-x}\text{O}_4$ ($x = 0.00, 0.01, 0.05$ and 0.09) showed in fig 7.5, two characteristic absorption peaks attributed to the conducting emeraldine salt, one is around 285 nm and other is at 430 nm. The first absorption band assigned at $\sim 300 \text{ nm}$ is due to the $\pi-\pi^*$ electronic transitions and other is assigned at 430 nm due to the polaron band also represents the presence of lone pair electrons of nitrogen [33-34]. The absorption increases with increasing Gd^{3+}

concentration of NiFe_2O_4 nanocomposites. In accordance with Beers law, the absorption is proportional to the number of absorbing molecules. These results suggest that there are interactions with $\text{NiSrGd}_x\text{Fe}_{2-x}\text{O}_4$ nanoparticles.

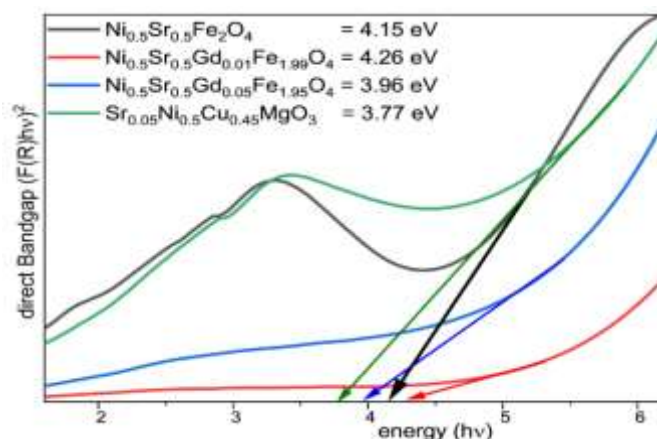


Fig 7.6 Bandgap energy of $\text{Ni}_{0.5}\text{Sr}_{0.5}\text{Gd}_x\text{Fe}_{2-x}\text{O}_4$ ($x = 0.00, 0.01, 0.05$ and 0.09) nanoferrites

The direct energy band gap (E_g) values were obtained by extrapolating the linear part of the $(\alpha h\nu)^2$ curve versus $(h\nu)$ as shown in fig 7.6. The energy band gap (E_g) values are tabulated in table 7.3. It is clear that there is a decrease in the band gap 3.77 to 4.26 eV of the Gd^{3+} doped nickel nanoferrites samples when compared to pure NiFe_2O_4 . The shift in band gap of the $\text{NiSrGd}_x\text{Fe}_{2-x}\text{O}_4$ nanoparticles with decreasing crystallite size is the result of quantum confinement effects arising from the small size regime [35].

Table 7.3: UV-Vis absorption band gap values of $\text{Ni}_{0.5}\text{Sr}_{0.5}\text{Gd}_x\text{Fe}_{2-x}\text{O}_4$ ($x = 0.00, 0.01 < x < 0.09$) nanoferrites.

Sl. No	Composition	Band gap (eV)
1	$\text{Ni}_{0.5}\text{Sr}_{0.5}\text{Fe}_2\text{O}_4$	4.15
2	$\text{Ni}_{0.5}\text{Sr}_{0.5}\text{Gd}_{0.01}\text{Fe}_{1.99}\text{O}_4$	4.26
3	$\text{Ni}_{0.5}\text{Sr}_{0.5}\text{Gd}_{0.05}\text{Fe}_{1.95}\text{O}_4$	3.96
4	$\text{Ni}_{0.5}\text{Sr}_{0.5}\text{Gd}_{0.09}\text{Fe}_{1.91}\text{O}_4$	3.77

7.3.6 Magnetic Measurements

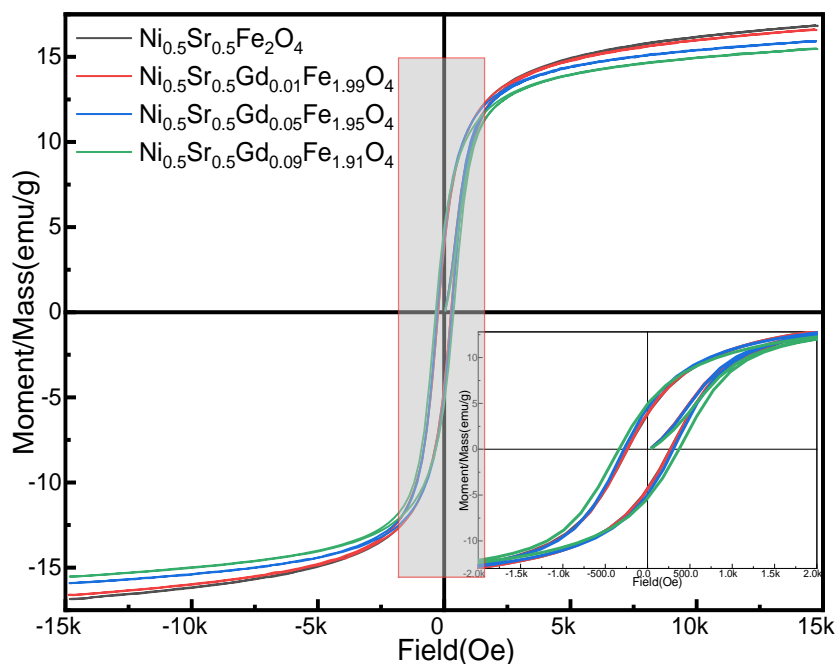


Fig 7.7 Hysteresis curves of $\text{Ni}_{0.5}\text{Sr}_{0.5}\text{Gd}_x\text{Fe}_{2-x}\text{O}_4$ ($x = 0.00, 0.01, 0.05$ and 0.09) nanoferrites

Vibrating sample magnetometer (VSM) (Make: CREST, Model: 20130523-01) was employed to characterize the magnetic properties. The magnetic hysteresis loops of $\text{NiSrGd}_x\text{Fe}_{2-x}\text{O}_4$ measured at room temperature are shown in Fig 7.7. It can be observed from M–H loops that soft magnetic behaviour exists for the pure and gadolinium doped nickel ferrites with a decrease in magnetization with increase in the concentration of Gd^{3+} ions ($x = 0.00, 0.01, 0.05$ and 0.09). The information about saturation magnetization (Ms), remanence magnetization (Mr), Coercivity (Hc), squareness ratio (S), Magneton number (η_B), anisotropy constant (K) and Yafet-Kittle angle α (Y-K) fields was deduced from respective M-H curves of the sample and Table 7.4. The magnetic parameters are calculated using the following relations [36, 37].

$$S = \frac{M_r}{M_s} \quad (7.12)$$

$$K = \frac{H_c \times M_s}{0.64} \quad (7.13)$$

Where, M_s is saturation magnetization (emu/g), M_r is remanent magnetization, $k = 0.64$ is constant magnetic anisotropic and H_c is the coercivity. The values of, Magnetron number (η_B) and Yafet and Kittel angles are given by the relation

$$\eta_B = \frac{M \times M_s}{5585} \quad (7.14)$$

$$\cos \alpha(Y - K) = \left[\frac{n_B + 5(1-x)}{(6-x)} \right] \quad (7.15)$$

where η_B is the magnetic moment (number of Bohr magnetrons), M_w is molecular weight of the composition (x) in g, M_s is saturation magnetization (emu/g), 5585 is the magnetic factor.

The magnetic properties of the NiFe_2O_4 with an inverse spinel structure can be explained in terms of the cations distribution and magnetization originates from Sr^{2+} and Fe^{3+} ions have A-A exchange at tetrahedral sites, while Ni^{2+} , Fe^{3+} , and RE^{3+} ions have B-B interactions at octahedral sites. Both the tetrahedral and octahedral ions have A-B super exchange interaction. [38, 39]. Hysteresis loops in fig 7.7 are typical for soft magnetic materials and the “S” shape of the curves together with the negligible coercivity ($H_c = \leq 0.60$ Qe) indicate the presence of small magnetic particles exhibiting super paramagnetic behaviors [40 - 42]. The observed magnetic behaviour of the present samples can also be explained on the basis of Neel’s model [43]. According to Neel, the Neel’s magnetic moment (calculated magneton number) is given by $M_s = M_B - M_A$, where M_B is a magnetic moment of B sublattice and M_A is magnetic moment of A sublattice. It is known that, the spinel crystal structure consists of two interstitial sites namely tetrahedral (A) and octahedral [B] site. Among these

interstitial sites, the inter sublattice A-B superexchange interaction and intra sublattice A-A and B-B superexchange interaction exists. A-B interaction is much stronger than the A-A interaction and B-B interaction. The values of M_B and M_A are calculated considering the following cation distribution based on the site preference energy of the Gd^{3+} ($7 \mu_B$) replaces Fe^{3+} ($5 \mu_B$) in an octahedral position (B site), and Gd^{3+} has higher spin magnetic moment than Fe^{3+} . The substitution of Gd^{3+} ions at the B site will affect the interaction between Ni–O–Gd ions, and affect the sublattice exchange energy between Ni–O–Fe [44, 45].

The magnetic moment of the Fe^{2+} ion decreased with the increasing of the Gd^{3+} ions, this action for this increase in value is due to the increasing of the super exchange interaction between the different sites, leading to an increase in the values ($7.50 - 6.93 \mu_B$). This indicates the increasing of the super-exchange interactions [41]. Magnetization values of the $NiSrGd_xFe_{2-x}O_4$ samples are decreases from for M_s 39.46 emu/g – 36.45 emu/g with increase of the Gd^{3+} ion content. M_r in the range of 20.35 – 18.59 emu/g at room temperature. H_c is in the scope of 3363 - 2418 Oe at room temperature. This reduction is associated with the equivalent reduction of Fe^{3+} ions to charge-compensating Fe^{2+} ions replaced with Gd^{3+} ions. Moreover, the magnetic moment of Fe^{2+} ions ($4 \mu_B$) is lower than that of the Fe^{3+} ions ($5 \mu_B$) [46, 47].

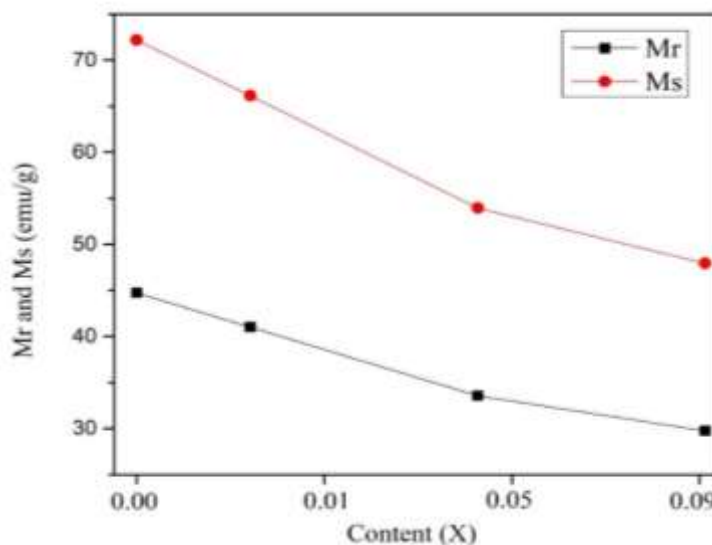


Fig 7.8 Variation of M_s and M_r of $Ni_{0.5}Sr_{0.5}Gd_xFe_{2-x}O_4$ ($x = 0.00, 0.01, 0.05$ and 0.09) as a function of Gd^{3+} contents

Fig 7.8. Show this variation of M_s and M_r with respect to the concentrations of the Fe^{3+} ion site of gadolinium ion substitution. In addition, substituted Gd^{3+} ions occupy the spins-up sites. The contrast of these ionic radii can cause strains that cause variations in electronic states and disorder in cubic spinel systems [48]. The squareness ratio values are observed in the scope of $0.52 - 0.50$ emu/g indicates that the particles are in the single magnetic domain, and those < 0.5 indicate particles with a multi-domain structure, shows that all the synthesized nickel nano-ferrites investigate the nature of a single magnetic domain [49, 50].

Fig 7.9. This indicates that the variation of $\eta\beta$ with $\alpha(Y-K)$ respect to the concentrations of the Gadolinium ion substitution Fe^{3+} ion site. M_r remanence for permanent magnetic field applications is a strong function of thickness, concentration and orientation. Furthermore, variants of could explain the variations of the magnitudes of M_s for their relationship between η_B and M_s [51].

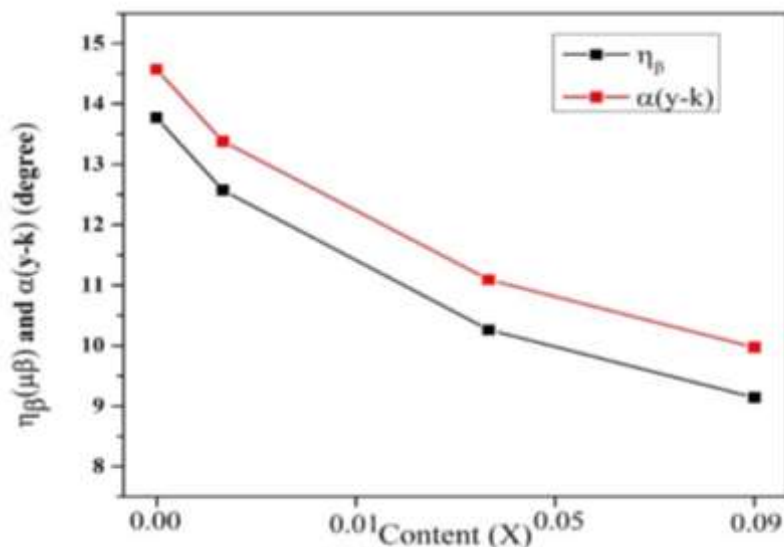


Fig 7.9 Variation of η_B and $\alpha(Y-K)$ of $Ni_{0.5}Sr_{0.5}Gd_xFe_{2-x}O_4$ ($x = 0.00, 0.01, 0.05$ and 0.09) as a function of Gd^{3+} contents

Furthermore, this suggests that the observed non-interacting and anisotropic particles are of the cubic anisotropy type. The anisotropy of $NiSrGd_xFe_{2-x}O_4$ decreasing with the increase of Gd^{3+} ions is due to the reduced particle size values are found to be 0.21 - 0.14 (erg/Oe). In this investigation, the coercive value decreases as the Gd^{3+} ion content increases. The coercive force obtained by reversing the direction of movement of the wall and that of rotation of the province to change the opposite direction of the applied magnetic field [52, 53]. In general, the effective clamping of the domain walls leads to coercivity, consequently a larger grain size H_c decreases. Smaller particle size materials were used to achieve high core loss. The H_c is mainly determined by the magnetocrystalline anisotropy and by typical particle size the variations of H_c and particle size are inversely proportional.

$\alpha(Y-K)$ Yafet-Kittel angle, the degree of spin canting effect is explained using Yafet- Kittle angle $\alpha(Y-K)$ [54]. The calculated values of $\alpha(Y-K)$ decrease from 8.33 – 7.72 degrees with increasing in Gd^{3+} ion concentration due to the

approximation of the molecular field using a non-collinear three sub-lattice model and an increasing tendency for triangular spin arrangement exchange interaction [55].

Table 7.4: Magnetic properties i.e. coercivity (Hc), saturation magnetization (Ms), remanence (Mr), squareness ratio (Mr/Ms), $\eta\beta$, K and $\alpha(Y-K)$ of $\text{Ni}_{0.5}\text{Sr}_{0.5}\text{Gd}_x\text{Fe}_{2-x}\text{O}_4$ ($x=0.00, 0.01 < x < 0.09$) nanoferrites.

Composition	M_s (emu/g)	Hc (Oe)	Mr (emu/g)	S (emu/g)	$\eta\beta$ ($\mu\beta$)	K (erg/Oe)	Cos $\alpha(y-k)$ (degree)
$\text{Ni}_{0.5}\text{Sr}_{0.5}\text{Fe}_2\text{O}_4$	39.46	3363	20.35	0.52	7.50	0.21	8.33
$\text{Ni}_{0.5}\text{Sr}_{0.5}\text{Gd}_{0.01}\text{Fe}_{1.99}\text{O}_4$	38.01	2977	19.76	0.52	7.23	0.18	8.06
$\text{Ni}_{0.5}\text{Sr}_{0.5}\text{Gd}_{0.05}\text{Fe}_{1.95}\text{O}_4$	37.72	2603	18.85	0.50	7.17	0.15	7.97
$\text{Ni}_{0.5}\text{Sr}_{0.5}\text{Gd}_{0.09}\text{Fe}_{1.91}\text{O}_4$	36.45	2418	18.59	0.51	6.93	0.14	7.72

7.3.7 Gas sensing Measurements

Gas sensing measurement were carried out by making use of an in-house fabricated gas sensing chamber. The prepared samples were pressed into pellets of the thickness of 0.7 – 1 mm and diameter of 13 mm, the two dots of silver paste were placed on the surface of the samples to get the ohmic contacts. The prepared pellet sample was kept inside the gas-sensing chamber and the electrical resistance of the sample was measured in air (R_a) and the presence of test gas (R_g) at room temperature. The butane gas sensing studies were characterized for all the prepared $\text{NiSrGd}_x\text{Fe}_{2-x}\text{O}_4$ samples at 150 °C temperature are shown in fig 7.10.

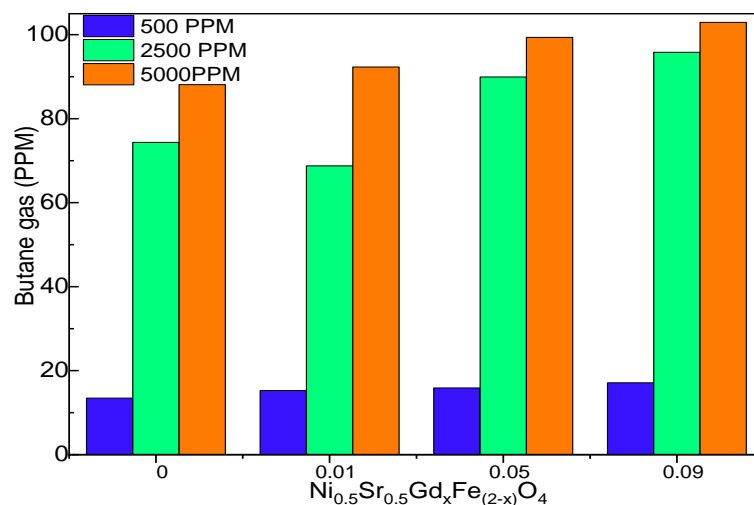


Fig 7.10 Variation of sensitivities of $\text{Ni}_{0.5}\text{Sr}_{0.5}\text{Gd}_x\text{Fe}_{2-x}\text{O}_4$ ($x = 0.00, 0.01, 0.05$ and 0.09) nanocomposite thick films for 500, 2500, 5000 PPM of butane gas vapors at room temperature

There are many parameters effects the gas sensing behavior of the sample such as aspect ratio, particle size, defects on surfaces, surface morphology, thickness of the pellet, chemical reaction rate etc., thus changes in the material resistance as the gas molecules diffuses on the surface. The change in resistance of the sample in the presence and absence of butane gas can be used as the sensing performance in terms of sensitivity, the sensitivity of the sensor can be calculated by using following equation and listed in table 7.5.

$$\text{Sensitivity (S)\%} = \left(\frac{R_g \sim R_a}{R_a} \right) * 100 \quad (6.16)$$

where, R_a is the resistance of a sensing material in air,

R_g is the resistance of a sensing material in the presence of test gas.

In this work, effect of different mol% Gd^{3+} incorporated to the B site of the $\text{Ni}_{0.5}\text{Sr}_{0.5}\text{Fe}_2\text{O}_4$ is investigated. The various concentrations of butane gas sensing performances of the all the prepared samples were studied at a constant temperature. The sensitivity of pure $\text{Ni}_{0.5}\text{Sr}_{0.5}\text{Fe}_2\text{O}_4$ nanoparticles for the 500, 2500 and 5000 PPM

of butane gas was 13.46%, 74.36%, 88.1% and its response time is 38s, 122s, 125s and recovered in 288, 365, 489s. The incorporation of Gd^{3+} to $Ni_{0.5}Sr_{0.5}Fe_2O_4$ nanoparticles, sensitivity of the samples increases with the concentration the Gd^{3+} because of the increase in the defect centers occurred in the Fe^{3+} . The sensitivities of $Ni_{0.5}Sr_{0.5}Gd_{0.01}Fe_{1.99}O_4$ nanoparticles for the 500, 2500 and 5000 PPM of butane gas was 15.25%, 68.76%, 92.31% and its response time is 45s, 136s, 141s and recovered in 244s, 314s, 309s. Sensitivities of $Ni_{0.5}Sr_{0.5}Gd_{0.05}Fe_{1.95}O_4$ nanoparticles for the 500, 2500 and 5000 PPM of butane gas was 15.89%, 89.92%, 99.35% and its response time is 47s, 138s, 148s and recovered in 258s, 341s, 352s. Sensitivities of $Ni_{0.5}Sr_{0.5}Gd_{0.09}Fe_{1.91}O_4$ nanoparticles for the 500, 2500 and 5000 PPM of butane gas was 17.11%, 95.82%, 102.93% and its response time is 58s, 147s, 159s and recovered in 197s, 354s, 421s.

Table 7.5: Butane gas - sensitivity, response time and recovery time of $Ni_{0.5}Sr_{0.5}Gd_xFe_{2-x}O_4$ ($x=0.00, 0.01 < x < 0.09$) nanoferrites.

Composition	Butane (PPM)			Sensitivity (%)			Response time (s)			Recovery time (s)		
$Ni_{0.5}Sr_{0.5}Fe_2O_3$	500	2500	5000	13.46	74.36	88.10	38	122	125	288	365	489
$Ni_{0.5}Sr_{0.5}Gd_{0.01}Fe_{1.99}O_4$	500	2500	5000	15.25	68.76	92.31	45	136	141	244	314	309
$Ni_{0.5}Sr_{0.5}Gd_{0.05}Fe_{1.95}O_4$	500	2500	5000	15.89	89.92	99.35	47	138	148	258	341	352
$Ni_{0.5}Sr_{0.5}Gd_{0.09}Fe_{1.91}O_4$	500	2500	5000	17.11	95.82	102.93	58	147	159	197	354	421

7.4 Conclusion

A series of rare earth Gd^{3+} doped $NiSrFe_2O_4$ nanoparticles were prepared by auto combustion method. The room temperature XRD patterns verified the existence of cubic spinel structure. Crystallite size of the synthesized sample is 27 - 30 nm. The FT-IR spectrum showed two absorption band that are characteristic of nanoferrites and with force constant the K_T values were less than the K_O values in the samples substituted with Gd^{3+} ions. FE-SEM Micrographs images were confirmed that the morphological structure is aggregated to the size of nanoparticles. The EDX spectrum confirms the doping concentration and freedom from impurity elements. The Tauc plots revealed an indirect allowed band gap in the range of 3.77 to 4.26 eV. The VSM analysis of coercivity showed a peak with particle size at a value smaller than the previously reported value of single-domain limit for $NiSrGdFe_2O_4$ that has been attributed to the enhanced role of the surface anisotropy as compared to the bulk for small sizes, which is the result of reduction in super exchange interaction. The maximum gas sensitivity is observed $NiSrGdFe_2O_4$ for 5000 ppm of butane gas at room temperature. This sample's response and recovery time are 159s and 421s, respectively. We can conclude that tailoring of structural, optical, gas sensor and magnetic properties can be achieved by substitution of proper amount of rare earth ions in cubic spinel phase.

7.5 Reference

- [1] V.L. Mathe, R.B. Kamble, Mater. Res. Bull. (2013),
- [2] M. Salavati-Niasari, F. Davar, T. Mahmoudi, Polyhedron 28 (2009) 1455–1458.
- [3] A. Alarifi, N.M. Deraz, S. Shaban, J. Alloys Compd. 486 (2009) 501–506.
- [4] Y. Kinemuchi, K. Ishizaka, H. Suematsu, W. Jiang, K. Yatsui, Thin Solid Films 407 (2002) 109–113.
- [5] P. B. Kharat, A.V. Humbe, J. S. Kounsalye. J Supercond Nov Magn 32 (2019) 1307-
- [6] P. B. Kharat, B. Sandeep. Somvanshi, P. Pankaj. Khirade, and K. M. Jadhav. ACS omega. (2020).
- [7] B. Sandeep. Somvanshi, P. B. Kharat, M. V. Khedkar, K. M. Jadhav, Ceram. Int. (2019).
- [8] R. M. Borade, B. Sandeep. Somvanshi, B. Swati, P. Rajendra, K. M. Jadhav, Mater Research Express. (2020).
- [9] K.S. Jithendra Kumara, G. Krishnamurthy, N. S. Kumar, N. Naik, T. M. Praveen, J. Magn Magn Mater. 451 (2017) 808-821.
- [10] K. S. Jithendra kumara, G. Krishnamurthy, B. E. Kumara swamy, N. D. Shashi kumar, S. Naik, B. S. Krishna and N. Naik, App Organ Chem. 31 (2016).
- [11] M. Veena, A. Somashekarappa, G. J. Shankaramurthy, H. S. Jayanna, H. M. Somashekarappa, J. Magn. Magn. Mater. 419 (2016) 375–385.
- [12] Muhamamd Naeem Ashiqa, Muhammad Fahad Ehsana, Muhammad Javed Iqbalb, Iftikhar Hussain Gulc, J. Alloys Compd. 509 (2011) 5119–5126.
- [13] F. Cheng, C. Liao, J. Kuang, Z. Xu, C. Yan, L. Chen, H. Zhao, Z. Liu, J appl phy, 85 (1999) 2782-2786.

- [14] G. Dascalu, G. Pompilian, B. Chazallon, V. Nica, O.F. Caltun, S. Gurlui, C. Focsa, *App Phy A*, 110 (2013) 915-922.
- [15] R. Thejas, G. D. Prasanna, G. Nagaraju, M. V. Murugendrappa and C. S. Naveen, *Proc I MechE Part E: J Process Mechanical Engineering*. 2022.
- [16] R Thejas, GD Prasanna³, Chaturmukha V. S, Sathish R., Swaroop K., and CS *Sensor Review* 42 (2022) 164–175.
- [17] R.S. Yadav, I. Kuřitka, J. Vilcakova, J. Havlica, L. Kalina, P. Urbánek, M. Machovsky, D. Skoda, M. Masař, M. Holek, *Ultrasonics Sonochemistry* (2017),
- [18] P. Sivakumar, R. Ramesh, A. Ramanand, S. Ponnusamy, C. Muthamizhchelvan, *Mater. Res. Bull.* 46 (2011) 2208–2211.
- [19] M.N. Akhtar, M.A. Khan, *J. Magn. Magn. Mater* (2018).
- [20] D. Makovec, A. Kořak, A. Źnidarřiř, M. Drofenic, *J. Magn. Magn. Mater.* 289 (2005) 32-35.
- [21] K. Maaz, S. Karim, A. Mumtaz, S. K. Hasanain, J. Liu, J. L. Duan, *J. Magn. Magn. Mater.* 321 (2009).
- [22] Kamellia Nejati and Rezvanh Zabihi, *Chem Cent.*, 6 (2012) 23.
- [23] J. Lakshmikantha, G. Krishnamurthy, B. M. Nagabhushan, C. S. Naveen and E. Melagiriappa, *J Supercond Nov Magn* (2022).
- [24] T. Prabhakaran, J. Hemalatha, *J. Alloys Compd.* 509 (2011) 7071–7077.
- [25] L. Guo, X. Shen, Y. Feng, *J. Alloys Compd.* 490 (2010) 301–306.
- [26] A.K. Nikumbh, A.V. Nagawade, G.S. Gugale, M.G. Chaskar, P.P. Bakare, J. *Mater. Sci.* 37 (2002) 637–647.
- [27] D.R. Lide, *CRC Handbook of Chemistry and Physics*, 76th ed, CRC Press, London, 1995.
- [28] M. Srivastava, S. Chaubey, A.K. Ojha, *Mater. Chem. Phys.* 118 (2009) 174–180.

- [29] K.B. Modi, S.J. Shah, N.B. Pujara, T.K. Pathak, N.H. Vasoya, I.G. Jhala, J. Mol. Struct. 1049 (2013) 250–262.
- [30] M. Rahimi, P. Kameli, M. Rajbar, H. Hajihashemi, H. Salamati, J. Mater. Sci. 48 (2013) 2969–2976.
- [31] K. Nakamoto, D. Huang, R. Wang. The Press Co of Chemical Industry, Beijing, (1986) 231–244.
- [32] Z. Noreen, I. Ahmad, F. Siddiqui, A.B. Ziya, T. Abbas, H. Bokhari. Ceram Int. 43 (2017) 10784–90.
- [33] B.S. Holinsworth, D. Mazumder, H. Sims, Q.C. Sun, M.K. Yurtisigi, S.K. Sarker, A. Gupta, W.H. Buther, J.L. Musfeldt, Appl. Phys. Lett. 103 (2013) 082406.
- [34] Q.C. Sun, H. Sims, D. Mazumder, J.X. Ma, B.S. Holinsworth, K.R.O. Neal, G. Kim G, W.H. Butler, A. Gupta, J.L. Musfeldt, Phys. Rev. B. 86 (2012) 205106.
- [35] T. Vigneswari, P. Raji, Int. J. Mater. Res. 109 (2018) 413– 421.
- [36] J. Lakshmikantha, G. Krishnamurthy, B.M. Nagabhushan, E. Melagiriappa, J Solid State Chem., 315 (2022) 123465.
- [37] J. Lakshmikantha, G. Krishnamurthy, R. Hanumantha Nayak, Malathesh Pari, N. Ranjitha, Nagaraj Naik. J of Ing chem com. (2022) 110175.
- [38] M. Chand, A. Kumar, K.S. Annveer, A. Shankar, Ind J Eng Mater Sci. 18 (2011) 385–9.
- [39] Zipare K, Dhumal J, Bandgar S, Mathe V, Shahane G. J Nanosci Nanoeng 1 (2015) 178–82.
- [40] Manova E, Tsoncheva T, Estournes C, Paneva D, Tenchev K, Mitov I, Petrov. Appl Catal A, 300(2) (2006) 170-180.
- [41] R.H. Kodama, A.E. Berkowitz, E.J McNi. Phys. Rev. Lett., 77 (1996) 394–397.

- [42] A.A. Kadam, S.S.Shinde, S.P.Yadav, P.S.Patil, K.Y.Rajpure, *J. Magn. Magn. Mater* 329 (2013) 59–64.
- [43] S. Alone, S.E. Shirsath, R. Kadam, K. Jadhav, *J. Alloys Compd*, 509 (2011) 5055-5060.
- [44] L.B. Tahar, M. Artus, S. Ammar, L. Smiri, F. Herbst, M.-J. Vaulay, V. Richard, J.-M. Grenèche, F. Villain, F. Fievet, *J. Magn. Magn. Mater*, 320 (2008) 3242-3250.
- [45] A. Nikumbh, R. Pawar, D. Nighot, G. Gugale, M. Sangale, M. Khanvilkar, A. Nagawade, *J. Magn. Magn. Mater.* 355 (2014) 201-209.
- [46] O.M. Hemeda, M.Z. Said, M.M. Barakat, *J. Magn. Magn. Mater.* 2001, 224, 132–142.
- [47] A.B. Nawale, N.S. Kanhe, K.R. Patil, S.V. Bhoraskar, V.L. Mathe, *J Alloys Compd*, 509(12) (2011) 4404-4413.
- [48] H. Nathani, R.D.K. Misra, *Mater Sci Eng B*, 113(3) (2004) 228-235.
- [49] J. Hu, Y. Ma, X. Kan, C. Liu, X. Zhang, R. Rao, M. Wang, G. Zheng, *J. Magn. Magn. Mater.* (2020).
- [50] K. B. Modi, M.K Rangolia, M.C. Chhantbar, H.H. Joshi, *J. Mater. Sci.* 41 (2006) 7308–7318.
- [51] T.P. Poudel, B.K. Rai, S. Yoon, D. Guragain, D. Neupane, S.R. Mishra, *J. Alloy. Compd.* 802 (2019) 609–619.
- [52] S. Yoon, K.M Krishnan, *J. Appl. Phys.* 109 (2011) 07B534.
- [53] H. Shenker, *Phys. Rev.* 107 (1957) 1246.
- [54] Y. Yaffet, C. Kittel, *Phys. Rev.* 87 (1952) 290.
- [55] M. Atif, M. Nadeem, R. Grossinger, R. Sato Turtelli, *J. Alloys Compd.* 509 (2011) 5720–5724

CHAPTER 8:-

CONCLUSION

In this chapter, a brief overview of the work down in the previous chapters of the thesis is presented.

Chapter-1

This chapter deals with the introduction about the nano technology, history of nano technology, ferrites, nano ferrites, classification of ferrites and their crystal structures have been explained briefly. Rare earth elements and substituted to nano ferrites. The magnetic properties of ferrites, ferromagnetic theory, electrical properties of ferrites, polarization of dielectrics. Brief account of electrochemical and gas sensor have been explained.

Chapter-2

In this chapter gives the information about the synthesis of self-propagation or solution combustion or auto combustion method by dual fuel of nano ferrites. The prepared nano ferrites were characterized and studies to determine the structural, morphological, thermal, optical, magnetic properties, dielectric properties, electrochemical and gas sensors. In addition, the procedure of recording physical parameter like, PXRD, FT-IR, FESEM, EDAX, TGA-DTA, UV-visible, VSM, LCR meter, cyclic voltammetry and gas sensor instruments were used.

Chapter-3

In the present work, $\text{Sr}_{(1-x)}\text{Ce}_x\text{Fe}_{12}\text{O}_{19}$ nanocrystalline ($x = 0.00 < x < 0.09$) hexaferrite was synthesized by self-propagation method using mixed fuels. X-ray diffraction studies confirmed the unique hexagonal magneto-plumbite phase for the all prepared SrM-HF's. The FESEM studies confirmed that the morphological structure was agglomerated with size of the nanoparticles. The magnetic parameter decreased with increasing concentration of the Cerium ion. The synthesized

hexaferrite exhibit a hard magnetic nature. The different route of exchange between the iron sub-lattices are discussed based on the improvement of the hyperfine fields. Such nanomaterials generally used in magnetic high density recording material, memory storage devices and permanent magnets of high frequency applications etc.

Chapter-4

M-SrHF's Powders $\text{Sr}_{(1-x)}\text{Gd}_x\text{Fe}_{12}\text{O}_{19}$ ($x = 0.00, 0.01 < x < 0.09$, in steps of 0.02) was prepared by auto combustion method using urea and citric acid mixtures as a dual fuel. The x-ray diffraction analysis confirms the M type-phase hexagonal structure. Crystallite size of the synthesized sample is 41 - 45 nm, it was observed that samples $x = 0.09$ exhibits about 5% of secondary phase of $\alpha\text{-Fe}_2\text{O}_3$, GdO_2 as a minor impurity phase. The FT-IR spectrum showed two absorption band that are characteristic of nanoferrites and with force constant the K_T values were less than the K_O values in the samples substituted with Gd^{3+} ions. FE-SEM Micrographs images were confirmed that the morphological structure is aggregated to the size of nanoparticles. The dielectric parameters decrease while AC conductivity increases with frequency. At a particular frequency, the dielectric constant, dielectric loss attain maximum, then begins to decrease with increase in composition. M-H curves were measured at room temperature, its reveals that hard magnetic material, magnetic parameters decrease as gadolinium ion concentration increases. The various exchange routes between iron sub-lattices due to increased hyperfine fields are discussed. The data obtained with Gd^{3+} doping on $\text{SrFe}_{12}\text{O}_{19}$ are with super exchange interaction, single domine particle structure and noncollinear three sub-lattice model and indicating an exceedingly wide application. The synthesized nanoparticles shows extraordinary properties, $\text{SrFe}_{12}\text{O}_{19}$ can be used for electro-magnetic devices, opto-

electronic devices, high frequency permanent magnets, storage devices, galvanometers, motors and recording media.

Chapter-5

In this chapter, A series of nanoferrites, $\text{Sr}_{(1-x)}\text{Ce}_x\text{Fe}_{12}\text{O}_{19}$ ($x = 0.00, 0.01, 0.05$ and 0.09) were successfully synthesized by auto-combustion method with dual fuel (urea and glycine). PXRD, FT-IR, FE-SEM and EDAX confirmed the formation of crystalline nanoparticles with a single-phase magnetoplumbite hexagonal structure. The average crystallite size was found in the range of 42 - 46 nm. The dielectric parameters decreases while AC conductivity increases with frequency. At a particular frequency, the dielectric constant, dielectric loss real part and imaginary part of impedance increases, attain maximum, then begins to decrease with increase in composition. M-H curves were measured at room temperature, it confirmed that these are hard magnetic particles and the values of magnetic parameters decreases as the cerium ion concentration increases. The data showed that the Ce^{3+} doping on $\text{SrFe}_{12}\text{O}_{19}$ induces super exchange interaction, noncollinear three sub-lattice model and single domine particle structure. The electro-catalysis of the SrHF's/GCE was investigated via cyclic voltammetric technique by using drop-coat method. The results indicated that SrHF's/GCE is efficient towards the detection of L-cysteine at different concentration.

Chapter-6

A series of rare earth Sr^{2+} doped $\text{Ni}_{(0.5)}\text{Cu}_{(0.5-x)}\text{Sr}_x\text{MgO}_3$ nanoparticles were prepared by auto combustion method. The room temperature XRD patterns verified the existence of cubic phase structure. Crystallite size of the synthesized sample is ~ 25 nm. The FT-IR spectrum showed two absorption band that are characteristic of nanoferrites and with force constant the K_T values were less than the K_O values in the

samples substituted with Sr^{2+} ions. FE-SEM Micrographs images were confirmed that the morphological structure is aggregated to the size of nanoparticles. The EDX spectrum confirms the doping concentration and freedom from impurity elements. The Tauc plots revealed an indirect allowed band gap in the range of 2.94 to 3.50 eV. The VSM analysis of coercivity showed a peak with particle size at a value smaller than the previously reported value of single-domain limit for $\text{NiSrGdFe}_2\text{O}_4$ that has been attributed to the enhanced role of the surface anisotropy as compared to the bulk for small sizes, which is the result of reduction in super exchange interaction. The maximum gas sensitivity is observed $\text{Ni}_{(0.5)}\text{Cu}_{(0.5-x)}\text{Sr}_x\text{MgO}_3$ 5000 ppm of butane gas at room temperature. This sample's response and recovery time are 11s and 133s, respectively. We can conclude that tailoring of structural, optical, gas sensor and magnetic properties can be achieved by substitution of proper amount of rare earth ions in cubic spinel phase. The electro-catalysis of the NiMgO /GCE was investigated via cyclic voltammetric technique. The results indicated that NiMgO /GCE is efficient towards the detection of dopamine at different concentration.

Chapter-7

A series of rare earth Gd^{3+} doped $\text{NiSrFe}_2\text{O}_4$ nanoparticles were prepared by auto combustion method. The room temperature XRD patterns verified the existence of cubic spinel structure. Crystallite size of the synthesized sample is 27 - 30 nm. The FT-IR spectrum showed two absorption band that are characteristic of nanoferrites and with force constant the K_T values were less than the K_O values in the samples substituted with Gd^{3+} ions. FE-SEM Micrographs images were confirmed that the morphological structure is aggregated to the size of nanoparticles. The EDX spectrum confirms the doping concentration and freedom from impurity elements. The Tauc plots revealed an indirect allowed band gap in the range of 3.77 to 4.26 eV. The VSM

analysis of coercivity showed a peak with particle size at a value smaller than the previously reported value of single-domain limit for $\text{NiSrGdFe}_2\text{O}_4$ that has been attributed to the enhanced role of the surface anisotropy as compared to the bulk for small sizes, which is the result of reduction in super exchange interaction. The maximum gas sensitivity is observed $\text{NiSrGdFe}_2\text{O}_4$ for 5000 ppm of butane gas at room temperature. This sample's response and recovery time are 159s and 421s, respectively. We can conclude that tailoring of structural, optical, gas sensor and magnetic properties can be achieved by substitution of proper amount of rare earth ions in cubic spinel phase.

Research articles published/communicated.

1. **J. Lakshmikantha**, G. Krishnamurthy, B. M. Nagabhushan, C. S. Naveen and E. Melagiriyyappa, Effect of Ce^{3+} Substitution on Sr^{2+} ; Structural and Magnetic Properties of Nanocrystalline $SrFe_{12}O_{19}$ Hexaferrites Prepared by Self-Propagation Method Using Mixed Fuels. J Supercond Nov Magn (2022). **Published in Journal of Superconductivity and Novel Magnetism. Springer Publication impact factor – 1.675**
2. **J. Lakshmikantha**, G. Krishnamurthy, B.M. Nagabhushan, E. Melagiriyyappa, Dielectric properties and magnetic behavior of Gd^{3+} substituted M-type $SrFe_{12}O_{19}$ nanoferrites by auto combustion method using urea and citric acid mixtures as a dual fuel. J. of Solid State Chemistry. 2022, **315**:p. 123465. **Published in Journal Solid State of Chemistry, Elsevier Publication impact factor – 3.656**
3. **J. Lakshmikantha**, G. Krishnamurthy, R. Hanumantha Nayak^b, Malathesh Pari^a, N. Ranjitha^a, Nagaraj Naik^c Synthesis, Structure, Thermal, Magnetic, Dielectric Properties of Ce^{3+} Doped M-Type $SrFe_{12}O_{19}$ And Electrochemical Determination of L-cysteine. J of Ing chem com. 2022, 110175. **Published in Journal Inorganic Chemistry Communications, Elsevier Publication impact factor – 3.428**
4. **J. Lakshmikantha**, G. Krishnamurthy, A study on Electrochemical, Gas sensing and Magnetic properties of Sr^{2+} doped $Ni_{0.5}Cu_{0.5}MgO_3$ synthesized by Auto combustion method. **Communicated.**
5. **J. Lakshmikantha**, G. Krishnamurthy, Electrochemical and Electrolysis of Gd^{3+} substituted to spinel ($NiSrFe_2O_4$) nano-ferrites; synthesis, structural, morphological and Magnetic properties. **Communicated**

Research articles co-published

- 1 N. Ranjitha , G. Krishnamurthy , M.N. Manjunatha, H. S. Bhojya Naik, Malathesh Pari , Vasantakumarnaik N K, **J. Lakshmikantha** , K. Pradeepa, Electrochemical determination of glucose and H_2O_2 using Co(II), Ni(II), Cu(II) complexes of novel 2-(1,3-benzothiazol-2-ylamino)-N-(5-chloro-2-hydroxyphenyl)acetamide: Synthesis, structural characterisation, antimicrobial, anticancer activity and docking studies, **Journal of Molecular Structure** 1274 (2023) 134483. <https://doi.org/10.1016/j.molstruc.2022.134483>. **Elsevier Publication impact factor – 3.841**

Papers Presented/ Attended International/ National Conference/ Seminars

- Participated in National level seminar on “Recent Development in Nano materials and their applications” on 18 and 19th March 2016. Organized by Department of Physics, Kuvempu University, Shankaraghatta, Shivamogga.
- Participated in National level seminar on “Recent Development in Chemical Science” (RDCS-2018)” on 28 and 29th December 2018. Organized by Department of PG Studies Chemistry and Industrial Chemistry Sahyadri Science College, shivamogga.
- Participated in National seminar on “Toolkit to Accelerate research” on 22-23 March 2019. Organized by Kuvempu University, Shankaraghatta, Shivamogga Library in collaboration with LIS Academy Bangalore.
- **Oral presentation** –Virtual International conference on “Interdisciplinary approaches in chemical sciences” IACS-2021 on 21-23th October 2021. Organized by Department of chemistry M.E.S’s Abasaheb Garware College, Maharashtra.
- **Oral presentation** - participated in the National Conference on “Recent Advances in Physics for Interdisciplinary Development” (RAPID – 2K21) on 29-30th September, 2021. Organized by Sri Saila Jagadguru Vageesha Panditharadya (S.J.V.P.) College and P.G.Centre. Harihara.
- **Poster presentation** – participated in the National Conference on “Impact of Chemistry and Biology to the Society and Industry” (ICBSI-2022) on 20-21th May 2022. Organized by Department of Industrial Chemistry, Kuvempu University, Shankaraghatta, Shivamogga.



Effect of Ce³⁺ Substitution on Sr²⁺; Structural and Magnetic Properties of Nanocrystalline SrFe₁₂O₁₉ Hexaferrites Prepared by Self-Propagation Method Using Mixed Fuels

J. Lakshmikantha¹ · G. Krishnamurthy¹ · B. M. Nagabhushan² · C. S. Naveen³ · E. Melagiriappa⁴

Received: 12 November 2021 / Accepted: 18 March 2022

© The Author(s), under exclusive licence to Springer Science+Business Media, LLC, part of Springer Nature 2022

Abstract

The nanocrystalline Sr_{(1-x)Ce_xFe₁₂O₁₉ ($x=0.00 < x < 0.09$) strontium M-type hexaferrites (SrM-HFs) were prepared by self-propagation method using mixed fuels. The structure, morphology, and composition were analyzed by X-ray diffractometer (XRD), field emission scanning electron microscopy (FE-SEM) technique, and energy dispersive X-ray analysis (EDAX), respectively. Vibrating sample magnetometer (VSM) instrument was used for the determination of magnetic properties of each prepared sample. XRD peaks reveal nanocrystalline nature with a hexagonal single phase magnetoplumbite-like crystal structure. The FESEM micrograph shows accumulation of hexaferrite nanocompact magnetic aggregation. In addition, the size of the particles reduced with the increase in of Ce³⁺ ion content. The VSM analysis confirmed that SrM-HFs are hard magnetic in nature. Moreover, it is observed that the saturation magnetization and magnetic parameters of strontium ferrites decrease with the increase of the content of Ce³⁺ ion. In addition, Ce³⁺ substituted SrFe₁₂O₁₉ are most useful for magnetic recording and memory devices.}

Keywords Hexaferrites · Hard ferrites · Force constant · Magnetic properties · Self-propagating method

1 Introduction

Ferrites are unit metal oxides mixed with iron oxides because the main part with the final formula AB₂O₄. Nanocrystalline ferrites play a very vital role in the manufacture of magnetic materials on account of novel physical properties, high-frequency devices, magnetic recording media, catalysis, transformer cores, radiation and absorption devices, medical diagnostics, ferrous fluids, and biomedical fields [1–3]. M-type hexaferrites have the chemical formula AFe₁₂O₁₉, where “A” is Ba, Sr, or Pb [3]. SrM-HFs

are important materials with high chemical stability, specific saturation magnetization, uniaxial magnetocrystalline property, anisotropy, coercivity, high Curie point (temperature) and electrical resistance as well as low dielectric losses [4–6]. Nanostructured SrM-HFs have received greater attention because of their technological and industrial applications that allow it to be used as a permanent magnet [7]. The intrinsic properties of SrM-HFs (SrFe₁₂O₁₉) are strongly impacted by the cation exchange and synthetic methods [8]. SrFe₁₂O₁₉ finds a challenging and competitive application with technological evolution, the foremost unremarkably used material for ferrite permanent magnets [9] that there is nice demand from makers of microwave gadgets, magnetic recording media, broadcast communications devices and so on [10]. Doping SrFe₁₂O₁₉ with transition metal ions or rare earth ions of similar size has resulted in a significant modification of its properties [11, 12]. The magnetic properties of doped magnetic nanoferrites based on both the parts and concentration of the doped part of element, morphology, particle size, and synthesis technique [13, 14]. The low amount doping of rare earth elements in SrFe₁₂O₁₉ leads to the significant changes in its electrical and magnetic properties [8, 11]. Many researchers have studied rare

✉ G. Krishnamurthy
gkrmnaiksahyadri@gmail.com

¹ Department of Chemistry, Sahyadri Science College, Shivamogga, Karnataka 577203, India

² Department of Chemistry, M.S. Ramaiah Institute of Technology, Bengaluru, Karnataka 560054, India

³ Department of Physics, School of Engineering, Presidency University, Bengaluru 560064, India

⁴ Research Resource Center, Visvesvaraya Technological University, Belagavi, Karnataka 590018, India

Published online: 27 May 2022



Content courtesy of Springer Nature, terms of use apply. Rights reserved.



Contents lists available at ScienceDirect

Journal of Solid State Chemistry

journal homepage: www.elsevier.com/locate/jssc



Dielectric properties and magnetic behavior OF Gd³⁺ substituted M-type SrFe₁₂O₁₉ nanoferrites by auto combustion method using urea and citric acid mixtures as a dual fuel



J. Lakshminantha^a, G. Krishnamurthy^{a,*}, B.M. Nagabhushan^b, E. Melagiriappa^c

^a Department of Chemistry, Sahyadri Science College, Kuvempu University Shivamogga, Karnataka, 577203, India

^b Department of Chemistry, M.S. Ramaiah Institute of Technology, Bangalore, 560054, India

^c Vasantrao Technological University, Belagavi, Karnataka, 590018, India

ARTICLE INFO

Keywords:

Hard ferrites
Magnetic properties
Dielectric constant
Dielectric loss, AC conductivity And rare earth elements

ABSTRACT

Nanosized M-type hexaferrites Sr_{1-x}Gd_xFe₁₂O₁₉ (x = 0.00; 0.01 < x < 0.09; steps of 0.02) have been synthesized by auto combustion method using urea and citric acid mixtures. Influence of Gd³⁺ ions substitution on structural, electrical and magnetic properties of Sr_{1-x}Gd_xFe₁₂O₁₉ nanoferrites were investigated by XRD, FTIR, FESEM, ICR meter and VSM techniques. The XRD studies confirmed the formation of single phase lattice whereas as the sample with x = 0.09 exhibits about 5% of secondary phase. It was found that the lattice parameter increased with increasing in Gd³⁺ ion content. FTIR spectra have shown two absorption bands. The dielectric parameters were described based on the Maxwell-Wagner's two layer model. It is observed that the dielectric constant (ε'), the loss tangent (tanδ), decrease whereas the AC conductivity (σ_{ac}) increases with increasing applied field frequency. Moreover, the vibrating sample magnetometer (VSM) analysis confirmed that M-SrHPs are hard magnetic in behavior. It was observed that the values of saturation magnetization (M_s), remanence magnetization (M_r), coercivity (H_c) and magnetic parameters of strontium ferrites decrease with the increase of the dopant Gd³⁺ in strontium ferrites. In addition, Gd³⁺ substituted SrFe₁₂O₁₉ are most useful for magnetic recording media and electro-magnetic devices.

1. Introduction

M-type strontium hexaferrites (M-SrHPs) have attracted more demand in the field of science and technology owing to their high Curie temperature (720 K), high saturation magnetization or high hysteresis loss, large magneto-crystalline, anisotropy, high intrinsic conductivity and good thermal or chemical stability [1,2]. In recent years, strontium hexaferrites (SrFe₁₂O₁₉) is the suitable are materials of optical, electrical and magnetic properties [3]. SrFe₁₂O₁₉ has heat thermal resistance, resistance of corrosion and significant for many applications [4]. Strontium hexaferrites are used as microwave gadgets [5,6], radiation and absorption devices [7], and magnetic recording media [8] due to their low cost and chemically stable materials. SrFe₁₂O₁₉ are used in broadcast communications devices [9], high frequency devices, magnetic coatings [10], absorbing ferric oxides, electric power generation, automotive electronics and magnetic catalysts [11]. The application are mainly depends on the composition, the magnitude and orientation of the magnetic

moment. Furthermore, the substitution of small amount of rare-earth elements (Sm³⁺, Gd³⁺, Er³⁺, Ce³⁺, Eu³⁺, Nd³⁺, Dy³⁺, etc) into SrFe₁₂O₁₉ nanoferrites significantly improves the electrical and magnetic properties of M-SrHPs [12]. The modifications are more bound up with the size, shape, orientation, and domain configuration of the nano structured [13-17].

In case of ferrites, the dielectric phenomenon can be explained on the basis of microstructural factors. The dielectric properties are stable at high frequencies and depend on synthesis process, sintering time and temperature, chemical composition of additives and grain structure. The study of dielectric properties provides the valuable information for potential applications [18]. In the present investigation, Fe³⁺ magnetic ions are distributed in five sub-lattices with a hexagonal structure (space group P63/mmc) [19]. 12(k), 2(a) and 2(b) sites exhibit spins (+) direction, but those in the 4(f₁) and 4(f₂) sites exhibit spins (-) direction. The net magnetic moment is comparing between the spin (+) direction and spin (-) direction with magnetic moments [20].

* Corresponding author. Department of Chemistry, Sahyadri Science College, Shivamogga, Karnataka, 577203, India.
E-mail address: gkumar@sahyadri@gmail.com (G. Krishnamurthy).

<https://doi.org/10.1016/j.jssc.2022.123465>

Received 22 March 2022; Received in revised form 28 July 2022; Accepted 30 July 2022

Available online 10 August 2022

0022-4596/© 2022 Published by Elsevier Inc.



Contents lists available at ScienceDirect

Inorganic Chemistry Communications

journal homepage: www.elsevier.com/locate/inoche



Short communication

Synthesis, structure, thermal, magnetic, dielectric properties of Ce³⁺ doped M-type SrFe₁₂O₁₉ and electrochemical determination of L-cysteine

J. Lakshmikantha^a, G. Krishnamurthy^{a,*}, R. Hanumantha Nayak^b, Malathesh Pari^a, N. Ranjitha^a, Nagaraj Naik^c

^a Department of Chemistry, Sahyadri Science College, Kowmpu University, Shivmoga, Karnataka 577203, India

^b Department of Science, Government Polytechnic, Ramnagara, Karnataka 562159, India

^c Department of Chemistry, University of Mysore, Mysore, Karnataka 570005, India

ARTICLE INFO

Keywords:

Rare earth element
Dielectric parameters
Magnetic properties and cyclic voltammetry (L-cysteine)

ABSTRACT

Cerium substituted SrFe₁₂O₁₉ with the nano composition of Sr_(1-x)Ce_xFe₁₂O₁₉ (x = 0.00, 0.01, 0.05 and 0.09) have been prepared using auto-combustion technique with dual fuel. The PXRD images confirmed a single-phase hexagonal crystalline structure similar to a magnetoplumbite for all samples. Fourier transform infra-red spectroscopy (FT-IR), field emission-scanning electron spectroscopy (FE-SEM), elemental mapping (EDS) were used to examine for the structure and morphology of the samples. The temperature dependent hexagonal phase formation and percentage weight loss was studied by thermogravimetric and differential thermal analysis (TG-DTA). Vibrating sample magnetometer (VSM) analysis confirmed that M-SrHF's are hard magnetic in nature and super paramagnetic, these are measured at room temperature. It was found that, with the increase of the dopant Ce³⁺ in strontium ferrites, the values of saturation magnetization (M_s), remanence magnetization (M_r), coercivity (H_{cj}) and magnetic parameters of strontium ferrites decrease. The electrochemical behavior of the SrHF's electrode and the electro-oxidation of L-cysteine was investigated using of cyclic voltammetry (CV). The best voltammetric response has been observed for a SrHF's electrode in buffer solution at pH of 7.0 with an acquisition and scan rate of 50 mV s⁻¹. The dielectric properties are measured in LCR meter and described based on the Maxwell-Wagner's two layer model. The electron hopping between Sr²⁺ and Sr³⁺, as well as Fe³⁺ and Fe²⁺ ions on B-sites, drives the conduction mechanism in these ferrites, these nano hexaferrites which shows its suitability in various technological applications.

1. Introduction

Hexaferrites has been shown to be supreme for the best permanent magnetic materials owing to their suitable properties for physical and chemical behaviors in optical, electrical and magnetic in nature [1,2]. Strontium Hexaferrites (SrHF's) have unique properties including more values of magnetic anisotropy, electrical resistance, Curie high temperature and low dielectric loss. Moreover, they possessed excellent chemical stability and corrosion resistance [3]. SrHF's nanomaterials are much lower electro-conductive than ferro-metallic magnets, assuring suppression of eddy currents and reduced energy loss in higher frequency [4,5]. They have been in a scouting of hexagonal ferrites based on the growing demand for low cost, narrative magnetic compounds with specific adjustable properties for a variety of industrial and technological applications [6], such as micro-electrochemical systems,

electricity generation, nanocatalysts [7,8]. The area of research is more attracted to the researchers from last few decades due to their promising magnetic nanomaterials with appropriate physicochemical properties, functionalized surface and improved biocompatibility have been broadly examined for different restorative, indicative, and remedial applications, for example, magnetic nanofluids (Ferrofluids), specific drug delivery, fluid hyperthermia, as a contrast enhancer in magnetic resonance or reverberation imaging (MRI), cell detachment, tissue fixing, biosensors, and magnetic fluid hyperthermia therapies (MFHT) of cancerous cells in human body. Nano-scaled materials with these attributes are primarily implementable in both the 'in-vitro' and 'in-vivo' bio-applications such as biological imaging (as contrast enhancer). Magnetic nanoparticles are alluring catalyst since they can be isolated from the response medium by applying an outside magnetic attractive field. Magnetic partition is a charming option in contrast to filtration or

* Corresponding author.
E-mail address: gkrishnamurthy@gmail.com (G. Krishnamurthy).

<https://doi.org/10.1016/j.inoche.2022.110175>

Received 5 August 2022; Received in revised form 14 October 2022; Accepted 27 October 2022

Available online 1 November 2022

1387-7003/© 2022 Elsevier B.V. All rights reserved.

KUVEMPU  **UNIVERSITY**

Jnana Sahyadri Shankarghatta-577451

**“STUDIES ON RARE EARTH METAL SUBSTITUTED FERRITES
NANO PARTICLES: STRUCTURAL, MORPHOLOGICAL AND
MAGNETIC PROPERTIES”**

Thesis Submitted to the Faculty of Science, Kuvempu
University for the award of the Degree of

**DOCTOR OF PHILOSOPHY
IN
INDUSTRIAL CHEMISTRY**

Submitted By

Mr. Lakshmikantha J. M.Sc

Research Scholar

Department of Industrial Chemistry,

Sahyadri Science College,

Kuvempu University

Under the Guidance of

Dr. G. Krishnamurthy M.Sc., M.Phil., Ph.D.,

Professor

Department of Chemistry & Industrial chemistry

Sahyadri Science College, Shivamogga

2022

In this chapter, a brief overview of the work down in the previous chapters of the thesis is presented.

Chapter-1

This chapter deals with the introduction about the nano technology, history of nano technology, ferrites, nano ferrites, classification of ferrites and their crystal structures have been explained briefly. Rare earth elements and substituted to nano ferrites. The magnetic properties of ferrites, ferromagnetic theory, electrical properties of ferrites, polarization of dielectrics. Brief account of electrochemical and gas sensor have been explained.

Chapter-2

In this chapter gives the information about the synthesis of self-propagation or solution combustion or auto combustion method by dual fuel of nano ferrites. The prepared nano ferrites were characterized and studies to determine the structural, morphological, thermal, optical, magnetic properties, dielectric properties, electrochemical and gas sensors. In addition, the procedure of recording physical parameter like, PXRD, FT-IR, FESEM, EDAX, TGA-DTA, UV-visible, VSM, LCR meter, cyclic voltammetry and gas sensor instruments were used.

Chapter-3

In the present work, $\text{Sr}_{(1-x)}\text{Ce}_x\text{Fe}_{12}\text{O}_{19}$ nanocrystalline ($x = 0.00 < x < 0.09$) hexaferrite was synthesized by self-propagation method using mixed fuels. X-ray diffraction studies confirmed the unique hexagonal magneto-plumbite phase for the all prepared SrM-HF's. The FESEM studies confirmed that the morphological structure was agglomerated with size of the nanoparticles. The magnetic parameter decreased with increasing concentration of the Cerium ion. The synthesized

hexaferrite exhibit a hard magnetic nature. The different route of exchange between the iron sub-lattices are discussed based on the improvement of the hyperfine fields. Such nanomaterials generally used in magnetic high density recording material, memory storage devices and permanent magnets of high frequency applications etc.

Chapter-4

M-SrHF's Powders $\text{Sr}_{(1-x)}\text{Gd}_x\text{Fe}_{12}\text{O}_{19}$ ($x = 0.00, 0.01 < x < 0.09$, in steps of 0.02) was prepared by auto combustion method using urea and citric acid mixtures as a dual fuel. The x-ray diffraction analysis confirms the M type-phase hexagonal structure. Crystallite size of the synthesized sample is 41 - 45 nm, it was observed that samples $x = 0.09$ exhibits about 5% of secondary phase of $\alpha\text{-Fe}_2\text{O}_3$, GdO_2 as a minor impurity phase. The FT-IR spectrum showed two absorption band that are characteristic of nanoferrites and with force constant the K_T values were less than the K_O values in the samples substituted with Gd^{3+} ions. FE-SEM Micrographs images were confirmed that the morphological structure is aggregated to the size of nanoparticles. The dielectric parameters decrease while AC conductivity increases with frequency. At a particular frequency, the dielectric constant, dielectric loss attain maximum, then begins to decrease with increase in composition. M-H curves were measured at room temperature, its reveals that hard magnetic material, magnetic parameters decrease as gadolinium ion concentration increases. The various exchange routes between iron sub-lattices due to increased hyperfine fields are discussed. The data obtained with Gd^{3+} doping on $\text{SrFe}_{12}\text{O}_{19}$ are with super exchange interaction, single domine particle structure and noncollinear three sub-lattice model and indicating an exceedingly wide application. The synthesized nanoparticles shows extraordinary properties, $\text{SrFe}_{12}\text{O}_{19}$ can be used for electro-magnetic devices, opto-

electronic devices, high frequency permanent magnets, storage devices, galvanometers, motors and recording media.

Chapter-5

In this chapter, A series of nanoferrites, $\text{Sr}_{(1-x)}\text{Ce}_x\text{Fe}_{12}\text{O}_{19}$ ($x = 0.00, 0.01, 0.05$ and 0.09) were successfully synthesized by auto-combustion method with dual fuel (urea and glycine). PXRD, FT-IR, FE-SEM and EDAX confirmed the formation of crystalline nanoparticles with a single-phase magnetoplumbite hexagonal structure. The average crystallite size was found in the range of 42 - 46 nm. The dielectric parameters decreases while AC conductivity increases with frequency. At a particular frequency, the dielectric constant, dielectric loss real part and imaginary part of impedance increases, attain maximum, then begins to decrease with increase in composition. M-H curves were measured at room temperature, it confirmed that these are hard magnetic particles and the values of magnetic parameters decreases as the cerium ion concentration increases. The data showed that the Ce^{3+} doping on $\text{SrFe}_{12}\text{O}_{19}$ induces super exchange interaction, noncollinear three sub-lattice model and single domine particle structure. The electro-catalysis of the SrHF's/GCE was investigated via cyclic voltammetric technique by using drop-coat method. The results indicated that SrHF's/GCE is efficient towards the detection of L-cysteine at different concentration.

Chapter-6

A series of rare earth Sr^{2+} doped $\text{Ni}_{(0.5)}\text{Cu}_{(0.5-x)}\text{Sr}_x\text{MgO}_3$ nanoparticles were prepared by auto combustion method. The room temperature XRD patterns verified the existence of cubic phase structure. Crystallite size of the synthesized sample is ~ 25 nm. The FT-IR spectrum showed two absorption band that are characteristic of nanoferrites and with force constant the K_T values were less than the K_O values in the

samples substituted with Sr^{2+} ions. FE-SEM Micrographs images were confirmed that the morphological structure is aggregated to the size of nanoparticles. The EDX spectrum confirms the doping concentration and freedom from impurity elements. The Tauc plots revealed an indirect allowed band gap in the range of 2.94 to 3.50 eV. The VSM analysis of coercivity showed a peak with particle size at a value smaller than the previously reported value of single-domain limit for $\text{NiSrGdFe}_2\text{O}_4$ that has been attributed to the enhanced role of the surface anisotropy as compared to the bulk for small sizes, which is the result of reduction in super exchange interaction. The maximum gas sensitivity is observed $\text{Ni}_{(0.5)}\text{Cu}_{(0.5-x)}\text{Sr}_x\text{MgO}_3$ 5000 ppm of butane gas at room temperature. This sample's response and recovery time are 11s and 133s, respectively. We can conclude that tailoring of structural, optical, gas sensor and magnetic properties can be achieved by substitution of proper amount of rare earth ions in cubic spinel phase. The electro-catalysis of the NiMgO /GCE was investigated via cyclic voltammetric technique. The results indicated that NiMgO /GCE is efficient towards the detection of dopamine at different concentration.

Chapter-7

A series of rare earth Gd^{3+} doped $\text{NiSrFe}_2\text{O}_4$ nanoparticles were prepared by auto combustion method. The room temperature XRD patterns verified the existence of cubic spinel structure. Crystallite size of the synthesized sample is 27 - 30 nm. The FT-IR spectrum showed two absorption band that are characteristic of nanoferrites and with force constant the K_T values were less than the K_O values in the samples substituted with Gd^{3+} ions. FE-SEM Micrographs images were confirmed that the morphological structure is aggregated to the size of nanoparticles. The EDX spectrum confirms the doping concentration and freedom from impurity elements. The Tauc plots revealed an indirect allowed band gap in the range of 3.77 to 4.26 eV. The VSM

analysis of coercivity showed a peak with particle size at a value smaller than the previously reported value of single-domain limit for $\text{NiSrGdFe}_2\text{O}_4$ that has been attributed to the enhanced role of the surface anisotropy as compared to the bulk for small sizes, which is the result of reduction in super exchange interaction. The maximum gas sensitivity is observed $\text{NiSrGdFe}_2\text{O}_4$ for 5000 ppm of butane gas at room temperature. This sample's response and recovery time are 159s and 421s, respectively. We can conclude that tailoring of structural, optical, gas sensor and magnetic properties can be achieved by substitution of proper amount of rare earth ions in cubic spinel phase.